Adaptor proteins form an interaction network during clathrin-mediated endocytosis

Dissertation submitted to the University of Hamburg
Universität Hamburg
Fakultät für Mathematik, Informatik und Naturwissenschaft
Fachbereich Chemie
Institut für Biochemie und Molekularbiologie

George Draper-Barr

Hamburg, January 2025

Defence date: 21.03.2025

Approval to Publish: 05.04.2025

Dissertation reviewers:

Professor Dr Kay Grünewald

Professor Dr Arwen Pearson

Examination commission:

Chair: Professor Dr Kay Grünewald

Deputy Chair: Professor Dr Maya Topf

Member: Dr Henning Tidow

The work presented in this dissertation was carried out in between October 2020 and October 2024 in the Team of Dr. Maria M. Garcia-Alai at the European Molecular Biology Laboratory (EMBL) in Hamburg, Germany.

Contents

I. Scientific publications

- Burastero, Osvaldo, George Draper-Barr, Bertrand Raynal, Maelenn Chevreuil, Patrick England, and Maria Garcia Alai. 2023. 'Raynals, an Online Tool for the Analysis of Dynamic Light Scattering'. Acta Crystallographica. Section D, Structural Biology 79 (Pt 8): 673–83. https://doi.org/10.1107/S2059798323004862.

- Draper-Barr, George, Lucas Defelipe, David Ruiz Carrillo, Emil Gustavsson, Meytal Landau, and Maria M. Garcia-Alai. 2024. "Sla2 is a Core Interaction Hub for Clathrin Light Chain and the Pan1/End3/Sla1 Complex." *BioRxiv*. https://doi.org/10.1101/2024.11.14.623549.

II. List of Abbreviations

Abbreviation	Full term
°C	Degree Celsius
µg	Microgram
µL	Microlitre
µm	Micrometre
µM	Micromolar
2D	Two-dimensional
3D	Three-dimensional
5IP	D-myo-inositol 1,2,3,5,6-pentakisphosphate
Å	Angstrom
ABD	Actin Binding Domain
ACB	Actin binding
AF	AlphaFold
AIC	Akaike Information Criteria
ANTH	AP180 N-Terminal Homology
AP	Adaptor Protein
CCP	Clathrin-Coated Pit
CCS	Clathrin-Coated Sites
CCV	Clathrin-Coated Vesicle
CD	Circular Dichroism
CHC	Clathrin Heavy Chain
CLC	Clathrin Light Chain
CLEM	Correlative Light and Electron microscopy

CME	Clathrin-Mediated endocytosis
cv	Column volume
Cryo-ET	Electron cryogenic-tomography
DLS	Dynamic Light Scattering
D:S	Droplet:Solution ratio
EH domain	Eps15 Homology Domain
EM	Electron Microscopy
ENTH	Epsin N-terminal Homolog
FRAP	Fluorescence Recovery After Photobleaching
FRET	Forster Resonant Energy Transfer
g	Gram
h	Hour
IDR	Intrinsically Disordered Regions
L	Litre
min	Minute
ml	Millilitre
mM	Millimolar
MP	Mass Photometry
ms	Millisecond
MST	MicroScale Thermophoresis
nanoDSF	nanoDifferential Scanning Fluorimetry
nm	Nanometre
nM	Nanomolar
PH	Pleckstrin homology

PIP	Phosphatidyl Inositol phosphate
$PI(4,5)P_2$	Phosphatidylinositol 4,5-bisphosphate
PQ	Poly-glutamine
RMSD	Root mean square deviation
SHD	Sla1 Homology Domain
SLiM	Short Linear Motifs
SPA cryo-EM	Single particle electron cryogenic-microscopy
THATCH	Talin-Hip1/R/Sla2p Actin-tethering C-terminal homology
UBA domain	Ubiquitin-associated domain
UIM	Ubiquitin Interaction motifs
USH	Up-Stream Helix

III List of Tables

IV List of Figures

1. German Abstract

Die Clathrin-vermittelte Endozytose ist ein hochkonservierter Prozess in Eukaryoten und essenziell für verschiedene Funktionen wie die Internalisierung von Rezeptoren und die Nährstoffaufnahme. Während der Clathrin-vermittelten Endozytose bilden sich selektive Protein-Komplexe in spezifischen Bereichen der Membran, was schließlich zur Bildung Clathrin-beschichteter Vesikel (CCV) führt. Die Kontrolle dieser Assemblierungen erfolgt durch regulatorische Protein-Protein-Interaktionen, an denen Proteine beteiligt sind, die zu verschiedenen Zeitpunkten während der Reifung der Clathrin-beschichteten Grube (CCP) eintreffen. Dazu gehört das Mid-Coat-Adapterprotein Sla2, das die Plasmamembran mit dem Aktin-Zytoskelett verbindet, welches die primäre treibende Kraft bei der Membraneinstülpung darstellt.

Die in dieser Arbeit vorgestellte Forschung beschreibt ein Interaktionsnetzwerk mit Sla2 als zentralem Knoten und den interagierenden Proteinen Clathrin-Leichtkette (CLC), Sla1 und Pan1 als Hauptfokus der biophysikalisch charakterisierten Interaktionen. Sla2, das homologe Protein in Pilzen, wird mit Hip1R, dem Homolog aus Metazoa, verglichen. Es zeigt sich, dass die zentrale Region von Sla2 eine zusätzliche Interaktion mit CLC eingeht, die in Hip1R nicht vorhanden ist. Diese Region ist zudem für die Regulation von Pan1 verantwortlich. Der Vergleich der Sequenzkonservierung mit Hip1R unterstreicht die Spezifität dieser pilzspezifischen Interaktion mit Pan1 und Sla1. In vivo zeigt sich, dass die nicht-konservierte Region eine dominante Rolle gegenüber der mit Hip1R geteilten Region spielt.

Die mittels kryogener Elektronenmikroskopie bestimmte Struktur der C-terminalen Region von Sla2 wird vorgestellt, um diese Ergebnisse in einen strukturellen Kontext zu setzen, da die hier beschriebenen Domänen durch die Interaktion mit CLC reguliert werden. Der Einsatz von AlphaFold3 ermöglichte mehrere zentrale Aspekte dieser Forschung: die Erstellung eines Ausgangsmodells für die Strukturoptimierung, die Vorhersage von Protein-Protein-Komplexen sowie die Annotation gefalteter Domänen in Sla1. Letzteres erlaubte es, die wahrscheinlichste Interaktionsstelle zwischen Sla2 und Sla1 auf die dritte SH3-Domäne einzugrenzen, anstatt auf eine andere gefaltete Domäne, die als PH-Domäne identifiziert wurde – eine Domänenklasse, die für ihre Fähigkeit zur Bindung von Phosphatidylinositol bekannt ist.

Zudem wurde gezeigt, dass die zentrale Region von Sla2 mit einem der Initiatorproteine der Endozytose, Ede1, interagiert. Ede1 bildet sowohl in vitro als auch in vivo Phasenseparationen, und wir zeigen, dass Sla2 in diese phasenseparierten Tropfen rekrutiert werden kann. Darüber hinaus kann Sla2 sowohl die Clathrin-Leichtkette als auch die Clathrin-Schwerkette in seine eigenen phasenseparierten Tropfen einbinden.

Diese Erkenntnisse liefern detaillierte Einblicke in die regulatorischen Interaktionen innerhalb der endozytischen Grube. Sie basieren auf biophysikalischen und biochemischen Daten, Fluoreszenzmikroskopie, struktureller Bestimmung durch zwei verschiedene Methoden, KI-gestütztem Protein-Protein-Interaktionsmodellieren sowie der in vivo-Analyse des Interaktionsnetzwerks um Sla2.

2. English Abstract

Clathrin-mediated endocytosis is a process in eukaryotes that is highly conserved across this domain of life, and is essential for several functions such as receptor internalisation and nutrition. During clathrin-mediated endocytosis, selective assemblies of protein complexes form in specific regions of the membrane, ending in the formation of clathrin-coated vesicles (CCV). Controlling these assemblies are regulatory protein-protein interactions, involving proteins arriving at all time points of the Clathrin-coated pit (CCP) maturation. This includes the mid-coat adaptor protein Sla2, which connects the plasma membrane and the actin cytoskeleton, which is the primary force generator during membrane invagination.

The work presented in this thesis presents an interaction network with Sla2 as the central node, and the interacting proteins Clathrin Light Chain (CLC), Sla1, and Pan1 as the primary focus of the biophysically characterised interactions. Sla2, the Fungi homolog, is compared to Hip1R, homolog from Metazoa. The central region of Sla2 is shown to have an additional interaction with CLC not found in Hip1R. This region is also responsible for the regulation of Pan1. Sequence conservation in comparison to Hip1R highlighted the specificity of this Fungi-specific interaction with Pan1 and Sla1. The non-conserved region is dominant over the shared region with Hip1R *in vivo*. The structure, determined by electron cryogenic-microscopy, of the C-terminal region of Sla2 is presented to contextualise these results as the domains detailed here are regulated by the interaction with CLC. The use of AlphaFold3 enabled several key functions of this research: initial model production for structure refinement, protein-protein complex prediction, and folded domain annotation for Sla1. This last function narrowed down the most likely interaction site between Sla2 and Sla1 through to the third SH3 domain instead of the other folded domain, which was determined to be a PH domain, which are characterised by the ability to bind phosphatidylinositol.

The central region of Sla2 has been shown to also interact with one of the initiator proteins of endocytosis, Ede1. Ede1 phase separates both *in vitro* and *in vivo* and we show that Sla2 can be recruited to phase separated droplets. In addition, Sla2 can recruit Clathrin Light Chain and Clathrin Heavy Chain into its own phase separated droplet.

These findings fill in details of the regulatory interactions in the endocytic pit, with biophysical and biochemical data, fluorescence microscopy, structural determination by two different methods, AI assisted protein-protein interaction modelling, and *in vivo* determination of the interaction network surrounding Sla2.

3. Introduction

3.1 Cells regulate interactions with their environment to survive

Life is defined by three essential functions: obtaining nutrition, responding to environmental changes (relation), and reproduction. At the cellular level, these functions depend on the plasma membrane, which defines the cell's boundaries and mediates its interactions. This barrier enables the cell to define and control the vast majority of interactions between the interior of the cell, the cytoplasm, and the exterior of the cell. In addition to the plasma membrane, internal membranes play crucial roles in organizing cellular functions. Internal membranes segregate molecules important for cellular activities to form sub-cellular compartments called organelles.

3.2 Cell membranes and lipid markers

The plasma membrane and internal cellular membranes act as dynamic platforms for cellular signalling and organization with islands and pockets of higher local concentrations of signals and markers dependent on the internal and external conditions of the cell; serving as messengers to initiate processes, inducing the recruitment of other proteins. These membranes contain lipid markers, specialized molecules that act as signals to recruit proteins and coordinate cellular processes. One critical signalling mechanism involves the modification of membrane lipids. Lipid phosphorylation, is particularly important for protein trafficking (De Craene et al. 2017). These markers are bound by protein domains such as the ANTH and ENTH domains described in previous research from the Garcia-Alai team has characterized the role of ANTH and ENTH domains in lipid binding. ANTH and ENTH domains are lipid-binding motifs that specifically recognize phosphoinositide. Phosphatidylinositol 4,5-bishosphate ($PI(4,5)P_2$) is bound by ANTH and ENTH domains found in the Sla2:Ent1/2 complex, which is one of the critical components of endocytosis in yeast (Lizarrondo et al.

2021). These lipid signalling pathways are tightly coupled to protein trafficking, ensuring efficient coordination of cellular processes.

3.3 Protein Trafficking

Vesicle-mediated transport is essential for both intracellular organization and communication with the extracellular environment (Rothman and Wieland 1996). This highly regulated system enables the coordination of specialized cellular activities across compartments (Alberts 2015; Palade 1975). Protein trafficking depends on specific protein families that form distinct transport networks through combinatorial protein-protein/lipid interactions (Cai, Reinisch, and Ferro-Novick 2007; Schekman and Orci 1996). Protein trafficking involves cargo selection, membrane deformation, vesicle formation, and delivery to target sites (Faini et al. 2013). These processes often involve lipid-binding adaptor proteins that recruit cargo and coat proteins to specific membrane regions.

The study of vesicle trafficking began with ground-breaking electron microscopy images of protein transport in pancreatic cells (Palade 1975). Since then, advancements in imaging techniques, genetic manipulation, and other methods have provided detailed insights into the adaptations to enhance the specificity and efficiency of these processes. Within the endocytic and secretory pathways, vesicles assemble to deliver transported proteins to their target sites (Robinson 1991). Some cargo proteins contain short linear peptide motifs, such as di-leucine motifs and YXXØ, which recruit adaptor proteins. These adaptor proteins contribute to the composition of the protein coat and subsequent destination of the cargo (Bonifacino and Traub 2003; Höning, Sandoval, and Von Figura 1998).

This complex system has evolved since the last eukaryotic common ancestor, approximately 1.09 billion years ago, and includes at least nine distinct vesicle coat complexes (Dacks and Field 2018), such as Clathrin, COPI, COPII, TSET, and others. Coat proteins, such as Clathrin, COPI, and COPII, form scaffolds on top of the membrane to drive membrane curvature and cargo sorting. The diversity of vesicle coat complexes, such as clathrin and COPI, reflects their evolutionary adaptations to specialized cellular functions. Determining the

trafficking systems and key proteins involved can be challenging, especially with more than 50 proteins identified in Clathrin Mediated Endocytosis alone (Kaksonen and Roux 2018). Adaptor Proteins (AP) have garnered significant interest due to their diverse roles in protein transport networks and their essentiality for cell survival (Boehm and Bonifacino 2002; De Matteis and Luini 2011; Dell'angelica and Bonifacino 2019; Shin, Nile, and Oh 2021).

3.4 Clathrin-Mediated Endocytosis

Clathrin-mediated endocytosis (CME) is one of the most well-studied pathways of membrane trafficking and receptor internalisation. In this process, membrane receptors are internalized into the cell as cargoes upon their activation, leading to the assembly of the endocytic machinery and the formation of a protein coat around the to-be-internalised region of the plasma membrane. Central to CME is the protein Clathrin, which assembles into a coat around endocytic sites, driving membrane invagination (Kirchhausen, Owen, and Harrison 2014).

Wide-ranging research on clathrin-mediated endocytosis in budding yeast has provided a detailed understanding of its timeline and components, involving over 60 proteins, as described in various genetic and microscopy studies (Kaksonen and Roux 2018; Mund et al. 2018; Skruzny et al. 2015).

The components of the endocytic machinery have been well characterized, and it has been shown that their arrival and function within the endocytic site are regulated by post-translational modifications like phosphorylation and ubiquitination (Mettlen et al. 2018). Based on their function in the endocytic coat, proteins have been categorized into different modules: early arriving proteins (e.g., Ede1, Sla2, and Ent1/2), coat proteins (e.g. Clathrin), WASP/Myo proteins, actin module proteins, and scission proteins (e.g., Dynamin)(Mund et al. 2018) (Figure 1).

CME occurs sequentially and can be divided into the following stages (Figure 1): (1) Initiation, Initiator proteins bind cargo and recruit the endocytic machinery after an increase in the local concentration of $PI(4,5)P_2$; (2) Maturation, The clathrin coat assembles, generating

membrane curvature, forming clathrin-coated pits; (3) Membrane invagination, Actin polymerization provides force for membrane deformation; and (4) Scission, the GTPase dynamin facilitates vesicle release. After scission, clathrin-coated vesicles are uncoated by chaperones such as Hsp70 and Auxilin, enabling vesicle recycling (Kang et al. 2009; Xing et al. 2010).

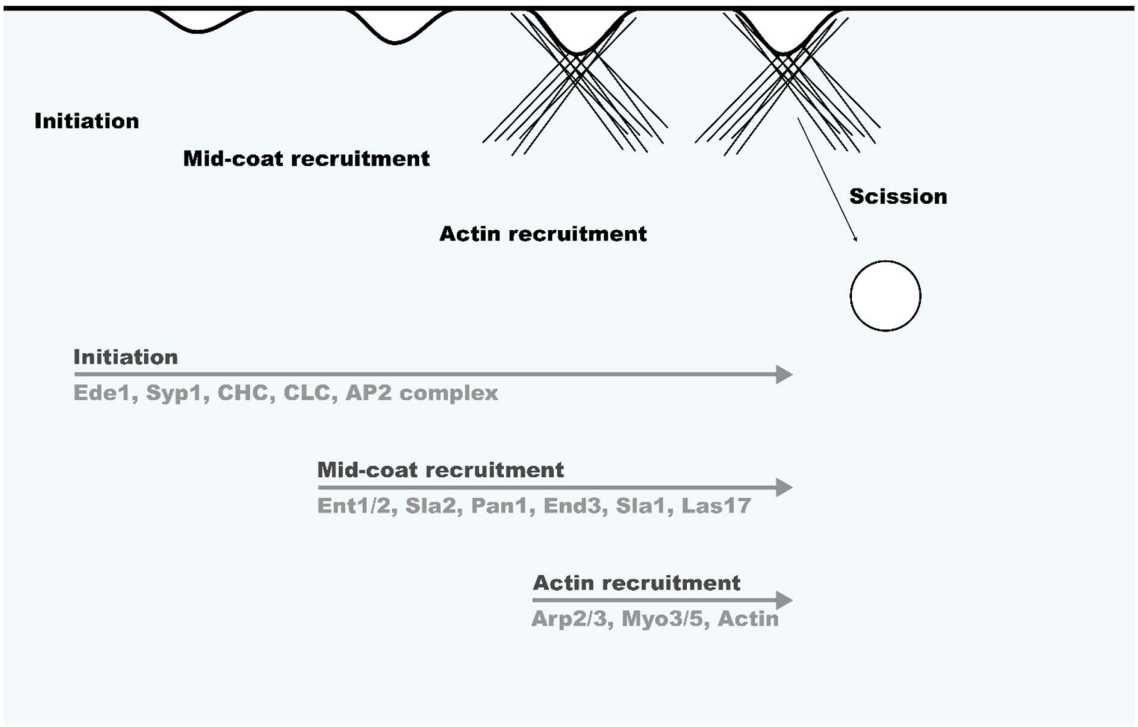

Figure 1: Clathrin-mediated endocytosis
The key stages of endocytosis for this study are labelled, along with the key proteins in the endocytic pit. For instance, Ede1 in the initiation phase, Sla2 in the mid-coat, and Arp2/3 in the Actin recruitment phase.

While CME is conserved across eukaryotes, yeast rely heavily on Actin for membrane invagination, whereas in mammalian cells, Actin is dispensable but clathrin polymerization is critical. The leads to a prominent difference in the size and shape of vesicles (smaller and oval-shaped in yeast compared to round and larger vesicles in higher eukaryotes (Kaksonen and Roux 2018). CME exemplifies the intricate coordination between membrane, protein, and cytoskeletal dynamics, enabling cells to adapt to their environment and internalize critical molecules.

3. 5 Connecting the plasma membrane to curvature generating processes

Clathrin, first identified in the 1970s, is a key protein driving vesicle formation during endocytosis. Clathrin was isolated from brain pig tissue, where its abundance highlights its role in synaptic vesicle trafficking, where it facilitates neurotransmitter receptor internalization in synaptic vesicles (B. M. Pearse 1976; B. M. F. Pearse 1975; Brown and Goldstein 1979).

The Clathrin heterodimer, comprising the heavy (CHC) and light (CLC) chains, forms a 'triskelion' structure that assembles into a lattice covering the surface of the endocytic pit (Ungewickell and Branton 1981). The Clathrin Light Chain has three segments: an N-terminal Intrinsically Disordered Region (IDR) that binds CHC and Sla2, a central helix that interacts with CHC's distal leg, and a C-terminal region thought to bind CHC's trimerization domain (Chen et al. 2002; Ybe, Perez-Miller, et al. 2007).

In Mammals, CHC exists in two splice variants that may regulate distinct processes, such as synaptic vesicle formation and muscle development (Moulay et al., 2020). CLC regulates clathrin coat assembly by interacting with CHC and other adaptor proteins, influencing lattice stiffness and membrane curvature (Biancospino et al. 2019; Redlingshöfer and Brodsky 2021; Obashi et al. 2023; Legendre-Guillemin et al. 2002; Boettner et al. 2011; Wilbur et al. 2008).

The trimerization of clathrin triskelia is pH-dependent, highlighting the role of electrostatic interactions in lattice formation (Ybe et al. 1998). Structural studies using electron cryo-microscopy (cryo-EM) and tomography have revealed the ability of Clathrin to form both flat and curved lattices at endocytic sites (Fotin et al. 2004; Morris et al. 2019; Paraan et al. 2020). Advances in electron cryo-tomography (cryoET) have allowed the determination of *in situ* clathrin coat structures, providing insights into their regularity (Serwas et al. 2022).

Structures of different clathrin cages and coats from purified samples or reconstituted systems, obtained through single particle analysis electron cryogenic-microscopy (SPA cryo-EM), have provided insights into the mechanism of coat assembly and its role as a platform for recruiting other endocytic proteins and cargo at the plasma membrane in clathrin-coated

sites (CCS)(Fotin et al. 2004; Morris et al. 2019; Vigers 1986; Bucher et al. 2018; Kukulski et al. 2012; Scott et al. 2018). Importantly, while clathrin is an abundant coat protein in yeast endocytic sites, it is not an absolute prerequisite for endocytosis. Correlative light and electron microscopy (CLEM) has revealed that Clathrin stabilizes membrane curvature but does not actively drive invagination (Avinoam et al. 2015; Kukulski et al. 2016).

The role of Clathrin during membrane remodelling has been a subject of debate in the field, with two prevalent models: the constant curvature model and the constant surface model (Scott et al. 2018; Sochacki and Taraska 2019). Clathrin has been shown to sense membrane curvature (Zeno et al. 2021), and its interactions with adaptors regulate the transition from flat to curved during CME (Bucher et al. 2018). Recent studies using super-resolution microscopy have demonstrated that clathrin can assemble both as a flat and curved coat at endocytic sites (Mund et al. 2022; Nawara et al. 2022).

Adaptor proteins, like Sla2 and Ent1, contain ANTH domains that anchor the clathrin coat to the plasma membrane. Intrinsically Disordered Regions (IDR) containing Short Linear Motifs (SLiMs) that facilitate binding to clathrin, other adaptors, and cargo. Some adaptors, like Epsins, also include Ubiquitin Interaction motifs (UIMs) to interact with Ubiquitinated cargoes (Szymanska et al. 2016).

The mid-coat adaptors Sla2 (Hip1R) and Ent1 (Epn1) have been studied in both yeast and higher eukaryotes. Sla2 and Ent1 act as mid-coat adaptors, bridging the clathrin lattice to the membrane and recruiting actin-binding proteins. Sla2 and Ent1 interact with the clathrin coat primarily through different motifs, Ent1 through a Short Linear Motif (SLiM) at the C terminus of its IDR and Sla2 through the coiled-coil region with Clathrin Light Chain (Figure 2) (Legendre-Guillemin et al. 2002; Defelipe, Veith, Burastero, Kupriianova, Bento, Skruzny, Köbel, et al. 2024; Rosenthal et al. 1999).

Initially identified as an Actin-binding protein involved in CME Sla2/Hip1R was later found to have connections with the clathrin coat through its coiled-coil domain, as observed through microscopy (Engqvist-Goldstein et al. 2001). The N-terminal ANTH (AP180 N-Terminal Homology) domain binds to the plasma membrane through interactions with $PI(4,5)P_2$ (Ford

et al. 2001). The AENTH complex formed between Ent1 and Sla2 is critical to the recruitment of Sla2 to the endocytic pit, with mutations *in vivo* causing a significant decrease in internalisation (Sun et al. 2005).

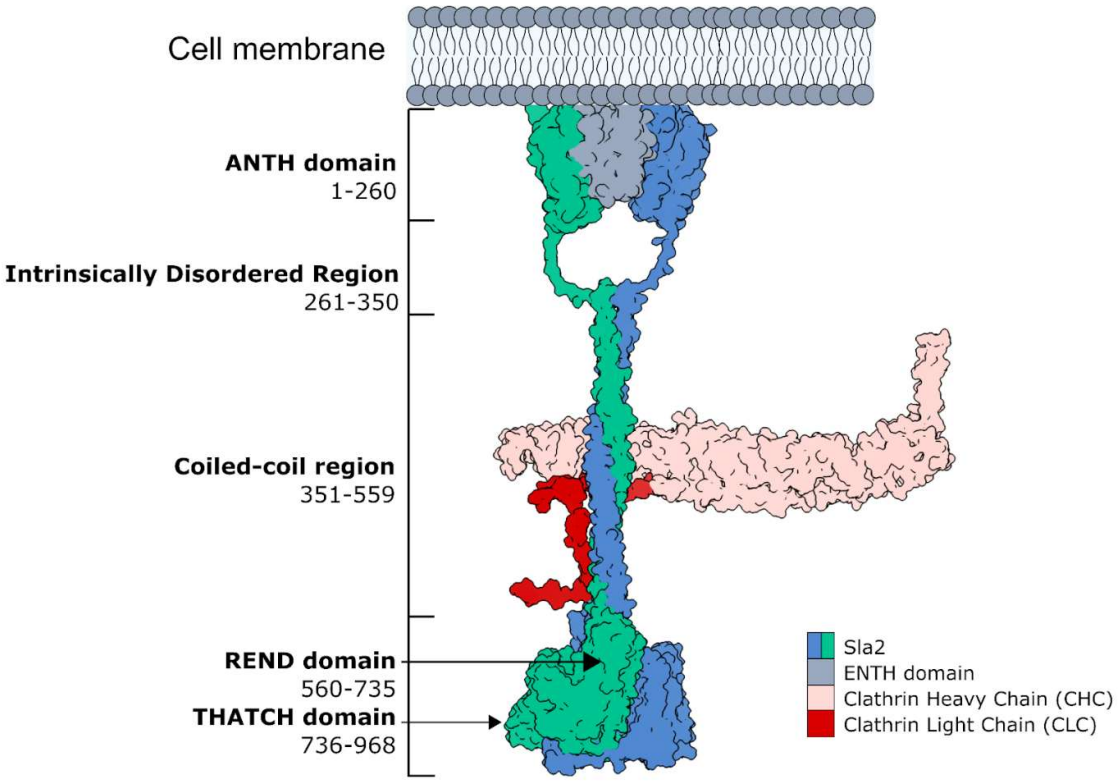

Figure 2: The protein network in common between Sla2 and Hip1R
Schematic diagram of the primary interactions for Hip1R/Sla2 in the endocytic pit in mid-coat formation. The ANTH domain of Sla2 covers residues 1-260, IDR from 261-350, coiled-coil from 351-559, REND domain from 560-735, and THATCH domain from 736-968. The ANTH domain complexes with the ENTH domain. The coiled-coil region interacts with the N-terminal IDR of CLC. Adapted from (Draper-Barr et al. 2024)

The Actin-binding domain from Sla2/Hip1R is named the Talin-Hip1/R/Sla2p Actin-tethering C-terminal homology (THATCH) domain, with critical residues for Actin binding on the termini of helices 3 and 4 of the THATCH core, determined through mutagenesis and Actin co-sedimentation assays (Brett et al. 2006; Smith and McCann 2007; McCann and Craig 1997). Cell biology studies have localised the Actin-binding domains of *Hs*Hip1R in proximity to Actin filaments at the endocytic site (Serwas et al. 2022). This interaction is in combination with Ent1 that contains a C-terminal Actin Binding Domain (ABD) (Skruzny et al. 2012). The ABD of Ent1

and C-terminus of Sla2 are redundancies for each other in the total connection network of the membrane to actin filaments.

Mutational studies of the Actin-binding domains of Ent1 and Sla2 show a significant decrease in internalisation only from a double mutant of both domains. This led to the proposal that Sla2 and Ent1/2 form a large island of protein motifs for recruitment of Clathrin and Actin. This would organise an Actin network over the plasma membrane surface and the relaxation of the Clathrin triskelia. Then in a series of events, controlled by phosphorylation of Ent1 by Prk1 and the Clathrin:Sla2 complex, the amount of Actin is trimmed in a direction specific manner at scission (Enshoji et al. 2022; Toshima, Toshima, Duncan, Cope, et al. 2007).

The THATCH domain is formed of two parts: the THATCH core that binds Actin, and the LATCH helix that is a key dimerisation motif of the C-terminal region (Smith and McCann 2007). Removing either portion stops the binding of Actin. The REND domain, a force sensing domain described in End4 (homologous to Sla2 from *S. pombe*) has been compared to the R12 domain of Talin (Ren and Berro 2022; Ren, Yang, Fujita, Jin, et al. 2023; Ren, Yang, Fujita, Zhang, et al. 2023). This domain is N-terminal of the THATCH domain, and unfolds above a force threshold that is exerted by Actin during endocytosis. This unfolding process eliminates the Actin binding of Sla2 as well, suggesting that the REND domain acts as a stabilising and a regulatory factor of the C-terminal region structure during endocytosis. The arrangement of the REND domain, the THATCH domain core and the LATCH helices in the complete structure of this region is unknown. Answering this would determine the availability of the Clathrin regulated Actin binding surface of the THATCH domain, as well as the relationship of the unfolding events of the THATCH and REND domains to expose this surface.

The central region of Sla2 understood to be of great importance to its role as an interaction hub for regulatory interactions in the CCP. Hip1R and its close homologue, Hip1, have been shown to interact directly *in vivo* with Clathrin Light Chain (CLC) (Wilbur et al. 2008; Chen and Brodsky 2005; Biancospino et al. 2019; Kelly et al. 2014; Obashi et al. 2023). This interaction occurs in the coil-coil region. The identity of the interaction surface was proposed from a crystal structure of the coiled-coil from Hip1, where the coiled-coil formed a platform for

potential binding partners (Legendre-Guillemin et al. 2005; Niu and Ybe 2008). In yeast and mammals, the interaction between CLC and Sla2/Hip1R inhibits Actin binding by the THATCH domain, as well as regulating the Clathrin lattice stiffness (Wilbur et al. 2008; Gingras et al. 2008; Brett et al. 2006; Smith and McCann 2007; Boettner et al. 2011). The exact location, magnitude, and function of the CLC interaction with Sla2 for the processivity of endocytosis was not previously described. This is particularly important as the endocytic system between Fungi and Metazoa differs in the critical role Actin takes in endocytosis of Fungi as opposed to Metazoa.

3.6 Actin polymerisation is controlled by protein-protein interactions

Sla2 features an Intrinsically Disordered Region (IDR, residues 261–350) followed by a coiled-coil segment (residues 351–559) between the ANTH domain and the C-terminal region (Figure 3). One of the important roles of Sla2 in the endocytic pit is the regulation of the Actin polymerisation complex Pan1/End3/Sla1. The Pan1/End3/Sla1 complex regulates Actin polymerization by modulating Arp2/3 and Las17, key players in endocytosis; shown by depletion experiments from the work of Sun et al. (Sun et al. 2015, 2019). Sla2 interacts with both Sla1 and Pan1, releasing Las17 and inhibiting Pan1's actin-polymerizing activity to ensure proper regulation (Gourlay et al. 2003; Toshima, Toshima, Duncan, Jamie, et al. 2007). Las17 is homologous to WASP from Metazoa, WASP is an auto-inhibited Actin polymerisation regulator as opposed to regulation by protein-protein interactions like Las17 (Zigmond 2000).

Sla1 contains three SH3 domains, two of which bind Las17, a Sla1 Homology Domain (SHD1) for cargo recognition, and a SAM domain (SHD2) for regulatory functions. SH3 domains bind proline-rich motifs, enabling Sla1 to interact with actin regulators like Las17 (Teyra et al. 2017; Dionne et al. 2022, 2021). The Sla1 Homology Domain (SHD1) is responsible for binding NPFxD motifs in endocytic cargo (Mahadev et al. 2007). The SAM domain (SHD2) negatively regulates Sla1 binding the Clathrin Heavy Chain via its variant Clathrin Binding Motif in the C-terminus (Di Pietro et al. 2010). The interactions with End3 are mediated through the C-terminal region (Whitworth et al. 2014; Sun et al. 2015). Pan1 shares

a modular architecture with Sla1, containing N-terminal EH domains that bind NPF motifs (Pierce, Toptygin, and Wendland 2013; Bradford, Whitworth, and Wendland 2015). These domains are shared with the EH domain containing human homologs Eps15 and EHD1/2. The contrast between Pan1 and Eps15 as well is that Pan1 interacts with End3 as part of the Pan1/End3/Sla1 complex. The Pan1 coiled-coil region is known to interact with Sla2 as part of the regulatory pathway for Actin polymerisation in the endocytic pit of yeast (Enshoji et al. 2022; Toshima, Toshima, Duncan, Cope, et al. 2007). This triple complex is unique to yeast. In Metazoa, N-WASP and related proteins fulfil similar Arp2/3 regulatory functions (Boczkowska et al. 2014; Duleh and Welch 2010). The specific residues and binding strengths of Sla2's interactions with Pan1 and Sla1 remain to be fully characterised. Understanding these regulatory interactions is critical for elucidating how cells maintain endocytic efficiency and adapt to dynamic cellular environments.

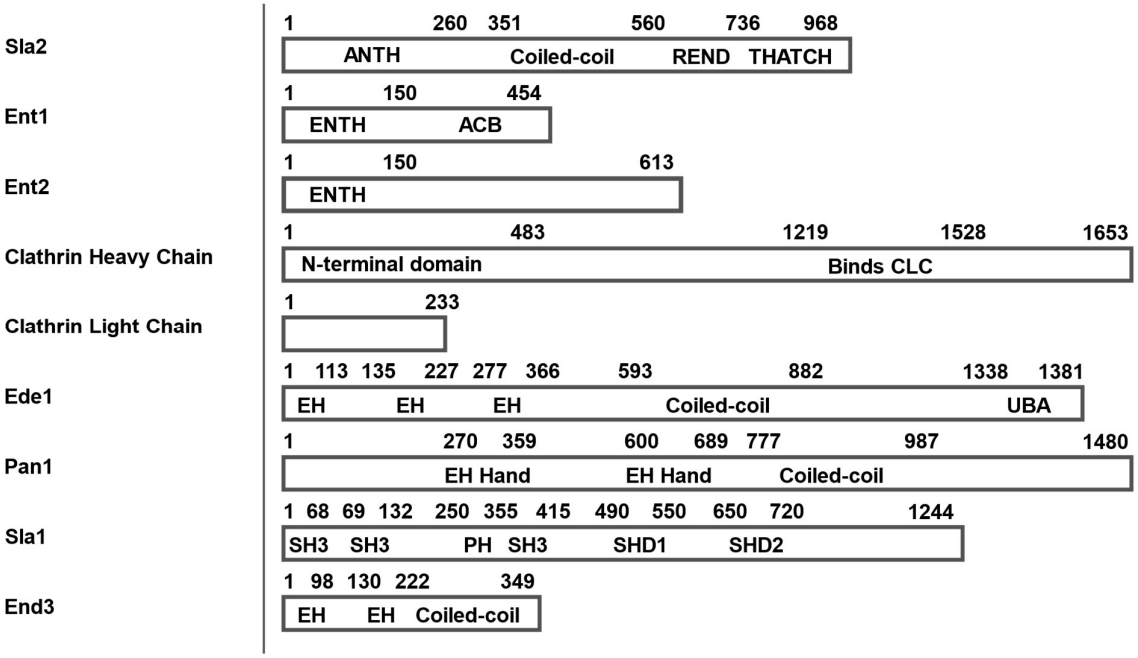

Figure 3: Domains of key endocytic proteins form the interaction network surrounding Sla2

Globular domains such as the ANTH and ENTH domains of Sla2 and the Epsins are labelled for the endocytic proteins that are involved in the primary complexes of interest revolving around Sla2.

3.7 Phase Separation in Endocytosis

Liquid-liquid phase separation (LLPS) and biomolecular condensates have recently gained attention as mechanisms for organizing cellular components without membranes. Examples of these organised cellular regions include P granules, nucleoli, and stress granules (Banani et al. 2017). These compartments concentrate molecules, facilitate reactions, and organize cellular processes. LLPS refers to the spontaneous formation of dense protein-RNA droplets that segregate specific molecules within the cytoplasm. Phase separation allows for the spatial and temporal regulation of cellular events, offering a way to compartmentalize without requiring a membrane. This phase separation framework also applies to sub-micrometre compartments that balance the concentration of specific components with dynamic molecule exchange, such as transcriptional super-enhancers (Sabari, Hyman, and Hnisz 2024). These concepts have led to investigation of phase separation in membrane trafficking (Case et al. 2019).

In the context of endocytosis, phase separation is thought to play a role in organizing the proteins at the endocytic site, influencing vesicle formation and dynamics. The CCS consists of highly conserved adaptor proteins that bind to both the membrane and cargo. These adaptors include the Adaptor Protein complex 2 (AP-2), Syp1 (FCHo1/2 in mammals), and Yap1801/2 (AP180). Additionally, conserved scaffold proteins like Clathrin, Ede1 (Eps15) participate in the early phase of endocytosis. Unlike the well-ordered assembly of the membrane-bending phase (Picco et al. 2015), the recruitment of early arriving proteins lacks a specific sequence (Carroll et al. 2012; Pedersen et al. 2020; Mund et al. 2022; Picco et al. 2015). Deletion of the genes encoding the earliest-arriving proteins does not completely block endocytosis (Brach et al. 2014), but it does decrease the frequency of endocytic events and compromise the regulation of cargo recruitment. Ede1 is a central player in the early stages of endocytosis, coordinating the recruitment of other adaptors and cargo (Stimpson et al. 2009; Boeke et al. 2014; Lu and Drubin 2017).

Ede1 is a multi-domain protein comprising 1381 amino acids. The N-terminal region contains three Eps15-homology (EH) domains that interact with NPF motifs within endocytic adaptors like Ent1/2 and Yap1801/2 (Maldonado-Báez et al. 2008). These domains are followed by a proline-rich IDR and a coiled-coil domain, which interact with Sla2 (Reider et al. 2009; Stimpson et al. 2009; Lu and Drubin 2017). The C-terminal half of Ede1 includes a Syp1-interacting region and a ubiquitin-associated (UBA) domain. The proline-rich region of Ede1 features a significant number of asparagine and glutamine residues. It can be considered as a poly-glutamine region (PQ region) indicative of prion-like domains that regulate protein phase separation (Franzmann et al. 2018; Franzmann and Alberti 2019). Analysis using PLAAC and predictions from AlphaFold (Jumper et al. 2021; Barrio-Hernandez et al. 2023; Abramson et al. 2024) shows there is around 36% of Ede1 that is intrinsically disordered, particularly within the PQ region and between the coiled-coil and UBA domain.

Fluorescently tagged Ede1 in yeast cells localizes to endocytic sites on the plasma membrane (Kukulski et al. 2012). However, under specific experimental conditions, Ede1 can also assemble into large condensates (Boeke et al. 2014). Ede1 condensates formed when the stoichiometry between Ede1 and endocytic adaptors is altered, such as Ede1 overexpression or deletion of three early adaptors (Boeke et al. 2014). Ede1 condensates form in cells overexpressing Ede1 or in mutants lacking key adaptors. While not observed in wild-type cells, studying these condensates further could yield insights into Ede1's role in early endocytic protein assembly. This phase separation phenomenon could be critical for regulating the assembly and disassembly of protein complexes at endocytic sites.

In a recent study (Kozak and Kaksonen 2022), the propensity of Ede1 to form cellular condensates was demonstrated, establishing that the cytosolic concentration of Ede1 is critically buffered and past this point forms segregated condensates in the cytoplasm. The paper goes on to specify the molecular determinants driving Ede1 condensation, highlighting these were also essential for its function in endocytosis; promoting the initiation and maturation of endocytic sites. Notably, these Ede1 condensates within the microscopy data confirms these condensates exhibit liquid, phase-separated droplet characteristics based on liquid

behaviour, molecule turnover, concentration dependency, temperature sensitivity, and dissolution by 1,6-hexanediol.

Fluorescence microscopy has been used to visualize these condensates, revealing their liquid-like properties and dynamic exchange of molecules, comparable to studies performed on the human homologue, Eps15 (Day et al. 2021). The cytosolic concentration of Ede1 in native and mutant cells hosting Ede1 droplets remains critical, implying liquid phase separation concentrates proteins at early endocytic sites. The central region of Ede1, the coiled-coil and PQ region, is crucial for both condensate formation and initiating endocytosis, examined through deletion strategies *in vivo* of each region. Prion-like domains from other proteins can mimic Ede1's function in condensate formation, and fusion of the central region with a lipid-binding domain enables condensation on the plasma membrane. This work also provided evidence that adding heterologous coiled-coil regions from other proteins such as kinesins, recover the condensate formation of truncated Ede1 but not the aberrant endocytic phenotype. These findings link endocytic assembly and protein phase separation, raising questions about the material properties of endocytic sites.

Distinguished by size, brightness, and stability, Ede1 condensates differ from endocytic sites. Although their precise function remains uncertain, the Wilfling lab (Lizarrondo and Wilfling 2024; Wilfling et al. 2020) propose a selective autophagy pathway mediated by Ede1, suggesting a potential role for Ede1 condensates in endocytosis and autophagy. This leads onto the investigation of Sla2, which arrives later than Ede1 and has clear interactions with Ede1 both in productive endocytosis and within the Ede1 condensates that were shown in the work of the Kaksonen lab. The phase separation of Ede1, along with its interactions with other adaptor proteins, may drive the organization and efficiency of endocytosis (Figure 4). Understanding phase separation in endocytosis could bring new insights into how cells regulate complex molecular processes, with potential implications for understanding cellular trafficking dysfunction.

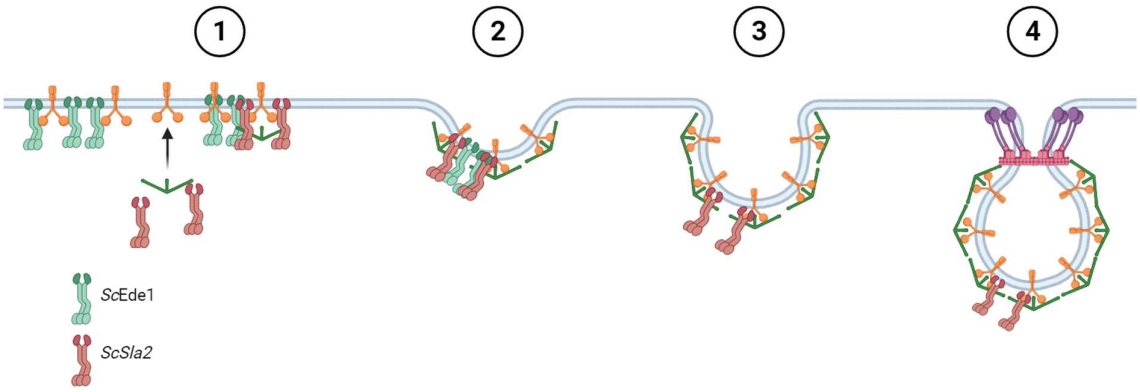

Figure 4: Illustration of Sla2 and Ede1 in Endocytosis

1 - The early coat protein Ede1 (Eps15 in mammals) and Clathrin is recruited to the membrane first through Ubiquitin and NPF motif interactions. Ede1 forms a large interaction network across the CCS. 2 - During the mid-coat process assembly timeframe, Sla2 is recruited and remains present until the very end of endocytosis. 3 - Ede1 leaves the CCP during later stages of coat development. 4 – Scission of the vesicle and subsequent intracellular transport of the cargo.

4. Objectives of this work

This work focuses on the interaction network involved in endocytosis, where protein-protein and protein-lipid interactions drive plasma membrane deformation and vesicle scission. In the fungal endocytic machinery, Sla2 (Hip1R in Metazoa) is one such interaction hub in the mid-coat of the Clathrin Coated Pit. Key proteins of interest within this dissertation include CLC, Sla1, Pan1, and Ede1 that have diverse roles in this fundamental biological process. Several groups have investigated the role of Sla2 and its binding partners during the course of endocytosis (Lizarrondo et al. 2021; Boettner et al. 2011; Toshima, Toshima, Duncan, Cope, et al. 2007). The open questions within the field include the precise mapping and magnitude of affinity for some of these interactions, hierarchy of these interactions *in vivo*, and comparison of the network behaviour between Fungi and Metazoa.

The first section described in this thesis addresses the following questions:

- What is the physical location and magnitude of the interactions between Sla2 and Clathrin Light Chain, Pan1, and Sla1?
- What is the hierarchy of binding sites between Sla2 and Clathrin Light Chain?
- What is the detailed structure of the Sla2 C-terminal region, and how does it relate to its function in endocytosis?

The following questions focus on phase separation and the role of coiled-coil regions in Ede1 and Sla2 during endocytosis.

- Does Ede1 phase separate *in vitro* and does it recruit Sla2 to droplets?
- Does Sla2 phase separate and which region of Sla2 is responsible for this phenomenon?
- Can Sla2 recruit interacting proteins into its phase-separated droplets?

5. Results

5.1 Sla2 forms complexes, via the coiled-coil, with CLC through two independent sites

5.1.1 Mass Photometry captures the Sla2:CLC complex at sub-micromolar concentrations

Clathrin Light Chain interacts with Sla2/Hip1R across both mammalian and fungal systems (Wilbur et al. 2008; Boettner et al. 2011). This interaction in the human system was shown to be mediated by the coiled-coil of Hip1R and the disordered N-terminus of CLC. In order to characterise this interaction, residues 351-968 of Sla2 (Sla2ccRTH) and NusA conjugated to CLC (NusA-CLC) were used for Mass Photometry (MP) experiments. Mass Photometry is a form of interference microscopy that utilises native protein marker calibrations against the experimental data to calculate the molecular weights of individual particles (Young et al. 2018; Cole et al. 2017). This method can identify masses of high affinity complexes with heterogeneous stoichiometry (Sonn-Segev et al. 2020; Niebling et al. 2022). NusA is a monomeric solubility tag, which provides significant mass to the CLC moiety for Mass Photometry (Davis et al. 1999). It is derived from *E. coli* and has no previously described interactions with either of the proteins on interest.

Samples were measured at 50 nM of each component, Sla2ccRTH and NusA-CLC, and in combination with each other. In the mixture of Sla2ccRTH and NusA-CLC peaks for the individual components were present as well as two other peaks. These peaks correspond to one dimer of Sla2 bound by one NusA-CLC and a large complex of undetermined stoichiometry (Figure 5b). The results for the individual components showed that the Sla2 construct is dimeric and the NusA-CLC is monomeric at these concentrations. The mixture of NusA and Sla2ccRTH showed no particles other than those particles with masses that correspond to the individual proteins. These results reassure us that there is no specific

interaction between NusA and Sla2 and therefore there is no effect of conjugating NusA to CLC on complex formation for measurement by MP (Figure 6).

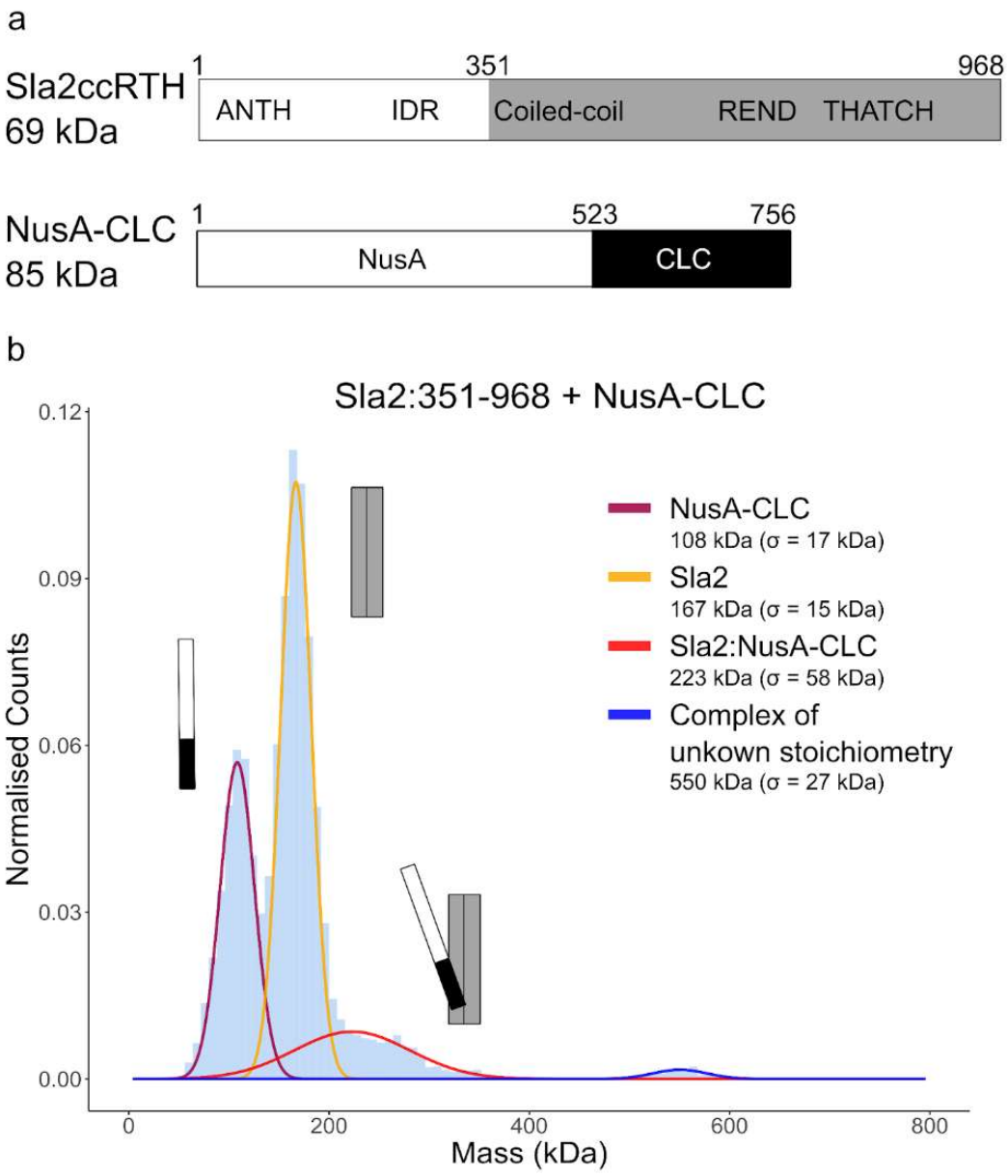

Figure 5: Mass Photometry captures the Sla2:CLC complex at sub-micromolar concentrations

(A) Sla2ccRTH construct explained in context of the full-length protein, NusA-CLC construct diagram showing the N-terminal moiety of a fusion protein, NusA, to the CLC full length polypeptide. (B) Mass Photometry measurements of a sample containing Sla2ccRTH and NusA-CLC. Two populations of particles were measured. The populations calculated masses were 108 kDa (σ = 17 kDa, 31 % counts, expected for NusA-CLC), and 167 kDa (σ = 15 kDa, 52 % counts, expected for Sla2ccRTH). Larger particles corresponding to a mass of 223 kDa (σ = 58 kDa, 15 % counts, expected for Sla2ccRTH+NusA-CLC), and 550 kDa (σ = 27 kDa, 1 % counts, unknown complex) are measured. Gaussian fitting of Refeyn 2.0 exported events were achieved through the eSPC program, PhotoMol (Niebling et al. 2022). Adapted from (Draper-Barr et al. 2024)

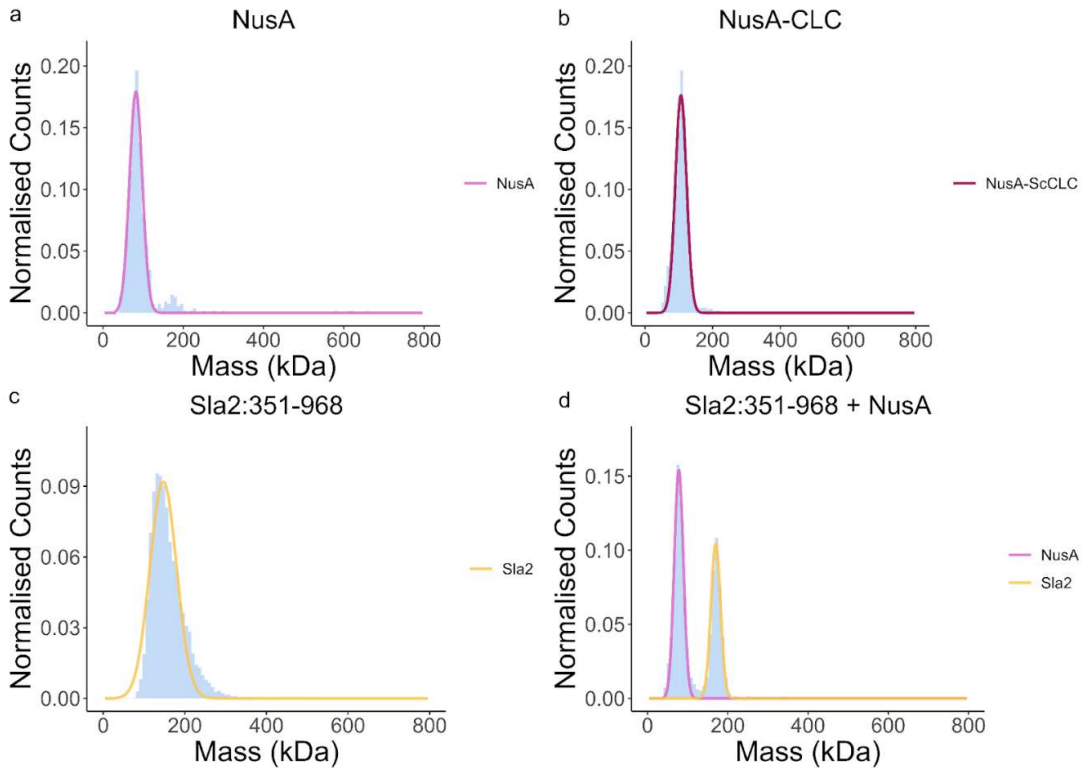

Figure 6: Controls for Mass Photometry measurements

(A) NusA is a monomer at 82 kDa (σ = 16 kDa). (B) NusA-CLC is monomeric as well with a monomeric mass of 106 kDa (σ = 17 kDa). (C) Sla2:351-968 is dimeric with a mass of 147 kDa (σ = 33 kDa). (D) The NusA moiety does not bind to the coiled-coil. NusA was measured at 78 kDa (σ = 11 kDa) and Sla2 at 170 (σ = 12 kDa). The mass of the expected NusA moiety is 56 kDa, NusA-CLC is 85 kDa, and Sla2:351-968 dimer is 138 kDa. Gaussian fitting achieved through the eSPC program, PhotoMol. Adapted from (Draper-Barr et al. 2024)

5.1.2 Two independent CLC binding sites in the Sla2 coiled-coil were determined by MicroScale Thermophoresis and mutagenesis

In order to understand the interface of CLC and the Sla2 coiled-coil further, the affinity of this complex was determined using Microscale Thermophoresis (MST) (Jerabek-Willemsen et al. 2011). MicroScale Thermophoresis is a technique that measures the differences in diffusion of labelled molecules along a temperature gradient. When accompanied by a ligand concentration series, this technique can assess the affinity of complexes based on the change in the diffusion of the labelled target. This technique is ideal for screening the affinity of proteins to ligands and other proteins, as it requires a low sample volume at moderate concentrations for ligands depending on the expected affinity. CLC was labelled for the measurements; it has

a high number of lysine residues across the whole polypeptide and also for any mutagenesis experiments it will be Sla2 that is mutated so labelling the unchanged protein is ideal.

The titration of Sla2cc (Sla2 residues 296-767) against labelled CLC showed two separate binding events with different K_ds (Figure 7). The value for the lower affinity site (Site 2) was determined as 3.0 μM (CI95: 2.07-4.29 μM) and the higher affinity site (Site 1) at ~100 nM across the three Sla2cc constructs tested. The affinity of Site 2 is in agreement with the micromolar range value previously reported for the interaction with CLC by the human homolog HIP1R (Wilbur et al. 2008; Biancospino et al. 2019). The stoichiometry for Site 2 determined by Isothermal Calorimetry for *Hs*Hip1R and *Hs*CLC was 1:1, so both chains have an independent site from each other although they are intertwined through the coiled-coil dimerisation interface. MST cannot determine this property of the interaction but it can be assumed that for Site 2, by sequence alignment and the homology of these proteins that Site 2 in Sla2 also interacts in a 1:1 stoichiometry.

To determine which portions of the Clathrin Light Chain are responsible for different sites, truncated CLC constructs were titrated against labelled Sla2cc. Site 1 was determined to be located in residues 70-140 of the CLC N-terminus, and Site 2 is located in residues 1-70, which corresponds to the Intrinsically Disordered Region also proposed in the human homolog (Figure 8). A consideration for the affinities by MST in the experiments presented here is that this does not consider the intrinsic dimerisation of Sla2. This will impact the K_d by the potential steric clashes when two molecules of CLC may try to bind the same Sla2 coiled-coil.

To remove Site 2, two mutants were generated from conserved residues in this region between Metazoa and Fungi. This would determine if this binding site is independent from the higher affinity site only seen in Sla2 (Figure 7a). Site 2 Mutant 1 replaced: Y478A, Y485A, R489A. Site 2 Mutant 2: H492A, L493A, N494R, L495A, L496A, R498G, K500D, K501E, L502A. Site 2 Mutant 2 is based on the conservation of the ‘landing pad’ motif seen in the Hip1 coiled-coil crystal structure (Niu and Ybe 2008).

Both mutants eliminated Site 2 independently of Site 1 (Figure 7d-e). The sensitivity and broad surface area required for Site 2, which contains numerous hydrophobic and charged

residues, can be seen from the two mutants. Cross-Linking-Mass-Spectrometry between Sla2cc and CLC:1-80 gave several intermolecular cross-links: residues 20, 21, and 29 of CLC cross-linked to Sla2 residue 477, and a cross-link between residues 55 of CLC and 505 of Sla2 (Figure 9). These cross-links also validated the AF3 model generated for a dimeric Sla2 coiled-coil and a single CLC moiety. AF3 models are a useful tool for visualisation of the protein interactions, and when validated by experimental methods can be used to suggest the specific contacts of these two proteins at a residue level (Figure 7 and Figure 9).

Alignment of both Sla2/Hip1R and CLC within the cross-linked regions (Site 2) shows high conservation across Fungi and Metazoa, suggesting a likely critical function originating early in Eukaryogenesis (Figure 9). In the AF3 model, coiled-coil residues are exposed to potential interactions to CLC (Figure 7a). The CLC charged residues E31, E38, and D44 co-ordinate Sla2 residues Y478, Y485, and R489. CLC F39 is in proximity to Sla2 Y485. In the proposed motif region found in Hip1 (Niu and Ybe 2008), H492 is contacting F27 of CLC and N494 with Q43. Sla2 L493 is in proximity with L28 and L47 of CLC in the AF3 models as well (Figure 7a).

Up until this point in the investigation, the molecular identity of Site 1 has only be determined to the region of CLC responsible for this interaction, residues 70-140 (Figure 8). In addition, the evidence from the mutagenesis of Site 2 in Sla2 show that Site 1 is not in the region of residues 478-505 and it is assumed that Site 1 is still a part of the coiled-coil. Sequence analysis in the coiled-coil across Fungi and Metazoa highlighted that the region C-terminal of Site 2 contains significant conservation only present in Fungi (Figure 10); particularly residues 515-546. The C-terminus of the CLC moiety in Figure 9 points towards the C-terminus of Sla2 and the cross-links supports this too. These all support the hypothesis of Site 1 occupying the region C-terminal of Site 2 in both CLC and Sla2.

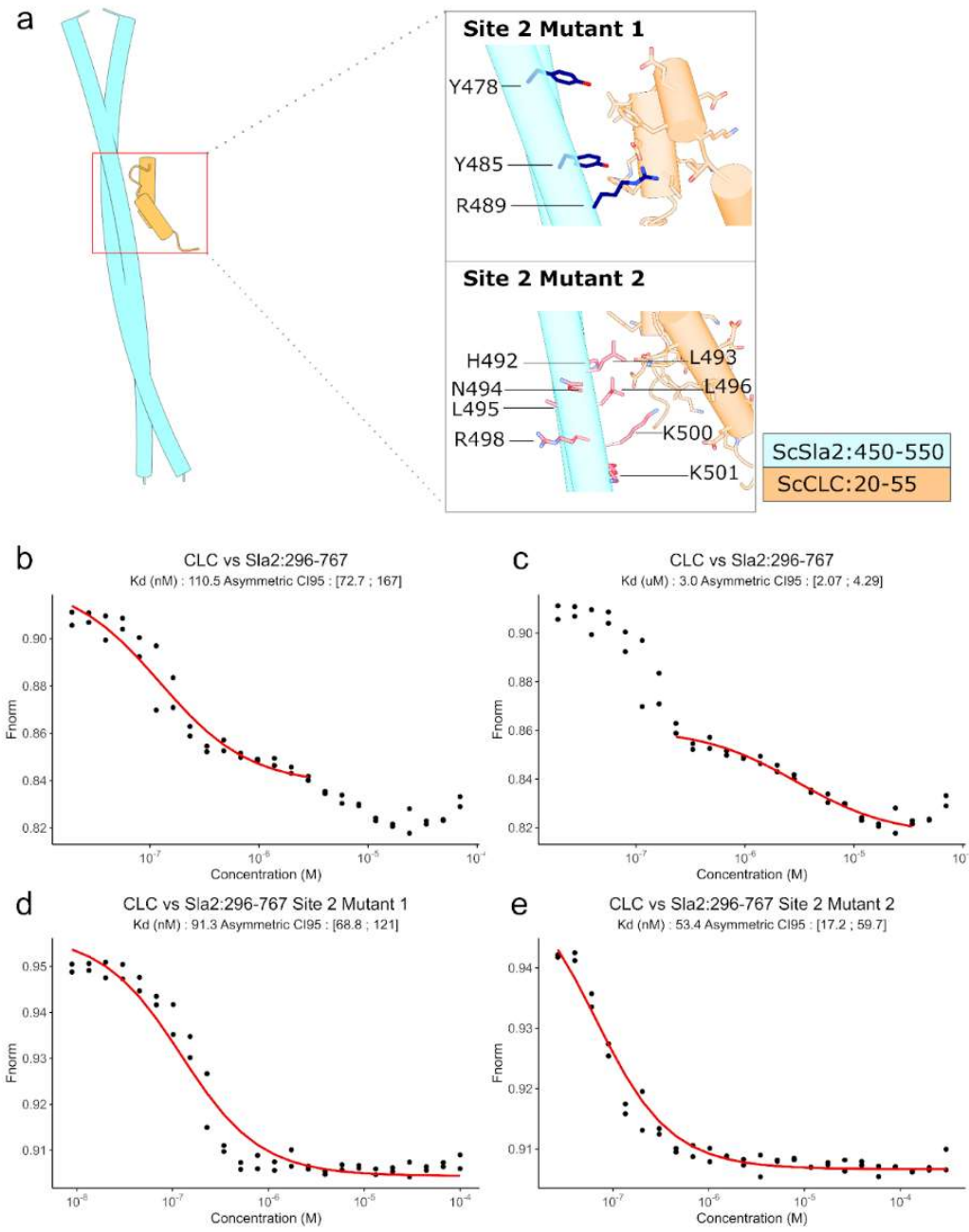

Figure 7: Sla2 has two independent binding sites for CLC

(A) AF3 model of the Sla2:CLC complex for residues 450-550 of dimeric Sla2 and 20-55 of CLC. Highlighted in the insets are the residues of the coiled-coil for one chain that are mutated in each construct used to map Site 2, dark blue for Site 2 Mutant 1 and red for Site 2 Mutant 2. (B-C) Fitted MST curves for the Wildtype Sla2 against labelled CLC. There are two separate binding events. (B) The high affinity event was measured at ~100 nM across the three constructs. (C) The low affinity event was measured at 3.0 μM (CI95: [2.07, 4.29]) solely in the Wild Type coiled-coil construct. (D-E) Two separate mutants of Sla2 were determined to abrogate binding for the lower affinity binding site of CLC. (D) Sla2cc Site 2 Mutant 1 (Y478A, Y485A, R489A) , and (E) Sla2cc Site 2 Mutant 2 (H492A, L493A, N494R, L495A, L496A, R498G, K500D, K501E, L502A). Both mutants only have one transition, which corresponds to Site 1 by the value of the K_d. Adapted from (Draper-Barr et al. 2024)

There is no structural information from the PDB or the produced AF3 models for the interaction of Sla2 and CLC in this region. The AlphaFold3 model has no confidence for an interaction between these two regions of CLC and Sla2. A deletion mutant of residues 515-546, Sla2cc ΔSite1 (Δ515-546), was created to test if this region was responsible for the second interaction site found between Sla2 and CLC (Figure 11a).

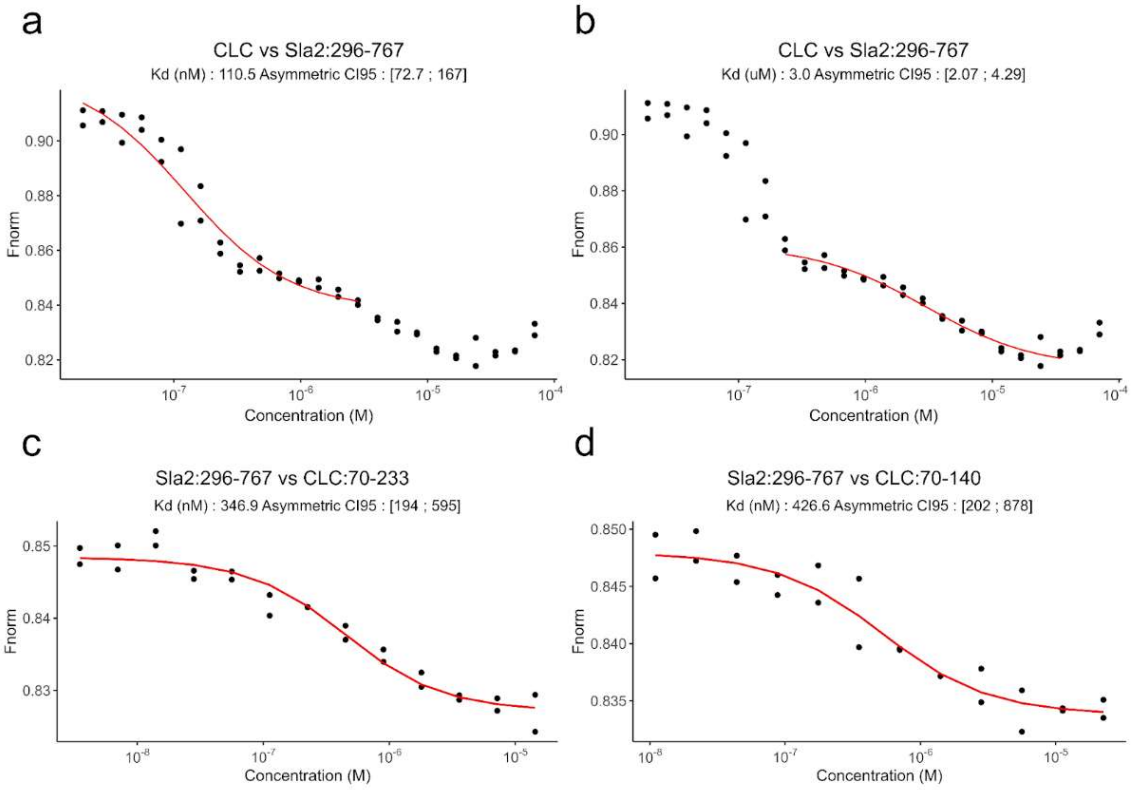

Figure 8: Microscale Thermophoresis maps the locations of the Sla2 binding sites within Clathrin Light Chain

(A-B) Sla2cc titrated against Clathrin Light Chain-Red-NHS labelled for MicroScale Thermophoresis. Two transitions were measured and separately determined in the hundred nanomolar range and low micromolar range. (C) CLC residues 70-233 titrated against Sla2cc-REDHS. (D) CLC:70-140 titrated against Sla2cc-REDNHS. A,C, and D have similar sub-micromolar K_d. These results show that CLC and Sla2 have two interaction interfaces, located in residues 1-70 and 70-140 of CLC. The measured affinities for these sites are an order of magnitude in difference; ~100-200 nM for Site 1 and 3.0 μM for Site 2. Adapted from (Draper-Barr et al. 2024)

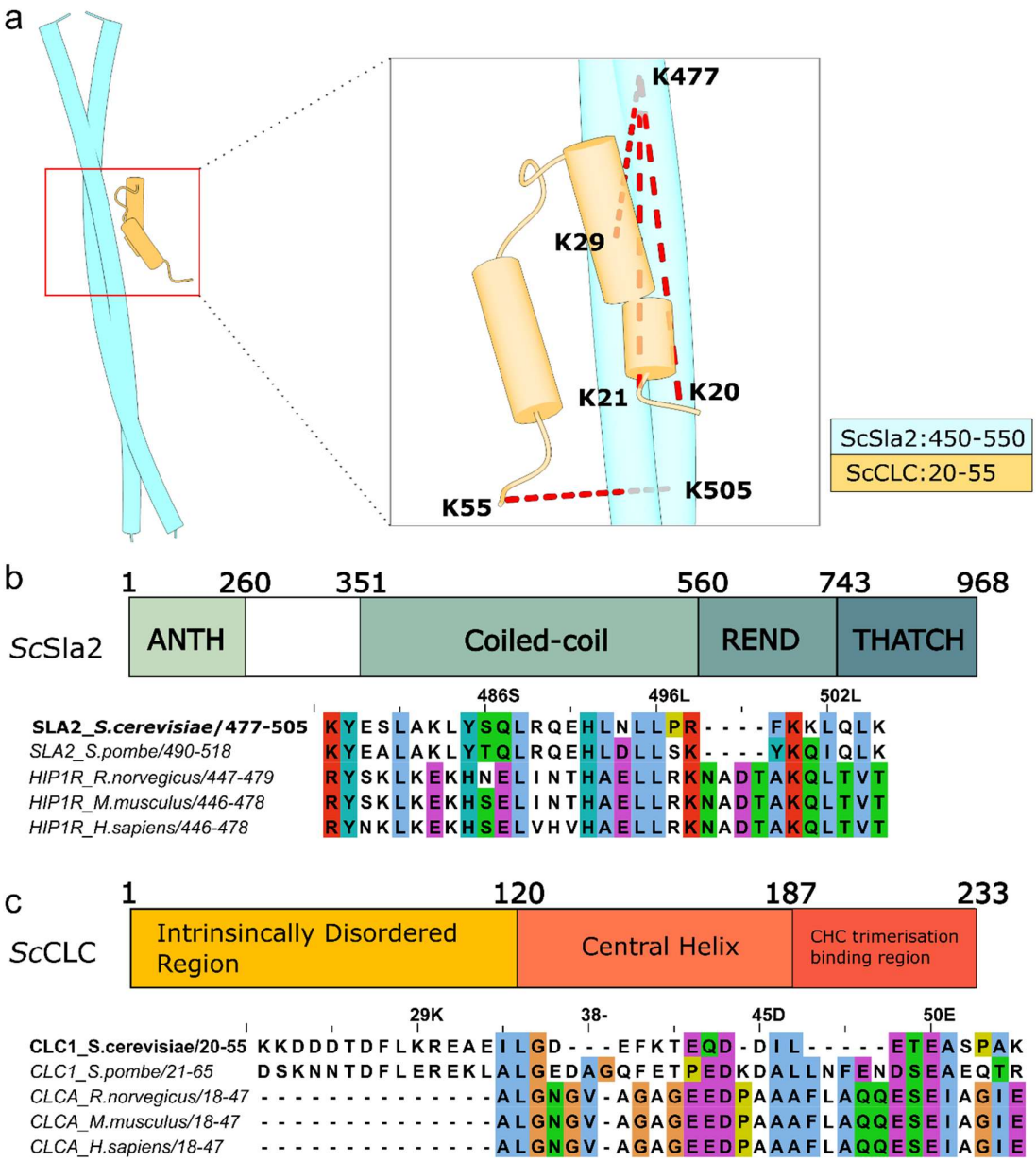

Figure 9: Site 2 is conserved in Sla2/Hip1R and CLC across Fungi and Metazoa

(A) AlphaFold 3 predictions of the dimeric Sla2 coiled-coil (450-550) and a monomer of CLC:20-55 were compiled with chemical cross-linking data mapped onto the model. The high confidence inter-molecular hits from BS3 cross-linking experiments are subsequently labelled (red dashed lines). (B) Sla2 domain architecture is labelled with residue numbering alongside a sequence alignment of the cross-linked region of Sla2 from the Sla2:CLC BS3 cross-linking experiments with two model yeast sequences and three mammalian model organisms shown in the figure. (C) The CLC architecture is labelled alongside the alignment of the cross-linked area of residues 20-55 with the same model organism protein sequences aligned to the *Saccharomyces cerevisiae* sequence. Adapted from (Draper-Barr et al. 2024)

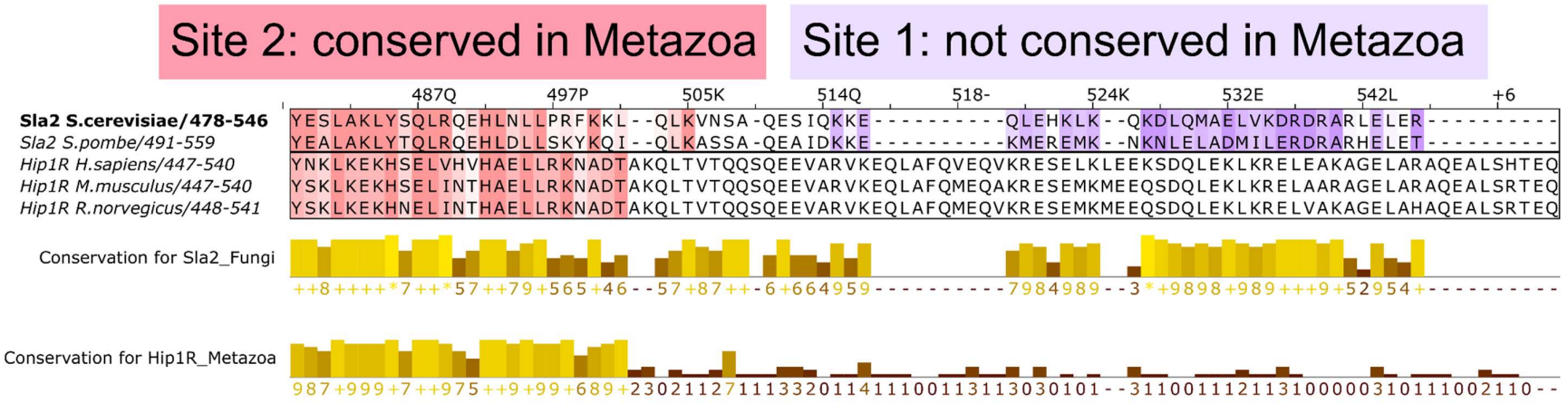

Figure 10: Sequence alignment of Sla2 and Hip1R shows sequence conservation differences in the central coiled-coil

Sequence alignments of the coiled-coil region of Sla2 and Hip1R in both Fungi and Metazoa, with representative model species shown in the figure. Site 2 (residues 478 to 505) is coloured in red with above 30 % conservation. The proposed Site 1 region between residues 515 and 546 of Sla2 and the aligned regions of the other sequences is also highlighted in purple above 30 % conservation. We can observe that there is significant conservation in the Site 1 region of Fungi not seen in Metazoa. Adapted from (Draper-Barr et al. 2024)

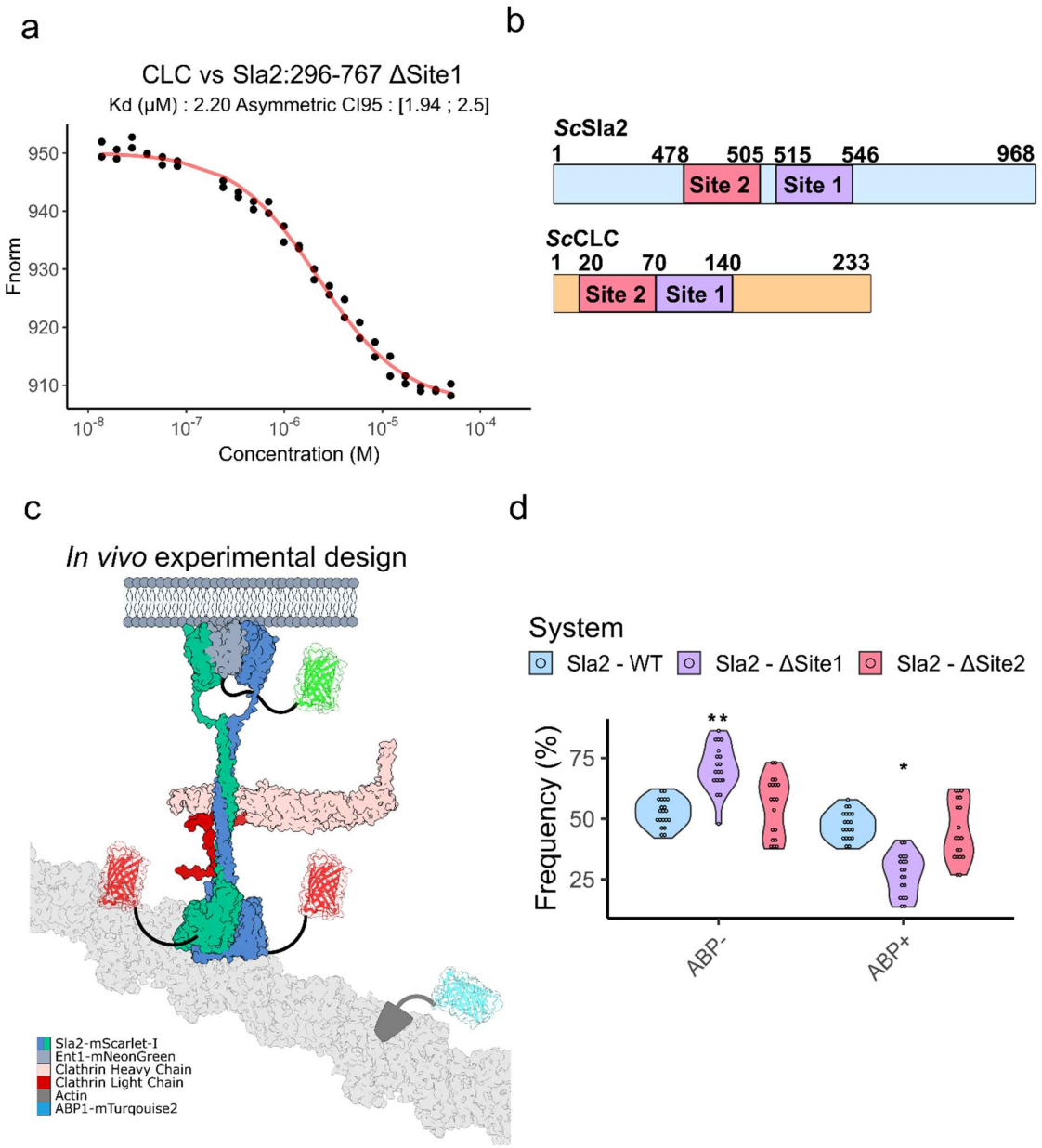

Figure 11: Fungi have a second dominant interaction site between Sla2 and CLC not found in Hip1R

(A) MicroScale Thermophoresis of Sla2cc ΔSite1 (Δ515-546) titrated against CLC (REDNHS labelled). (B) A diagram of Sla2 and CLC and the locations of the binding sites between these two proteins. The high affinity interaction (Site 1) between Sla2 and CLC is found between residues 515 and 546 of the coiled-coil and Site 2 is located further towards the N-terminus of Sla2 at residues 478 to 505. (C) Endocytic dynamics was measurable using an endogenously tagged Ent-1-mNeonGreen, Abp1-mTurqouise2 S. cerevisiae strain with ectopically expressed Sla2-mScarlet-I under an endogenous promoter. (D) Abp1 positive and negative events determined by cmeAnalysis (Aguet et al. 2013) for Sla2 WT, ΔSite1, and ΔSite2 (ΔYYR). ΔSite1 is significantly reduced in the percentage of Abp1+ events as compared to WT and also ΔSite2. Asterisks indicate statistically significant differences (*p-value < 0.0005, using P value adjustment method: BH). Adapted from (Draper-Barr et al. 2024)

Circular Dichroism was used to determine the secondary structure and thermal stability of the Sla2cc constructs used for MST determination of K_d measurements (Figure 12). Circular Dichroism measures the selective absorption of polarised light across the far-UltraViolet spectrum, and from these measurements the secondary structure of proteins in solution can be estimated for sample characterisation and optimisation (Miles, Janes, and Wallace 2021).These constructs were folded with a very similar helical content compared to the Wildtype sequence. This is a quality control measure so that any results taken from the biophysical experiments can be trusted for further validation *in vivo*. Using this construct then to measure MST against labelled full-length CLC gave only one transition with a K_d value in the micromolar range, corresponding to Site 2 (Figure 11a). From this result we can map Site 1 to residues 515-546 of Sla2 (Figure 11b) and conclude that this site is a specific interaction not seen in Metazoa through sequence conservation.

To determine whether either of the two sites are important to the normal function of endocytosis, *in vivo* endocytic dynamics were measured within *S. cerevisiae*. To track the progress of endocytosis, Abp1 and Ent1 were endogenously tagged with mTurqouise2 and mNeonGreen respectively as previously done by Defelipe et al. (Defelipe, Veith, Burastero, Kupriianova, Bento, Skruzny, Kölbel, et al. 2024) (Figure 11c). Endogenous Sla2 is knocked out and ectopically expressed Sla2 is cloned into a vector containing the native promoter for Sla2. Sla2 sequences for WildType, Site 2 Mutant 1 (ΔSite2), and ΔSite1 were expressed in three different cell lines (Figure 11d).

To measure endocytosis from start to finish there needs to be a marker considered to be the connected to the beginning and end of the measurable process. The start marker used is Ent1 as although it is a mid-coat protein it is present till the end of endocytosis. Abp1 is a key component of Actin recruitment and polymerisation. This process is necessary for membrane invagination and vesicle formation, and therefore is associated with productive endocytic events (Skruzny et al. 2020). Therefore endocytic events can be classified into two categories (using the program cmeAnalysis (Aguet et al. 2013)): Productive events, Ent1 and Abp1 positive (Abp1+) or Non-productive events, Ent1 positive and Abp1 negative (Abp1-) (Figure

13). From the endocytic events measured using TIRF microscopy for all three strains, the ΔSite1 mutant causes a significant decrease in Abp1+ events, ΔSite2 has no such distinction from the WildType (Figure 11d). The microscopy data collection and analysis was done with the help of Lucas Defelipe and Yeast cell line production was done by Katharina Veith.

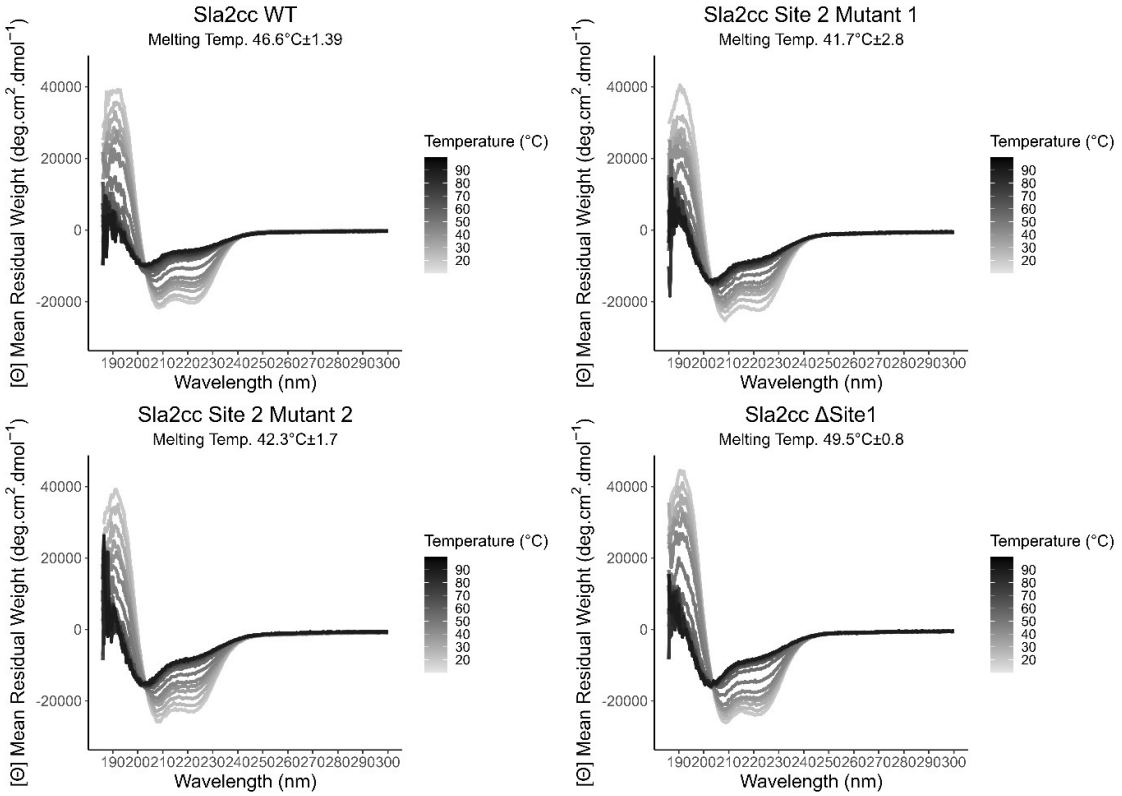

Figure 12: Circular Dichroism of Sla2cc for comparison of WildType to mutant constructs used for biophysical characterisation

Circular Dichroism temperature ramps from wavelengths 180 nm to 300 nm. (A) Sla2cc WT, (B) Sla2cc Site 2 Mutant 1, (C) Sla2cc Site 2 Mutant 2, (D) Sla2cc ΔSite1. Circular Dichroism was performed to determine if the mutants used to characterise the CLC binding sites were folded correctly. Due to background noise, the spectra were used from 186 nm onwards. The constructs were all folded in similar secondary structure contents at 20 °C, with between 52 % and 58 % alpha helical content, the rest was distributed primarily between disordered regions and some low amounts of beta sheets and turns. The Far UV CD curves between 20 °C and 90 °C provided a suitable basis for fitting a melting temperature to each construct. The stabilities do not drop below 40 °C, but the Site 2 mutants do drop as compared to the WildType, and the Site 1 mutant increases the Sla2cc melting temperature by 3 °C. Fittings for melting temperature and secondary structure prediction from the Circular Dichroism curves were done using ChiraKit from the eSPC online toolkit https://spc.embl-hamburg.de/app/chirakit. Adapted from (Draper-Barr et al. 2024)

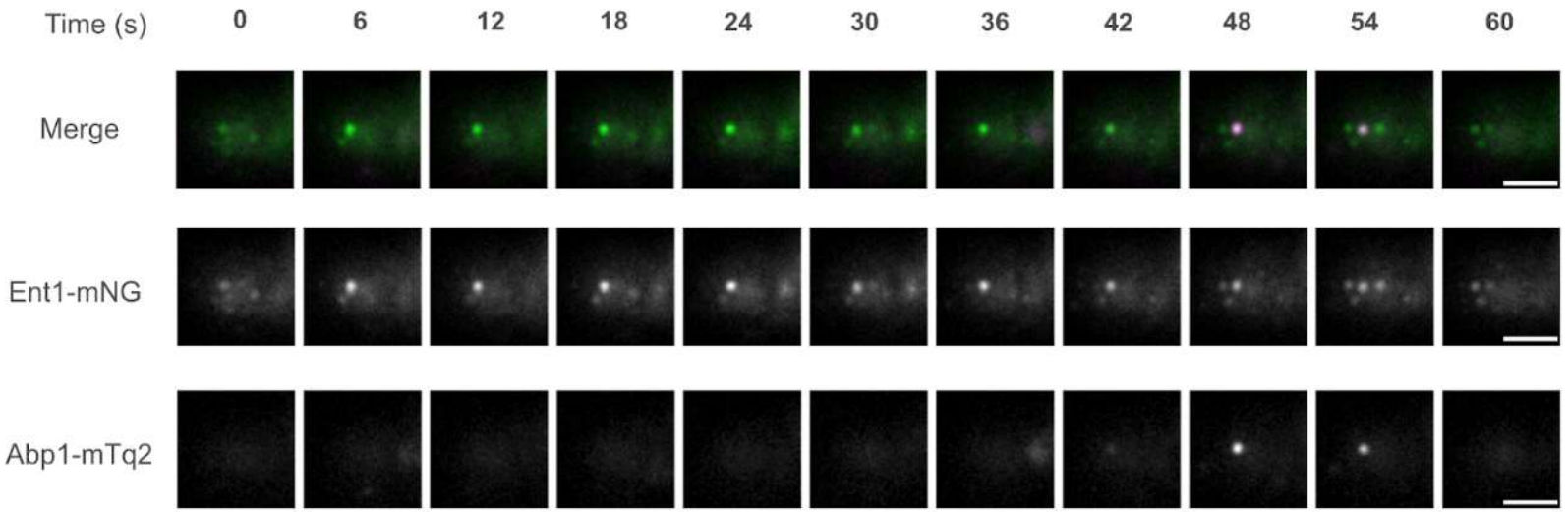

Figure 13: TIRF microscopy of *S. cerevisiae* endogenously tagged with Ent1-mNeonGreen and Abp1-mTurqouise2 can be used to classify productive endocytic events

A time-lapse sequence capturing a single endocytic event that demonstrates the co-localization of Ent1 fused with mNeonGreen (displayed in green) and Abp1 fused with mTurquoise2 (shown in magenta) in a wild-type Sla2 cell. Adapted from (Draper-Barr et al. 2024)

5.1.3 Structural determination of the Sla2 C-terminal region

The experimental structures of the REND domain and the relative positions of the THATCH domain were unknown up until this point, except for computational models produced by programs such as AlphaFold, Rosetta, and ESM. The arrangement of the THATCH domain is important as it creates context for the Actin binding capacity of Sla2.

To answer this question about a key interaction in endocytosis within Fungi, the structure of the C-terminal domains of Sla2 were resolved via electron cryo-microscopy (cryo-EM). Sla2ccRTH was used for the grid, this construct contains the full coiled-coil and C-terminal region. The micrograph processing resulted in a density map at a resolution of 3.62 Å (Figure 14). The $FSC_{(0.143)}$ resolution was determined through Refmac (Murshudov et al. 2011).

A model was fitted from a base AF3 prediction of the Sla2 C-terminal domains (Figure 14). The high confidence of the AF3 model on top of the good initial fit of the model into the map made the process significantly faster. The mean RMSD of the AF3 model to the experimental model is 3.0 Å (Figure 17). The atomic model and cryo-EM half-maps have been submitted to the PDB and have been validated, with the ID code, 9HDD. Data analysis and feedback on interpretation of the data was supervised by Emil Gustavsson (Supervised by Professor Dr. Meytal Landau, Landau Group).

Unfortunately, the coiled-coil was not resolved in the density map. This is most likely due to the high flexibility or thin nature of this region and hence cannot be resolved during particle 2D and 3D alignment. The complete C-terminal region (REND and THATCH domains) was not previously determined in any homologous protein and hence a computationally derived reference model was needed. The isolated THATCH domain core helical bundle of *Hs*Hip1R has been previously crystallised (PDB: 1r0d) and can be used for comparison to the structure presented here (Brett et al. 2006) (Figure 15 and Figure 16).

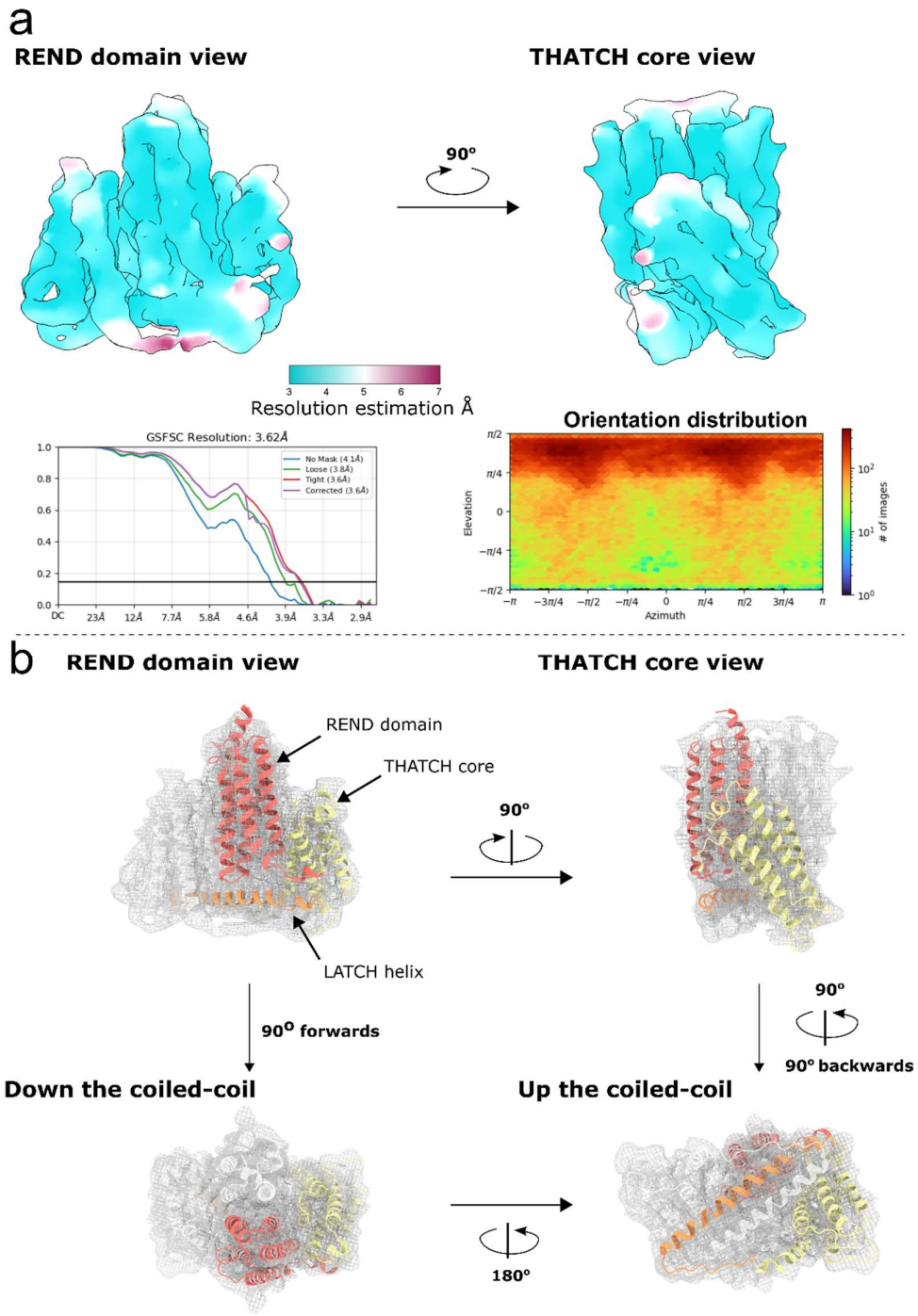

Figure 14: Sla2 C-terminal domains form well defined helical bundles

(A) Density map resolved from the Sla2ccRTH construct sample. The maps are colour coded according to the local resolution estimation by cryoSPARC v4. There are two graphs presented as well for the density map, on the bottom left, the GSFSC Resolution graph determined post auto-tightening of the map and, bottom right, the orientation distribution map of the particles. Estimation of the resolution through Refmac is 3.62 Å. (B) Sla2 residues 560 to 968 are modelled into the locally filtered density map shown for one chain, obtained from micrographs collected on Sla2ccRTH. This construct contains all of the coiled-coil region as well as the C-terminal domains, however we modelled the REND domain through to the end of the LATCH helix. Adapted from (Draper-Barr et al. 2024)

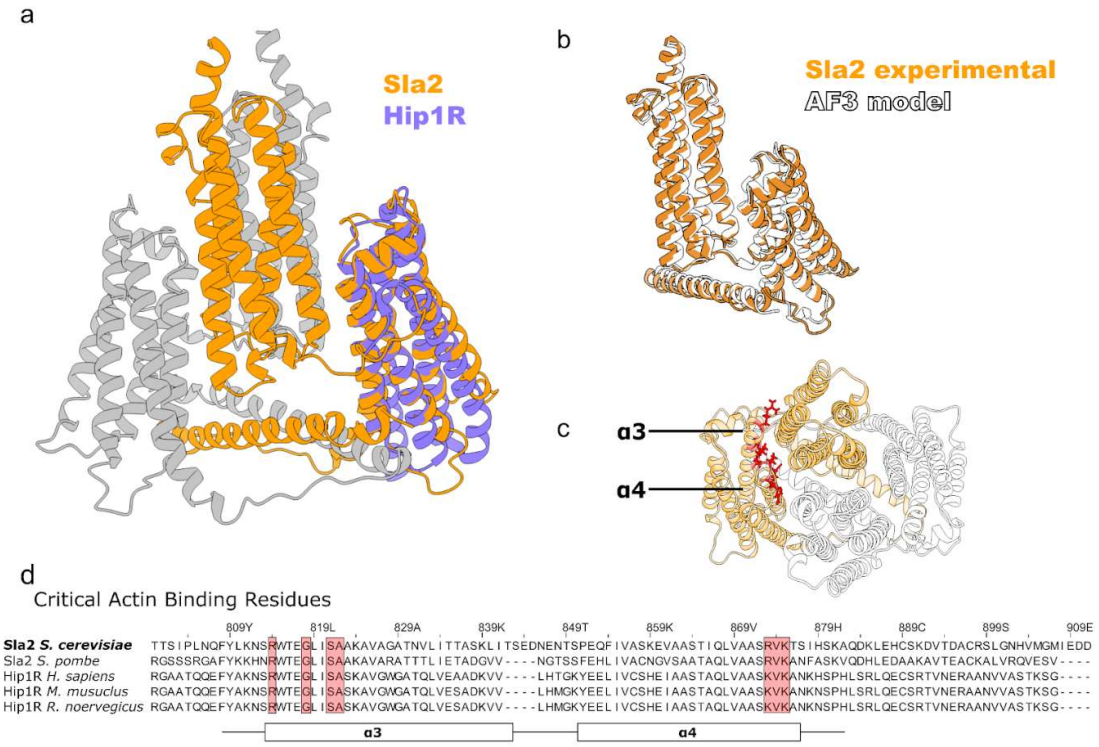

Figure 15: Actin binding residues conserved between Sla2 and Hip1R are not solvent available

(A) Overlay of the ScSla2 560-968 model with the *Hs*Hip1R THATCH core crystal structure (PDB:1r0d) matched to Chain A of our structure. The overall RMSD of 1r0d to the residues 735-909 of Sla2 is 6.3 Å, however the overall fold is the same and the RMSD of the Actin binding residues is 0.8 Å. (B) Overlay of one chain of both the Sla2 experimental model and the AF3 computational model for residues 560-968 of Sla2. The RMSD of the chains is 2 Å. (C) The view of our model from the perspective of looking down the coiled-coil. Highlighted are residues that are conserved and considered critical for binding Actin fibrils in red. These residues are in contact with the REND domain interface. (D) Alignments of helices 3 and 4 of the THATCH domain for the Fungi Sla2/End4 and Metazoa Hip1R sequences with representative species shown. *Hs*Hip1R THATCH domain studies showed residues in the N- and C-termini of α3 and α4 respectively are critical to Actin binding (Brett et al. 2006). These residues are highlighted in red. Adapted from (Draper-Barr et al. 2024)

The *Hs*Hip1R THATCH core has an overall RMSD of 1r0d to the residues 735-909 of Sla2 of 6.3 Å. Although this is a poor overall RMSD, the fold is the same when it comes to the orientation and arrangement of the five alpha helices. The RMSD of the Actin binding residues in the THATCH core is 0.8 Å. Due to the high sequence and structural conservation with Hip1R and mutational studies on the THATCH core (Brett et al. 2006) the Actin binding region of Sla2 (ACB) can be highlighted in the structure with confidence. The proposed Actin binding surface is not fully available to the solvent and has several contacts to the REND domains (Figure 16).

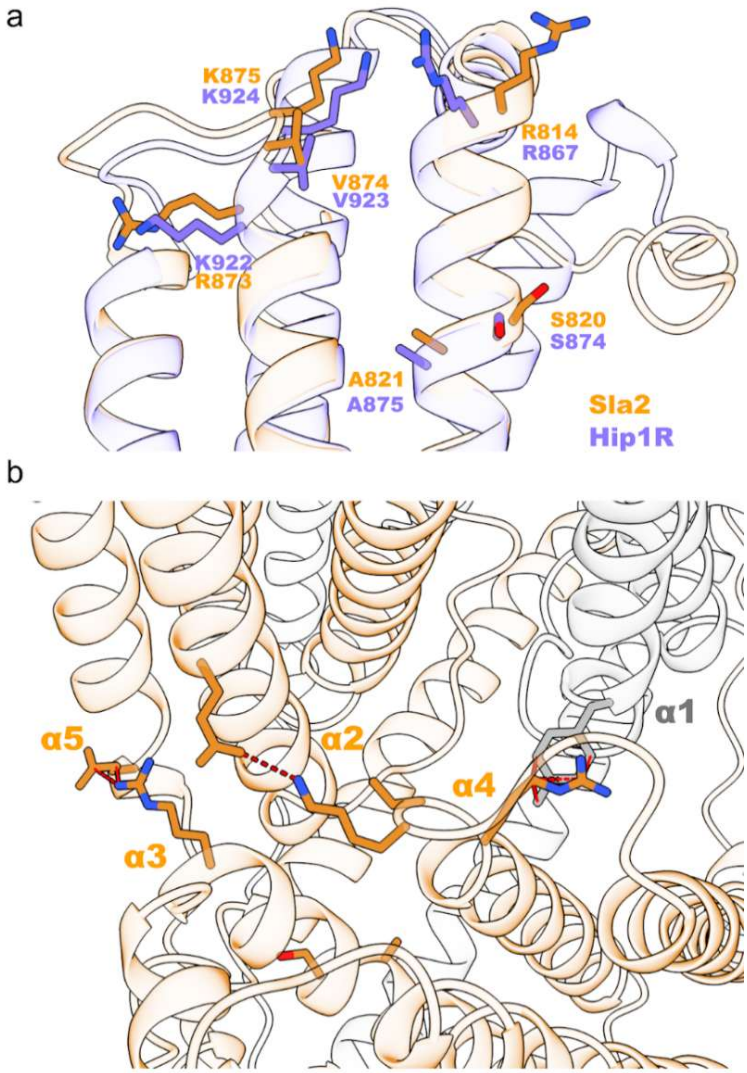

Figure 16: The THATCH domain Actin binding surface contacts the REND domains of both chains

(A) Overlay of the THATCH domain structures of Sla2 and Hip1R, with Actin binding residues highlighted and labelled. The Sla2 THATCH domain is orange and the Hip1R crystal structure is purple. The positions have an RMSD of 0.8 Å. (B) The Sla2 REND and THATCH domains shown with Actin binding residues and their contacts to the REND domains highlighted with red dashed lines. The context of the other domains in our structure show that the ACB of one chain contacts the REND domain of both chains. Helix 3 of the THATCH domain contacts helix 5 of the REND domain. Helix 4 of the THATCH domain contacts Helix 2 of the self-chain REND domain and helix 1 of the other chain. Adapted from (Draper-Barr et al. 2024)

The REND domain forms a dimeric five helical bundle in a similar fashion to the R12 domain of Talin, the LATCH helices are, as predicted, an antiparallel dimer with the respective C-termini position towards the THATCH core domain of its own chain (Figure 18a). The N-

terminus faces helix 3 of the opposite chain THATCH core and passes under the REND domain to then reach the self-chain THATCH core helix 3 with the LATCH helix C-terminus.

The proposed dimerisation surface for the LATCH helix from Talin-1 (Smith and McCann 2007) is not consistent with our model (Figure 18b). Within the experimentally determined model, the LATCH helix starts at 925 through to 968 and the portion of Sla2 between residues Q837 to Y962 is not perfectly aligned. The THATCH core interface with the REND domain face consists of helices 3-5 of the THATCH domain. The buried solvent accessible area is 65 $Å^2$ between the LATCH helices and REND domains of the Sla2 C-terminal structures (Figure 18c). The buried surface area of a single chains THATCH domain with the REND domains of both chains is 750 $Å^2$.

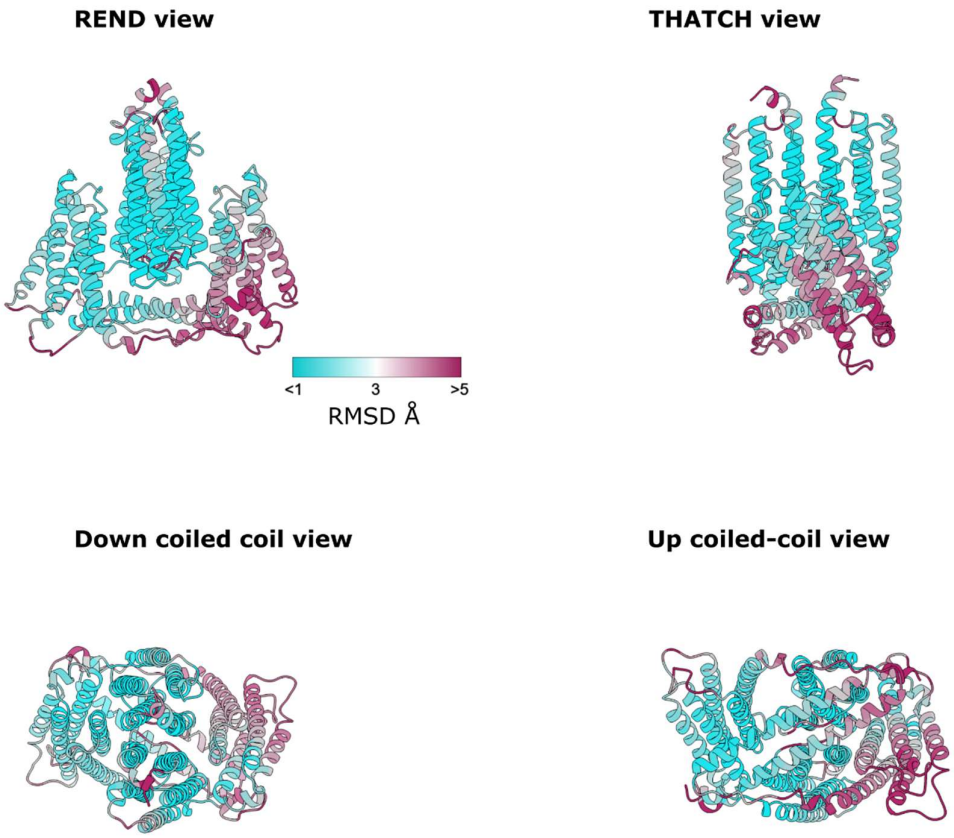

Figure 17: Comparison of the experimental REND/THATCH domain structure to the AF3 model

The RMSD of the experimental Sla2 C-terminal structure from the AF3 base model is plotted onto the structure with the colour scheme presented in the REND domain view (top left). The REND domain and one of the THATCH domains have a low RMSD to that of the AF3 model but one THATCH core has a much higher RMSD as well as the termini of the LATCH helices.

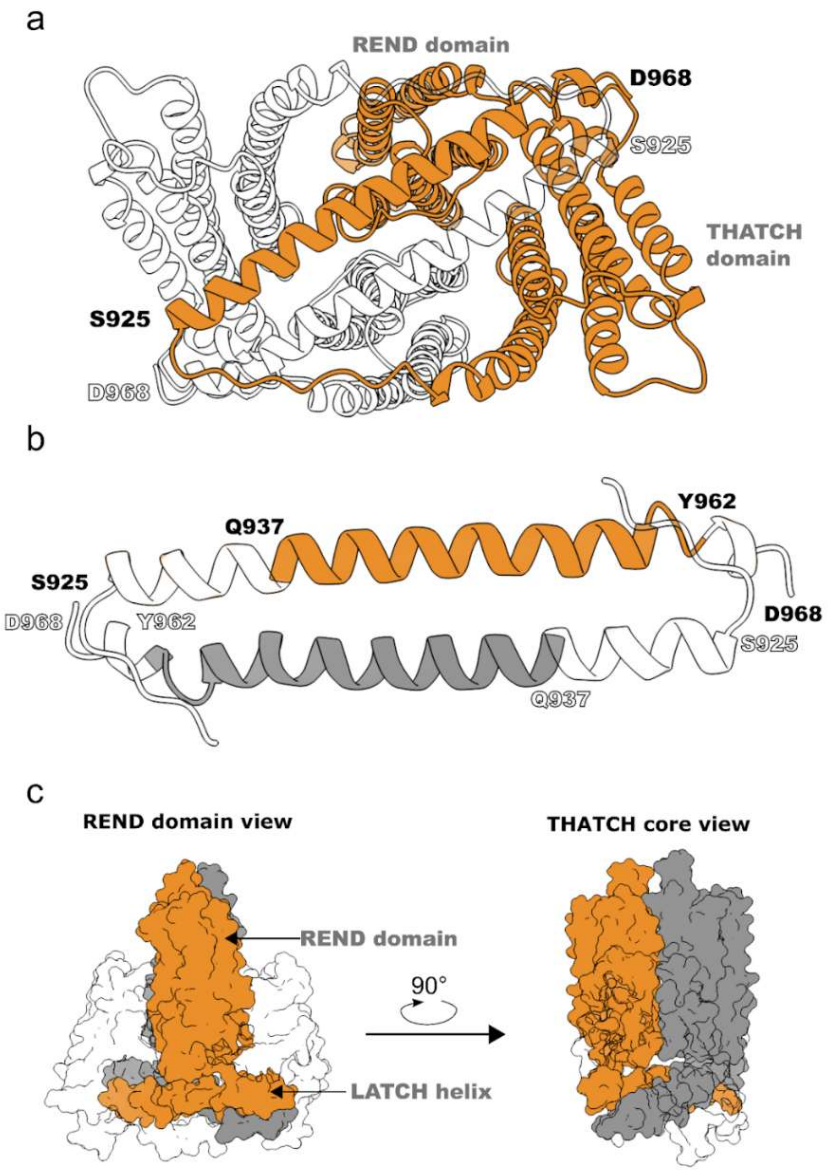

Figure 18: Sla2 LATCH helix forms an antiparallel dimer between the THATCH domains

(A) The Sla2 cartoon highlights that the LATCH helix is antiparallel and goes from contacting the opposite chain THATCH domain to the THATCH domain of the self-chain. (B) LATCH helix cartoon representation from our model from residues 920-968, with N- and C- terminal residues added for the LATCH Helix (925 and 968). Q937 and Y962 are labelled from the work on Talin that proposed a dimerisation motif for the THATCH domain. The antiparallel dimer proposed from homology in Talin-1 is not similar to our structure. The region 937-962 is not symmetrically aligned. The C-terminal portion of the LATCH helix contacts with not only the N-terminus of the partner helix but also the loop connecting to the THATCH core. (C) The surface representation of the REND and LATCH helices show that there is little buried surface area between the two domains. The REND and LATCH regions are coloured orange and grey by chain, and the THATCH core for both chains are transparent. Adapted from (Draper-Barr et al. 2024)

5.1.4 Small Angle X-Ray Scattering of Sla2 highlights the elongated nature of the coiled-coil in solution

Small Angle X-ray Scattering (SAXS) is a powerful method for studying the overall shape and conformation of proteins in solution (Roessle and Svergun 2019). One of the other questions surrounding Sla2 is the conformation of the coiled-coil. The AF3 model of the full-length dimer of Sla2 that the coiled-coil would form a relatively straight conformation before reaching the REND domain. It is not clear whether the model is correct as there is no prior information as to whether without tension on the protein between the membrane and the Actin filaments that Sla2 would retain an elongated structure. The Sla2ccRTH construct, used throughout this work, was imaged by Small Angle X-Ray Scattering on the P12 beamline at DESY. The data was collected with the help and guidance of Cy Jeffries (Blanchet Team, EMBL Hamburg). The data was analysed through DAMMIF (online server) (Franke and Svergun 2009).

The SAXS data revealed that the coiled-coil region of Sla2 adopts an extended, elongated conformation, which is crucial for its interaction with other proteins. Understanding the coiled-coil's elongated nature is essential for interpreting its role in protein-protein interactions at the endocytic site. The *ab initio* model gave a prolate particle with rounded structure on one end (Figure 19). The Kratky plot for the fitted and raw data show good fitting for this model. When overlaid with the AF3 model of the same construct, it is clear that the prediction of the coiled-coil as a relatively straight form is correct even with low-resolution structural data.

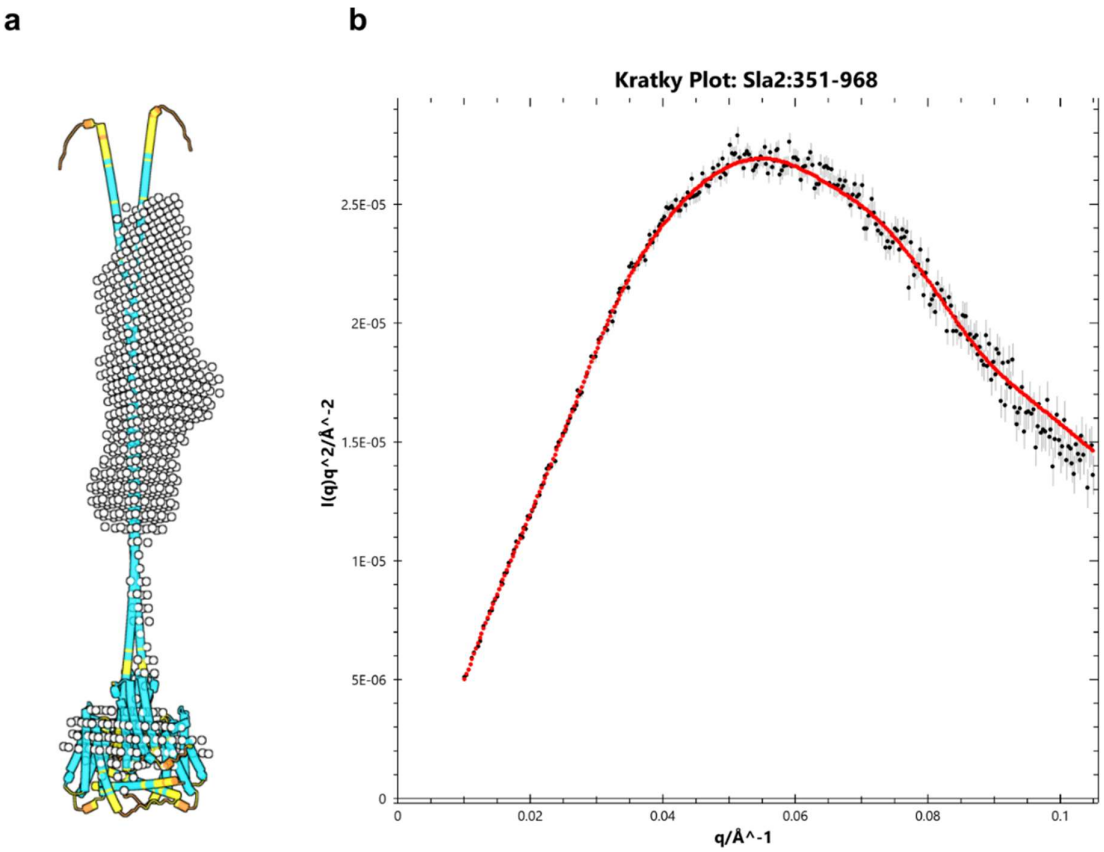

Figure 19: Small Angle X-Ray Scattering of Sla2:351-968

(A) The *ab initio* bead model of *Sc*Sla2:351-968 from SAXS experiments at 2.22 mg/ml gave an elongated prolate model. When aligned to the AF3 model of the same construct the length of the two models is similar given the expected flexibility in solution of the protein. (B) Kratky plot as produced by ATSAS analysis using dammif and dammin, with the raw data plotted in black and the fitting curve plotted in red (Manalastas-Cantos et al. 2021).

5.1.5 *Chaetomium thermophilum*, a thermophilic fungus, can be used for structural studies of full length Sla2

The full length Sla2 protein was only possible to be expressed and purified from a construct from *Chaetomium thermophilum* (*Ct*). *Chaetomium thermophilum* is a model organism for Fungi, which grows at 50-55 °C (Kellner and Hurt 2022). Thermophilic organisms such as *C. thermophilum* offer the advantage of thermostable proteins that are resistant to degradation, even at high temperatures. The ability to express full-length Sla2 from *C. thermophilum* was crucial for capturing the structural integrity of the protein, including the coiled-coil and C-terminal domains. *Ct*Sla2 was used in the previous work of the Garcia Alai Team for the description of the AENTH complex (Lizarrondo et al. 2021).

Prior purifications of the *Ct*Ent1 ENTH domain were done with the help of former PhD student of the Garcia Alai Team, Javier Lizarrondo. This domain was used alongside purified full length *Ct*Sla2 for structural studies. In combination with equimolar amounts of the ENTH domain from *Ct*Ent1 and 200 µM $PI(4,5)P_2$ the resolved 3D class density map had 4 Sla2 dimers present (Figure 20). Two dimers were reasonable well resolved but two were poorly filled and clearly lacked information.

To improve the quality of the data for interpretation, a mask of the region for two of the Sla2 C-terminal dimers was used to locally refine the map (Figure 21). The use of local refinement with a mask of a certain region is used to facilitate improved resolution where there are clearly other areas of the map that cannot be improved to the same extent. This resulted in a local improvement of the map for the masked region to a level where secondary structure could be interpreted confidently. Residues 608-1050 of *Ct*Sla2 were modelled with AlphaFold3 and this model was used for fitting into the map with ISOLDE in ChimeraX (Figure 20). The agreement between the AF3 model and the experimental map is similar to that of the *Sc*Sla2 C-terminal region.

The main core of the C-terminal region is largely unaffected including the REND domain and the coiled-coil facing portion of the THATCH domain (Figure 22). The RMSD between the AF3 model and the fitted model across the best resolved dimer is 3.7 Å. As seen in Figure 22b, the significant differences are generally found at the edges of the folded domains. The distance between the loop that primarily interacts with the REND domain of the second Sla2 dimer, and the C-terminal residue of the other chain in the dimer is 34 Å in the cryo-EM structure and 41 Å in the AF3 model. This reduction in distance increases the contacts formed between the two dimers when docked in the density map (Figure 23).

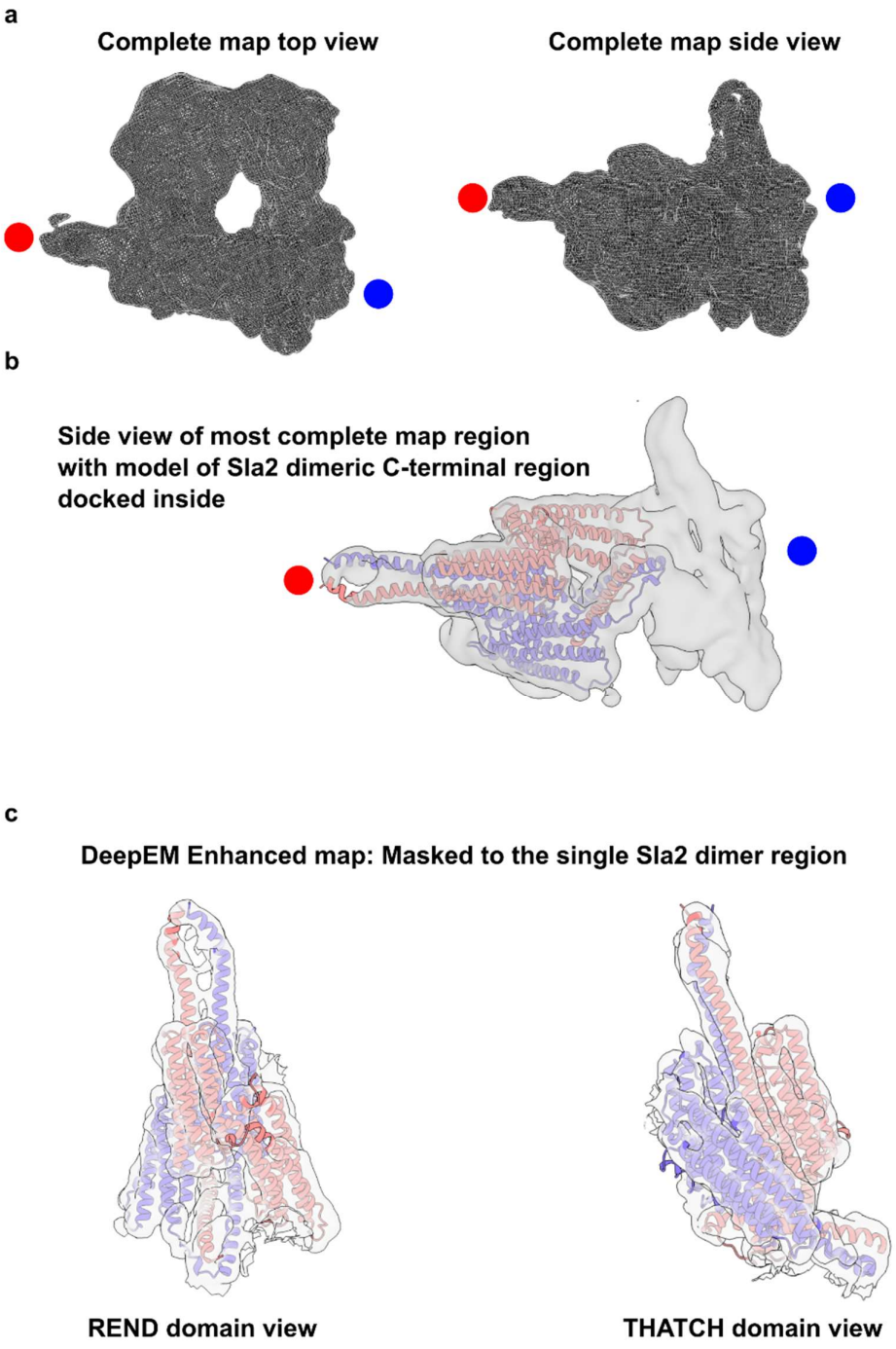

Figure 20: Unique *Ct*Sla2 C-termini structure observed in a CtSla2:ENTH:PIP_2 sample

(A) The complete 3D class after refinement is roughly 180 Å by 180 Å. The density seemed at first glance to be 4 monomers of the same structure. The best resolved density region is between the red and blue circles. (B) The AF3 model for dimeric *Ct*Sla2 608-1050 is fit into the density and highlighted in red/blue by chain. From seeing the fit of a single dimer, it can be inferred that the overall map displays four dimeric Sla2 C-terminal regions. (C) A DeepEM enhanced map masked to the *Ct*Sla2 model after optimisation in ChimeraX using ISOLDE (Croll 2018).

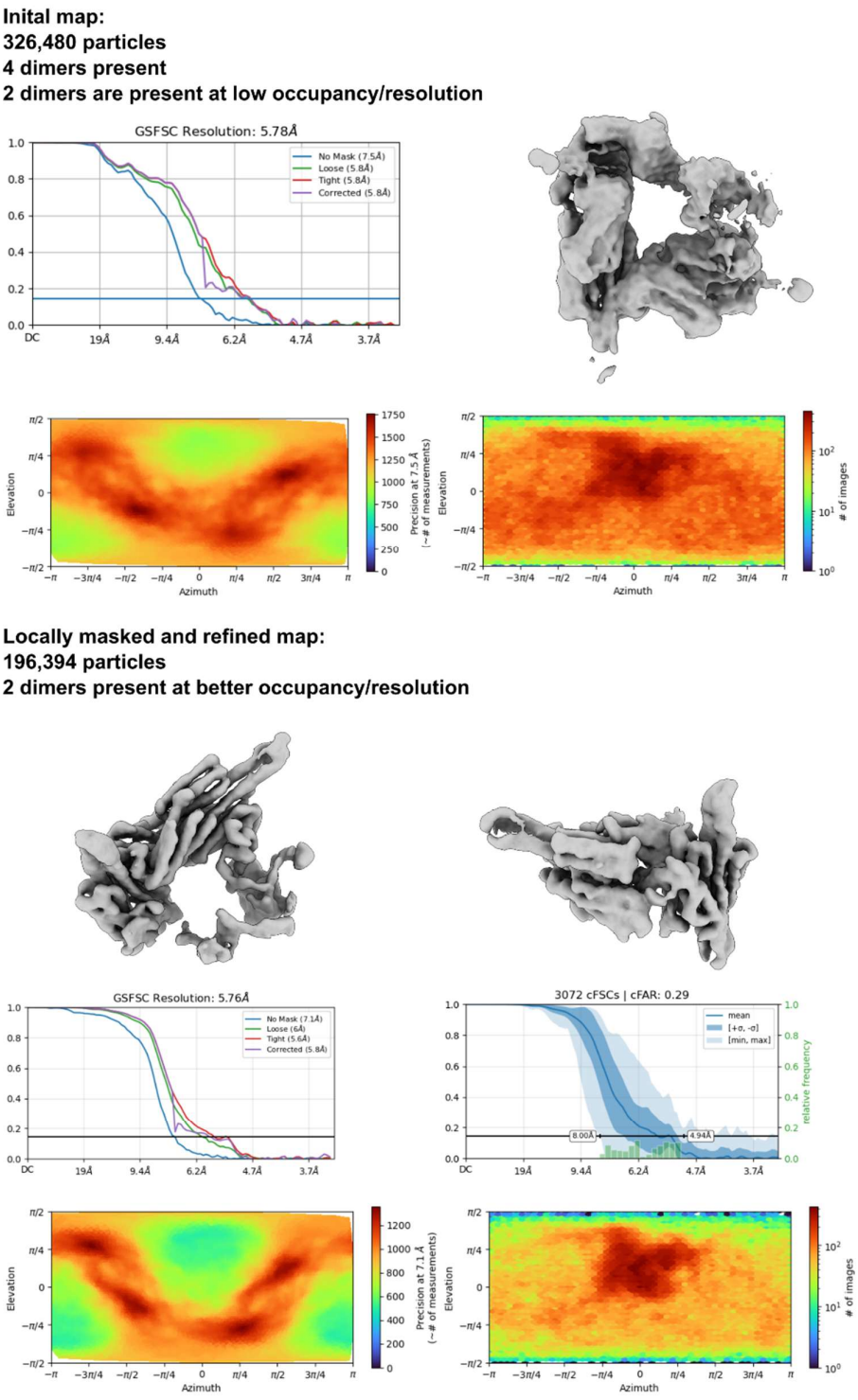

Figure 21: Refinement of *Ct*Sla2 C-terminal regions from *Ct*Sla2:ENTH:PI(4,5)P_2 sample

(Top) The initial map of produced from the particles picked from the micrographs is shown from the top view. GSFSC curves, Precision graphs, and image orientation are shown with the top view of the map. (Bottom) The z-flipped, locally masked, and refined map shown from the top and side view of the map. The particles used to define this map were filters via 3D classification with a 'junk' class to remove poor particles. The GSFSC, Precision, and Orientation graphs are presented as well.

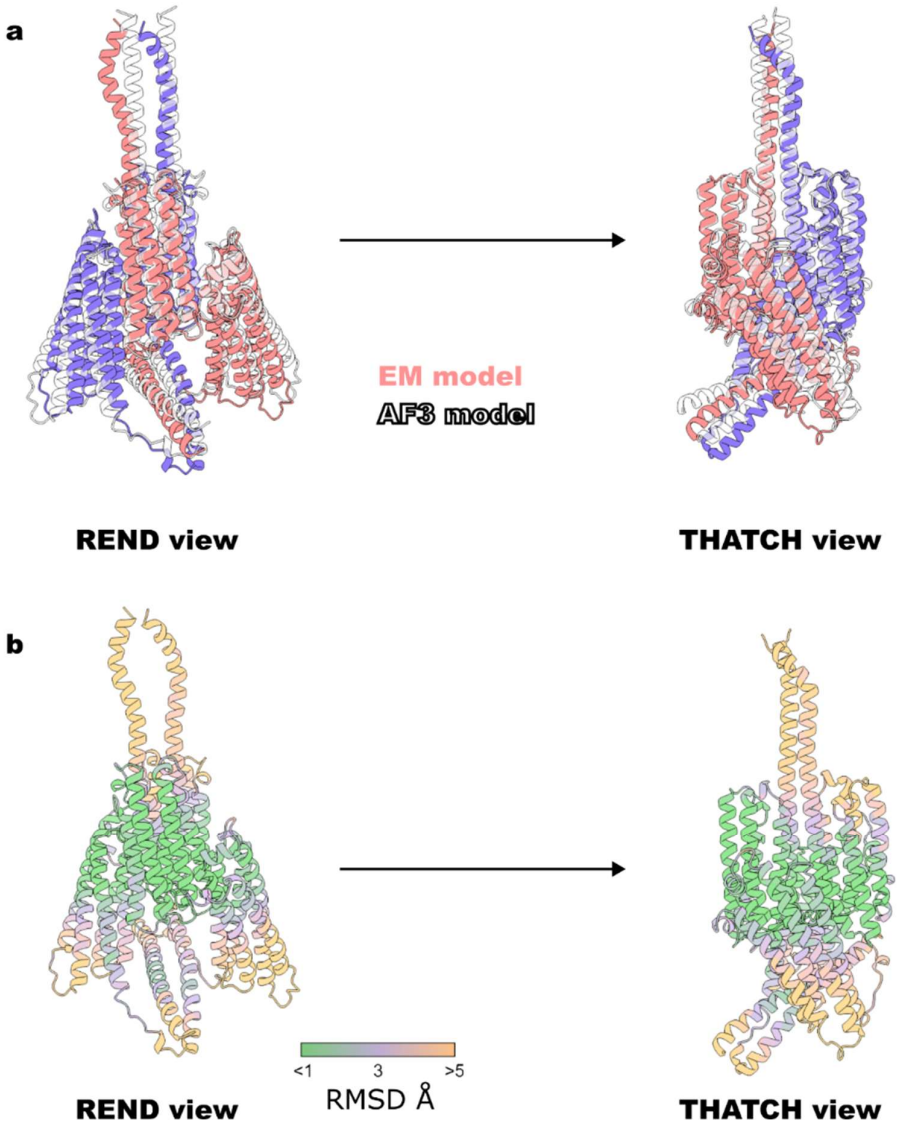

Figure 22: The C-terminal region of *Ct*Sla2 distorts in the presence of ENTH and PI(4,5)P_2

(A) Alignment of the AF3 model and cryo-EM determined model show a well aligned core of the REND and THATCH domains. The region of the THATCH domain containing the Actin Binding Residues is relatively unchanged, however the region facing away from the coiled-coil is moved significantly towards the LATCH helices. (B) The RMSD of the EM model from the AF3 model is coloured onto the model, with distances equal to or less than 1 Å as green, and 5 Å or above as yellow. The core regions have low RMSD to the AF3 model but the region of the THATCH core facing away from the coiled-coil have significantly high RMSD values.

The region of interest is the interface between the two dimers, the dimer in red (Chain A) and blue (Chain B) is considered to be Dimer 1 (Figure 23). The first surface of interest from Dimer 1 is the THATCH domain interhelix loops facing away from the coiled-coil that contacts the REND domain of Dimer 2. This includes the two helices that contain the ACB surface of the THATCH domain. The REND domain also contacts the N-terminus of Dimer 1 Chain B LATCH helix. With far fewer contacts as compared to the REND:THATCH interface but still it contributes to the vice-like effect on the two dimers interacting.

The second interface is from the LATCH helix of Dimer 1 Chain B and the REND domain loops of helices 2 and 3 facing the coiled-coil from Dimer 2 Chain A. The furthest distance between two residues in this two Sla2 dimer model is 18 nm, is relevant later when discussing larger complexes of *Ct*Sla2 C-terminal regions at 50 °C. The formation of this oligomeric particle in the sample as observed by cryo-EM is an interesting development in the understanding of the function and regulation of the THATCH and REND domains. These domains will be shown later to function in the formation of segregated droplets from *Ct*Sla2. This relates back to the idea of concentrating interacting proteins to overcome moderate-low affinity protein-protein complexes like Sla2:Actin to improve the outcome of the endocytic process.

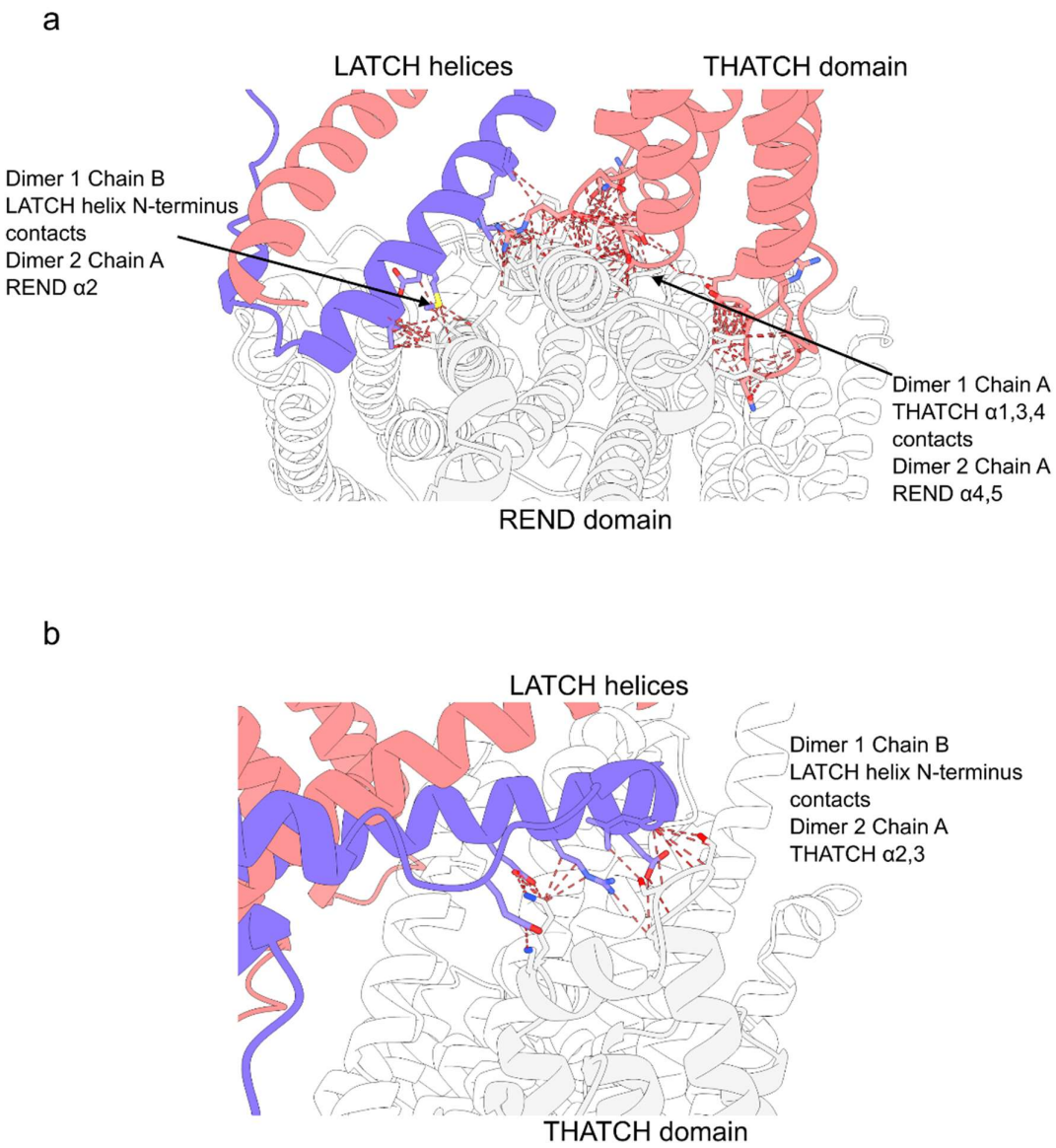

Figure 23: Contacts between individual *Ct*Sla2 dimers are between the Actin binding domain and the force sensing domains

(A) Contacts between the REND domain of the second dimer and the first dimer are shown in red dashed lines and the primary locations are labelled by arrows. The C-terminal helices of the REND domain contacts the THATCH domain of only one chain of the dimer. The N-terminal helices contact the LATCH helix of the other chain of the first dimer. (B) That same LATCH helix which contacts the REND domain also has close contacts to the THATCH domain of the first chain of the second dimer.

5.2 Sla2 forms two complexes with the Pan1/End3/Sla1 regulatory complex

5.2.1 Sla1, via its third SH3 domain, binds a Proline-Rich Motif within the Intrinsically Disordered Region of Sla2

Sla2 interacts with Sla1, which is part of the cycle of disrupting the Pan1/End3/Sla1 complex to modulate Actin polymerisation and recruitment at endocytic sites (Gourlay et al. 2003; Maldonado-Báez et al. 2008; Toshima, Toshima, Duncan, Jamie, et al. 2007; Bradford, Whitworth, and Wendland 2015). For the purpose of narrowing down the area of interest in Sla1, the region that is known to interact with Las17 is between 1-130 residues of Sla1, encompassing the first two SH3 domains (Figure 24) (Rodal et al. 2003). To understand the complete region of Sla1 that may be responsible for Sla2 binding, Sla1 residues 120 to 510 were modelled using AF3, this is the region between SH3_2 and SHD1 in the Sla1 annotated structure and has been indicated as the region responsible for the Sla2:Sla1 complex (Gourlay et al. 2003) (Figure 24a). As can be seen in Figure 24a, there are two well-folded domains. There is the 3rd SH3 domain and a confidently-predicted, unannotated folded domain between residues 250-341.

After re-running the reduced Sla1 region corresponding to this unknown domain in AF3, the output "*.pdb" file was used for a FoldSeek search (van Kempen et al. 2024). FoldSeek is an online tool for searching structural databases for homologous structures rather than amino acid sequence, which you can limit to certain species proteomes. The models retrieved can be both experimentally and computationally determined. The highest-ranking structurally homologous domains, within the AlphaFold predicted *S. cerevisiae* structural proteome, belong to the Pleckstrin Homology (PH) domain family (Lemmon 2007). These domains bind Phosphatidyl Inositol phosphates (PIPs). One of the highest-ranked hits against this search structure was the 2nd OPY1 PH domain (Ling et al. 2012), which specifically binds $PI(4,5)P_2$ (Figure 25). Searching FoldSeek using the AF3 model of the isolated 2nd OPY1 PH domain

returned the proposed Sla1 PH domain as a confident hit within the *S. cerevisiae* structural proteome. The other domain in the Sla1:120-510 AF3 model is the previously annotated 3rd Sla1 SH3 domain (residues 355-415) (SH3_3) (Figure 24a).

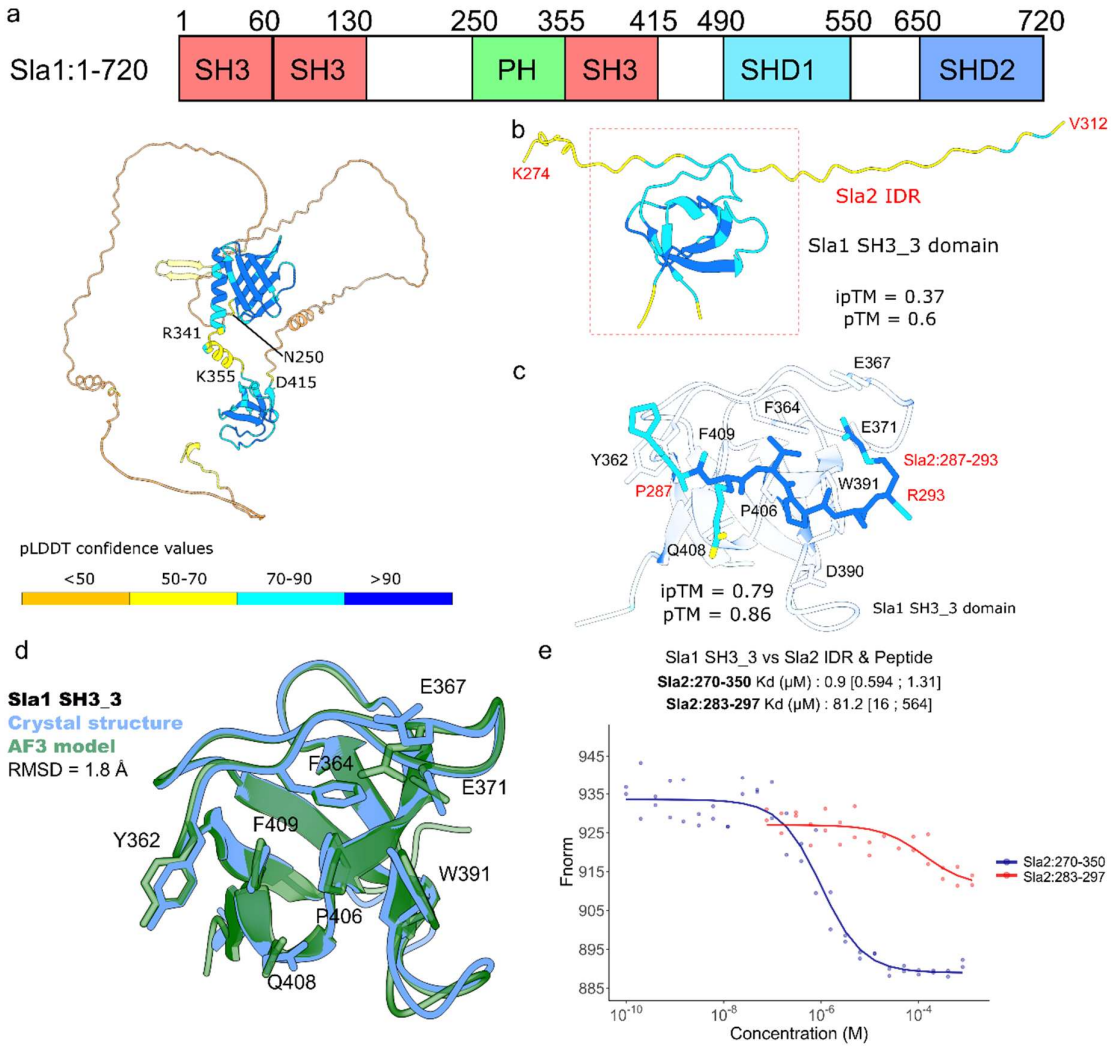

Figure 24: Sla1 SH3_3 domain binds the Sla2 IDR

(A) Domain architecture of Sla1 residues 1-720 and AF3 model of Sla1 residues 120-510. (B) AF3 predicted complex of Sla1 SH3_3 and the extensive Proline rich IDR of Sla2 (residues 274-312). (C) The complex of Sla1 SH3_3 and Sla2:287-293 was remodelled to reduce the error in the modelled interaction with the excess peptide region around the proline motif. The peptide is coloured as in the previous panels with the pLDDT score colour scheme. The contact residues between the motif and the SH3 domain are with the one-letter code and residue number. (D) Overlay of the crystal structure of the Sla1 SH3_3 domain (including a protein expression cleavage scar) with the AF3 model of the same amino acid sequence. The key residues that are found to be coordinating peptide motifs in other structures of SH3 domains are labelled and shown in cartoon form for both models. Aromatic residues spread through the binding cleft as well as two polar/charged residues that coordinate positively charged residues at the C-terminus of the Pro-rich motif. (E) MST of Sla2:270-350 and Sla2:283-297 titrated against Red-NHS labelled Sla1 SH3_3, which gave a binding K_d of 0.9 μM and 81.2 μM, respectively. These results confirm that the Sla2 IDR binds to the Sla1 SH3 domain. Adapted from (Draper-Barr et al. 2024)

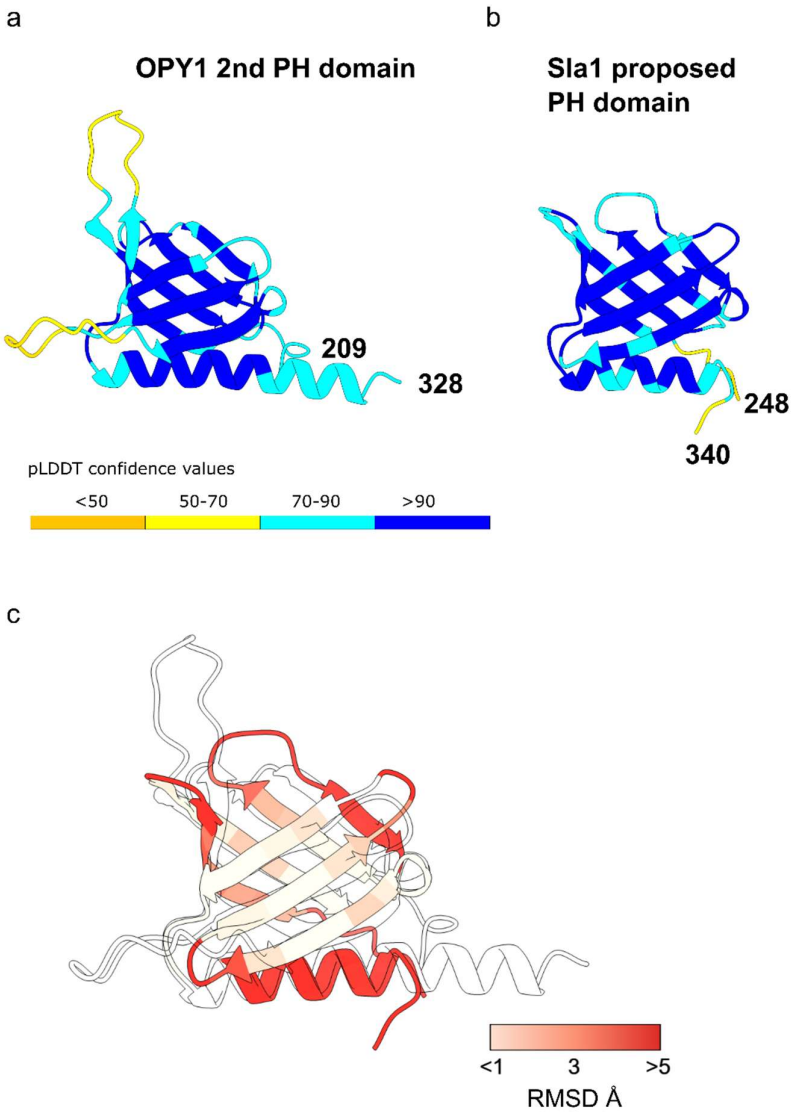

Figure 25: AF3 and FoldSeek elucidate a possible PH domain in the central region of Sla1

(A) AF3 model of the 2nd PH domain of *Sc*OPY1, modelled only from residues 209-328 of *Sc*OPY1. Reducing the residue boundaries for AlphaFold has been shown to improve the confidence of the models. (B) AF3 model of the folded region between the 2nd and 3rd SH3 domain of Sla1, which I now propose as a PH domain. (C) The proposed Sla1 PH domain structurally aligned to OPY1 2nd PH domain as the reference structure. The Sla1 PH domain is coloured by RMSD to the reference structure. Average RMSD is 5.1 Å across the model.

The only domains present are a proposed PH domain, that binds lipids, and a SH3 domain, which binds peptides. With this in mind, the hypothesis for the Sla2:Sla1 complex was that the primary interaction area from Sla2 would be the proline-rich disordered region between the ANTH and coiled-coil region of Sla2 forming a complex with the 3rd SH3 domain of Sla1. To

initially screen the likelihood of this hypothesis, an AF3 model was produced of residues 274 to 312 of Sla2 (the proline-rich region of the IDR) alongside one moiety of Sla1 residues 355 to 414 (SH3_3) (Figure 24b). The SH3_3 domain was modelled in proximity to residues 287-293 of Sla2, with an ipTM score of 0.37. The ipTM score for the model of the Sla1 SH3_3 domain with the isolated peptide (residues 287 to 293) was 0.79 (Figure 24c and Figure 26). The key residues involved are similar to that of crystal structures of other SH3 domains bound Proline rich peptides (Massenet et al. 2005; Jia et al. 2023; Wu et al. 1995). The pTM score given by AF3 is a measure of confidence for the 3D position of all the atoms, whereas the ipTM score reflects the confidence for the positions of interacting atoms at an interface. A score above 0.6 for both, combined with additional experimental evidence, strongly indicates that the predicted model is likely to be correct.

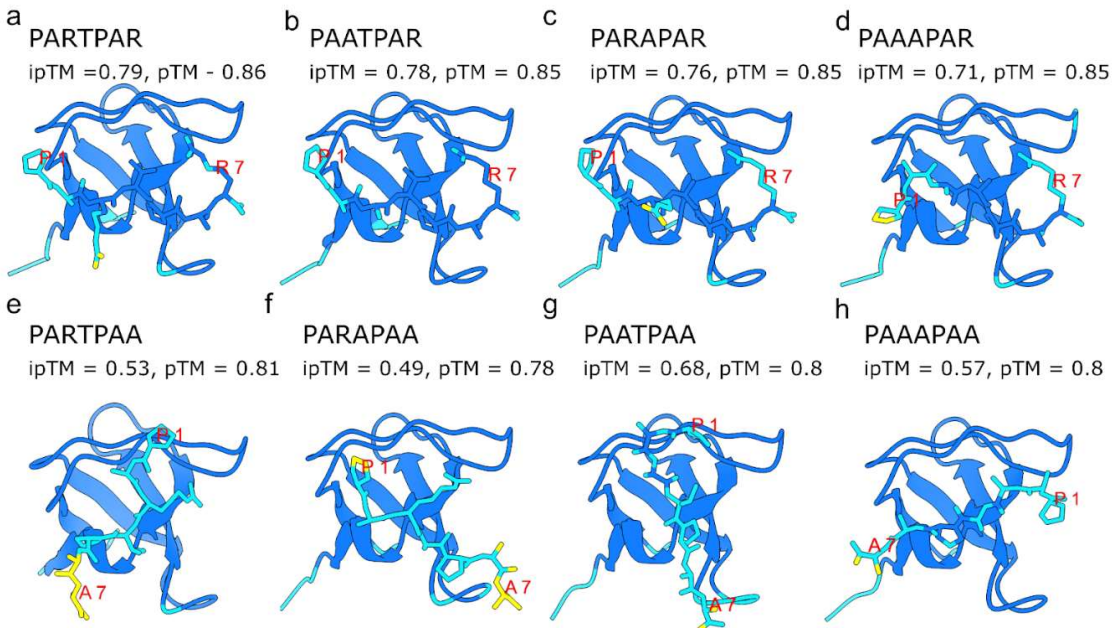

Figure 26: AF3 models highlight that the PxxxPxR motif found in Sla2 is sufficient to predict the Sla1 SH3_3:Sla2 complex

(A-H) - AF3 models of Sla1 SH3_3 and seven residue peptides listed above the model along with the ipTM and pTM scores. Alanine replacements for residues in the motif show a decrease in the ipTM scores, particularly when the C-terminal Arginine is replaced with an Alanine. The colouring scheme is the AlphaFold3 pLDDT colour scale as used for the other models in this work. Adapted from (Draper-Barr et al. 2024)

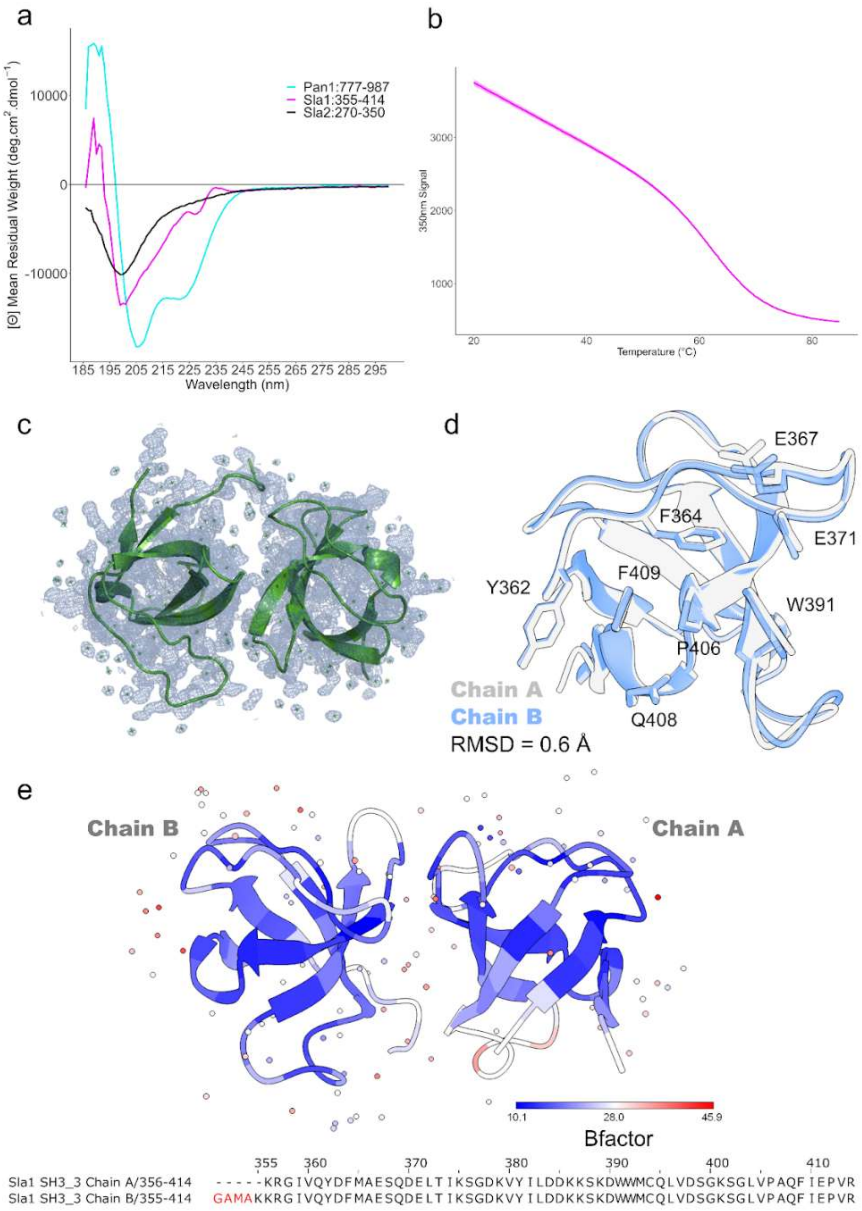

Figure 27: Biophysical characterisation and structural studies of polypeptides used to explore the Sla2 interaction network

(A) Far-UV Circular Dichroism spectra for Pan1:777-987, Sla1:355-414, and Sla2:270-350. Secondary structure content estimations using the ChiraKit software from the eSPC online tool kit (see methods) retrieved the following percentage values for Pan1:777-987 (Alpha 33.6, Beta 10.9, Turns 14.1, Disordered 40.6); Sla1:355-414 (Alpha 13.9, Beta 28.1, Turns 11.8, Disordered 45.4) and Sla2:270-350 (Alpha 11.1, Beta 28.4, Turns 14.0, Disordered 45.0). (B) Thermal stability fluorescence-based assay to assess a melting curve of Sla1:355-414 at 350 nm (nanoDifferential Scanning Fluorimetry), the Tm fitted from the curve corresponds to 64.6 ± 0.1 ºC SD = 0.0067 across 3 replicates. (C) Models of the Sla1 SH3_3 domains, with Oxygen atoms representing the modelled water molecules, fit into the electron density map at 1 σ. (D) The two chains of Sla1 SH3_3 overlaid and key residues labelled from the peptide binding groove. The chains have an overall RMSD of 0.6 Å. (E) The complete crystal unit model including waters coloured by Bfactor. The respective Chains are labelled as well as the sequence of residues modelled for each chain at the bottom. The average Bfactor across the model is 19 Å^2. Adapted from (Draper-Barr et al. 2024)

To test the hypothesis *in vitro* the SH3_3 domain of Sla1 (residues 355-414) was cloned and expressed using a GST purification tag. Far UV Circular Dichroism spectrum and thermal denaturation experiments indicate that the domain is folded and displays a two state cooperative unfolding (Kotov et al. 2021; Burastero et al. 2021) (Figure 27a-b). The Sla1 SH3_3 was able to be crystallised and the structure of the Sla1 SH3_3 domain was resolved at 1.49 Å (deposited in the wwPDB under 9HDB) (Table 10) (Figure 27c-e). The data was collected at the P13 beamline, EMBL Hamburg, DESY with the help of Gleb Bourenkov (Schneider Team). The correlation between the AF3 model and the crystal structure is very high at an overall RMSD of 1.8 Å, which supports the confidence in the expression construct for use in biophysical analysis of the Sla1:Sla2 complex (Figure 24d). Data analysis and interpretation was assisted by David Ruiz-Carillo.

The convergence of the experimental and computational methods validates the use of the biophysical data, confident that the Sla1 SH3_3 domain is folded as expected. For consistency, MST was used to characterise the interaction between the complete intrinsically disordered region (IDR) of Sla2 and isolated Proline-rich peptide 283-297 with the SH3_3 domain (Figure 24e). The IDR was confirmed as a disordered polypeptide through Circular Dichroism as well (Figure 27a). The K_d for the SH3_3 domain and the complete IDR (residues 270-350) is in the micromolar range, which is almost two orders of magnitude stronger than that of the peptide alone. The increase in affinity by the additional N- and C-terminal regions around the peptide motif can be observed in other SH3 systems, such as with the GRB2 SH3 domains, where the complete IDR increases affinity for the peptide by up to 100-fold (Bartelt et al. 2015; Dionne et al. 2021).

Our biophysical evidence of the interaction, the experimental structure of the Sla1 SH3_3 domain, and AF3 models of the protein complex supports the hypothesis that the Sla1 SH3_3 domain interacts with the PARTPAR motif in the Sla2 IDR. The secondary results showed that the complete IDR sequence has a positive impact on the SH3 domain Sla2 peptide interaction, which was an unexpected find and is supported by other evidence in the field. As the N-terminal residue of the Sla2 peptide interacts with Y362 of the Sla1 SH3 domain and continues

to the C-terminal Arginine residue that coordinates with E371, the PARTPAR motif is classified as a (-) direction binding motif of $P^0xxxP^4xR^6$ (Bartelt et al. 2015; Teyra et al. 2017). This is similar to two other interesting cases of a PPxxPxR motif binding SH3 domains (Jia et al. 2023; Wu et al. 1995)(Figure 28). The motif PxxxPxR is sufficient for modelling the SH3 domain complex, with Alanine replacements of the non-proline residues showing little shift in the ipTM score apart from the terminal Arginine residue (Figure 26). In the IDR of Sla2/End4 proteins across Fungi this motif is present in 15 examples and a $P^0xxP^3xR^5$ motif is more conserved with 155 examples in our selected sequences. The PxxPxR sequence is another common class of motifs bound by SH3 domains (Teyra et al. 2017). In the IDR of Metazoa Hip1R sequences, only one example exists of the $P^0xxxP^4xR^6$ and none of the $P^0xxP^3xR^5$ motif within the IDR. Sla1 and the Sla2 IDR proline-rich motif are both only found in Fungi.

5.2.2 Further computational modelling of complexes made by Sla1

This section focuses on computational modelling to predict and analyse the structural interactions between Sla1 and its binding partners, providing insights not accessible through experimental methods alone. Understanding the interactions made by Sla1, particularly with Sla2 and Las17, is crucial for determining how endocytic adaptor proteins coordinate actin regulation and membrane remodelling. The Sla1:Las17 complex has been comprehensively characterised biophysically (Feliciano and Di Pietro 2012; Sun et al. 2015), it is an inhibitory complex alongside the helping hand of Bbc1, Lsb1, and Lsb2 (Spiess et al. 2013; Rodal et al. 2003).

The interaction was narrowed down to the region of residues 300-400 of Las17 with Sla1 SH3_1 and SH3_2. This utilised an Actin polymerisation fibrillation assay with combinations of Las17 and Sla1 regions and the level of Arp2/3 complex activation. This region encompasses several PxxP motifs across the IDR region in the centre of Las17, referred to as P1-P12. AlphaFold3 models of the Las17 region with SH3_1 & SH3_2 (residues 1-130) show that the IDR loops around the SH3 domains and forms a divalent interaction between

the proteins. This would support the evidence that it is such a strong interaction with a sub-micromolar K_d (Figure 29).

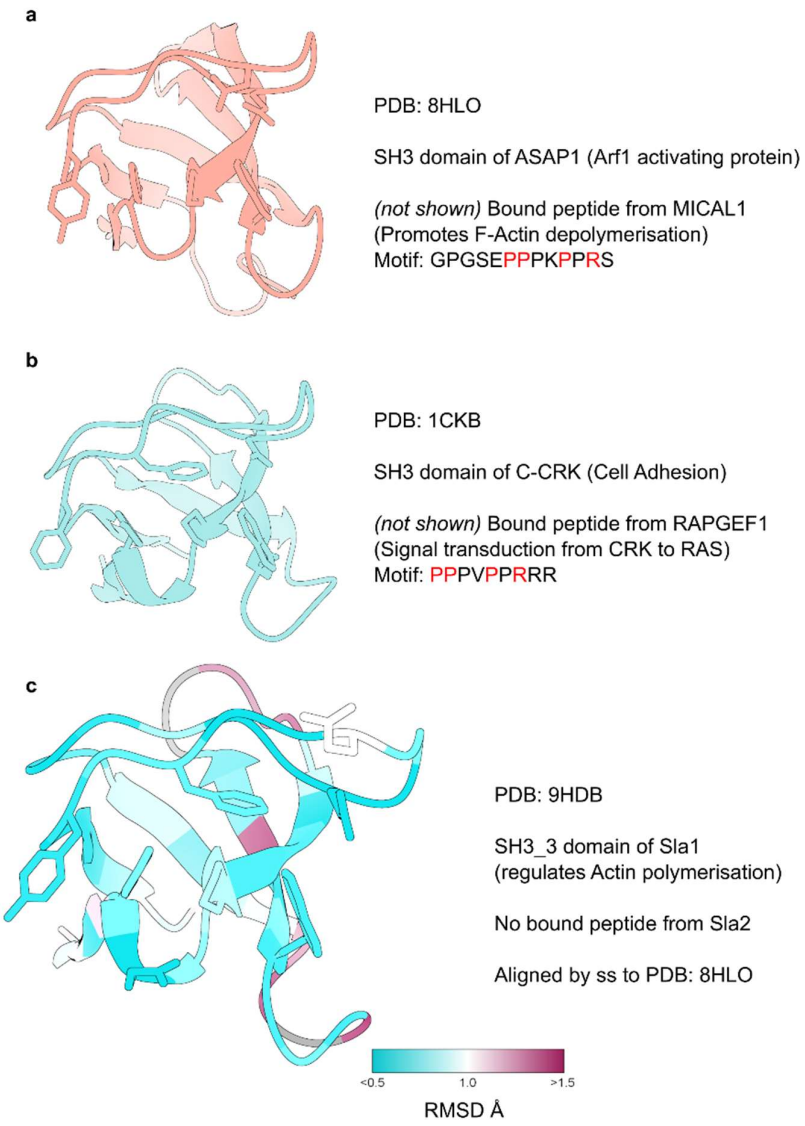

Figure 28: Crystal structures of SH3 domains with similar peptide preference show closely related positions of side chains in the peptide binding groove

(A and B) PDB entries 8HLO and 1CKB shown without the Proline-Rich Motif shown. These crystal structures contain ligands with the same (-) direction motif as Sla2. Side chains of key residues for the SH3 domain are shown in stick form. The key processes of the SH3 domain containing protein and motif are in parentheses next to the structure. (C) Crystal structure of Sla1 SH3_3 domain coloured by RMSD to the PDB:8HLO structure as the structure with highest sequence similarity of the two previously shown crystal structures. The average RMSD across 52 pruned pairs in the structures is 0.7 Å, across all 61 is 3.3 Å.

These interactions are similar to that of SH3_3 with the Sla2 IDR, where the proline-rich motif termini go in the same direction as the binding groove. This results in its classification as a Class II motif, where it also follows the consensus motif of the Sla2 IDR as $P_0xxP_3xR_5$. It could also be said that as in the work of Felciano and Di Pietro that this motif particularly for P10 and P12 these motifs have surrounding regions that could be Class I motifs running in the opposite direction N-termini to the binding groove hence it would then be $R_5xP_3xxP_0$. However, it does seem that the structural and sequence homology for the shortened AF3 model resulted in the Class II orientation for this model. The longer the Las17 IDR modelled potentially this may alter the final model, but a longer IDR would most likely lower the quality of the model.

Returning to the analysis of the PH domain proposed in the Sla1 central region. There are several PH domains crystallised with ligands. Aligning these with the AF3 model for the PH domain of *Sc*Sla1, revealed that the crystal structure of the PH domain from *Hs*Pleckstrin bound by D-myo-inositol 1,2,3,5,6-pentakisphosphate (5IP) has the highest structural similarity (PDB: 2i5f). The RMSD over the whole PH domain is 4.1 Å (Figure 30a). However, there are key residues with very low RMSD values such as *Sc*Sla1 F280 that is highly similar to the Y277 of the *Hs*Pleckstrin PH domain that coordinates the innermost portion of the inositol ligand. Leaving the 5IP ligand from the 2i5f crystal structure and the *Sc*Sla1 PH domain visible after structural alignment, and looking for close contacts between them shows highly similar residues. These contacts were only on one side of the binding pocket of the Sla1 PH domain (Figure 30c). The lack of positive residues on one side of the binding groove could leave space for the acyl chain of $PI(4,5)P_2$ to pass through if indeed this proposed PH domain is functional and can bind lipids on the endocytic membrane. The presence of a lipid binding domain in Sla1 suggests that another aspect to the localisation of Sla1 to the CCS is by a specific interaction to $PI(4,5)P_2$.

There are limitations of the models presented here, namely that these are computationally modelled protein complexes. These are supported by biophysical evidence in the case of the Sla1:Las17 complex, but for the proposed PH domain this analysis is purely based on the

sequence and structural alignments performed here. These predictions should be tested using mutagenesis and biophysical assays, such as ITC or liposome co-sedimentation assays to confirm the specifics of the proposed properties of this domain.

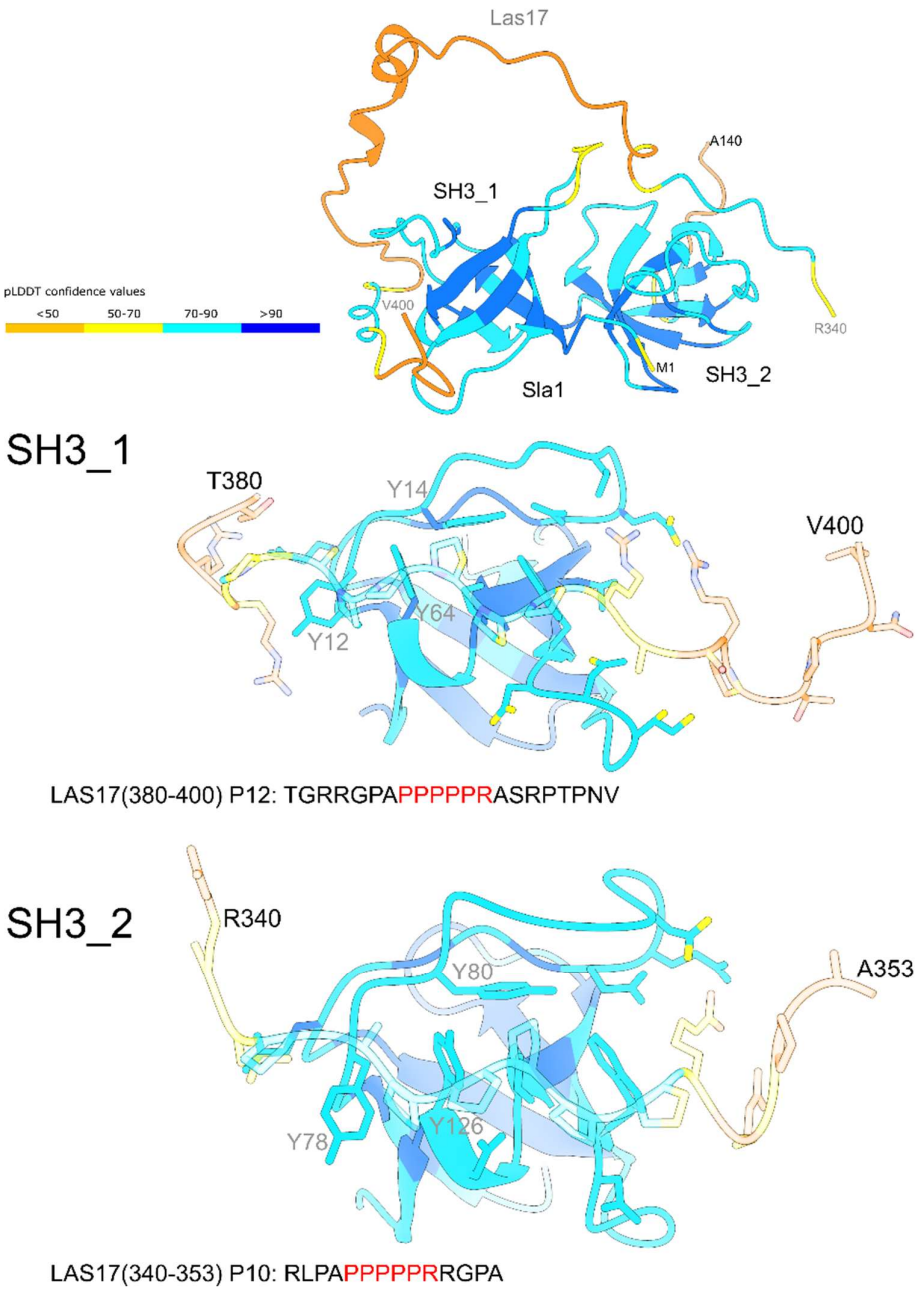

Figure 29: Sla1 SH3 domains 1 and 2 bind a truncated Las17 IDR in a predicted as Class II PxxP motif arrangement

The complete interaction regions of Las17 and Sla1 are shown (top) with full AF3 confidence values coloured onto the models. SH3_1 and SH3_2 are shown individually with the respective contact regions of Las17:340-400. The three key Tyrosine residues used for classifying motif type are labelled in each SH3 domain for comparison.

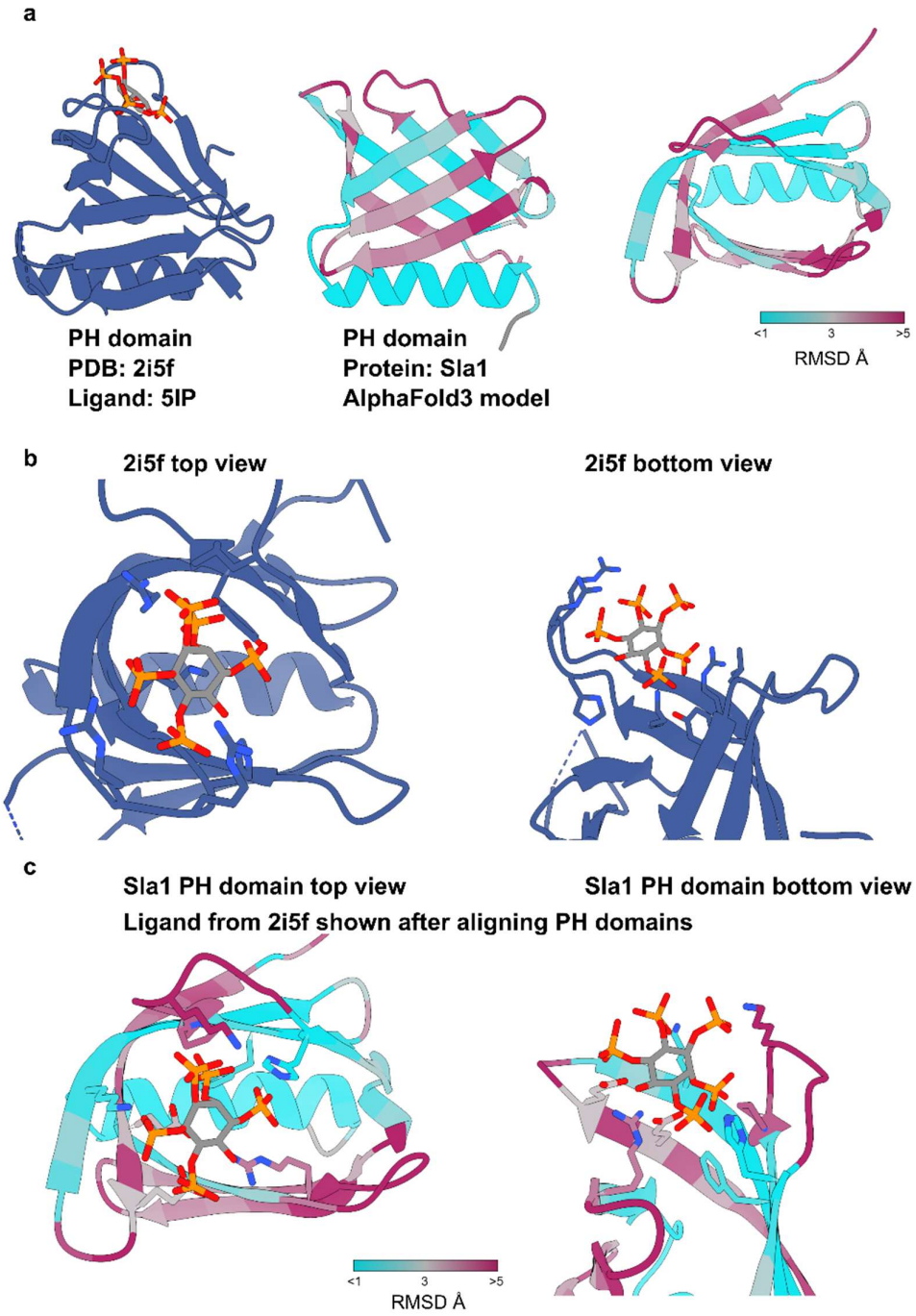

Figure 30: The crystal structure of the *Hs*Pleckstrin PH domain with a bound Phosphatidyl inositol highlights conservation of lipid coordinating side chains in the Sla1 probative PH domain

(A) PH domain from *Hs*Pleckstrin bound by D-myo-inositol 1,2,3,5,6-pentakisphosphate was crystallised to a high resolution (Jackson et al. 2007). Structural alignment of the PH domain predicted for *Sc*Sla1 gave a similar RMSD as the PH domain of OPY1, 4.3 Å overall but 39 of the paired atoms had an RMSD < 1 Å. (B) The binding pocket of the PH domain from PBD: 2i5f shows coordinating side chains engulf the ligand from all sides. (C) After structural alignment the total model for Sla1 was left and the 5IP ligand was kept from the 2i5f crystal structure. This revealed similar placement of several coordinating side chains for the 5IP ligand, revealed in stick form.

5.2.3 The coiled-coil of Pan1 interacts with the Sla2 coiled-coil, competing with CLC at Site 2

Pan1 is the other player in the Pan1/End3/Sla1 complex that has a regulatory role within endocytosis. This protein has a very extended profile with many interactions domains for other endocytic proteins (Figure 3) (Bradford, Whitworth, and Wendland 2015; Enshoji et al. 2022). The Sla2:Pan1 interaction is mediated by the coiled-coils of both Sla2 and Pan1 (Toshima, Toshima, Duncan, Jamie, et al. 2007). Pan1:777-987 was expressed and purified to investigate the strength of the interaction between Pan1 and Sla2. The interaction was quantified with MST measured against labelled Sla2cc (Figure 31a). The binding experiments showed that Sla2 has an affinity for Pan1 of 0.6 μM. The affinity is in line with parameters used in the Pan1 inhibition assay done by Toshima et al. In this study, 100 nM of Sla2p was sufficient to partially inhibit Actin polymerisation by 50 nM of Pan1 in combination with 10 nM Arp2/3 (Toshima, Toshima, Duncan, Jamie, et al. 2007).

After the measurements, biophysical characterisation was done on Pan1:777-987 via Far UV Circular Dichroism. The results indicate a predominantly alpha helical secondary structure content for Pan1:777-987 (Figure 27a) as predicted by prior secondary structure prediction. This gives credence to the MST data, as the polypeptide produced for the experiments is well-folded.

To complement the MST data, BS3 facilitated cross-linking was performed on Pan1 and Sla2 for use in Cross-Linking Mass-Spectrometry. These revealed cross-links clustering in the Sla2 coiled-coil central region and at the C-terminal end of the construct in the first helix of the THATCH domain (Figure 32). There were three times as many cross-links found in the Site 2 region as the Site 1 region. There is a conspicuous lack of cross-links in the region between residues 560-730. These residues cover the REND domain as determined by the cryo-EM structure (Figure 14), which suggests that the interaction is specific in nature to the central region of the coiled-coil and are focused on the conserved interaction between Fungi and Metazoa.

AF3 models were a key tool in visualising the map of interactions involving Sla2, Pan1, and CLC. Models were produced for Sla2 residues 450-550, CLC residues 20-55 (Site 2 binding region of CLC), and Pan1 residues 800-940 in different ratios (Figure 31b-e). The complex of Pan1 with Sla2 is predicted with moderate-low confidence but with higher confidence in the individual folds of the polypeptides (Figure 31b). The models show that the CLC Site 2 complex is confident as the ipTM is above 0.6 in the Sla2:CLC complex (Figure 31c).

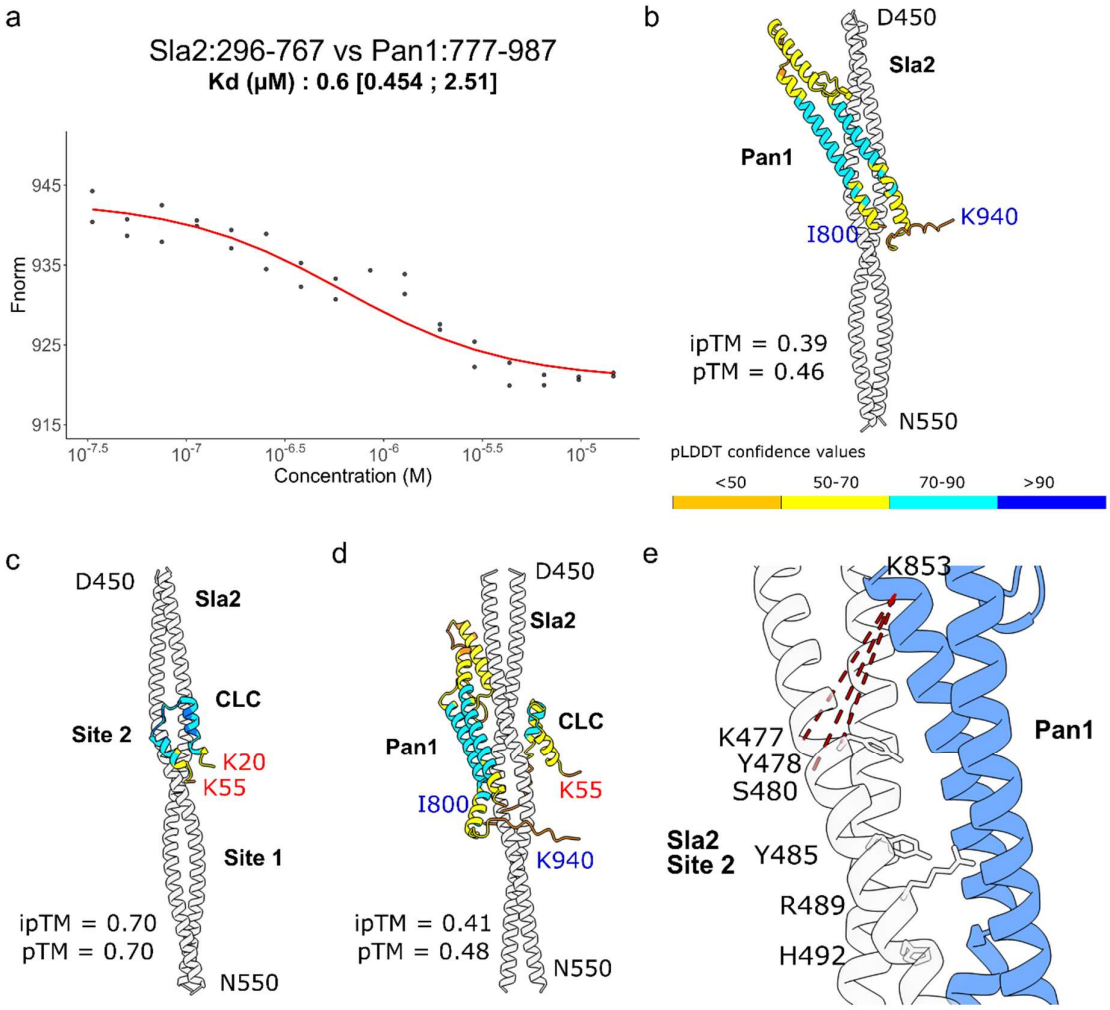

Figure 31: Pan1 and Sla2 interact through their coiled-coils, potentially at Site 2
(A) MicroScale Thermophoresis titration of Pan1:777-987 against RED-NHS labelled Sla2:296-767. This gave a resulting global K_d of 0.6 μM, CI95 [0.454; 2.51]. (B-D) AlphaFold3 models of Sla2:450-550, Pan1:800-940, and CLC combined in different ratios. (B) 2xSla2:CLC, (C) 2xSla2:Pan1, and (D) 2xSla2:CLC:Pan1. (E) Close up of the interface of the Sla2 dimer and Pan1 in (B). Key labelled residues in one Sla2 monomer are Y478, Y485, R489, and H492 that form Site 2 residues mutated in our two Site 2 mutant constructs, corroborating our hypothesis that Pan1 is competing for Site 2. Three cross-links between Sla2 and Pan1 are labelled in red dashed lines that were in the highest scored cross-links of our Pan1:Sla2 cross-linking dataset and correspond also to residues in proximity to each other in the AF3 model. Adapted from (Draper-Barr et al. 2024)

Previous *in vivo* FRET measurements from Skruzny et al., show the Sla2:Pan1 complex have high FRET efficiency. This experiment required the fluorophore labelled C-termini of both Sla2 and a truncated construct Pan1 (1-1050). The high FRET efficiency indicates that the C-termini of both Sla2 and Pan1 are very close in physical space (Skruzny et al. 2020). This conclusion from the FRET experiments concurs with the AlphaFold3 model shown in Figure 31b. The reduced ipTM score of Sla2:Pan1 when compared to the Sla2:CLC complex may be the result of insufficient structural and sequence homology available during the AlphaFold3 model generation. The Pan1 moiety covers Site 2, pictured by comparison to the Sla2:CLC model (Figure 31d). The location of the modelled interaction between Pan1 and Sla2 in both instances is predicted to be blocking Site 2, key residues for this site are labelled on the Sla2 coiled-coil (Figure 31e). This is consistent with the high number of cross-links in this region between Pan1 and Sla2 as compared to Site 1. The additional crosslinks found across Pan1 to the N-terminal portion of the THATCH domain may be as a result of the flexibility of this region. In combination, these results show that Pan1 forms a coiled-coil that binds to Sla2 Site 2 with a comparable K_d to CLC.

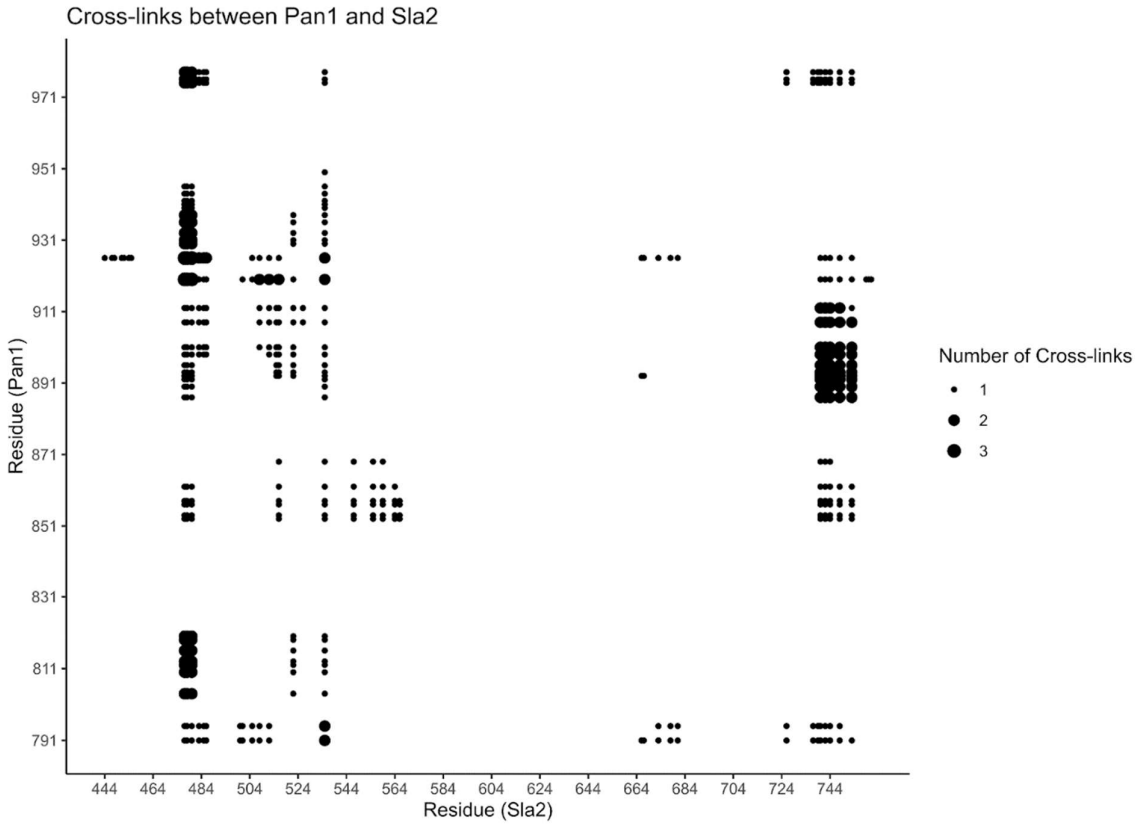

Figure 32: Cross-Linking Mass Spectrometry of Sla2 and Pan1 shows binding of Pan1 to the coiled-coil in proximity to Site 2 and Site 1

BS3 cross-linking of Sla2:351-968 and Pan1:777-987, the cross-links were filtered to match the constructs used for MST. There were no cross-links in the N-terminal region of the Sla2 construct and there is a clustering of cross-links in the Site2/1 region. The number of cross-links in Site 2 is 3 times greater than those in the Site 1 region. There are significant cross-links in the C-terminus of the construct but this can be attributed to the flexible nature of the coiled-coil and the high number of lysines exposed on the loops of the THATCH domain. Adapted from (Draper-Barr et al. 2024)

5.2.4 Pan1 self-associates in the coiled-coil region

The coiled-coil of Pan1 showed an interesting Size Exclusion Chromatography elution profile. The profile was consistent with a much larger particle, even considering the extended nature of coiled-coils. This suggested an oligomeric state for the Pan1cc. Pan1cc was labelled with the RED-NHS kit, the same label for MST as used for Sla2cc and CLC for biophysical characterisation. The MST profile, as shown in a, provides a single transition that corresponds to a K_d of 7 μM (Figure 33).

The AlphaFold3 model for two moieties of Pan1:777-987 (Figure 33) shows that the central section between residues 810-950 is predicted to be folded with a pLDDT value between 70 and 90. This is a good indicator that the coiled-coil proposed is likely to fold in this manner. The N- and C- terminal regions have poor pLDDT scores, suggesting very low structural homology leading to low confidence and hence the fold of this region may not be trustworthy. Cross-linking Pan1cc at a final concentration of 20 μM with an excess of BS3 cross-linker gave a large number of cross-links to plot and analyse (Figure 33c).

The first section of the cross-links that are more easily attributed within the AF3 model is the central helical bundle between residues 845-915, highlighted in the blue circle. The residues 845-945 form a pair of anti-parallel helices. The cross-links highlighted in red would correspond to the cross-linking of residues at the termini of the helices that would only be possible in the self-chain interactions; residues 810-820 to 940-950 and 840-850 to 910-920. Within purple highlighted regions are the cross-links that would correspond the dimer interface as seen in the AF3 model.

On the edges of the Pan1cc molecules, 777-810 and 945-987, the cross-linking may not be as reliable, due to the inherent flexibility of the coiled-coil region shown by the lower pLDDT score of the AF3 model. This is in addition to the solvent accessibility of this region, which would increase aberrant cross-linking between non-complexed Pan1 molecules. Therefore, from this computational model, alongside the biophysical and biochemical data, that Pan1 oligomerisation is possible through the same region that binds to Sla2 and that at high local

concentrations the Pan1 oligomerisation could have an influence on complex formation between Sla2 and Pan1.

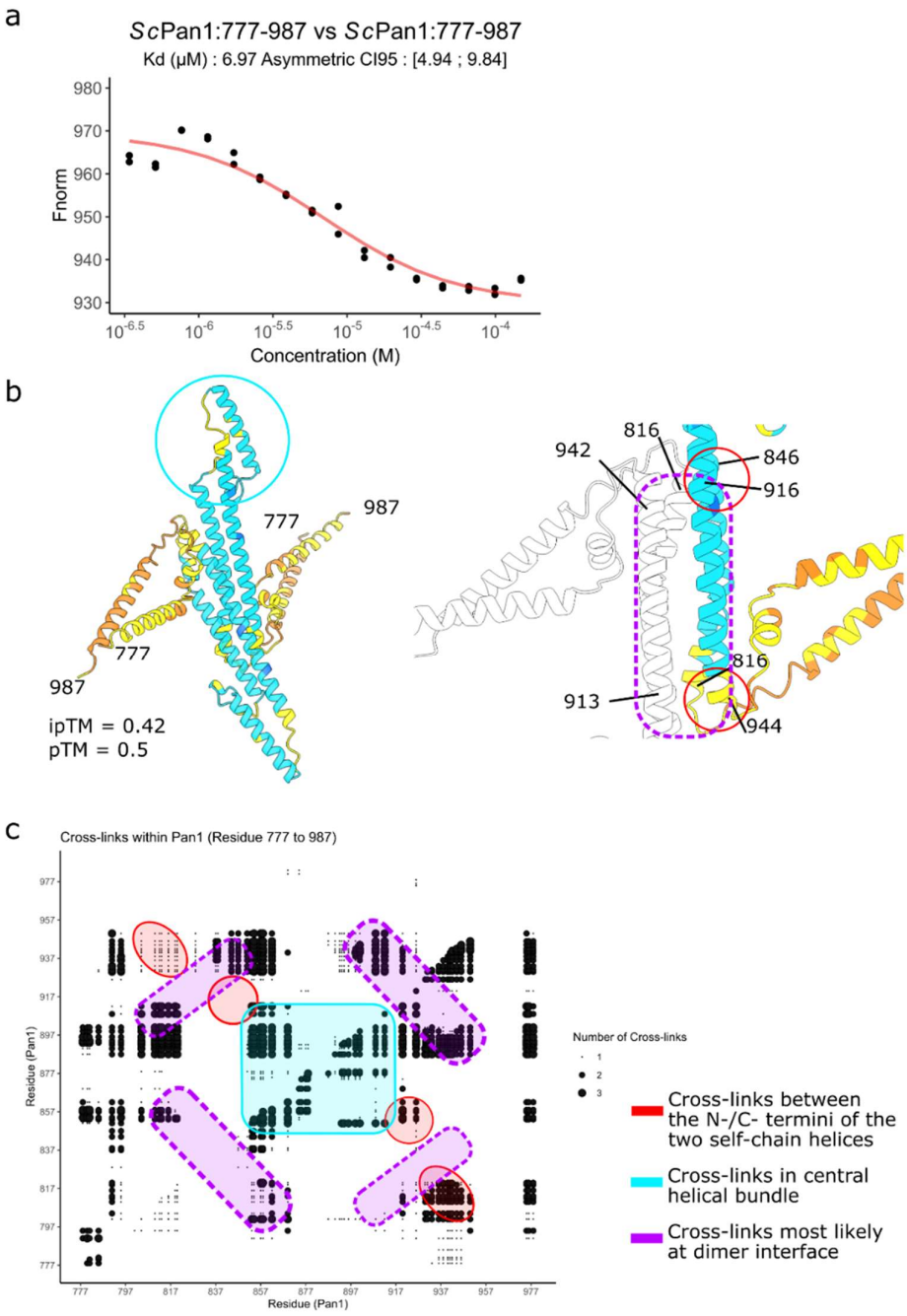

Figure 33:The coiled-coil region of Pan1 self-associates with a lower affinity than the interaction of Pan1 with Sla2

(A) MicroScale Thermophoresis titration of Pan1:777-987 against RED-NHS labelled Pan1:777-987. This gave a resulting global Kd of 7 μM, CI95 [4.94; 9.84]. (B) The AF3 model for a Pan1cc dimer coloured by pLDDT score and the ipTM and pTM score for the model listed as well. With a zoom in view of the dimer interface on the right of the primary model image. (C) Cross-linking of Pan1cc at a concentration of 20 μM is plotted, Site 1 against Site 2 from the unique site pairs. Red, blue, and purple highlighted regions in the plotted graph and on the zoomed-in model image.

5.3 Dynamic Light Scattering can be used as tool to investigate macromolecular condensates of endocytic adaptor proteins

5.3.1 Sla2 from *Chaetomium thermophilum* exhibits concentration and crowding agent dependent condensation at 20 and 50 °C

During the course of this work, the aim was to determine the C-terminal region structure of Sla2. The construct *Ct*Sla2:608-1050 was initially used for this task. This polypeptide includes the REND and THATCH domains with a short section of coiled-coil. The thermostability of *Chaetomium thermophilum* proteins was a key factor in using this protein as a starting point for structural work.

Initial characterisation of the construct by nanoDifferential Scanning Fluorimetry (nanoDSF) determined the thermostability profile of the protein for use in biophysical and structural studies. nanoDSF measures absorption of tryptophan and tyrosine resides in a protein sample at 330 and 350 nm over time during a temperature ramp from 20 °C to 90 °C. The melting temperature for this construct was determined as 64 °C through first derivative analysis of 350 nm absorbance via MoltenProt (Kotov et al. 2021; Burastero et al. 2021) (Figure 34).

Dynamic Light Scattering (DLS) of this construct during the temperature ramp showed that when the temperature reached 50 °C larger particles were detected. DLS relies on calculating radius of gyration through the change in the intensity of scattered light. These particles were in the range of 10-100 nm (Figure 35). This phenomenon is not a result of unfolded protein aggregation as the T_m of this construct is 64 °C, which is above the temperature that we see these particles forming. The formation of these larger particles was triggered at high protein concentrations. The appearance of a concentration threshold for this phenomenon also supports that it is not a protein aggregate provoked by misfolding. The presence of these particles at 50 °C is also important as this is the temperature at which *Chaetomium thermophilum* thrives best, so this may be a phenomenon possible *in vivo*.

The radius of the particles in the DLS is also of interest, it is in the range of 20-50 nm. This correlates similarly with the cryo-EM particle size observed when there is a crowding interaction between the REND and THATCH domains. The appearance of the REND/THATCH oligomeric particles seems to occur at a high concentration of the C-terminal region. This would occur *in vivo* when the AENTH complex is formed, concentrating Sla2 locally. Additionally, this is possible *in vitro* using a crowding agent such as Polyethylene Glycol (PEG).

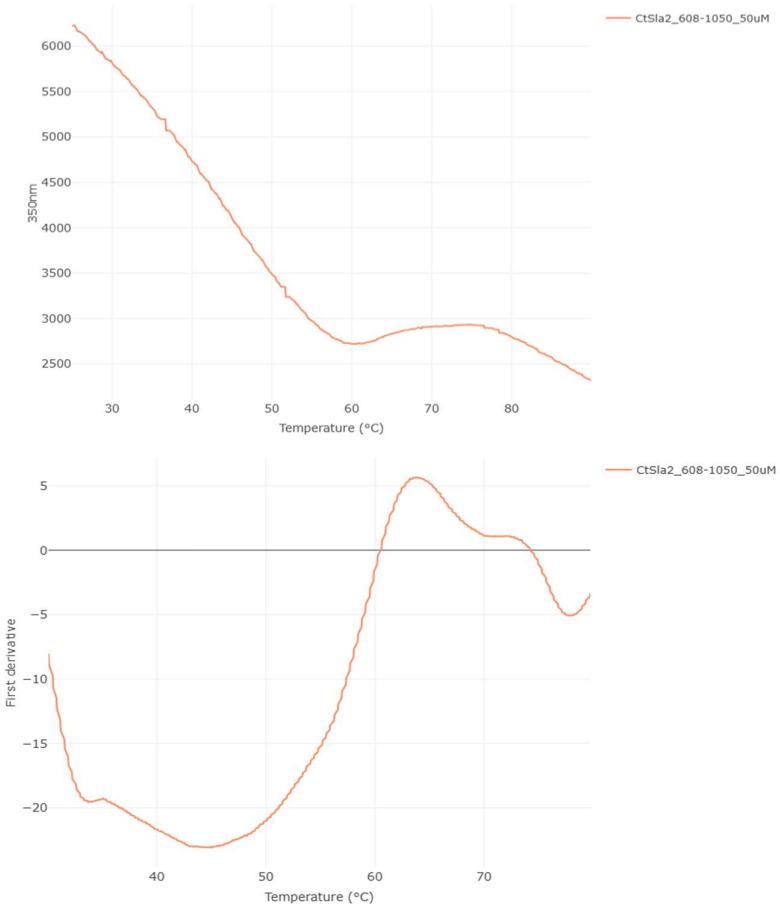

Figure 34: nanoDifferential Scanning Fluorimetry of *Ct*Sla2:608-1050
Thermal denaturation assay of *Ct*Sla2:608-1050 showed a single transition. (Top) 350 nm absorbance across a temperature ramp and (Bottom) First derivative of the afore mentioned temperature ramp. The resulting Tm was 64 °C. Melting temperature estimation (using the first derivative) was done with the MoltenProt tool (spc.embl-hamburg.de) (Kotov et al. 2021; Burastero et al. 2021).

To determine what the nature of the particles were *Ct*Sla2 was mixed with PEG at high concentrations to take any effect to the extreme. The sample produced droplets (Figure 35).

The droplets were liquid in nature and coalesced during imaging. Taking the work of Ren et al. (Ren, Yang, Fujita, Zhang, et al. 2023) in addition to this initial finding, there were questions opening up about whether this was a potential avenue for investigating protein condensates involving the REND domain. During the course of their work expanding on the role of the REND domain in the Actin binding cycle, Ren et al. highlighted that REND domains form punctae when conjoined to a lipid binding domain and do not spread evenly over the membrane. Suggesting that this phenomenon may be some form of condensation.

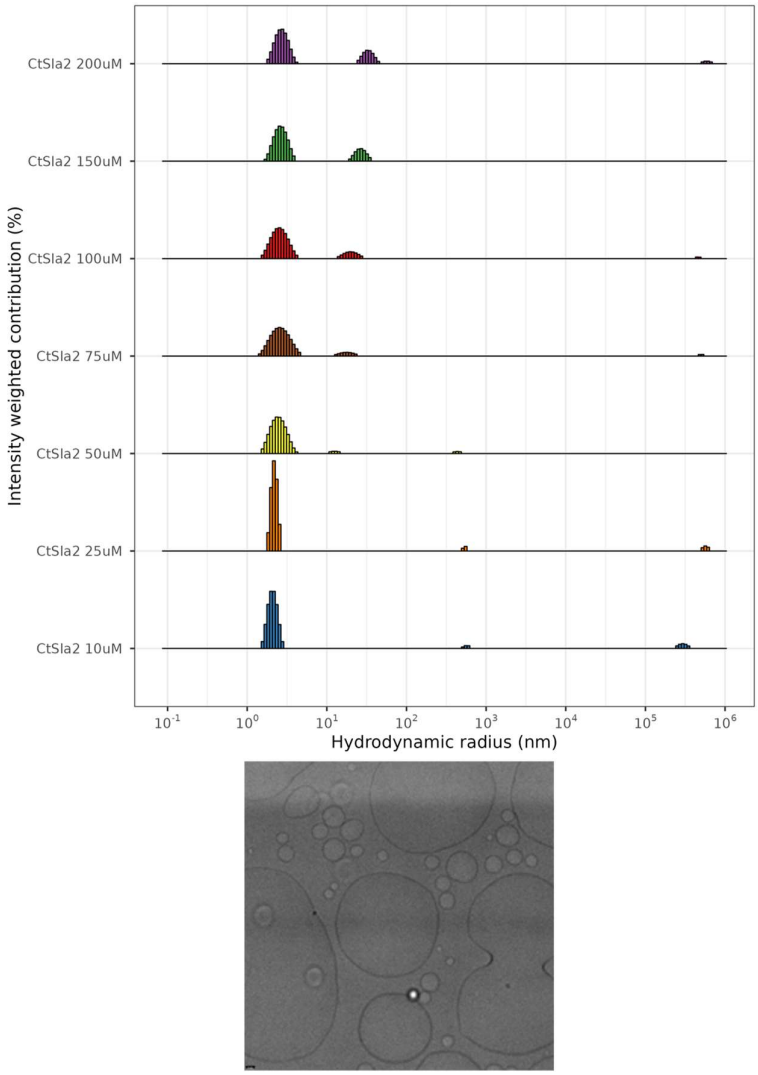

Figure 35: Condensate formation of *Ct*Sla2 at 20 and 50 °C

(Top) Dynamic Light Scattering data plotting of a concentration gradient of *Ct*Sla2:608-1050 at 50 °C. DLS data was plotted using Raynals, a software in the eSPC online website (Burastero et al. 2023). (Bottom) Differential interference contrast microscopy images taken by Lucas Defelipe of 150 µM *Ct*Sla2:608-1050 in 7.5 % PEG 8K.

5.3.2 Dynamic Light Scattering shows *Sc*Sla2 forms large particles at room temperature in the presence of PEG

As primarily my interest is in the role of proteins in *Saccharomyces cerevisiae,* as with the other interactions studied here, I focused on developing *Sc*Sla2 protein constructs for testing condensate formation in 2.5 % PEG 8K. The initial thoughts came from the high Proline and Glutamine content of the Sla2 IDR and the coiled-coil mediated interactions between Sla2 and other proteins in the endocytic pit such as Ede1 (Kozak and Kaksonen 2022). Protein constructs also included a C-terminal mScarlet-I tag for use in fluorescence microscopy. Three constructs were produced: Sla2 PQ (residues 281-350) (a portion of the IDR), cc (351-743), and PQcc (281-743). Screening these constructs in Dynamic Light Scattering showed that only PQcc construct formed larger particles at 14 μM but not 7 μM (Figure 36). Visual inspection of Sla2cc-mScarlet-I at high concentrations above 20 μM did show condensation but was not recorded using DLS. As we wanted to work with the most effective constructs for this work, we decided to use only Sla2 PQcc for future work on droplet formation by endocytic adaptor proteins. This provides the highest coverage of Sla2 and reduces the concentration limitations on droplet formation.

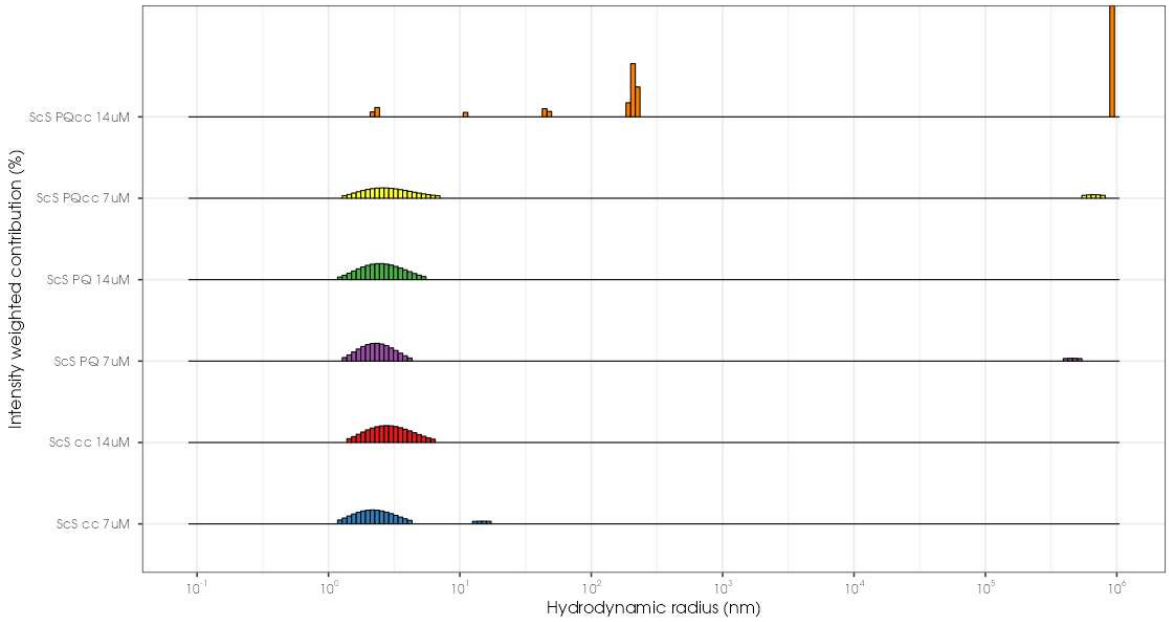

Figure 36: Sla2 construct screening for phase separation

Dynamic Light Scattering measured using the nanoTemper Panta and plotted using the online software, Raynals (Burastero et al. 2023). In 2.5 % PEG 8K, Sla2 constructs did not form larger particles, except at 14 μM, however the sample was not turbid to the eye. These preliminary results suggest that Sla2 does not phase separate at similar concentrations to Ede1 (or Fcho1/2 when comparing to previous work on phase separation on Eps15 and Fcho1/2 (Day et al. 2021; Yuan et al. 2024)).

5.3.3 The THATCH domain alone cannot form large particles

As the work on the *Ct*Sla2 construct contained the THATCH domain, a construct for *Sc*Sla2 THATCH domain was used to confirm whether the THATCH domain alone had any effect indicating droplet formation in Sla2. Concentration screening of the THATCH domain in 2.5 % PEG 8K showed no large particle formation, indicating that the THATCH domain most likely has no effect on the droplet formation in *Ct*Sla2:608-1050 when the REND domain is not present (Figure 37). This is particularly exciting as this would reinforce the idea that the REND domain can increase the ability of Sla2 to form puncta on the membrane (Ren, Yang, Fujita, Zhang, et al. 2023). Although as seen in the structure determined in Figure 20, there are interactions between the REND and THATCH domains in these oligomers.

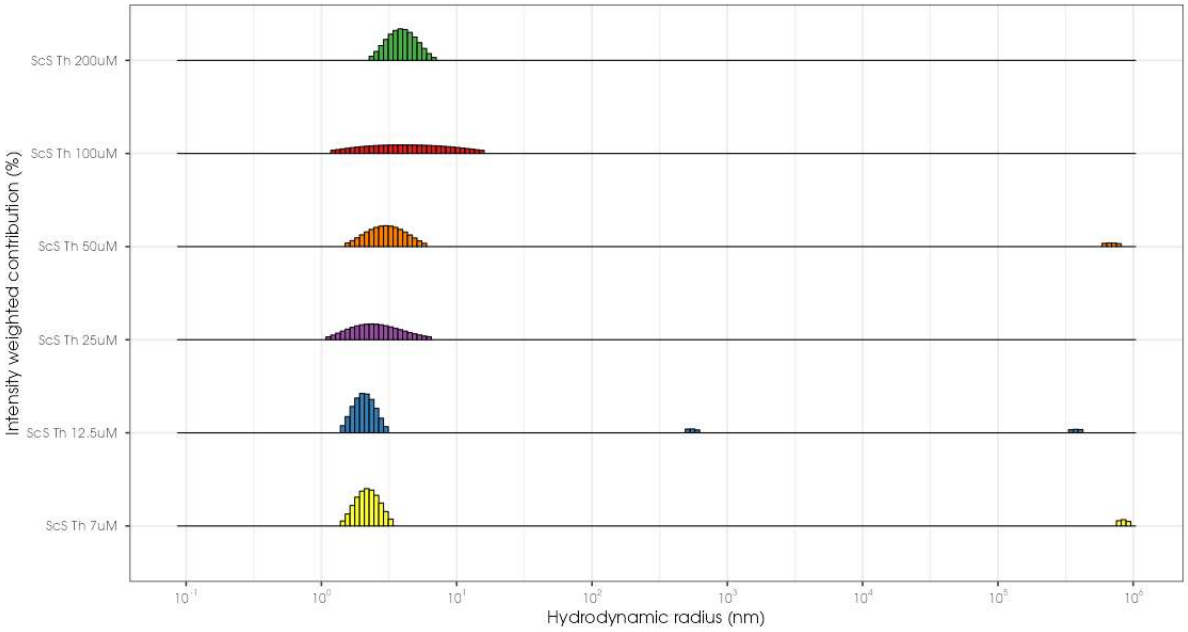

Figure 37: *Sc*Sla2:743-968 concentration screening for larger particle formation
Dynamic Light Scattering data for Sla2:743-968, at concentrations ranging from 7-200 μM. The THATCH domain at any protein concentration tested, in SEC buffer containing 2.5% PEG 8K, did not form particles larger than 10 nm.

5.3.4 Ede1 forms large particles at lower concentrations than Sla2 reinforcing its role as an initiator in phase separation

Dynamic Light Scattering screening for phase separation was applied to the initiator coat protein Ede1, which has been clearly shown to phase separate and nucleate protein recruitment to the membrane in productive endocytic events (Kozak and Kaksonen 2022; Yuan et al. 2024). Ede1 has a PQ region (residues 366-591) and a coiled-coil (residues 591-900) known to interact with Sla2. Hence there was value in looking further into the characteristics of the interaction of Sla2 and Ede1 in phase separated droplets. Ede1 can be seen to form larger particles at lower concentrations than Sla2, 7 μM (Figure 38). The length of the PQ segment of Ede1 is more than twice the length and contains twice the proportion of Asparagine, Proline and Glutamine residues compared to the Sla2 PQ (residues 281-350) region, which may contribute to the difference in their properties.

The comparison from the Dynamic Light Scattering experiments show that Ede1 forms large aggregates or particles at the measured concentrations (below 10 µM) compared to Sla2 that shows limited change in particle size below this threshold. This is in combination with observed turbidity in the capillary before measurement.

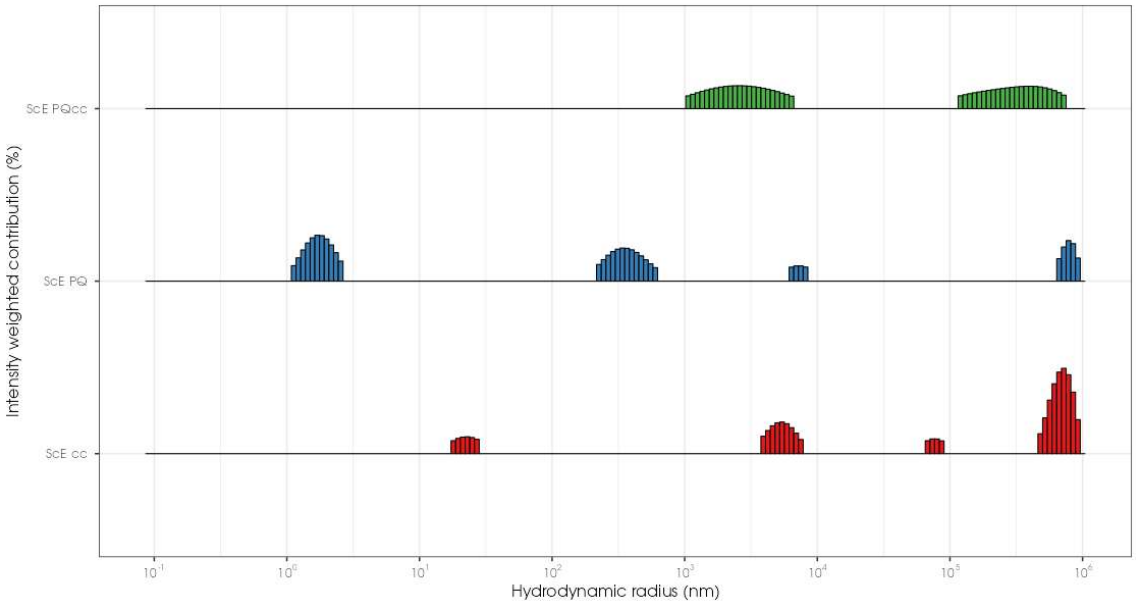

Figure 38: Ede1-mNG constructs form large particles with the addition of 2.5 % PEG 8K at low concentrations

At 7 µM of protein and 2.5% Polyethylene glycol (PEG) 8K, all constructs of the Ede1 protein tagged C-terminally with mNeonGreen exhibited larger particles in the capillary. However, the coiled-coil containing constructs have a higher percentage of intensity in the larger radius particles, particularly the complete region within the PQcc construct.

5.4 Phase separation *in vitro* of endocytic proteins can be probed by fluorescence microscopy

5.4.1 Ede1 and Sla2 can form liquid droplets in 2.5% PEG 8K

As the DLS data suggests that in PEG containing solutions the Ede1 and Sla2 full PQcc construct form large particles. We directly imaged these samples after mixing them with 2.5 % PEG 8K using fluorescence microscopy (Figure 39). Sla2 did not form droplets below 10 μM; however, at concentrations above this threshold, droplets formed, fused, and grew over time. Ede1 readily formed liquid droplets across a range of concentrations, with higher concentrations leading to faster droplet formation and fusion. This is congruent with the other data of Ede1 and Eps15 and its propensity to form droplets. At concentrations below its droplet formation threshold, Sla2 was recruited into Ede1 droplets, indicating a specific interaction between the two proteins. (Figure 39d).

The ratio of intensity between the droplet and solution phase (D:S) is an interesting point of comparison between the different conditions used for microscopy. The cytosolic concentration of Ede1 is buffered when Ede1 is over-expressed in yeast cells and the excess protein forms cytosolic droplets that selectively recruit endocytic adaptor proteins (Kozak and Kaksonen 2022). The D:S ratio can help us compare the protein network changes during endocytosis based on the presence of other actors. Representative droplets are presented for each of the samples (Figure 40). Between the two phases Ede1 at a total protein concentration of 45 μM the Droplet:Solution is on average 19:1 (Figure 40a). The D:S ratio for Sla2 droplets at 25 μM is 5:1. At 45 μM Ede1 and 5 μM Sla2, the D:S ratio for Ede1 is reduced to 9:1 and the ratio for Sla2 is 7.5:1. At 45 μM Ede1 with an additional 25 μM Sla2, Ede1 has a ratio of 17:1 and Sla2 increases to 12:1.

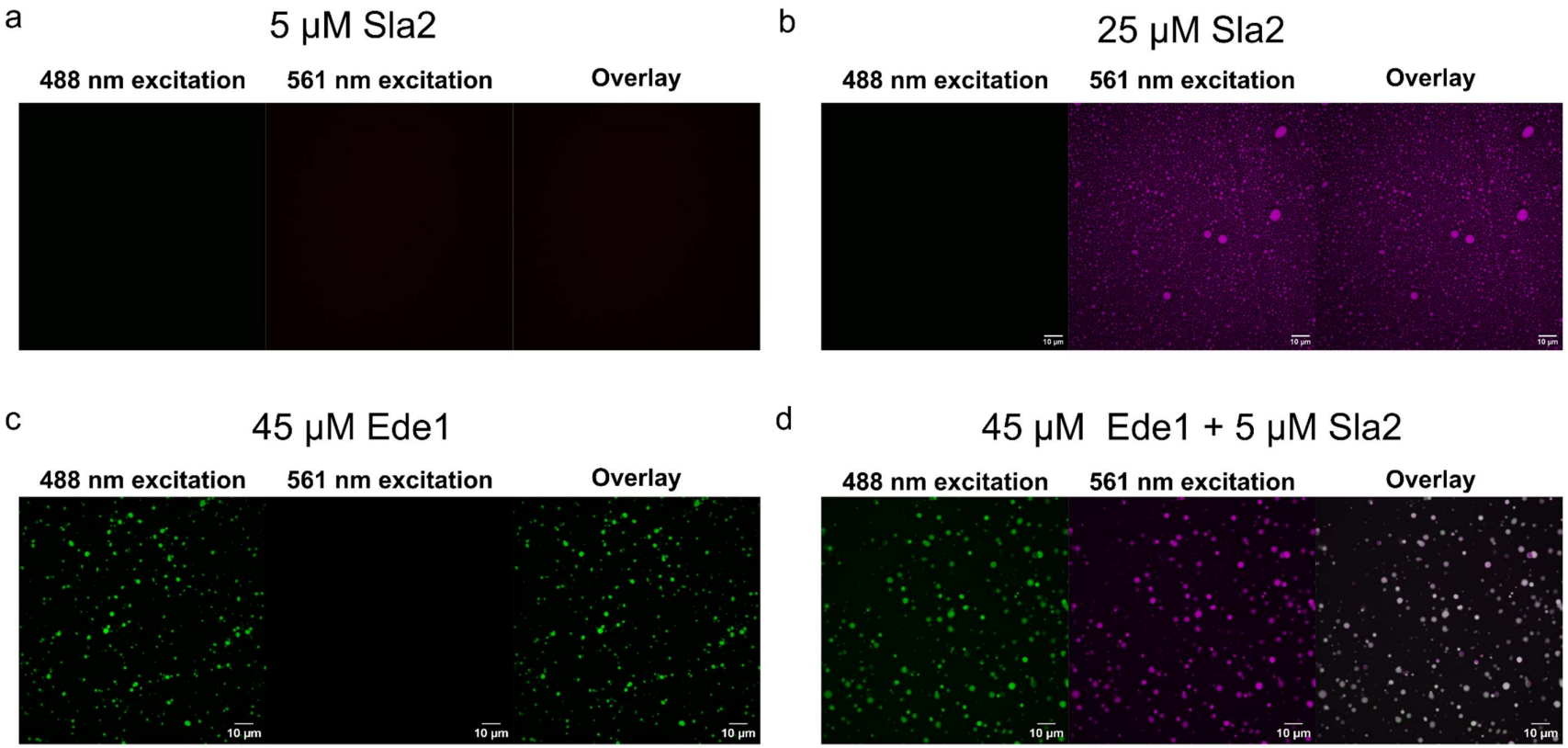

Figure 39: Condensation of endocytic adaptor proteins in 2.5% PEG 8K

Representative images from fluorescence microscopy of Sla2 and Ede1 samples used for phase separation trials, sequentially imaged with 488 nm and 561 nm excitation. (A) 5 μM Sla2 PQcc. (B) 25 μM Sla2 PQcc. (C) 45 μM Ede1 PQcc. (D) 45 μM Ede1 + 5 μM Sla2. Both Sla2 and Ede1 central regions are capable of phase separation at high concentrations. At 5 μM, Sla2 is not capable of forming droplets by itself. Sla2 is capable of forming droplets at 25 μM, and is recruited to Ede1 droplets at concentrations where it cannot independently form droplets.

The addition of Sla2 at concentrations lower than the critical droplet concentration alters the Ede1 D:S ratio, while at higher Sla2 concentrations this effect diminishes. These results indicate that increasing Sla2 concentrations reduce Ede1 segregation into droplets while promoting Sla2 droplet formation, demonstrating a concentration-dependent interplay between the two proteins. This reduction in Ede1 segregation may result from Sla2 competing for binding sites within the droplet or altering droplet composition through its own phase separation properties. These observations suggest that Sla2 may rely on Ede1 to nucleate or stabilize phase-separated compartments during endocytic processes.

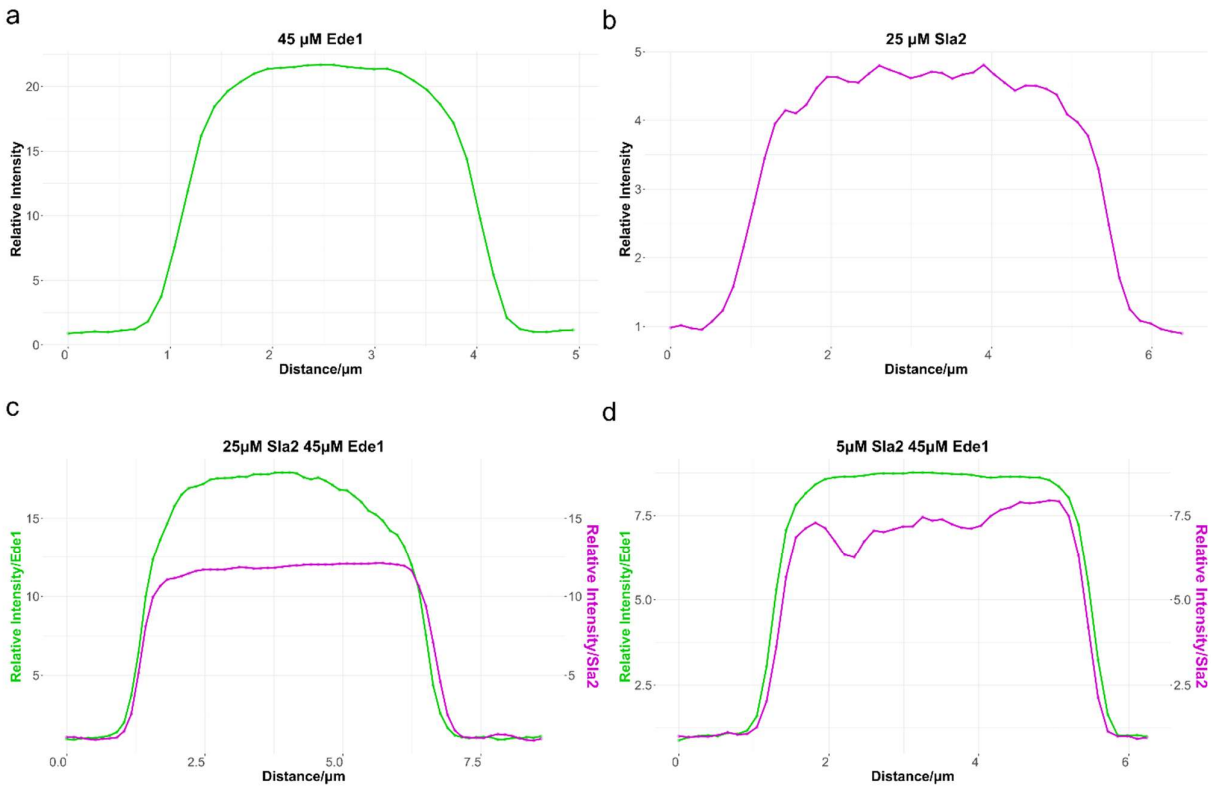

Figure 40: Ede1 and Sla2 Droplet:Solution ratio changes dependent on total protein concentration

(A-D) Relative Intensities across sample droplets in the images taken for subsequent time-lapse analysis of droplet recovery. The intensity values were normalised to the average of the first 5-pixel values outside the droplet for each channel.

Atg16 is a coiled-coil containing protein involved in autophagy. It is not involved in endocytosis (Fujioka et al. 2010, 2024). Atg16 is not known to interact with Ede1. Ede1 coordinates Atg8 into condensates during autophagy (Wilfling et al. 2020). To determine if the recruitment of sub-condensation concentrations of Sla2 is a specific interaction, a construct of Atg16 was produced with a C-terminal mScarlet-I tag. There is no enrichment or depletion of Atg16 in the droplets as compared to the solution (Figure 41). This highlighted that there is no non-specific recruitment to the droplet phase and mScarlet-I & mNeonGreen cannot mediate recruitment to the droplet.

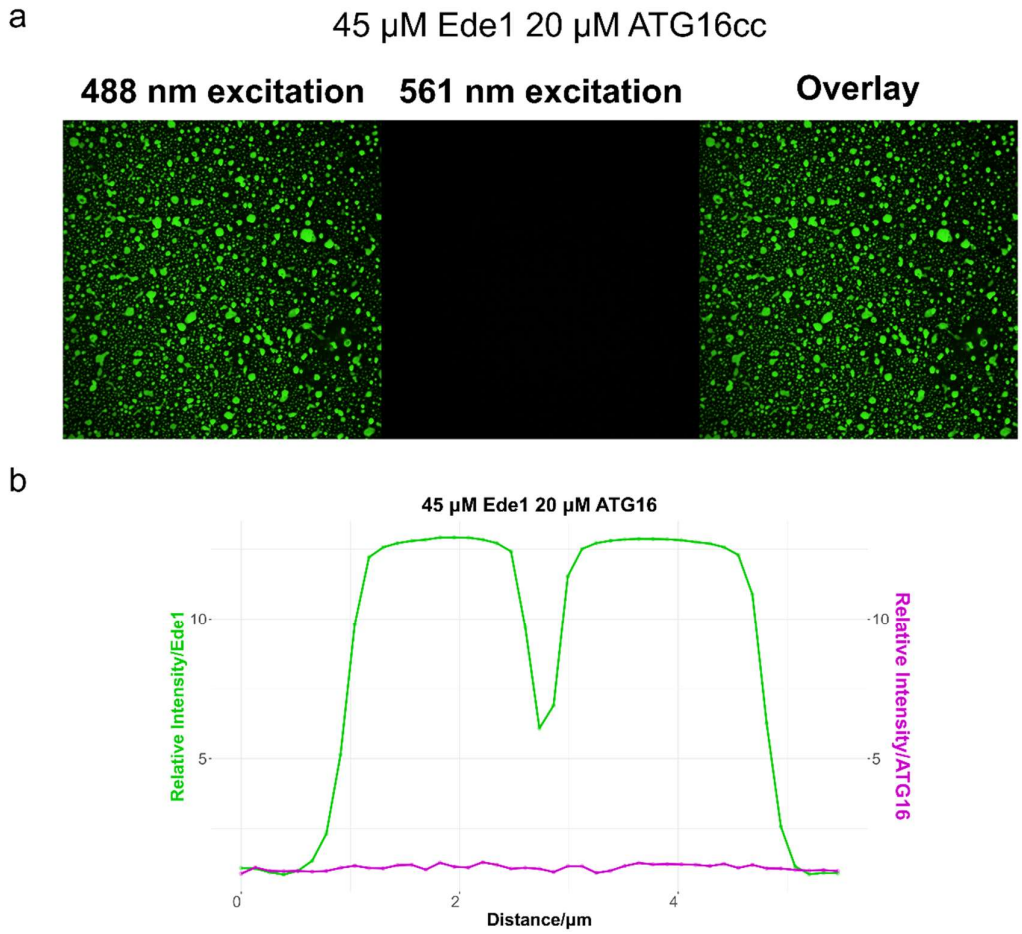

Figure 41: Ede1 cannot recruit the coiled-coil of ATG16 to condensates
(A) Frames taken from Ede1 and ATG16cc containing samples mixed with 2.5 % PEG 8K where Ede1 is at condensation capable concentrations. (B) A representative line segment is plotted for both relative intensities to the background, calculated as the first 5 pixels of the line segment. There is no enrichment above the solution for ATG16.

5.4.2 Sla2 can recruit the Clathrin heterodimer to liquid droplets

Clathrin Light Chain interacts with both the Clathrin Heavy Chain and Sla2 coiled-coil. Whether this interaction will work in the liquid droplet phase *in vitro* is relevant for the liquid phase of productive endocytic events. The rapid exchange with the cytosol and the endocytic pit facilitates the exchange of adaptor proteins as they are needed, such as early arriving proteins (Ede1) leaving during the course of endocytosis.

A construct of Clathrin Heavy Chain conjugated to a C-terminal mNeonGreen moiety was used to probe whether Clathrin was recruited to the droplet. The region from CHC was residues 1172-1574, which only interacts with the Clathrin Light Chain central helix (Chen et al. 2002). 10 μM of Clathrin heterodimer was added to 25 μM Sla2 solutions and then mixed with 2.5 % PEG 8K, 10 μM each of CHC-mNeonGreen and full length Clathrin Light Chain. There was a clear presence of CHC-mNeonGreen in the Sla2 droplets, four times enrichment in the droplets above the solution (Figure 42). At this concentration no droplets were formed by the Clathrin heterodimer in the presence of PEG.

5.4.3 Segregation of Sla2 to droplets is impacted by coiled-coil-binding proteins

The impact of coiled-coil proteins on Sla2 in the context of the observed condensates is an interesting avenue. The recruitment of proteins to the endocytic pit through protein condensation will be impacted by the total protein interaction network. Initially, Sla2 was mixed with CLC, Pan1, and Ede1 (at 5 μM for each and additionally 10 μM for CLC) and then in the microscopy slide mixed to a final concentration of 2.5% PEG 8K. The D:S ratio was determined for Sla2, (Figure 43). CLC and Ede1 did not have significant effects on the D:S of Sla2 between the two CLC containing samples. The addition of Pan1 increased the D:S of Sla2 two-fold.

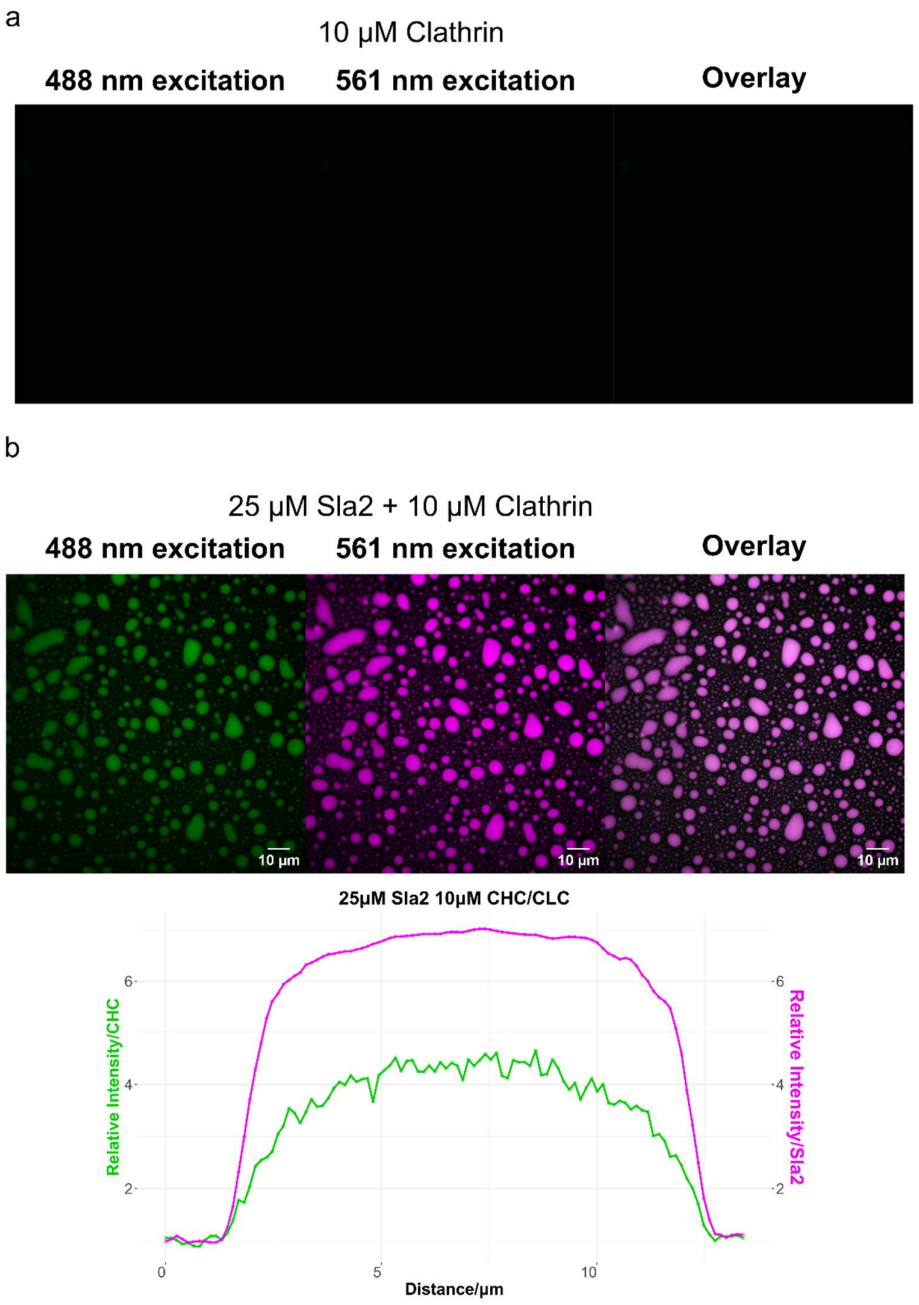

Figure 42: Sla2 and Clathrin co-localise in droplets

Fluorescence microscopy, sequentially imaged under 488 nm and 561 nm excitation and an overlay (A) 10 µM Clathrin in 2.5 % PEG 8K, no droplets were formed. (B) 25 µM Sla2 PQcc + 10 µM Clathrin with representative droplet intensities plotted relative to the background value.

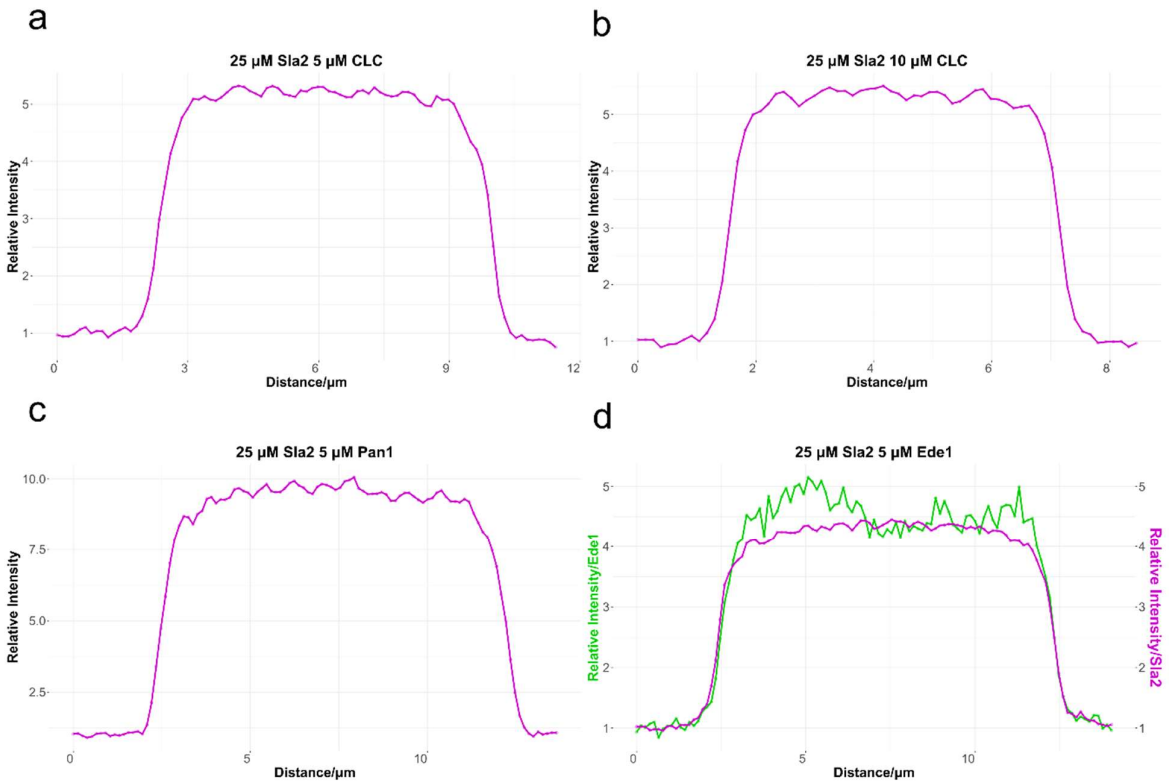

Figure 43: Droplet to Solution ratio of Sla2 is affected by the addition of coiled-coil binding proteins

(A-D) Representative droplets are plotted across Distance and Relative Intensity to the background for 25 µM Sla2 with CLC (5 and 10 µM) (A-B), Pan1 (5 µM) (C), and Ede1 (5 µM) (D). The relative intensity of Sla2 for CLC containing samples was 5.5:1, Pan1 caused an increase in Sla2 ratio to 9:1, and Ede1 caused no change from the Sla2 only containing sample at 4.5:1. Ede1 has the same D:S as Sla2 in this case.

5.4.4 Utilising Fluorescence Recovery After Photobleaching to investigate Sla2 diffusion in liquid droplets

Phase-separated droplets exhibit two key properties: partitioning from the solution and molecular diffusion. Diffusion occurs both within the droplet and between the droplet and the surrounding solution. This dynamic exchange of molecules is critical in biological processes, such as viral factories in infected cells, where rapid molecule turnover ensures efficient reactions (Banani et al. 2017; Guseva et al. 2020). By photobleaching proteins within a single plane of individual droplets, it can be assessed whether the protein movement within droplets followed fluid-like (Simple) diffusion or Anomalous diffusion, which indicates altered dynamics. One caveat is that we cannot distinguish between molecules diffusing with the droplet itself

and those diffusing from the solution. Diffusion in droplets is typically calculated by Simple and Anomalous Diffusion Calculations (Taylor et al. 2019). The change from Simple to anomalous diffusion may be an effect of LLPS combining with percolation of specific moderate-affinity protein-protein interactions occurring between the proteins in the sample that restrict molecule movement.

$$\text{Simple Diffusion : } I(t) = I0 \cdot \exp\left(-\left(\frac{t}{\tau}\right)\right) + I\infty$$

1. I(t) is the intensity at time t
2. I_0 is initial intensity
3. I_∞ is the intensity at large magnitudes of time
4. τ is the characteristic time constant for the diffusion process

$$\text{Anomalous Diffusion : } I(t) = I0 \cdot \exp\left(-\left(\frac{t}{\tau}\right)^{\alpha}\right) + I\infty$$

1. I(t) is the intensity at time t
2. I0 is initial intensity
3. I∞ is the intensity at large magnitudes of time
4. τ is the characteristic time constant for the diffusion process
5. α is the anomalous diffusion exponent

Once fitting is done for the Fluorescence Recovery After Photobleaching (FRAP) data for both Simple and Anomalous diffusion calculations, the Akaike Information Criteria values for both models are calculated (Akaike 1981). The AIC compares the goodness of fit between the two models. A lower AIC value indicates that the anomalous diffusion model better explains the experimental data. If the AIC of the Anomalous Diffusion model is lower than that of the Simple Diffusion model then it can be said that the anomalous diffusion model fits better than the simple model.

This testing was done for several samples of 25 μM of Sla2. The first samples measured were freshly mixed Sla2 with PEG 2.5 % and measuring the sample after 30 minutes, which is referred to as the ‘Aged’ sample. This was to compare the viscosity over the lifetime of the droplets and whether the tau and alpha values would change. The AIC values for Anomalous diffusion for all samples are better than Simple diffusion (Figure 44). Our results reveal that protein-protein interactions alter the rate of diffusion from that of the simple model.

Comparing then the alpha values show the change in diffusion behaviours, when α = 1 this is considered normal diffusion. When α < 1 this is considered sub-diffusion, where the environment contains obstacles of some kind to exchange between the droplet and the solution reservoir of Sla2. When α > 1, this is super diffusion, where diffusion is greater than normal and this is most likely due to active transport processes or long-range correlations.

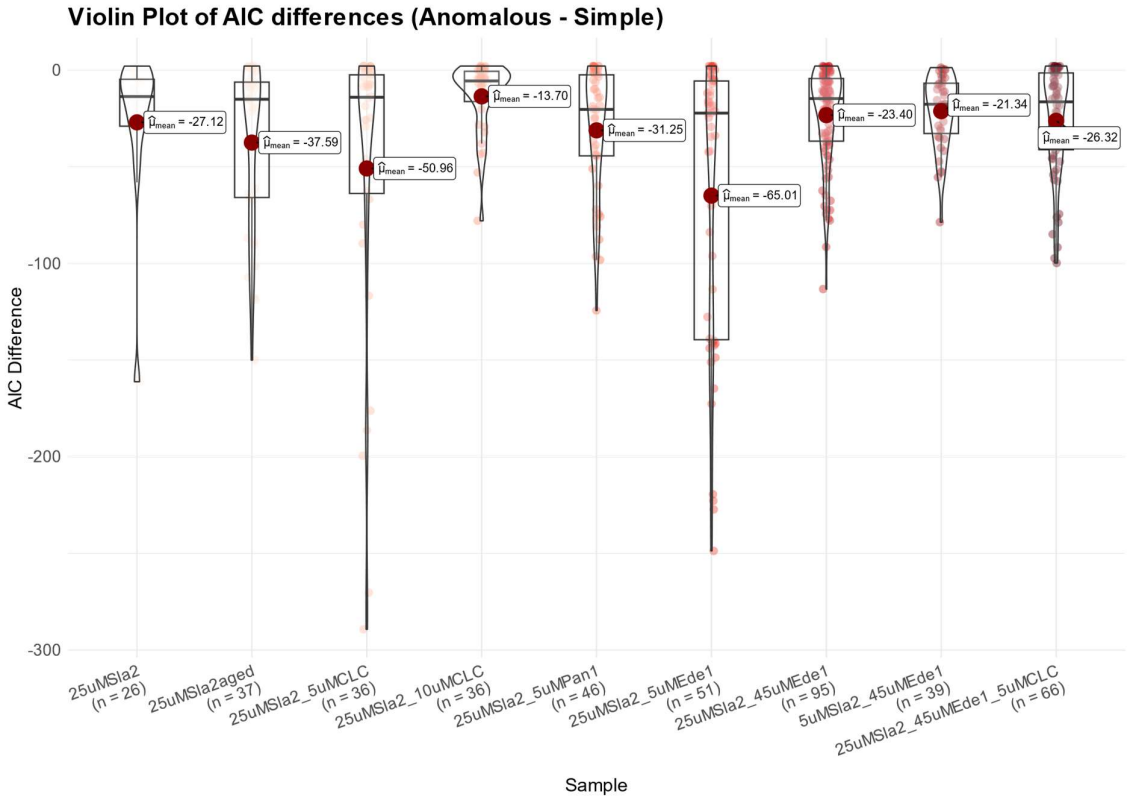

Figure 44: Akaike Information Criteria values suggest that Anomalous diffusion is a better fit for Sla2 diffusion in condensates

AIC values for the Anomalous and Simple diffusion models for each sample droplets were subtracted from each other, and subsequently plotted in a violin plot. The average for the AIC difference is negative, indicating that the anomalous diffusion model in general fits the data better for each droplet than the simple diffusion model.

The alpha and tau values for the first set of samples vary between the samples, (Figure 45 and Figure 46). The alpha values are not significantly different to each other, and are in general similar to Simple diffusion. But there is a general trend for all to have an alpha less than 1. This suggests that a sub-diffusion model dictated by local restrictions on protein movement through protein-protein interaction networks.

The effect of aging was the first port of call, as the fresh mixing of samples for imaging may be more or less based on the change in diffusion over time. The difference in Sla2 diffusion between freshly mixed versus aged droplets shown a significant increase in the tau value and the alpha value for the aged Sla2 droplets drop below 1 but statistical testing shows only tau is significantly different between the two samples (Figure 45, Figure 46 and Figure 47). Tau values showed significant variation across samples. Aged Sla2 droplets exhibit higher tau values during FRAP, indicating slower diffusion over time compared to freshly mixed samples. This suggests that while the diffusion is close to simple diffusion the rate of exchange of molecules decreases once the sample has formed droplets. The D:S ratio is unchanged over time, but the droplets are fused over time and take up a larger volume as compared to the solution (Figure 47).

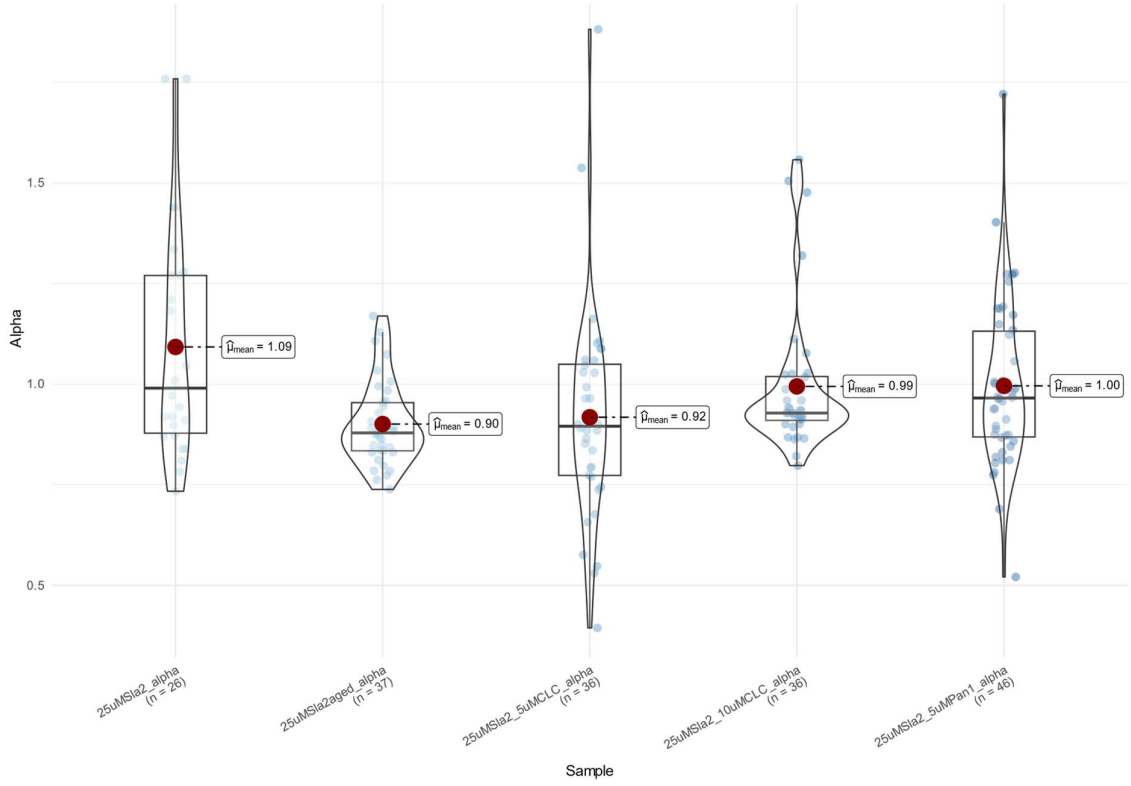

Figure 45: Alpha values for anomalous diffusion models for Sla2 (+ coiled-coil binding protein) droplets

The calculated alpha values for each Anomalous diffusion applied to each droplet in the samples are plotted in a violin plot. The trimmed mean and the p value to each of the other samples, adjusted by Benjamini-Hochberg correction, is plotted on top of the violin plots.

The key difference observed in these sample is the tau of 5 μM CLC addition to the Sla2 mixture, which is resolved by increasing the concentration of CLC to 10 μM. So, while the D:S of Sla2 is unchanged between CLC concentrations, at low CLC concentrations the rate of exchange with the solution is significantly higher than both Sla2 alone and the higher concentrations of CLC where it returns to that of the control. The addition of Pan1 has no effect on tau as compared to Sla2 alone and is significantly different to 5 μM CLC addition to the Sla2 mixture (Figure 46). The addition of Pan1, unlike CLC at the same concentration, had no significant effect on tau, suggesting that Pan1 interactions do not influence Sla2 mobility within droplets. This highlights a specificity of CLC in modulating droplet dynamics.

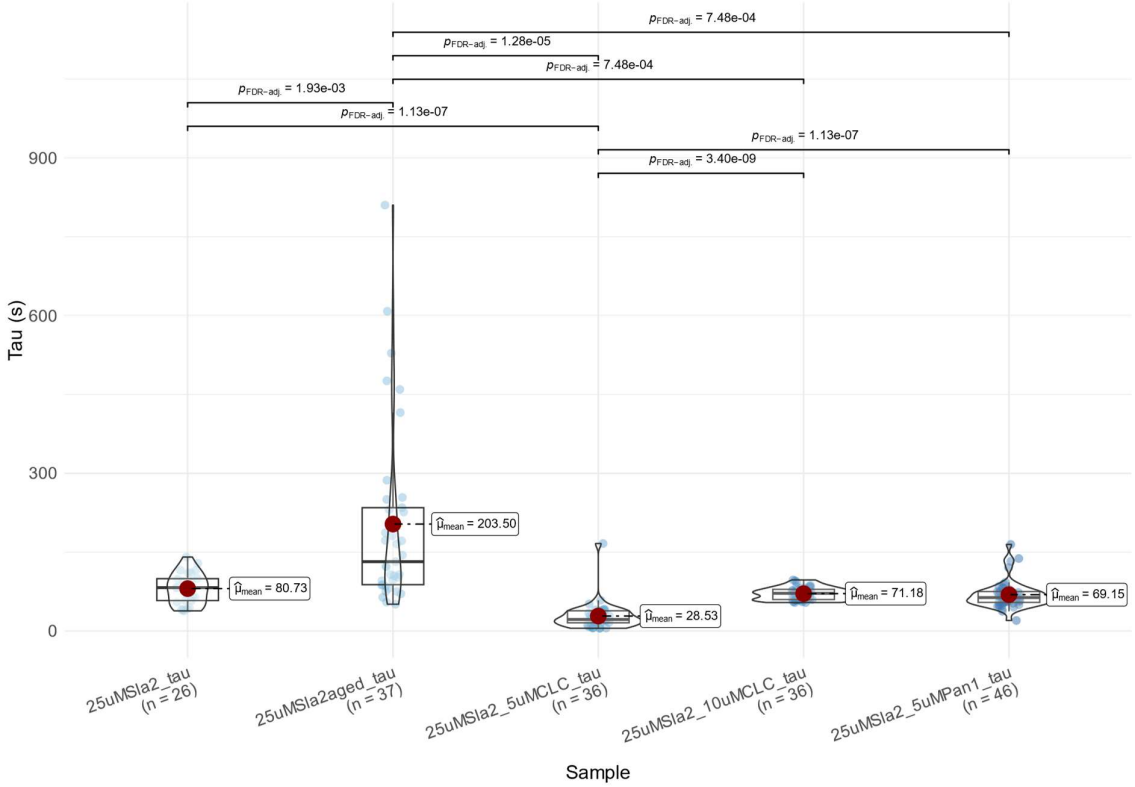

Figure 46: Tau values can vastly differ between droplets containing 25 μM Sla2 and different coiled-coil binding proteins

Tau values for the Anomalous diffusion models are plotted, with the same p-value calculation against the other samples with Benajmini-Hochberg correction for multiple comparisons.

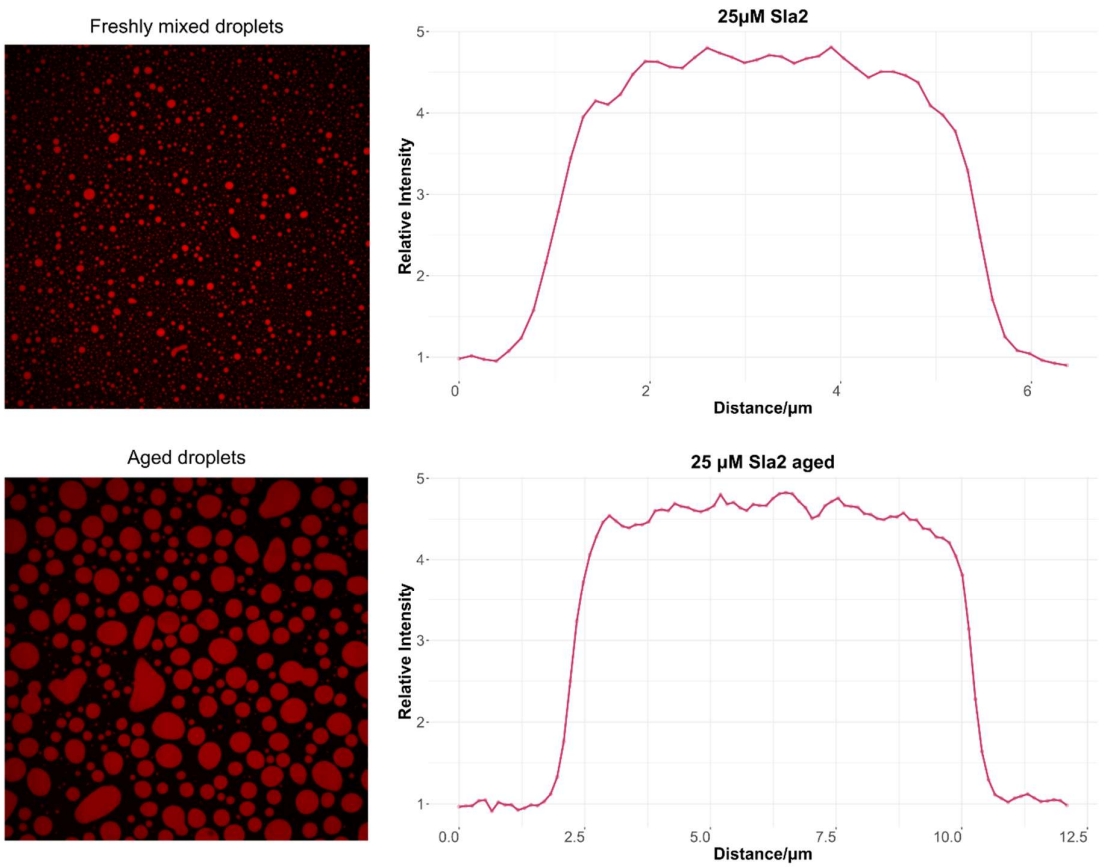

Figure 47: Over time Sla2 droplets coalesce but do not segregate the protein further from the solution

25 μM Sla2 mixed with 2.5 % PEG 8K forms droplets, when left to settle for several minutes the droplets fuse over time forming large condensates. The Relative Intensity values are plotted against distance for representative droplets.

The analysis of the Ede1 containing samples versus the control of Sla2 alone revealed several points of interest. Initially the analysis started with alpha values of the diffusion models (Figure 48). The values of alpha for only Sla2 and Ede1 samples are all significantly lower than Sla2, the addition of 5 μM CLC to the 25 μM Sla2 + 45 μM Ede1 sample increased the alpha back to the similar level of Sla2 alone. The increase of Ede1 concentration from 5 to 45 μM shows an increase in alpha, as Ede1 crosses the critical concentration for droplet formation. At higher concentrations, Ede1 reaches critical levels for droplet formation, which may reduce molecular crowding and restore normal diffusion.

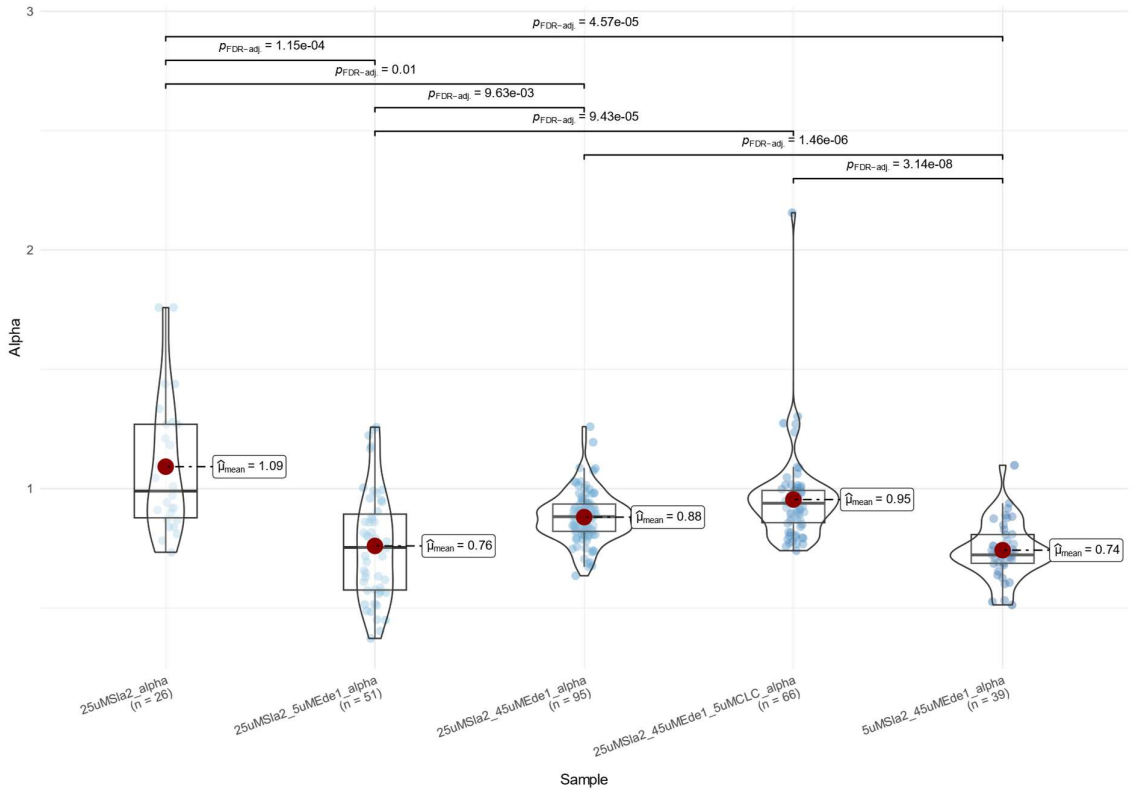

Figure 48: Alpha values for Anomalous diffusion when Ede1 is present with Sla2 are indicative of sub-diffusion

The alpha values for the droplets are plotted for the samples containing Ede1 and pair-wise compared to each other as well as the alpha values for 25 μM Sla2.

Comparison of the tau values for these Ede1 containing samples showed in general a similar tau for Sla2 diffusion within the droplets apart from the CLC + Ede1 containing sample. This is a similar effect as to the Sla2 + 5 μM CLC sample, the change in alpha by the addition of Ede1 is removed by the addition of CLC (Figure 49). Ede1 significantly reduced alpha values, indicating sub-diffusion. The addition of 5 μM CLC to Ede1-containing droplets restores alpha values, suggesting that CLC may mitigate protein crowding or alter droplet composition, allowing more fluid-like movement. The interplay between Sla2, Ede1, and CLC reveals a finely tuned regulatory system, where Ede1 introduces crowding and restricts diffusion, while CLC restores dynamics, potentially by satisfying Sla2 interactions instead of Ede1, influencing droplet architecture. Ede1 may act as a molecular scaffold, creating protein-protein interaction networks that restrict diffusion (low alpha) while maintaining moderate exchange rates (tau). This could reflect its role in organizing early endocytic sites. Ede1

selectively organizes endocytic proteins into crowded, sub-diffusive environments. These assemblies likely function as hubs for cargo clustering and vesicle initiation, while CLC modulates the fluidity of Sla2 with the exchange of interaction by Ede1 back to other adaptors.

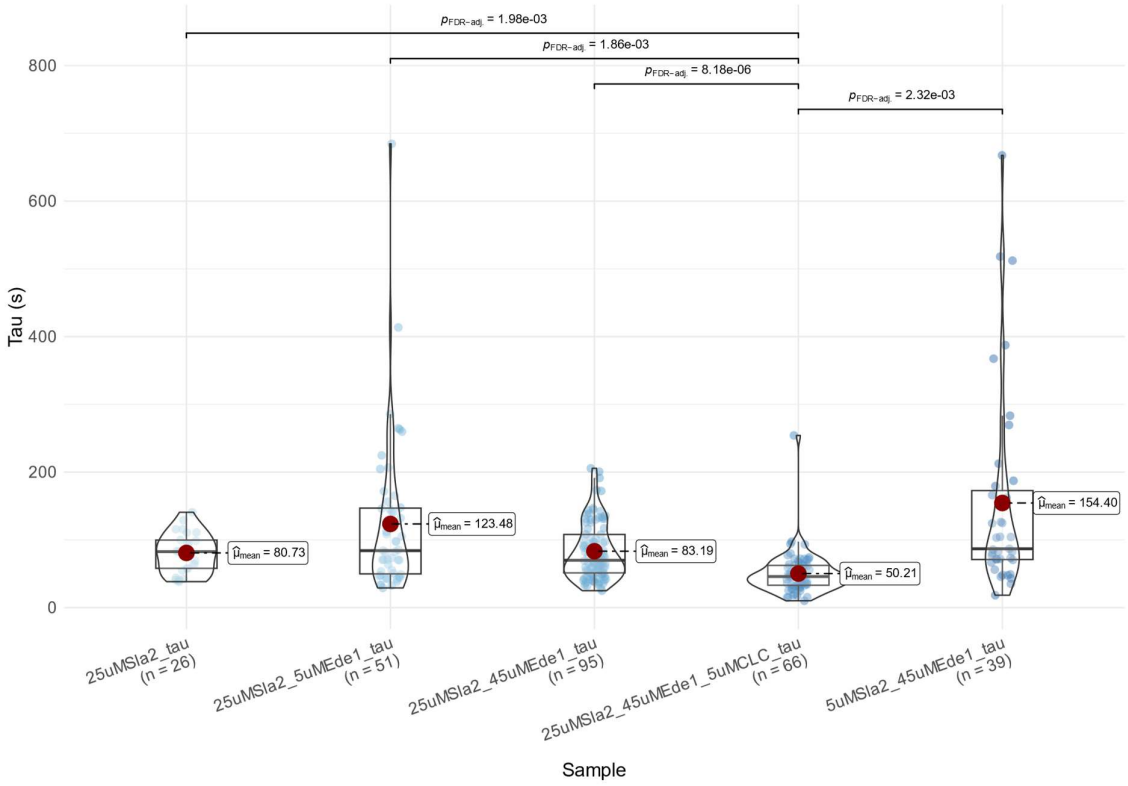

Figure 49: Tau values for the Ede1 containing samples are not significantly different to each other unless CLC is present

Tau values calculated from the droplet anomalous diffusion statistics, plotted for each sample with significance bars between pairwise comparisons that fell below $p < 0.05$.

The droplets formed by Sla2 and Ede1 have the properties of phase separation compounded with percolation highlighted through some key factors. The droplets are readily formed, and have no significant concentration gradient between the centre and edge of the droplet. The droplets fuse over time and are generally liquid in behaviour. The diffusion of protein is close to that of simple diffusion but due to percolation the alpha drops in some situations. This is expected through the protein-protein interactions occurring that have a stronger affinity than simple non-specific interactions. These are all indicators that the coiled-coils of these proteins *in vitro* are capable of phase separation. This phenomenon could be a vital component of protein recruitment and exclusion from the endocytic pit.

6 Discussion

6.1 The Sla2 interaction found in both Fungi and Metazoa co-ordinates a regulatory motif in the N-terminus of CLC

The results for the interaction of the Clathrin Light Chain to the coiled-coil of Sla2 shows divergence between Fungi and Metazoa. The Sla2/End4 coiled-coil from Fungi contains two independent binding sites with different magnitudes of affinity for CLC. The first that was characterised in this work is the conserved site found in both Fungi and Metazoa. The second site that was found was named Site 1, located C-terminal to the conserved site. The nomenclature decision is because of the higher affinity and dominant phenotype of the new site over the conserved site, now named Site 2. The respective binding region of CLC for Site 1 is C-terminal region of the Site 2 binding region of CLC, which is part of the region that interacts with the Clathrin Heavy Chain.

The conserved site (Site 2) has a clear role already explored prior to this work, the binding region in CLC contain an acidic patch motif (EED in *Hs*CLC, EQD in *Sc*CLC) that binds the knee region of Clathrin Heavy Chain. This regulates the clathrin lattice stiffness during membrane curvature in endocytosis (Ybe, Mishra, et al. 2007; Brodsky 2012; Chen and Brodsky 2005; Scott et al. 2018; Ybe et al. 1998).

The structural alignment inside the cross-linked region (Site 2) for both regions of CLC and Sla2 in the AF3 model clearly show the acidic motif closely associated with the coiled-coil (Figure 50). The acidic motif seen in these models is coordinated by residues in the Site 2 region, specifically in the area proposed from the Hip1 coiled-coil crystal structure as a ‘landing pad’ for interaction partners (Niu and Ybe 2008). However, it shouldn’t be lost that the complete region is critical to coordinating the Site 2 interaction as shown by Site 2 Mutant 1 as well as Mutant 2 (Figure 7).

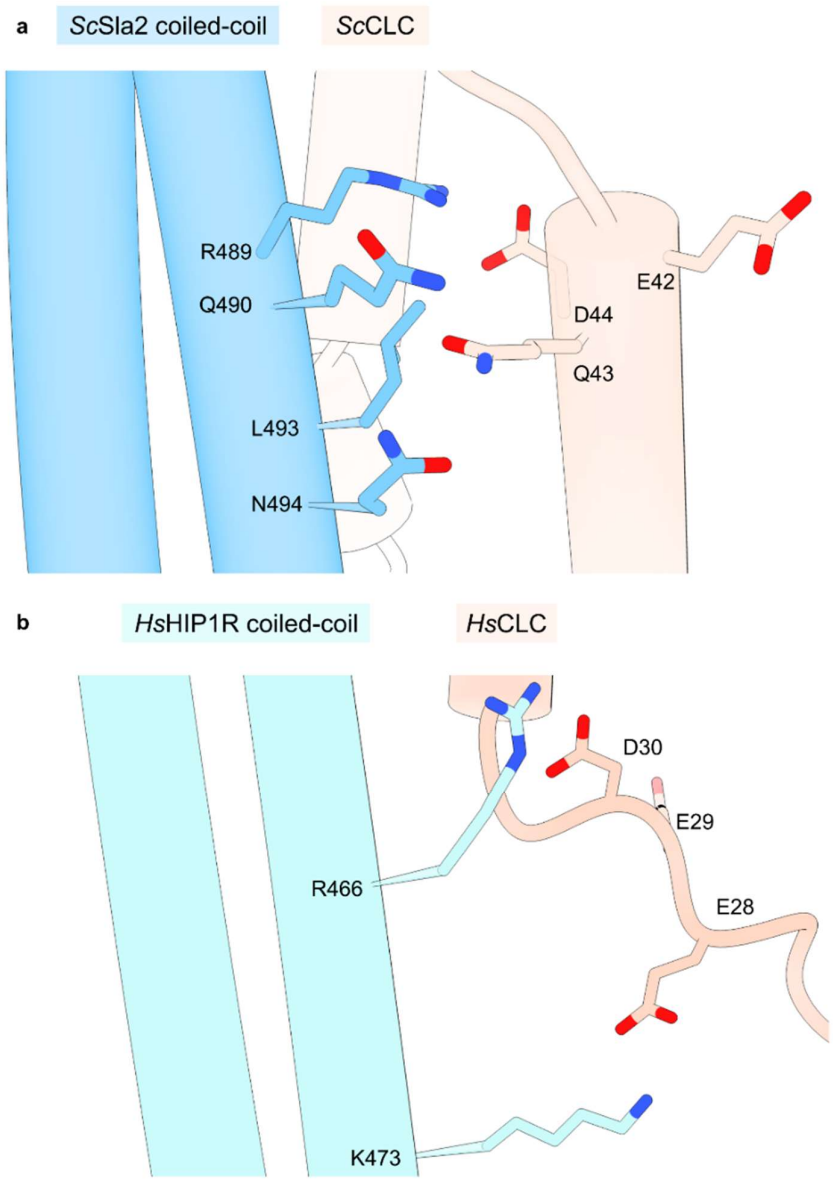

Figure 50: The acidic motif of Clathrin Light Chain is coordinated by Sla2/Hip1R in the Site 2 region in AlphaFold3 predictions

(A) Cylinder representation of alpha helices from the AF3 model of dimeric Sla2:450-550 and CLC:20-55 from *Saccharomyces cerevisiae*. (B) The aligned sequences from *Homo sapiens* homologues HIP1R and CLC also modelled with AF3. In both sets of models, the acidic motif within CLC is shown in stick form, and residues found to have side chains within 4 Å of the motif residues are also shown in stick form.

6.2 Sequence conservation of the Fungi-specific interaction between Sla2 and CLC is only found in Sla2 and not CLC

The sequence alignment for Site 1 region in Sla2 and Hip1R (the human homolog of Sla2) shows little similarity (Figure 10) and no high-affinity complex was found by the prior work on Hip1R (Biancospino et al. 2019). In addition, the region for Site 1 in CLC is highly conserved between Fungi and Metazoa (Figure 51). Our results show that Site 1 is also the dominant of the two sites in yeast when mutated *in vivo* (Figure 11). The sequence similarity in CLC at Site 1 between Metazoa and Fungi, and not in Sla2/Hip1R may suggest that Site 1 emerged in Fungi due to an evolutionary pressure on competition for Site 2 that cannot lead to reciprocal changes in CLC as the interaction with the distal leg of CHC must remain unmodified. This interaction between CLC and CHC is critical to the triskelion stability(Chen et al. 2002).

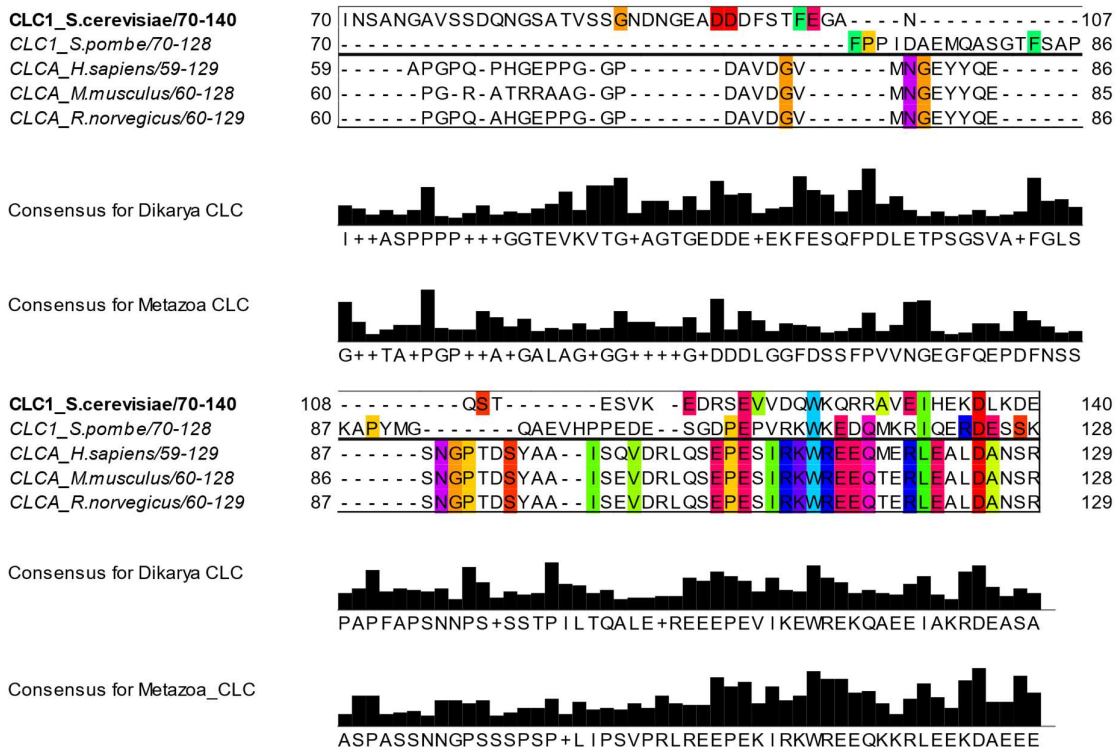

Figure 51: Sequence alignment of CLC in Site 1 region shows little difference in sequence conservation between Fungi and Metazoa

Alignment of non-redundant sequences within the region of 70-140 of *Sc*CLC, which shows very high identity in the C-terminal region that corresponds to the start of the central helix of CLC. This is the same for both Fungi and Metazoa consensus sequences. Residues are highlighted in their Clustal colours when the sequence is above 20% identity.

6.3 The competition at Site 2 on Sla2 between Pan1 and CLC may have been the evolutionary pressure to cause Site 1 to arise

The cross-linking data for the interaction of Pan1 with Sla2 has significant proximity to the CLC interaction with the coiled-coil, particularly Site 2. The MST data for the Pan1:Sla2 complex formation showed a similar magnitude K_d as CLC for Site 2. This would imply Pan1 can compete with Clathrin Light Chain for Sla2 in the endocytic pit, particularly as other domains within Pan1 recruit it to the endocytic pit to increase the local concentration. The other interactions of CHC to other adaptor proteins mean that it arrives prior to Pan1 in the endocytic event timeline. This could have been the selection pressure in Fungi that led to the co-evolution of CLC binding Site 1 in Sla2. Site 1 has a different physical location from Site 2 and a higher affinity for CLC. Therefore, when CLC is bound to both Site 1 and Site 2 the competition for the coiled-coil by Pan1 is reduced or possibly shared depending on if both CLC and Pan1 can be bound at the same time to Sla2.

Productive endocytic events are significantly decreased in the Sla2 Site 1 mutant as compared to the WildType. The change in the efficacy of endocytosis could be explained as the effective competition for Site 2 increases. Only the Site 2 interaction remains for both proteins. The Pan1 interaction may reduce the CLC occupation on the coiled-coil as now CLC only relies on the moderate affinity for Site 2 as opposed to the WildType. In this situation, it would lead to the regulatory pathway of Actin polymerisation being out of balance and Clathrin lattice stiffness is not regulated correctly. If this was possible to do, electron cryo-tomography could allow me to see whether the Actin network forms characteristic ‘comet tails’ in the Site 1 mutant yeast cells. An element of discussion about Site 1 is that the location in CLC overlaps with the CLC central helix that binds to CHC. Whether the Clathrin heterodimer is weakened through this interaction or has some other allosteric effect on CHC is a matter for further research.

6.4 The difference in regulation between Las17 in Fungi and WASP in Metazoa appears alongside the Sla1:Sla2 complex formation

The changes in the sequence and importance of Sla2 as an interaction hub as compared to Hip1R can be seen through the Sla1:Sla2 complex of the Sla1 SH3_3 domain and the Sla2 IDR proline-based motif. The other two SH3 domains in the Sla1 N-terminal region coordinate Las17 (Figure 29). WASP, homologous to Las17 in Metazoa, is auto-inhibited whereas Las17 in Fungi is negatively regulated by Sla1, Bbc1, Bzz1, Lsb1/2, and so on (Zigmond 2000; Sun et al. 2015; Rodal et al. 2003; Feliciano and Di Pietro 2012; Spiess et al. 2013). This regulation and recruitment of Las17 through the Sla1:Sla2 complex is a key aspect to its function, unlike the Metazoa equivalent.

Sla1 has several extra domains beyond those of the SH3 domains as is seen in Figure 24a, including SHD1 that binds endocytic targets. Possibly the ability of Sla1 to be recruited and regulated within the endocytic pit at the correct timepoint require several interactions to increase the net attractive forces like the cargo motif binding and the Sla2 IDR. This has a knock-on effect on Las17 in the endocytic pit, the occurrence of a high affinity interaction between Sla2 and the regulator of Las17 is an important interaction node. This would target Actin polymerisation more effectively to avoid actin comets that render endocytosis unproductive. For comparison to Metazoa, Hip1R and WASP are the only two of the three proteins present in this branch of life and have no known interaction. The sequence alignment clearly shows no conserved proline-rich motifs in the IDR region of Hip1R and WASP is recruited in other ways to the endocytic pit. The involvement with regulation and recruitment of Las17 occur with the Sla2 IDR modification appear together in this branch of the tree of life.

6.5 The structure of the Sla2 C-terminus and adaptor protein network suggest a mode of Sla2 activation prior to Actin recruitment

The structure of the Sla2 C-terminal region is presented in this work, not only for *Saccharomyces cerevisiae* but also *Chaetomium thermophilum*. In the context of prior investigations into *Hs*Hip1R for Actin binding studies, these structures reveal that the THATCH domain Actin binding (ACB) surface is not freely available in either of the conformations described (Figure 15, Figure 16, and Figure 20). These residues cluster at the face of the THATCH core in the direction of the coiled-coil, coordinated by the REND domains (Figure 16).

As a result of the ACB facing the coiled-coil, when Sla2 binds Actin, it could act like a hook. This would allow the force of the cytoskeleton to pull the membrane outwards similar to the model proposed for the action of Talin (Gingras et al. 2008). This mechanism relates to the structure of the unfolding cycle of the REND domain and Up-Stream-Helix (USH) from the work of Ren et al. (Ren, Yang, Fujita, Jin, et al. 2023; Ren and Berro 2022). The REND domain in our structure forms a dimer with a large interface between the two chains, providing the structural basis for the large force required to unfold it. This is additionally important when the LATCH helix has to unzip during the Actin binding process and the THATCH domains must remain close together during Actin binding. The REND domain has an activation effect on the action of the THATCH domain. This may act potentially through the formation of a liquid-like condensate, shown through the work of Ren et al., and the fluorescence microscopy results shown here (Figure 35) (Ren, Yang, Fujita, Zhang, et al. 2023). The increased local concentration of Sla2 due to membrane recruitment may also be a factor in overcoming the moderate affinity for Actin that was shown in Hip1R (Wilbur et al. 2008).

Additionally from the work of Ren et al., it was shown that the force redistribution in endocytosis can be mediated through the IDR and coiled-coil region of Sla2 (Ren, Yang, Fujita, Jin, et al. 2023). Our data on the Pan1/End3/Sla1 complex shows that Sla1 will bind to the IDR while Pan1 interacts with actin fibrils when not inhibited by Sla2. The Sla1 interaction

will not be interrupted regardless of the Pan1:Sla2 complex forming and then breaking. The force transmission, through Pan1:End3:Sla1:Sla2 complex, alters the stress on the REND and Upstream Helix (USH) of the THATCH domain. This would affect the unfolding cycle on top of the force distributed by Actin on Sla2 (Sun et al. 2015; Toshima, Toshima, Duncan, Jamie, et al. 2007). The force distributed by Sla1/End3/Pan1 interaction to F-Actin and subsequently Sla2 was calculated at roughly 8 pN, which is sufficient to unfold the USH but not the REND domain (Ren, Yang, Fujita, Zhang, et al. 2023). This would be sufficient to activate the THATCH domain for Actin binding. It is not known whether while CLC inhibits Sla2, this interaction modifies the force transmission to the USH.

The unfolding of the USH would lead to an extended distance between the REND and THATCH domain allowing helix 3 and 4 to hook the Actin fibril. Taking the formula from Kohn et al. (Kohn et al. 2004), L = 0.360 x ('Number of residues' -1), we can surmise that the extended length of the unfolded linker between the REND and THATCH (with an unfolded USH) would be a maximum 40 residues (residues 731-770), therefore L = 14 nm. The diameter of an Actin fibril is 7 nm, allowing for the Actin binding domains to hook around the fibres and be physically possible for the REND dimer to stay dimerised. The necessary experiments to determine whether this is the case is to determine the complex via a structural method, most likely via electron cryo-microscopy, the bound structure of the THATCH domain using the Sla2ccRTH construct.

6.6 Phase separation *in vitro* could offer insight into the interaction network of Sla2 in the endocytic pit

Ede1, a key driver of phase separation in both yeast and mammals (Kozak and Kaksonen 2022; Day et al. 2021), requires much lower concentrations to form condensates compared to Sla2. This ability highlights Ede1's strong propensity to nucleate dynamic molecular assemblies, which are critical for organizing endocytic components at the plasma membrane. This characteristic is illustrated through the lower concentrations required to phase separate for Ede1 compared to Sla2, which requires much higher concentrations.

Sla2 and Ede1 colocalise in liquid droplets without a density gradient, confirming the liquidity of these droplets and that these two proteins do not segregate one or the other to a particular position. While Sla2 and Ede1 colocalize *in vitro*, their interactions *in vivo* are influenced by additional factors, such as cargo recruitment by Ede1 and lipid-specific interactions by Sla2, which direct them to distinct locations within the endocytic pit.

During the early endocytic process there is a high concentration of Ede1 and a low concentration of Sla2 initially, with Sla2 increasing over time. The different ratios of the proteins allow us to mimic to an extent the changes over the course of endocytosis. In the microscopy experiments, the presence of Ede1 at condensate-forming concentrations increased the segregation of Sla2 to the droplet phase by a factor of two and decreased the amount of Ede1 significantly. As the initial content of Sla2 increases, the greater the segregation to the droplet for both proteins. However *in vivo* segregation of Sla2 by Ede1 is more complicated as there may be other client coiled-coil-containing proteins at high concentrations capable of phase separating alongside Ede1 or altering the protein-protein network capable of recruiting Sla2 to the phase-separated region.

Under ‘early endocytic’ conditions, high Ede1 and low Sla2 concentrations, the reduced alpha values reflect the crowded environment within the condensate, which mimics the nucleation of protein assemblies at the plasma membrane. The alpha is below 1, which is consistent with sub-diffusion, and means that the diffusion of molecules is hindered by short-range protein-protein interactions. This restriction may be necessary to assist with concentrating proteins at the endocytic site and initiate membrane remodelling. The interaction between the two proteins will occur before the interaction of Sla2 and the plasma membrane. When the concentration of Sla2 and Ede1 are both above the critical concentration for droplet formation the alpha value increases above that of the early endocytic value but still below when no Ede1 is present. Highlighting the restrictive role of Ede1 on Sla2 movement *in vitro* and maybe in the endocytic pit.

As endocytosis progresses, Ede1 is gradually lost. Ede1 at sub-condensation concentrations did not increase the segregation of Sla2 to the droplet phase and instead

matched the level of Sla2 itself. This indicates that the recruiting effect of Ede1 may only apply above its own critical concentration. The alpha values of the droplet are significantly below that of the Sla2 control and the critically concentrated Ede1 & Sla2 droplet. This would suggest that when Sla2 is above condensation concentrations and Ede1 is reduced but not gone, the extra interactions from Ede1 linking the Sla2 molecules increases the viscoelastic properties of the protein network.

The interaction capacity of Ede1 is linked to the size of the surface areas available for interaction. Ede1 PQ IDR has 230 residues long, 3 times that of Sla2, and the coiled-coil is 310 residues, 1.5 times the length of the coiled-coil of Sla2 (when disregarding the REND domain in the Sla2 PQcc construct). When mixed with Sla2, the lower interaction capacity of each Sla2 molecule may play a significant role. As a result, they cannot be readily satisfied by interactions with other molecules within the droplet. This behaviour potentially contributes to the sub-diffusion properties observed when Ede1, at sub-condensation concentrations, is present in the droplets alongside Sla2; acting as a glue between the Sla2 molecules.

The differences between the droplets of the control and then in the presence of CLC and Pan1 are primarily that of tau in the anomalous diffusion model and not the diffusion model alpha constant. The presence of low amounts of CLC increases the speed at which Sla2 can be exchanged, however higher amounts of CLC remove the difference in tau to that of Sla2 alone. So, while CLC doesn't increase the segregation of Sla2 via the D:S ratio it does initially increase the ability of Sla2 to exchange with the solution more readily. Our experimental results indicated that CLC altered the exchange of Sla2 between the solution and droplets, and conversely Pan1 did not influence tau or alpha values. This behaviour may be attributed to Pan1's ability to self-associate, allowing it to satisfy its interactions without altering Sla2 mobility. However, Pan1 increases the segregation of Sla2 into the solution by a factor of two.

The presence of 5 μM CLC with condensation capable concentrations of both Sla2 and Ede1, alleviated the reduction in alpha for the diffusion model to that closer to the control. Possibly this was through the CLC interaction with the Sla2 coiled-coil, reducing the restriction

on movement of Sla2 within the droplet by providing an alternative method of satisfying the coiled-coil interaction between Sla2 and Ede1.

Overall, the changes in alpha and tau values provide evidence that proteins like Ede1 and Sla2 form dynamic condensates where molecular crowding and exchange rates are tightly regulated. There are certain protein interactions, such as those involving CLC, that regulate the dynamics and exchange rates within condensates and solutions containing Sla2 above critical concentrations. Such regulation is reflective of their role in organizing and stabilizing endocytic protein networks during cargo recruitment, Actin polymerisation, and vesicle budding.

7. Outlook

The results I have presented here highlight Sla2 as an interaction hub with four key players of the endocytic coat. This has involved quantifying the strength of these interactions between Sla2 and the respective binding partners as well as mapping these interactions to more specific regions than was previously possible. This has furthered understanding of the nature and strength of these interactions for their subsequent role in endocytosis.

Starting from the N-terminus of Sla2 with the proline-based motif in the IDR of Sla2 that binds the SH3_3 domain of Sla1 to enhance its role at the endocytic pit along with Pan1 and End3. The additional folded domain found in the AF3 models, determined by structural comparison to crystal structures was identified as a probative PH domain. This domain should be defined with biophysical characterisation and mutational studies *in vivo* for membrane specificity if it is indeed a PH domain that binds $PI(4,5)P_2$. If this does bind PIP, is it a poor binder or why is it that Sla1 is recruited so much later than the Pan1/End3 dimer in mid-coat recruitment?

The phase separation of the IDR region with Ede1 and how it impacts the Sla2:Sla1 complex is important as well. The specific moderate affinity motif in the IDR versus the low affinity but extensive interaction of the IDR from Sla2 and Ede1 should be investigated to determine if this interaction occludes Sla1, enhances the recruitment of Sla1, or has limited effects on the binding capacity. This could be done *in vitro* with similar methods as used for the effect of segregation of Ede1 and Clathrin in Sla2 condensates. Phase separation as mechanism of recruitment of adaptor proteins needs to be studied further in Sla2. This could be done using Giant Unilamellar Vesicles to analyse the phase separation of Sla2 on membranes and its effects on membrane curvature. This technique may also be used to look at the effects of phase separation to recruit Actin fibrils and the Clathrin heterodimer. This would complement the previous work in the literature done on N-WASP phase separation and Actin polymerisation regulation.

Progressing through the domain architecture of Sla2 we arrive at the coiled-coil, which not only enables regulation of Actin binding through CLC interactions, it also interacts back to the Pan1/End3/Sla1 complex with Pan1. I characterised two interactions between Sla2 and CLC, one of which is conserved with Metazoa and a second higher affinity site that has no homology in Metazoa. The non-conserved site being dominant when mutated *in vivo* and may have evolved based on the presence of Pan1 in Fungi and not Metazoa. An important question remains about the function of the two Clathrin bindings inhibiting Actin binding, namely does either site have specific effects on inhibition? The binding of Pan1 to Sla2 has not been characterised in the presence of Actin and this may be control experiment that needs to be shown as well if it has an effect on affinity or not.

I have determined the dimeric structure of the C-terminal Actin binding region of Sla2 puts the domains regulated by Clathrin Light Chain into three-dimensional context. The structure now of this same region in complex with Actin fibrils is of key importance, this will be possible primarily through electron cryo-microscopy. This would determine if the Sla2:Actin complex forms a hook on the fibril as predicted as well as the orientation of the THATCH domain and LATCH helix.

Alongside this, the *Chaetomium thermophilum* homologue was seen to form tetramers of the dimeric C-terminal region in the presence of ENTH domain and $PI(4,5)P_2$. If this interaction surface has functional properties for facilitating Actin binding this would be very exciting to explore further. Mutational studies on the conserved residues that form these interactions in the *Ct*Sla2 structure in *Sc*Sla2 would be ideal to then bring mutational studies *in vivo* as performed on the Clathrin binding sites. Experiments on Sla2, with mutations in the interaction region from the tetrameric *Ct*Sla2 structure, could be designed to determine changes *in vitro* on the propensity of this to region to phase separate, *in vitro* Actin binding studies, and *in vivo* endocytic productivity under different turgor conditions.

The properties of the coiled-coil regulatory interactions and how they affect force transmission between the membrane and Actin would be particularly interesting for the future. This could be done using optical tweezers or SPR to determine the affinity and also force

capacity for Actin binding by Sla2 in the presence Pan1, CLC, and Sla1. This is a next step to determine if binding partners in the endocytic pit modulate the stability of Sla2 during force transmission to the plasma membrane. Actin recruitment and force transmission is the key point of fungal endocytosis, hence furthering the understanding of Sla2 and how the complete network regulates force transmission would be of great benefit to the membrane trafficking community.

Overall, the results presented in this thesis can provide additional insights into the complex network that dictates the outcome of endocytosis. These connections highlight the significant diversion between Fungi and Metazoa shown by the sequence conservation of fungal proteins as compared to their animal counterparts. This interaction network still has lots more opportunities to be explored through biophysical, computational, cellular biology, and structural methods.

8. Methods

8.1 Protein production and purification

Saccharomyces cerevisiae cDNA was used for all protein expression apart from a codon optimised Sla1:355-414 cDNA, which was synthesised by GenScript (Piscataway, U.S.A.) into a pUC57 vector. The plasmids for each construct and therefore the resistance genes used for selection are in the Appendix. Chemi-competent *E. coli* BL21 (DE3) cells already pre-transformed with the pLysS plasmid (Novagen) were transformed with 100 ng of plasmid DNA and grown overnight at 37 °C with 30 µg/ml of kanamycin for the pETM30 and pETM11 vectors, 50 µg/ml ampicillin for the pnEA vector. For protein expression, a 1:100 dilution of the preculture was done in Terrific Broth medium (20 g tryptone, 24 g yeast extract, 4 ml Glycerol per litre, 0.072 M K_2HPO_4 and 0.017 M KH_2PO_4). Cells were grown at 37 °C until reaching OD 0.8. Then, the temperature was reduced to 16 °C, and induction was achieved by adding IPTG to a final concentration of 0.25 mM. Induction was performed overnight. Cells were harvested at 4,500 g for 20 minutes at 10 °C and stored at -20 °C until purification.

Cells were resuspended in 5 mL of lysis buffer (30 mM Tris pH 7.5, 300 mM NaCl, +400 U DNAse I, and a tablet of Complete EDTA-free protease inhibitor cocktail, Roche, per 100 mL of buffer) per gram of cells. Rupture of the cells was achieved by using an Emulsiflex C3 (Avestin, Ottawa, Canada) cell disruptor at 15 kPsi three times. A centrifugation at 40,000 g for 50 minutes at 4 °C was performed to clear the lysate.

For purification of 6xHisNusA-CLC, *Ct*Sla2 constructs, and constructs used for phase separation experiments, the lysate was loaded onto a Ni-NTA (Carl Roth, Germany) gravity column equilibrated with buffer A (30 mM Tris pH 7.5, 300 mM NaCl, 5 % v/v glycerol, and 10 mM imidazole). The column was washed with 10 column volumes (CV) of buffer A and eluted with buffer B (30 mM Tris pH 7.5, 300 mM NaCl, 5 % v/v glycerol and 200 mM imidazole), collecting 1 mL fractions. The purity of the protein samples was assessed using SDS-PAGE.

For Sla2cc, Sla2ccRTH, CLC (1-233, 1-80, 70-140, 70-233), Pan1:777-987, and Sla1:355-414 polypeptides, lysates were loaded onto GST-Sepharose4B gravity columns (Cytiva, Germany). Lysis buffer in these cases contains 30mM Tris pH 7.5, 300 mM NaCl, 5 % v/v glycerol, +400 U DNAse I and a tablet of Complete EDTA-free protease inhibitor cocktail, Roche, per 100 mL of buffer. Buffer A contains 30 mM Tris pH 7.5, 300 mM NaCl and 5 % v/v glycerol. On-column cleavage at 4 °C overnight was done after washing the column into 30 mM Tris pH 7.5, 300mM NaCl, 5 % v/v glycerol, 0.5 mM TCEP. For cleavage 1 mg of TEV per ml of beads was used.

The samples were loaded onto a Superdex 200 HiLoad 16/600 size-exclusion chromatography (SEC) column for *Sc*CLC and *Sc*Pan1 constructs; Sla2, CHC, and Ede1 constructs were loaded onto a Superose 6 HiLoad 16/600. Sla1 SH3_3 and Sla2 IDR were loaded onto a Superdex 75 10/300 size-exclusion chromatography column. In each case, the SEC column was equilibrated with SEC buffer (30 mM HEPES pH 8, 150 mM NaCl, 0.5 mM TCEP). Fractions were analysed for purity using SDS-PAGE, pooled, concentrated to between 5 and 20 mg/ml, flash frozen in liquid nitrogen, and stored at -70 °C until used.

The Sla2:283-297 peptide was purchased from NovoProLabs (Shanghai, China) with a purity of at least 98% and TFA-free (Acetate-salt). Sequenced as PVSTPARTPARTPTP. The peptide was solubilized in SEC buffer at 10 mM concentrations.

8.2 Cloning and generation of mutants within pETM-30-Sla2cc and pRS315-5'UTR Sla2-mScarlet-I

Polymerase Chain Reaction (PCR) was used to amplify a fragment of DNA with a specific sequence. The reaction mixture consists of dNTPs (10 mM), 0.5 µM of each primer, 1 ng of template DNA (containing the sequence to be amplified) and 1 Unit of Phusion DNA polymerase/50 µL of PCR reaction. This reaction mixture was prepared using a stock of 2x Green Phu-Sso7d mix prepared by the EMBL Protein Production Core Facility (Heidelberg, Germany) and the primers and template DNA were added at the desired final concentrations. The reaction has the steps: initial DNA denaturation (1 minute at 98 °C); a short DNA

denaturation phase (30 seconds at 98 °C); an annealing step, where the primers hybridize with the template DNA (30 seconds at 62 °C); and elongation, where the polymerase synthesizes the complementary chain to the template DNA (72 °C, time adjusted depending on the length of the sequence to be amplified, 30 seconds per kilobase of amplified sequence). These steps were repeated for 25-30 cycles. SLiCE cloning (Guo et al. 2022; Zhang, Werling, and Edelmann 2012) was performed using SLiCE extracts from bacterial cells. Amplified cDNA for proteins of interest were ligated into plasmid of choice at 37 °C before denaturation of enzymes at 65 °C and subsequent transformation into DH5α E. Coli cells before subsequent picking and sequencing by Sanger sequencing (Microsynth, Göttingen, Germany).

Mutants were generated by Quikchange mutagenesis. Whole plasmid PCR was performed using overlapping primers, subsequently 0.5 µL of Dpn1 restriction enzyme was added to digest the original vector. E. coli cells were transformed with the PCR mix and selected on LB agar plates before subsequent picking and sequencing by Sanger sequencing (Microsynth, Göttingen, Germany).

Table 1: Primers used for cloning

Construct	**Primer name**	**Cloning strategy**	**Sequence**
pRS315_Sla2	Sla2_F	SLICE	ATGTCCAGAATAGATTCAGATCTG CAGAA
	Sla2_R	SLICE	CTGTTATCCCTAGCGGATCCTCAA TCATCATCCTGGTTATAGTAGGCAT G
	mSc-I_F	SLICE	ACCAGGATGATGATGGCGGAGGG GGTAGCATGGTTTCTAAAGGCGAA GCCG
	mSc-I_R	SLICE	TATCCCTAGCGGATCCTTACTTGTA CAATTCATCCATACCACCAG
	UTR_F	SLICE	TACCGGGCCCCCCCCCCCAGCAC GAAACGAAAAC
	UTR_F	SLICE	ATCTATTCTGGACATCCTGTTCTAG CTGCTAGTACTATCACTACTACTGC TATG
Sla2_S1	Sla2_S1	Knock_out	CAGCCATAGCAGTAGTAGTGATAG TACTAGCAGCTAGAACAGGATGCG TACGCTGCAGGTCGAC
Sla2_S2	Sla2_S2	Knock_out	ATATATTTATATTAACGTTTATCTTT ATATATAAAAAGTACAATTCATGAT CAATCGATGAATTCGAGCTCG

pETM30-Sla2cc/ pRS315 Sla2_deltaYYR	deltaYYR_F	QuikChange	GGATCAATTGGATGTTTGGGAAAG AAAAGCTGAGTCTTTAGCCAAGCT A
	deltaYYR_R	QuikChange	TAGCTTGGCTAAAGACTCAGCTTTT CTTTCCCAAACATCCAATTGATCC
	deltaYYR_F2	QuikChange	GAAAAGCTGAGTCTTTAGCCAAGC TAGCCTCCCAGTTGGCTCAAGAGC ATCTAAATCTTTTAC
	deltaYYR_R2	QuikChange	GTAAAAGATTTAGATGCTCTTGAGC CAACTGGGAGGCTAGCTTGGCTAA AGACTCAGCTTTTC
pETM30-Sla2cc/ pRS315 Sla2_deltaMotif	deltaMotif_F	QuikChange	GCTGCACCTGGTTTTGATGAAGCG CAGTTAAAGGTGAATAGTGCGCAG GA
	deltaMotif_R	QuikChange	CCAGGTGCAGCACGTGCAGCCTCT TGACGCAACTGGGAGTATAGC
pETM30-Sla2cc/ pRS315 Sla2_delta515-546	delta515-546_F	QuikChange	GAATAGTGCGCAGGAATCCATTCA GTCCATTAATAATGCAGAGGCGGA C
	delta515-546_R	QuikChange	GTCCGCCTCTGCATTATTAATGGA CTGAATGGATTCCTGCGCACTATT C
pETM30_Sla2_IDR	IDR_F	SLICE	TTTTCAGGGCGCCATGGCCGTGGA CGAGTCAAAAGAGATTAAG
	IDR_R	SLICE	GCTCGAATTCGGATCCTTACTGTG GAAAAATGGCGTTAG
pETM30_CLC_1-80	CLC_1-80_F	QuikChange	GTGCGGTGAGCAGCGATTGACTTA AGCAATTGGGATCCTAAT
	CLC_1-80_R	QuikChange	ATTAGGATCCCAATTGCTTAAGTCA ATCGCTGCTCACCGCAC
pETM30_CLC_70-140/ pETM30_CLC_70-233	CLC_70_F	SLICE	TTTCAGGGCGCCATGATTAACAGC GCGAACGGTG
pETM30_CLC_70-140	CLC_140_R	SLICE	GAATTCGGATCCTTACTCGTCCTTC AGATCTTTTTCGTG
pETM30_CLC_70-233	CLC_233-R	SLICE	GAATTCGGATCCTTACGCGCCCGG CGC
pnEA-vHisGST_CLC_351-968	Sla2_351_F	SLICE	TTTACTTCCAGGGCCATATGGCGA CGGCACAAATGCAG
	Sla2_R	SLICE	AGACTATTAGGATCCATCATCATCC TGGTTATAGTAGGCATGC
pETM30_Sla1_SH3_3	Sla1_F	SLICE	TTCAGGGCGCCATGGCCAAGAAAA GGGGAATAGTACAATATG
	Sla1_R	SLICE	CTCGAATTCGGATCCTTAACGAAC CGGCTCGATGAAC
pETM30_Pan1_777-987	Pan1_F	SLICE	TTCAGGGCGCCATGGCCGCGAAA CCAAAATATGCTGGG
	Pan1_R	SLICE	CTCGAATTCGGATCCTTAACAAATA AATCAGTGACTGAGTCATCTCCC

8.3 Computational modelling and alignment

Jalview was used to visualise sequence alignments of CLC and Sla2 sequences and homologous protein sequences using MAFFT and MUSCLE alignment parameters (Katoh et al. 2002; Edgar 2004). Sequences for alignment were provided using UniprotKB; for CLC 100 representative sequences were found for both Fungi and Metazoa after screening sequences for maximum 95 % identity and length between 200-400 residues. For Sla2, Sla2/End4 protein names were used to find Fungal sequences in UniProtKB and Hip1R in Metazoa below 95 % identity and length between 800-1200 residues. The residues were regrouped after alignment of all the sequences back into Fungal and Metazoa and coloured in each group based on conservation. AlphaFold3 (AF3) online servers were used for the computationally derived structural models. FoldSeek was used on AF3 models of Sla1 residues 251-360 and 2nd OPY1 PH domain for bidirectional search within the yeast structural proteome (van Kempen et al. 2024).

8.4 MicroScale Thermophoresis

CLC, Sla1:355-414 and Sla2cc were labelled using the 2nd Generation RED-NHS labelling kit (Nanotemper, Munich, Germany). The reaction was done in SEC buffer, in the dark, at room temperature, for 30 minutes, with a 3-fold excess of dye used per molecule of protein. Proteins were passed through the enclosed PD-10 columns provided by the manufacturer to remove unlinked dye from the protein samples and to restore the proteins back into SEC buffer. Proteins were directly aliquoted from the elution fractions and frozen in liquid nitrogen for -70 °C storage. Concentrations between 25-100 nM of each labelled protein, depending on the label efficiency for each polypeptide, were used for titrations against ligands at 25 °C. Samples were incubated together for 5 minutes prior to measurement. In the case of labelled CLC the titrations were against Sla2cc (WildType, Site 2 Mutant 1, Site 2 Mutant 2, ΔSite1). For labelled Sla2cc it was CLC:70-140, CLC:70-233, and Pan1:777-987. Labelled Sla1:355-414 was titrated against unlabelled Sla2:270-350 and Sla2:283-297. MST data was exported and compressed into *zip file* for each set of analyte and ligand MST runs (n=2) and loaded

into ThermoAffinity (spc.embl-hamburg.de) for data analysis before exporting the fitting data and replotting in R (Burastero et al. 2021).

8.5 Thermal Stability assay / nanoDifferential Scanning Fluorimetry (nanoDSF)

Sla1:355-414 was diluted to 20 µM in the SEC buffer described in the purification protocol. 3 capillaries with 10 µL each were inserted into the Prometheus nanoDifferential Scanning Fluorimeter (NanoTemper, Munich, Germany). A temperature ramp from 20-95 °C was performed, the temperature range 20 to 85 °C was used for analysis due to noise at the high temperature range. Processed data was exported from the Prometheus software and loaded into MoltenProt (Burastero et al. 2021; Kotov et al. 2019) for Tm fitting. Processed 350 nm signal data was replotted in R, averaging the three replicates for 350 nm signal.

8.6 Dynamic Light Scattering

Samples were diluted to required concentrations in SEC buffer. 3 capillaries with 10 µL each were inserted into the Panta nanoDifferential Scanning Fluorimeter (NanoTemper, Munich, Germany). The instrument was set to 20 or 50 °C, and then 10 acquisitions were taken for each capillary. Data was exported and loaded into (Burastero et al. 2023) for data averaging and fitting. Plots were exported from Raynals directly.

8.7 Mass Photometry

Constructs of Sla2:296-767, 6xHisNusA-CLC, and 6xHis-NusA were measured separately and in combination using a 1:19 dilution into the SEC buffer from a stock solution of 1 µM. The proteins were all purified into the final SEC buffer as in the protein purification section. Refeyn 2.0 (Refeyn, Oxford, United Kingdom) was used to collect. After loading the clean coverslip, 19 µL of buffer is applied to the sample compartment for focusing before mixing 1 µL of sample. Mass-contrast calibration was done prior to data export using Native protein marker (Thermofisher). Data analysis was performed on the calibrated movies using the eSPC tool

Photomol, where gaussian fitting and binning of the data was performed before replotting in R (Niebling et al. 2022).

8.8 Circular Dichroism

Sla2cc constructs, Sla1:355-414, Sla2:270-350, and ScPan1:777-987 were dialysed overnight into 30 mM NaPO4 pH 7.5, 150 mM NaF using a Slide-A-Lyzer MINI Dialysis Device 10K MWCO 0.5 ml (Thermo Scientific). These samples were then measured from 180-300 nm in a 400 µL, 1 mm pathlength quartz cuvette (Hellma, Müllheim, Germany) using a ChiraScan Circular Dichroism Spectrophotometer (Applied Photophysics, Leatherhead, UK), equipped with a Quantum Northwest TC 125 temperature controller (Liberty Lake, Washington, USA) set at 20 °C. Sla2cc WildType and Sla2:270-350 were measured at 0.25 mg/ml and all other samples were measured at 0.125 mg/ml. Three replicates of the spectrum were recorded, each with a step size of 1 nm and a response time of 1 second. Temperature ramps from 20-90 °C for Sla2cc constructs, 1 °C per minute increase and CD measured at 5 °C intervals. All data was buffer-subtracted and converted to Mean Residue Weight Extinction for analysis to be able to compare samples of different concentrations and residue length. The ChiraKit server from the eSPC online toolkit was used to analyse the data for Melting Temperature and Secondary Structure contents https://spc.embl-hamburg.de/app/chirakit.

8.9 Grid preparation

Sla2ccRTH was diluted into SEC buffer at a concentration of 20 µM. For cryo-EM grid preparation, Quantifoil 300 mesh Au R 2/2 holey carbon grids were glow-discharged in a Cressington 208 carbon coater at 10 mA and 0.1 mbar air pressure for 60 s. The sample was then applied to the grid and vitrified using a Vitrobot mark IV (FEI/Thermo Scientific) with a blot force of -3 and a blot time of 3 s. The relative humidity (RH) was ≥ 90 % and temperature 5–6 °C. Liquid ethane was used as the cryogen.

8.10 Electron cryo-microscopy and data processing

A Krios G3i electron microscope (FEI/Thermo Scientific) at the Centre for Structural Systems Biology (CSSB) Cryo-EM facility, operated at an accelerating voltage of 300 keV equipped with a K3 BioQuantum (Gatan) filter using a Falcon III direct electron detector operating in integrating mode for data collection. Cryo-EM data were acquired using EPU software (Thermo Fisher) at a nominal magnification of 120,000 X , with a pixel size of 0.68 Å per pixel. Movies of a total fluence of ~ 45 electrons per $Å^2$ were collected at a dose of 1 $e^-/Å^2$ per frame. A total number of 5,725 movies for the dataset was acquired at an underfocus range of 0.5 to 2.0 µm.

Processing of the Sla2ccRTH data was done using cryoSPARC v4 (Punjani et al. 2017). All final parameters for the model are found in (Supplementary Table 1). The general pipeline followed several stages. Micrographs were corrected for beam-induced motion using patch motion correction and patch CTF correction in cryoSPARC. Particles were picked initially using the blob picker at 120-180 Å in diameter and particles were extracted using 1.5 times the size of the blob diameter. To generate 2D classes and a 3D reconstruction, several rounds of 2D classification and selection was done. Then the best 2D classes were used to do template picking on the micrographs. A subset of these was used to generate an initial model and all particles were subjected to rounds of 3D classification to remove 'bad' particles via heterogeneous 3D refinement tools. Around 250,000 particles were taken forward to model refinement in C2 symmetry. Non-uniform refinement in cryoSPARC v4 was used to further improve the resolution of the density map and the final reconstruction was sharpened with a Resolution determined filter after the final Local Refinement job. Model building into the density map given from this dataset was done using an initial AlphaFold3 model for residues 560-968 of Sla2 (Supplementary Data) and manipulation in ChimeraX with the Molecular Dynamics tool ISOLDE(Croll 2018). Refinement of the model was completed in PHENIX (Adams et al. 2010). The model was uploaded with the relevant density maps into the wwPDB for resolution estimation and final reports for model fitting.

Overview of the cryo-EM processing pipeline for *Sc*Sla2:351-968

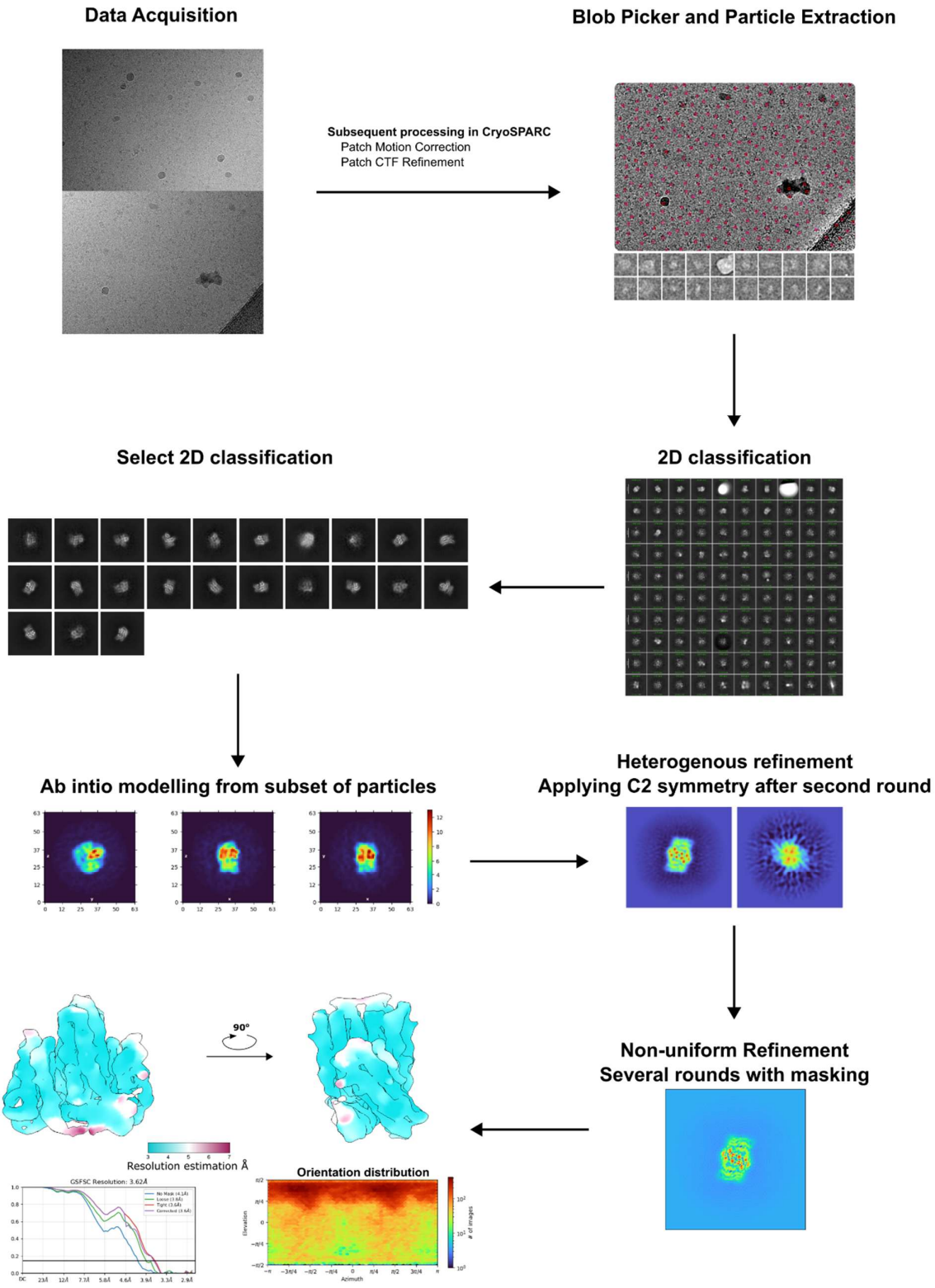

8.11 Protein crystallisation and model refinement

Sla1 SH3_3 was co-crystallised at 9 mg/ml with 1 mM of the Sla2:283-297 peptide in 0.1 M HEPES pH 7.5 and 20% PEG 10000. Crystals formed overnight at 19 °C and harvested after 3 days. The dataset was collected at P13 operated by EMBL at the PETRA III storage ring (DESY, Hamburg, Germany) (see Supplementary Table 3). The dataset was reduced and scaled using AIMLESS(Evans and Murshudov 2013). The structure was solved using molecular replacement, using MOLREP(Vagin and Teplyakov 1997) and using a search model of the complete Sla1_SH3_3 expression construct with the GAMA cleavage scar. Iterative refinement and model-building cycles were performed using REFMAC(Murshudov et al. 2011) and Coot(Emsley and Cowtan 2004) in the CCP4i2 suite of programs(Potterton et al. 2018).

8.12 Fluorescence Microscopy and Fluorescence Recovery After Photobleaching

Fluorescence microscopy was performed using a Nikon Eclipse Ti microscope (Nikon Instruments, Melville, NY) controlled by Meta-Morph (Molecular Devices, Sunnyvale, CA), equipped with a Plan Apo VC 100×/1.4 Oil OFN25 DIC N2 objective (with Type NF immersion oil; Nikon), a Perfect Focus System (Nikon), and a Neo sCMOS camera (Andor Technology, South Windsor, CT; 65-nm effective pixel size). A µ-Plate 8-well chamber slide (Ibidi, Germany) was used for loading samples. Equal volumes of protein and PEG solutions were mixed in the well to maximise mixing and to enable imaging shortly after droplet formation. Sequential imaging of both channels was done at one second intervals for three minutes, made using the SPECTRA X Light Engine (Lumencor, Beaverton, OR) for excitation with a 488/651-nm dual-band bandpass filter for mNeonGreen/mScarlet-I emission (Brightline; Semrock, Lake Forest, IL). Bleaching of the sample was achieved with a RAPP optoelectronics (Germany) UGA-42 473 and 571 nm laser. Recovery of droplets was calculated for individual Regions of Interest imported from SysCon from 30 seconds into imaging using the first 5 seconds of imaging to normalise data within the droplet. Plotting of

the data for both the AIC assessment of the individual ROI fitting and the tau and alpha values were done using ggplot and pairwise comparisons were done using a Mann–Whitney U-test implemented in R.

8.13 Measurement of endocytic dynamics

Generation of competent yeast cells with endogenously tagged Ent1p-mNeonGreen and Abp1-mTurquoise2

A 5 mL preculture of cells was incubated overnight at 30 °C with shaking in the appropriate medium. The OD of the overnight culture was determined and a new 50 ml culture with fresh medium was inoculated to OD of 0.15. Cells were grown at 30 °C until reaching an OD_{600nm} between 0.4 and 0.6. Cells were spun down at 3000 g, at 4 °C for 5 minutes, discarding the supernatant. Cells were resuspended in 30 mL of sterile water and spun down again at 3000x g, at 4 °C for 5 minutes, and the supernatant was discarded. Cells were resuspended in 1 ml of sterile water and spun down in a tabletop centrifuge at 4 °C for 5 minutes at 3000 g, and the supernatant was discarded. Cells were resuspended in 300 µL competent cell solution (5 % v/v glycerol; 10 % v/v DMSO), aliquoted in 50 µL, and stored at -70 °C (cooled down as slowly as possible).

Generation of sla2pΔ cells expressing pRS315-Sla2_mScarlet

Competent *Saccharomyces cerevisiae* cells (MK100 WT: MATa; his3Δ200; leu2-3,112; ura3-52; lys2-801) with Ent1p endogenously tagged with mNeonGreen and Abp1 tagged with mTurquoise2 were transformed with a vector containing the 5' UTR of Sla2, the ORF of Sla2 fused in the 3' with mScarlet (pRS315-Sla2_mScarlet) containing the LEU auxotrophy factor cassette using the following protocol (Gietz and Schiestl 2007). Cells were grown overnight in YPD media and fresh YPD media was inoculated to an OD 600 nm of 0.1-0.15. The culture was grown until an OD600nm of 0.4-0.6 was reached. Cells were spun down at 3000 g for 5 min, the supernatant was discarded, the pellet was resuspended in 30 mL cold H2O and spun down as before described, supernatant was discarded. Cells were resuspended with 1 mL of 100 mM lithium acetate and transferred to a 1.5 mL centrifuge tube, spun down for 15 s in a

tabletop microcentrifuge. Supernatant was discarded and 400 µL of 100 mM lithium acetate was added to resuspend the cells. 50 µL of the cell suspension was mixed with precooled 240 µL 50 % PEG 3350, 10 µL of plasmid pRS315-Sla2_mScarlet carrying Sla2 gene tagged with mScarlet and LEU selection marker and 25 µL of 2 mg/mL ssDNA was added and vortexed. Cells were incubated at 30 °C for 30 min and at 42 °C for 25 min. Transformation solution was spun down for 15 s, supernatant was discarded and 100 µL H2O were added to plate cells on SC-Leu Agar plates. The same protocol was followed for transformation to knock out endogenous Sla2, only the cells before transformation were grown in SC-Leu medium. Once colonies were found, competent cells were prepared and transformed with a URA resistance cassette with homology arms to endogenous Sla2 gene (See Supplementary Table 2 for primer S1/S2 sequence) using the established PCR cassette protocol (pFA6a-KlURA3 Vector)(Janke et al. 2004).

Lifetime TIRF microscopy

To determine the effect of mutating the Sla2 coiled-coil in how endocytosis progresses, cells tagged with Ent1p-mNeonGreen, Sla2-mScarlet and Abp1-mTurquoise2 were used. Yeast cells previously described were grown overnight at 30 °C with shaking in a 24-well plate using LD(=low-fluorescence SD)-Trp-, Leu- medium (yeast nitrogen base without amino acids supplemented with the corresponding DropOut media, Foredium, CYN402). Cells were diluted in fresh medium with a starting OD600 nm of 0.1 and allowed to grow at 30 °C with shaking for several hours (4-6hs) until they reached log phase (OD600 nm 0.6-1.2). Micro slide 8-well glass bottom plates (Catalogue 80807, Ibidi, Gräfelfing, Germany) were treated with 50 µL of a 1 mg/ml Concanavalin A (prepared in 10 mM sodium phosphate buffer pH 6, 10 mM CaCl2,1 mM MnCl2, 0.01 % NaN3, Catalog C2010, Sigma Aldrich) solution, incubated for 5 minutes and then washed twice with 50 µL of fresh medium. 50 µL of cell suspension was applied, incubated for 5 minutes and removed. Then each well was washed twice with 50 µL of fresh medium. Finally, 50 µL of fresh medium was added.

TIRF Microscopy was done at room temperature (21 °C) using a Nikon Eclipse Ti2 microscope equipped with 405 nm and 488 nm lasers and an ORCA-Fusion BT Digital CMOS

camera installed in the Advanced Light and Fluorescent Microscopy (ALFM) Facility in CSSB Hamburg (DESY, Hamburg, Germany). An oil immersion 100x objective was used (NA 1.49). For each field of view, a 5-minute movie was taken. Exposure for each channel was 500 ms in a 2 s interval (0.5 fps for each channel). Depending on cell density, movies were taken in 7 to 10 fields of view. Background subtraction was done with FIJI68. cmeAnalysis(Aguet et al. 2013) was used to track and classify the tracked particles. These events were further classified into Abp1 positive and Abp1 negative events using the dual colour tracking functionality available in the package. Running parameters for tracking and classification were kept as default by the package. Data was plotted with ggplot2 and Pairwise comparisons were done using a Mann–Whitney U-test implemented in R(Mann and Whitney 1947).

8.14 Cross-linking and LC-MS/MS

Sla2cc+CLC:1-80 and Sla2cc+Pan1:777-987 cross-link samples were mixed in equimolar amounts to a final 20 µM total protein concentration. BS3 X-linker was added at 0.5 mM and incubated for 30 mins at 25 °C. Quenched with 100 mM Tris pH 8 for an hour. Samples were then sent at room temperature to the Proteomics Core Facility in Heidelberg for desalting and Peptide-Size exclusion chromatography.

The subsequent methodology was performed at the EMBL Proteomics Facility, Heidelberg. For the digestion, 5 mM TCEP, 20 mM CAA and 1 µg trypsin were added and incubated at 37 °C overnight. Next day, reaction was stopped by the addition of 1 % TFA. Digested peptides were concentrated and desalted using an OASIS® HLB µElution Plate (Waters) according to manufacturer instructions. Crosslinked peptides were enriched using size exclusion chromatography(Leitner et al. 2012). In brief, desalted peptides were reconstituted with SEC buffer (30 % (v/v) ACN in 0.1 % (v/v) TFA) and fractionated using a Superdex Peptide PC 3.2/30 column (GE) on a 1200 Infinity HPLC system (Agilent) at a flow rate of 0.05 ml/min. Fractions eluting between 50-70 µL were evaporated to dryness and reconstituted in 30 µl 4 % (v/v) ACN in 1 % (v/v) FA.

Collected fractions were analysed by liquid chromatography (LC) -coupled tandem mass spectrometry (MS/MS) using an UltiMate 3000 RSLC nano LC system (Dionex) fitted with a trapping cartridge (µ-Precolumn C18 PepMap 100, 5 µm, 300 µm i.d. x 5 mm, 100 Å) and an analytical column (nanoEase™ M/Z HSS T3 column 75 µm x 250 mm C18, 1.8 µm, 100 Å, Waters). Trapping was carried out with a constant flow of trapping solvent (0.05 % trifluoroacetic acid in water) at 30 µL/min onto the trapping column for 6 minutes. Subsequently, peptides were eluted and separated on the analytical column using a gradient composed of Solvent A ((3 % DMSO, 0.1 % formic acid in water) and solvent B (3 % DMSO, 0.1 % formic acid in acetonitrile) with a constant flow of 0.3 µL/min. The outlet of the analytical column was coupled directly to an Orbitrap Fusion Lumos (Thermo Scientific, SanJose) mass spectrometer using the nanoFlex source. The peptides were introduced into the Orbitrap Fusion Lumos via a Pico-Tip Emitter 360 µm OD x 20 µm ID; 10 µm tip (CoAnn Technologies) and an applied spray voltage of 2.1 kV, instrument was operated in positive mode. The capillary temperature was set at 275 °C. Only charge states of 4-8 were included. The dynamic exclusion was set to 30 sec. and the intensity threshold was $5e^4$. Full mass scans were acquired for a mass range 350-1700 m/z in profile mode in the orbitrap with resolution of 120000. The AGC target was set to Standard and the injection time mode was set to Auto. The instrument was operated in data dependent acquisition (DDA) mode with a cycle time of 3 sec between master scans and MSMS scans were acquired in the Orbitrap with a resolution of 30000, with a fill time of up to 100 ms and a limitation of 2e5 ions (AGC target). A normalised collision energy of 32 was applied. MS2 data was acquired in profile mode.

All data was analysed using the cross-linking module in Mass Spec Studio v2.4.0.3524 (www.msstudio.ca, doi: 10.1074/mcp.O116.058685). Parameters were set as follows: Trypsin (K/R only), charge states 4−8, peptide length 7−50, percent Evalue threshold = 50, MS mass tolerance = 10 ppm, MS/MS mass tolerance = 10, elution width = 0.5 min. BS3 cross-links residue pairs were constrained to KSTY on both sides. Identifications were manually validated, and cross-links with an E-value corresponding to <0.05% FDR were rejected. The data export

from the Studio was filtered to retain only cross-links with a unique pair of peptide sequences and a unique set of potential residue sites.

8.15 Small Angle X-Ray Scattering

The SAXS data presented in this work was collected using the P12 beamline (EMBL P12, PETRAIII, DESY, Germany) with a PILATUS 6M pixel detector (DECTRIS, Switzerland) (20 × 0.1 s frames). For batch measurements, typically a dilution series of the protein, protein complex, or protein-lipid complex is prepared using the buffer from the last purification step of the proteins in order to avoid buffer miss matched. In case when this was not available, proteins were dialysed over-night into fresh buffer and the dialysis buffer was used for the dilution series and as the sample buffer. Samples were flown through a capillary and data acquired at 20 °C. The sample-to- detector distance was 3.0 m, covering a range of momentum transfer 0.01 s 0.72 ˚ A1 ($s = 4\pi \sin\theta/\lambda$). In most cases, data frame comparison showed no detectable radiation damage. Data from the detector was normalized, averaged, buffer subtracted, and placed on an absolute scale that is relative to water, according to standard procedures using the automatic pipeline implemented in P12. All data manipulations were performed using PRIMUSqt and the ATSAS software package(Blanchet et al. 2015; Petoukhov and Svergun 2012; Mertens 2023). The forward scattering I(0) and radius of gyration, Rg were determined from Guinier analysis: I(s) = I(0)exp((sRg)2/3)). The indirect Fourier transform method was applied using the program GNOM to obtain the distance distribution function p(r) and the maximum particle dimensions Dmax. From the distance distribution function, low-resolution ab-initio 3D models were generated using DAMMIF (Franke and Svergun 2009).

8.16 Materials

8.13.1 Chemicals used in this work

Table 2: Chemicals used in this work

Name	Supplier	Catalogue Number
1,4-dithiothreitol (DTT) >99%	Roth	3483-12-3
Agarose SERVA for DNA electrophoresis	Serva	11404.07
Albumin from Bovine Serum (BSA)	Sigma-Aldrich	A7906
Ampicillin sodium salt	Roth	HP62.1
Chloramphenicol	Roth	3886,3
Chloroform >= 99.8% analysis	Sigma-Aldrich	288306
Complete EDTA-free protease inhibitor	Roche	04 693 132 001
D (+) Sucrose	Roth	4621.1
di-C8-PI(4,5)P2	Avanti Polar lipids	85185 840046
EDTA Tetrasodium salt 86-88%	Roth	3619.1
Ethane	Merck	295302
Ethanol > 99.8%	Roth	9065,3
Ethidium Bromide	Roth	HP471
HEPES >99.5%	Roth	7365-45-9
Hydrochloric acid 32%	Roth	X896.1
Imidazole >99%	Roth	X998.4
Isopropyl-β-d thiogalactopyranoside (IPTG)	Roth	2316.4

Kanamycin sulphate	Roth	T832.4
LB Agar	Roth	X965.1
LB Broth Low Salt Granulated	Melford	GL1703
LDS Sample Buffer	Novex	NP0008
Magnesium chloride hexahydrate >99%	Roth	2189.1
Nickel (II) chloride hexahydrate	Roth	4489.2
Pentane	Merck	60089
Potassium chloride >99,5%,p.a., ACS, ISO	Roth	6781.1
SDS Pellets	Roth	CN30.3
Sekusept Plus	Ecolab	104372E
Sodium chloride, >99,5%, p.a., ACS, ISO	Roth	3957.2
Sodium fluoride ≥99 %, extra pure	Roth	2618.1
Sodium hydroxide, pellets, >99%, p.a., ISO	Roth	6771
TB powder	Melford	T1510-1000.0
TRIS hydrochloride, Pufferan, >99%, p.a.	Roth	9090.3
Tris(2-carboxyethyl) phosphine hydrochloride (TCEP)	Soltec BioScience	M115
TRIS, Pufferan, >99,9%, Ultra Qualitaet	Roth	5429.3

8.13.2 Molecular Biology Reagents used in this work

Table 3: Molecular Biology Reagents used in this work

Name	Supplier
Cutsmart buffer	New England Biolabs
Monarch miniprep kit	New England Biolabs
Nucleospin gel and PCR clean up kit	Machinery Nagel
RED-NHS 2nd Generation Labelling Kit	nanoTemper

8.13.3 Consumables used in this work

Table 4: Consumables used this in work

Name	Supplier	Catalogue Number
10K Centrifugal Filter Devices	Merck	
Amicon® Ultra-15 Centrifugal Filters– 30 kDa cutoff	Merck	UFC903024
Centrifugal Filter Unit Zeba™ Spin Desalting Columns, 7K MWCO, 0.5 mL	ThermoFisher	89883
Filter Papers	Whatman	1001-090
Gene Ruler 1 kb DNA ladder	Roth	SM0311
Instant Blue (coomassie based staining solution)	Serva	
Loading Dye Purple	Sigma-Aldrich	B7024S
Mix & Go! E. coli Transformation kit	Zymo research	T3001
Monolith Standard grade MST capillaries	Nanotemper	MO-K022
Ni-NTA agarose beads	Invitrogen	R901-15
NuPAGE™ 4 to 12%, Bis-Tris, 1.0–1.5 mm, Mini Protein Gels	ThermoFisher Scientific	NP0323PK2
PageRuler™ Plus Prestained Protein Ladder, 10 to 250 kDa	ThermoFisher Scientific	26619
PageRuler™ Un stained Protein Ladder	ThermoFisher Scientific	26614
PC Membranes 0.1µm	Avanti® Polar Lipids	610005
PC Membranes 0.2µm	Avanti® Polar Lipids	610006
Prometheus NT.48 Standard grade nanoDSF capillaries	Nanotemper	PK002
Sealing film PARAFILM®	Roth	CNP8.1
Syringe filter, Filtropur S, PES, pore size: 0.45 µm, for clear filtration	Starsted	83.1826

8.13.4 Equipment used in this work

Table 5: Equipment used in this work

Name	Supplier
Analytik Jena UVP Chemstudio	Analytik Jena
Agilent 1260 with autosampler and fraction collector	Agilent
AKTA Pure with F9C fraction collector	Cytivia
Analytical scale	Sartorius
Avanti JXB-26 Centrifuge	Beckmann Coulter
Centrifuge 5424 R	Eppendorf
Centrifuge 5810 R	Eppendorf
Electrophoresis chamber for SDS gels	Invitrogen
EmulsiFlex-C3 homogenizer	Aventi
Freezer -20 °C	Liebherr
Freezer -80 °C	Eppendorf
Fridge 4 °C	Liebherr
Fumehood	Waldner
JLA 25.50 rotor for Avanti JXB-26 centrifuge	Beckmann Coulter
JLA 8.100 rotor for Avanti JXB-26 centrifuge	Beckmann Coulter
Microwave	Severin
MilliQ machine	Millipore
Nanodrop 2000c	Thermoscientific
Magnetic stirrer plate	Roth
Nanotemper Prometheus NT.48	Nanotemper
Nanotemper Monolith	Eppendorf
NewBrunswick™ Innova® 42 Incubator Shaker	Eppendorf
NewBrunswick™ Innova® 44 Incubator Shaker	Eppendorf

Name	Supplier
Octet RED96 System	Molecular Devices
PCR Mastercycler	Eppendorf
pHmeter	Toledo
Power Supply	Consort
Rockimager	Formulatrix
Rotating wheel	Stuart
Scales	Sartorius
Superdex® 200 HiLoad 16/600 pg	Cytivia
Superdex® 200 Increase 10/300	Cytivia
Superose 6 Increase 10/300	Cytivia
Superose 6 HiLoad 16/600 pg	Cytivia
Superdex® 75 Increase 10/300	Cytivia
Scorpion Screen Builder ARI-arts	Robbins Instruments
Schott Glass bottles	Schott Duran®
Heating water bath	VWR
MiniStar Microcentrifuge	VWR
MiniSpin® centrifuge	Eppendorf
Vortex	Scientific Industries
Shaking platform Edward	Bühler GmbH
Cell culture Erlenmeyer flasks	Schott Duran®
1 L (1000 mL) Polypropylene Bottle Assembly for JLA-8.1000 rotor	Beckman Coulter C31597
50 mL Polypropylene Bottle with Cap Assembly, 29 x 104mm for JA 25.50 rotor	Beckman Coulter 361694

8.13.5 *E. coli* strains used in this work

Table 6: *E. coli* cell lines used in this work

Name	Description	Application	Antibiotic Resistance	Source
DH5α	Fφ80dlacZΔM15Δ (lacZYA-argF) U169 recA1 endA1 tonA hsdR17 (rK-, mK+) phoA supE44 λ-thi-1 gyrA96 relA1	T1 Phage resistant, general purpose cloning, plasmid propagation		Life Technologies
BL21(DE3)	Deficient in lon and ompT proteases	General purpose expression host		EMBL Hamburg
BL21 pLysS GOLD	Deficient in lon and ompT proteases, pLysS plasmid	High stringency expression host	Chloramphenicol	Novagen

8.13.6 Media used in this work for molecular cloning and protein expression

LB medium

- 10 g/L tryptone
- 5 g/L yeast extract
- 5 g/L NaCl

TB medium

- 12 g/L tryptone
- 24 g/L yeast extract
- 9.4 g/L K_2HPO_4
- 2.2 g/L KH_2PO_4
- 8 mL/L glycerol

LB-Agar

- 15 g/L agar
- 10 g/L tryptone
- 5 g/L yeast extract
- 5 g/L NaCl

9 References

Abramson, Josh, Jonas Adler, Jack Dunger, Richard Evans, Tim Green, Alexander Pritzel, Olaf Ronneberger, et al. 2024. “Accurate Structure Prediction of Biomolecular Interactions with AlphaFold 3.” *Nature* 630 (8016): 493–500. https://doi.org/10.1038/s41586-024-07487-w.

Adams, Paul D., Pavel V. Afonine, Gábor Bunkóczi, Vincent B. Chen, Ian W. Davis, Nathaniel Echols, Jeffrey J. Headd, et al. 2010. “PHENIX: A Comprehensive Python-Based System for Macromolecular Structure Solution.” *Acta Crystallographica. Section D, Biological Crystallography* 66 (Pt 2): 213–21. https://doi.org/10.1107/S0907444909052925.

Aguet, François, Costin N. Antonescu, Marcel Mettlen, Sandra L. Schmid, and Gaudenz Danuser. 2013. “Advances in Analysis of Low Signal-to-Noise Images Link Dynamin and AP2 to the Functions of an Endocytic Checkpoint.” *Developmental Cell* 26 (3): 279–91. https://doi.org/10.1016/j.devcel.2013.06.019.

Akaike, Hirotugu. 1981. “Likelihood of a Model and Information Criteria.” *Journal of Econometrics* 16 (1): 3–14. https://doi.org/10.1016/0304-4076(81)90071-3.

Alberts, B. et al. 2015. *Molecular Biology of the Cell*. 6th ed. Taylor and Francis Group, New York.

Avinoam, Ori, Martin Schorb, Carsten J. Beese, John A. G. Briggs, and Marko Kaksonen. 2015. “ENDOCYTOSIS. Endocytic Sites Mature by Continuous Bending and Remodeling of the Clathrin Coat.” *Science* 348 (6241): 1369–72. https://doi.org/10.1126/SCIENCE.AAA9555.

Banani, Salman F., Hyun O. Lee, Anthony A. Hyman, and Michael K. Rosen. 2017. “Biomolecular Condensates: Organizers of Cellular Biochemistry.” *Nature Reviews. Molecular Cell Biology* 18 (5): 285–98. https://doi.org/10.1038/NRM.2017.7.

Barrio-Hernandez, Inigo, Jingi Yeo, Jürgen Jänes, Milot Mirdita, Cameron L. M. Gilchrist, Tanita Wein, Mihaly Varadi, Sameer Velankar, Pedro Beltrao, and Martin Steinegger. 2023. “Clustering Predicted Structures at the Scale of the Known Protein Universe.” *Nature* 622 (7983): 637–45. https://doi.org/10.1038/s41586-023-06510-w.

Bartelt, Rebekah R., Jonathan Light, Aldo Vacaflores, Alayna Butcher, Madhana Pandian, Piers Nash, and Jon C. D. Houtman. 2015. “Regions Outside of Conserved PxxPxR Motifs Drive the High Affinity Interaction of GRB2 with SH3 Domain Ligands.” *Biochimica et Biophysica Acta* 1853 (10 Pt A): 2560–69. https://doi.org/10.1016/j.bbamcr.2015.06.002.

Biancospino, Matteo, Gwen R. Buel, Carlos A. Niño, Elena Maspero, Rossella Scotto di Perrotolo, Andrea Raimondi, Lisa Redlingshöfer, et al. 2019. “Clathrin Light Chain A Drives Selective Myosin VI Recruitment to Clathrin-Coated Pits under Membrane Tension.” *Nature Communications* 10 (1): 1–15. https://doi.org/10.1038/s41467-019-12855-6.

Blanchet, Clement E., Alessandro Spilotros, Frank Schwemmer, Melissa A. Graewert, Alexey Kikhney, Cy M. Jeffries, Daniel Franke, et al. 2015. “Versatile Sample Environments and Automation for Biological Solution X-Ray Scattering Experiments at the P12 Beamline (PETRA III, DESY).” *Journal of Applied Crystallography* 48 (Pt 2): 431–43. https://doi.org/10.1107/S160057671500254X.

Boczkowska, Malgorzata, Grzegorz Rebowski, David J. Kast, and Roberto Dominguez. 2014. “Structural Analysis of the Transitional State of Arp2/3 Complex Activation by Two Actin-Bound WCAs.” *Nature Communications* 5 (1): 3308. https://doi.org/10.1038/ncomms4308.

Boehm, Markus, and Juan S. Bonifacino. 2002. “Genetic Analyses of Adaptin Function from Yeast to Mammals.” *Gene*. https://doi.org/10.1016/S0378-1119(02)00422-5.

Boeke, Dominik, Susanne Trautmann, Matthias Meurer, Malte Wachsmuth, Camilla Godlee, Michael Knop, and Marko Kaksonen. 2014. “Quantification of Cytosolic Interactions Identifies Ede1 Oligomers as Key Organizers of Endocytosis.” *Molecular Systems Biology* 10 (11): 756. https://doi.org/10.15252/MSB.20145422.

Boettner, Douglas R., Helena Friesen, Brenda Andrews, and Sandra K. Lemmon. 2011. “Clathrin Light Chain Directs Endocytosis by Influencing the Binding of the Yeast Hip1R Homologue, Sla2, to F-Actin.” *Molecular Biology of the Cell* 22 (19): 3699–3714. https://doi.org/10.1091/mbc.E11-07-0628.

Bonifacino, Juan S., and Linton M. Traub. 2003. “Signals for Sorting of Transmembrane Proteins to Endosomes and Lysosomes.” *Annual Review of Biochemistry* 72: 395–447. https://doi.org/10.1146/annurev.biochem.72.121801.161800.

Brach, Thorsten, Camilla Godlee, Iben Moeller-Hansen, Dominik Boeke, and Marko Kaksonen. 2014. “The Initiation of Clathrin-Mediated Endocytosis Is Mechanistically Highly Flexible.” *Current Biology: CB* 24 (5): 548–54. https://doi.org/10.1016/J.CUB.2014.01.048.

Bradford, Mary Katherine, Karen Whitworth, and Beverly Wendland. 2015. “Pan1 Regulates Transitions between Stages of Clathrin-Mediated Endocytosis.” *Molecular Biology of the Cell* 26 (7): 1371–85. https://doi.org/10.1091/mbc.E14-11-1510.

Brett, Tom J., Valerie Legendre-Guillemin, Peter S. McPherson, and Daved H. Fremont. 2006. “Structural Definition of the F-Actin-Binding THATCH Domain from HIP1R.” *Nature Structural & Molecular Biology* 13 (2): 121–30. https://doi.org/10.1038/nsmb1043.

Brodsky, Frances M. 2012. “Diversity of Clathrin Function: New Tricks for an Old Protein.” *Annual Review of Cell and Developmental Biology* 28 (July): 309–36. https://doi.org/10.1146/annurev-cellbio-101011-155716.

Brown, M. S., and J. L. Goldstein. 1979. “Receptor-Mediated Endocytosis: Insights from the Lipoprotein Receptor System.” *Proceedings of the National Academy of Sciences of the United States of America* 76 (7): 3330–37. https://doi.org/10.1073/pnas.76.7.3330.

Bucher, Delia, Felix Frey, Kem A. Sochacki, Susann Kummer, Jan Philip Bergeest, William J. Godinez, Hans Georg Kräusslich, et al. 2018. “Clathrin-Adaptor Ratio and Membrane Tension Regulate the Flat-to-Curved Transition of the Clathrin Coat during Endocytosis.” *Nature Communications 2018 9:1* 9 (1): 1–13. https://doi.org/10.1038/s41467-018-03533-0.

Burastero, Osvaldo, George Draper-Barr, Bertrand Raynal, Maelenn Chevreuil, Patrick England, and Maria Garcia Alai. 2023. “Raynals, an Online Tool for the Analysis of Dynamic Light Scattering.” *Acta Crystallographica. Section D, Structural Biology* 79 (Pt 8): 673–83. https://doi.org/10.1107/S2059798323004862.

Burastero, Osvaldo, Stephan Niebling, Lucas A. Defelipe, Christian Günther, Angelica Struve, and Maria M. Garcia Alai. 2021. “ESPC: An Online Data-Analysis Platform for

Molecular Biophysics.” *Acta Crystallographica. Section D, Structural Biology* 77 (Pt 10): 1241–50. https://doi.org/10.1107/S2059798321008998.

Cai, Huaqing, Karin Reinisch, and Susan Ferro-Novick. 2007. “Coats, Tethers, Rabs, and SNAREs Work Together to Mediate the Intracellular Destination of a Transport Vesicle.” *Developmental Cell* 12 (5): 671–82. https://doi.org/10.1016/j.devcel.2007.04.005.

Carroll, Susheela Y., Helen E. M. Stimpson, Jasper Weinberg, Christopher P. Toret, Yidi Sun, and David G. Drubin. 2012. “Analysis of Yeast Endocytic Site Formation and Maturation through a Regulatory Transition Point.” *Molecular Biology of the Cell* 23 (4): 657–68. https://doi.org/10.1091/mbc.E11-02-0108.

Case, Lindsay B., Xu Zhang, Jonathon A. Ditlev, and Michael K. Rosen. 2019. “Stoichiometry Controls Activity of Phase-Separated Clusters of Actin Signaling Proteins.” *Science (New York, N.Y.)* 363 (6431): 1093–97. https://doi.org/10.1126/science.aau6313.

Chen, Chih Ying, and Frances M. Brodsky. 2005. “Huntingtin-Interacting Protein 1 (Hip1) and Hip1-Related Protein (Hip1R) Bind the Conserved Sequence of Clathrin Light Chains and Thereby Influence Clathrin Assembly in Vitro and Actin Distribution in Vivo.” *The Journal of Biological Chemistry* 280 (7): 6109–17. https://doi.org/10.1074/JBC.M408454200.

Chen, Chih Ying, Michael L. Reese, Peter K. Hwang, Nobuyuki Ota, David Agard, and Frances M. Brodsky. 2002. “Clathrin Light and Heavy Chain Interface: α-Helix Binding Superhelix Loops via Critical Tryptophans.” *The EMBO Journal* 21 (22): 6072–82. https://doi.org/10.1093/emboj/cdf594.

Cole, Daniel, Gavin Young, Alexander Weigel, Aleksandar Sebesta, and Philipp Kukura. 2017. “Label-Free Single-Molecule Imaging with Numerical-Aperture-Shaped Interferometric Scattering Microscopy.” *ACS Photonics* 4 (2): 211–16. https://doi.org/10.1021/acsphotonics.6b00912.

Croll, Tristan Ian. 2018. “ISOLDE: A Physically Realistic Environment for Model Building into Low-Resolution Electron-Density Maps.” *Acta Crystallographica. Section D, Structural Biology* 74 (Pt 6): 519–30. https://doi.org/10.1107/S2059798318002425.

Dacks, Joel B., and Mark C. Field. 2018. “Evolutionary Origins and Specialisation of Membrane Transport.” *Current Opinion in Cell Biology* 53: 70–76. https://doi.org/10.1016/j.ceb.2018.06.001.

Davis, G. D., C. Elisee, D. M. Newham, and R. G. Harrison. 1999. “New Fusion Protein Systems Designed to Give Soluble Expression in Escherichia Coli.” *Biotechnology and Bioengineering* 65 (4): 382–88. https://doi.org/10.1002/(sici)1097-0290(19991120)65:4<382::aid-bit2>3.0.co;2-i.

Day, Kasey J., Grace Kago, Liping Wang, J. Blair Richter, Carl C. Hayden, Eileen M. Lafer, and Jeanne C. Stachowiak. 2021. “Liquid-like Protein Interactions Catalyse Assembly of Endocytic Vesicles.” *Nature Cell Biology* 23 (4): 366–76. https://doi.org/10.1038/s41556-021-00646-5.

De Craene, Johan Owen, Dimitri L. Bertazzi, Séverine Bär, and Sylvie Friant. 2017. “Phosphoinositides, Major Actors in Membrane Trafficking and Lipid Signaling Pathways.” *International Journal of Molecular Sciences* 18 (3): 634. https://doi.org/10.3390/IJMS18030634.

De Matteis, Maria Antonietta, and Alberto Luini. 2011. “Mendelian Disorders of Membrane Trafficking.” *The New England Journal of Medicine* 365 (10): 927–38. https://doi.org/10.1056/nejmra0910494.

Defelipe, Lucas A., Katharina Veith, Osvaldo Burastero, Tatiana Kupriianova, Isabel Bento, M. Skruzny, Knut Köbel, C. Uetrecht, R. Thuenauer, and M. García-Alai. 2024. “Subtleties in Clathrin Heavy Chain Binding Boxes Provide Selectivity among Adaptor Proteins of Budding Yeast.” *BioRxiv*, May. https://doi.org/10.1101/2024.05.30.596561.

Defelipe, Lucas A., Katharina Veith, Osvaldo Burastero, Tatiana Kupriianova, Isabel Bento, Michal Skruzny, Knut Kölbel, Charlotte Uetrecht, Roland Thuenauer, and Maria M. García-Alai. 2024. “Subtleties in Clathrin Heavy Chain Binding Boxes Provide Selectivity among Adaptor Proteins of Budding Yeast.” *Nature Communications* 15 (1): 1–15. https://doi.org/10.1038/s41467-024-54037-z.

Dell'angelica, Esteban C., and Juan S. Bonifacino. 2019. "Coatopathies: Genetic Disorders of Protein Coats." *Annual Review of Cell and Developmental Biology* 35: 131–68. https://doi.org/10.1146/annurev-cellbio-100818-.

Di Pietro, Santiago M., Duilio Cascio, Daniel Feliciano, James U. Bowie, and Gregory S. Payne. 2010. "Regulation of Clathrin Adaptor Function in Endocytosis: Novel Role for the SAM Domain." *The EMBO Journal* 29 (6): 1033–44. https://doi.org/10.1038/emboj.2010.5.

Dionne, Ugo, Émilie Bourgault, Alexandre K. Dubé, David Bradley, François J. M. Chartier, Rohan Dandage, Soham Dibyachintan, et al. 2021. "Protein Context Shapes the Specificity of SH3 Domain-Mediated Interactions in Vivo." *Nature Communications* 12 (1): 1597. https://doi.org/10.1038/s41467-021-21873-2.

Dionne, Ugo, Lily J. Percival, François J. M. Chartier, Christian R. Landry, and Nicolas Bisson. 2022. "SRC Homology 3 Domains: Multifaceted Binding Modules." *Trends in Biochemical Sciences* 47 (9): 772–84. https://doi.org/10.1016/j.tibs.2022.04.005.

Draper-Barr, George, Lucas Defelipe, David Ruiz Carrillo, Emil Gustavsson, Meytal Landau, and Maria M. Garcia-Alai. 2024. "Sla2 Is a Core Interaction Hub for Clathrin Light Chain and the Pan1/End3/Sla1 Complex." *BioRxiv*. https://doi.org/10.1101/2024.11.14.623549.

Duleh, Steve N., and Matthew D. Welch. 2010. "WASH and the Arp2/3 Complex Regulate Endosome Shape and Trafficking." *Cytoskeleton (Hoboken, N.J.)* 67 (3): 193–206. https://doi.org/10.1002/cm.20437.

Edgar, Robert C. 2004. "MUSCLE: Multiple Sequence Alignment with High Accuracy and High Throughput." *Nucleic Acids Research* 32 (5): 1792–97. https://doi.org/10.1093/nar/gkh340.

Emsley, Paul, and Kevin Cowtan. 2004. "Coot: Model-Building Tools for Molecular Graphics." *Acta Crystallographica. Section D, Biological Crystallography* 60 (Pt 12 Pt 1): 2126–32. https://doi.org/10.1107/S0907444904019158.

Engqvist-Goldstein, Åsa E. Y., Robin A. Warren, Michael M. Kessels, James H. Keen, John Heuser, and David G. Drubin. 2001. "The Actin-Binding Protein Hip1R Associates with Clathrin

during Early Stages of Endocytosis and Promotes Clathrin Assembly in Vitro." *The Journal of Cell Biology* 154 (6): 1209–23. https://doi.org/10.1083/JCB.200106089/VIDEO-1.

Enshoji, Mariko, Yoshiko Miyano, Nao Yoshida, Makoto Nagano, Minami Watanabe, Mayumi Kunihiro, Daria E. Siekhaus, Junko Y. Toshima, and Jiro Toshima. 2022. "Eps15/Pan1p Is a Master Regulator of the Late Stages of the Endocytic Pathway." *The Journal of Cell Biology* 221 (10). https://doi.org/10.1083/jcb.202112138.

Evans, Philip R., and Garib N. Murshudov. 2013. "How Good Are My Data and What Is the Resolution?" *Acta Crystallographica. Section D, Biological Crystallography* 69 (Pt 7): 1204–14. https://doi.org/10.1107/S0907444913000061.

Faini, Marco, Rainer Beck, Felix T. Wieland, and John A. G. Briggs. 2013. "Vesicle Coats: Structure, Function, and General Principles of Assembly." *Trends in Cell Biology* 23 (6): 279–88. https://doi.org/10.1016/j.tcb.2013.01.005.

Feliciano, Daniel, and Santiago M. Di Pietro. 2012. "SLAC, a Complex between Sla1 and Las17, Regulates Actin Polymerization during Clathrin-Mediated Endocytosis." *Molecular Biology of the Cell* 23 (21): 4256–72. https://doi.org/10.1091/mbc.E11-12-1022.

Ford, M. G., B. M. Pearse, M. K. Higgins, Y. Vallis, D. J. Owen, A. Gibson, C. R. Hopkins, P. R. Evans, and H. T. McMahon. 2001. "Simultaneous Binding of PtdIns(4,5)P2 and Clathrin by AP180 in the Nucleation of Clathrin Lattices on Membranes." *Science* 291 (5506): 1051–55. https://doi.org/10.1126/science.291.5506.1051.

Fotin, Alexander, Yifan Cheng, Piotr Sliz, Nikolaus Grigorieff, Stephen C. Harrison, Tomas Kirchhausen, and Thomas Walz. 2004. "Molecular Model for a Complete Clathrin Lattice from Electron Cryomicroscopy." *Nature* 432 (7017): 573–79. https://doi.org/10.1038/nature03079.

Franke, Daniel, and Dmitri I. Svergun. 2009. "DAMMIF, a Program for Rapid Ab-Initio Shape Determination in Small-Angle Scattering." *Journal of Applied Crystallography* 42 (Pt 2): 342–46. https://doi.org/10.1107/S0021889809000338.

Franzmann, Titus M., and Simon Alberti. 2019. "Protein Phase Separation as a Stress Survival Strategy." *Cold Spring Harbor Perspectives in Biology* 11 (6): a034058. https://doi.org/10.1101/cshperspect.a034058.

Franzmann, Titus M., Marcus Jahnel, Andrei Pozniakovsky, Julia Mahamid, Alex S. Holehouse, Elisabeth Nüske, Doris Richter, et al. 2018. “Phase Separation of a Yeast Prion Protein Promotes Cellular Fitness.” *Science* 359 (6371). https://doi.org/10.1126/SCIENCE.AAO5654/SUPPL_FILE/AAO5654S8.MP4.

Fujioka, Yuko, Nobuo N. Noda, Hitoshi Nakatogawa, Yoshinori Ohsumi, and Fuyuhiko Inagaki. 2010. “Dimeric Coiled-Coil Structure of Saccharomyces Cerevisiae Atg16 and Its Functional Significance in Autophagy.” *The Journal of Biological Chemistry* 285 (2): 1508–15. https://doi.org/10.1074/JBC.M109.053520.

Fujioka, Yuko, Takuma Tsuji, Tetsuya Kotani, Hiroyuki Kumeta, Chika Kakuta, Toyoshi Fujimoto, Hitoshi Nakatogawa, and Nobuo N. Noda. 2024. “Phase Separation Promotes Atg8 Lipidation for Autophagy Progression.” *Cell Biology*. bioRxiv. https://www.biorxiv.org/content/10.1101/2024.08.29.610189v1.full.pdf.

Gietz, R. Daniel, and Robert H. Schiestl. 2007. “High-Efficiency Yeast Transformation Using the LiAc/SS Carrier DNA/PEG Method.” *Nature Protocols* 2 (1): 31–34. https://doi.org/10.1038/nprot.2007.13.

Gingras, Alexandre R., Neil Bate, Benjamin T. Goult, Larnele Hazelwood, Ilona Canestrelli, J. Günter Grossmann, Hong Jun Liu, et al. 2008. “The Structure of the C-Terminal Actin-Binding Domain of Talin.” *The EMBO Journal* 27 (2): 458–69. https://doi.org/10.1038/SJ.EMBOJ.7601965.

Gourlay, Campbell W., Hilary Dewar, Derek T. Warren, Rosaria Costa, Nilima Satish, and Kathryn R. Ayscough. 2003. “An Interaction between Sla1p and Sla2p Plays a Role in Regulating Actin Dynamics and Endocytosis in Budding Yeast.” *Journal of Cell Science* 116 (Pt 12): 2551–64. https://doi.org/10.1242/jcs.00454.

Guo, Ruiyan, Weiyu Zhao, Linhua Wei, Shoutao Zhang, Lijie Feng, and Yanan Guo. 2022. “A Variety of Simple and Ultra-Low-Cost Methods Preparing SLiCE Extracts and Their Application to DNA Cloning.” *Journal of Microbiological Methods* 202 (106565): 106565. https://doi.org/10.1016/j.mimet.2022.106565.

Guseva, Serafima, Sigrid Milles, Malene Ringkjøbing Jensen, Nicola Salvi, Jean-Philippe Kleman, Damien Maurin, Rob W. H. Ruigrok, and Martin Blackledge. 2020. “Measles Virus Nucleo- and Phosphoproteins Form Liquid-like Phase-Separated Compartments That Promote Nucleocapsid Assembly.” *Science Advances* 6 (14): eaaz7095. https://doi.org/10.1126/sciadv.aaz7095.

Höning, Stefan, Ignacio Sandoval, and Kurt Von Figura. 1998. “A Di-Leucine-Based Motif in the Cytoplasmic Tail of LIMP-II and Tyrosinase Mediates Selective Binding of AP-3.” *The EMBO Journal* 17 (5): 1304–14. https://doi.org/10.1093/emboj/17.5.1304.

Jackson, Sean G., Yi Zhang, Richard J. Haslam, and Murray S. Junop. 2007. “Structural Analysis of the Carboxy Terminal PH Domain of Pleckstrin Bound to D-Myo-Inositol 1,2,3,5,6-Pentakisphosphate.” *BMC Structural Biology* 7 (1): 80. https://doi.org/10.1186/1472-6807-7-80.

Janke, Carsten, Maria M. Magiera, Nicole Rathfelder, Christof Taxis, Simone Reber, Hiromi Maekawa, Alexandra Moreno-Borchart, et al. 2004. “A Versatile Toolbox for PCR-Based Tagging of Yeast Genes: New Fluorescent Proteins, More Markers and Promoter Substitution Cassettes.” *Yeast (Chichester, England)* 21 (11): 947–62. https://doi.org/10.1002/yea.1142.

Jerabek-Willemsen, Moran, Chistoph J. Wienken, Dieter Braun, Philipp Baaske, and Stefan Duhr. 2011. “Molecular Interaction Studies Using Microscale Thermophoresis.” *Assay and Drug Development Technologies* 9 (4): 342–53. https://doi.org/10.1089/adt.2011.0380.

Jia, Xuanyan, Leishu Lin, Shun Xu, Lingxuan Li, Zhiyi Wei, Cong Yu, and Fengfeng Niu. 2023. “Crystal Structure of the SH3 Domain of ASAP1 in Complex with the Proline Rich Motif (PRM) of MICAL1 Reveals a Unique SH3/PRM Interaction Mode.” *International Journal of Molecular Sciences* 24 (2): 1414. https://doi.org/10.3390/ijms24021414.

Jumper, John, Richard Evans, Alexander Pritzel, Tim Green, Michael Figurnov, Olaf Ronneberger, Kathryn Tunyasuvunakool, et al. 2021. “Highly Accurate Protein Structure Prediction with AlphaFold.” *Nature* 596 (7873): 583–89. https://doi.org/10.1038/s41586-021-03819-2.

Kaksonen, Marko, and Aurélien Roux. 2018. “Mechanisms of Clathrin-Mediated Endocytosis.” *Nature Reviews. Molecular Cell Biology* 19 (5): 313–26. https://doi.org/10.1038/nrm.2017.132.

Kang, Dong Soo, Ronald C. Kern, Manojkumar A. Puthenveedu, Mark von Zastrow, John C. Williams, and Jeffrey L. Benovic. 2009. “Structure of an Arrestin2-Clathrin Complex Reveals a Novel Clathrin Binding Domain That Modulates Receptor Trafficking.” *The Journal of Biological Chemistry* 284 (43): 29860–72. https://doi.org/10.1074/jbc.M109.023366.

Katoh, Kazutaka, Kazuharu Misawa, Kei-Ichi Kuma, and Takashi Miyata. 2002. “MAFFT: A Novel Method for Rapid Multiple Sequence Alignment Based on Fast Fourier Transform.” *Nucleic Acids Research* 30 (14): 3059–66. https://doi.org/10.1093/nar/gkf436.

Kellner, Nikola, and Ed Hurt. 2022. “Transformation of Chaetomium Thermophilum and Affinity Purification of Native Thermostable Protein Complexes.” *Methods in Molecular Biology (Clifton, N.J.)* 2502: 35–50. https://doi.org/10.1007/978-1-0716-2337-4_2.

Kelly, Bernard T., Stephen C. Graham, Nicole Liska, Philip N. Dannhauser, Stefan Höning, Ernst J. Ungewickell, and David J. Owen. 2014. “AP2 Controls Clathrin Polymerization with a Membrane-Activated Switch.” *Science* 345 (6195): 459. https://doi.org/10.1126/SCIENCE.1254836.

Kempen, Michel van, Stephanie S. Kim, Charlotte Tumescheit, Milot Mirdita, Jeongjae Lee, Cameron L. M. Gilchrist, Johannes Söding, and Martin Steinegger. 2024. “Fast and Accurate Protein Structure Search with Foldseek.” *Nature Biotechnology* 42 (2): 243–46. https://doi.org/10.1038/s41587-023-01773-0.

Kirchhausen, Tom, David Owen, and Stephen C. Harrison. 2014. “Molecular Structure, Function, and Dynamics of Clathrin-Mediated Membrane Traffic.” *Cold Spring Harbor Perspectives in Biology* 6 (5). https://doi.org/10.1101/cshperspect.a016725.

Kohn, Jonathan E., Ian S. Millett, Jaby Jacob, Bojan Zagrovic, Thomas M. Dillon, Nikolina Cingel, Robin S. Dothager, et al. 2004. “Random-Coil Behavior and the Dimensions of Chemically Unfolded Proteins.” *Proceedings of the National Academy of Sciences of the United States of America* 101 (34): 12491–96. https://doi.org/10.1073/pnas.0403643101.

Kotov, Vadim, Kim Bartels, Katharina Veith, Inokentijs Josts, Udaya K. Tiruttani Subhramanyam, Christian Günther, Jörg Labahn, et al. 2019. “High-Throughput Stability Screening for Detergent-Solubilized Membrane Proteins.” *Scientific Reports 2019 9:1* 9 (1): 1–19. https://doi.org/10.1038/s41598-019-46686-8.

Kotov, Vadim, Georg Mlynek, Oliver Vesper, Marina Pletzer, Jiri Wald, Celso M. Teixeira-Duarte, Herve Celia, et al. 2021. “In-Depth Interrogation of Protein Thermal Unfolding Data with MoltenProt.” *Protein Science: A Publication of the Protein Society* 30 (1): 201–17. https://doi.org/10.1002/pro.3986.

Kozak, Mateusz, and Marko Kaksonen. 2022. “Condensation of Ede1 Promotes the Initiation of Endocytosis.” *ELife* 11 (April). https://doi.org/10.7554/eLife.72865.

Kukulski, Wanda, Andrea Picco, Tanja Specht, John A. G. Briggs, and Marko Kaksonen. 2016. “Clathrin Modulates Vesicle Scission, but Not Invagination Shape, in Yeast Endocytosis.” *ELife* 5 (JUN2016). https://doi.org/10.7554/ELIFE.16036.

Kukulski, Wanda, Martin Schorb, Marko Kaksonen, and John A. G. Briggs. 2012. “Plasma Membrane Reshaping during Endocytosis Is Revealed by Time-Resolved Electron Tomography.” *Cell* 150 (3): 508–20. https://doi.org/10.1016/j.cell.2012.05.046.

Legendre-Guillemin, Valerie, Martina Metzler, Martine Charbonneau, Lu Gan, Vikramjit Chopra, Jacynthe Philie, Michael R. Hayden, and Peter S. McPherson. 2002. “HIP1 and HIP12 Display Differential Binding to F-Actin, AP2, and Clathrin: IDENTIFICATION OF A NOVEL INTERACTION WITH CLATHRIN LIGHT CHAIN*.” *The Journal of Biological Chemistry* 277 (22): 19897–904. https://doi.org/10.1074/jbc.M112310200.

Legendre-Guillemin, Valerie, Martina Metzler, Jean-Francois Lemaire, Jacynthe Philie, Lu Gan, Michael R. Hayden, and Peter S. McPherson. 2005. “Huntingtin Interacting Protein 1 (HIP1) Regulates Clathrin Assembly through Direct Binding to the Regulatory Region of the Clathrin Light Chain.” *The Journal of Biological Chemistry* 280 (7): 6101–8. https://doi.org/10.1074/jbc.M408430200.

Leitner, Alexander, Roland Reischl, Thomas Walzthoeni, Franz Herzog, Stefan Bohn, Friedrich Förster, and Ruedi Aebersold. 2012. “Expanding the Chemical Cross-Linking

Toolbox by the Use of Multiple Proteases and Enrichment by Size Exclusion Chromatography." *Molecular & Cellular Proteomics: MCP* 11 (3): M111.014126. https://doi.org/10.1074/mcp.M111.014126.

Lemmon, Mark A. 2007. "Pleckstrin Homology (PH) Domains and Phosphoinositides." *Biochemical Society Symposium*, no. 74: 81–93. https://doi.org/10.1042/BSS0740081.

Ling, Yading, Christopher J. Stefan, Jason A. Macgurn, Anjon Audhya, and Scott D. Emr. 2012. "The Dual PH Domain Protein Opy1 Functions as a Sensor and Modulator of PtdIns(4,5)P_2 Synthesis." *The EMBO Journal* 31 (13): 2882–94. https://doi.org/10.1038/emboj.2012.127.

Lizarrondo, Javier, David P. Klebl, Stephan Niebling, Marc Abella, Martin A. Schroer, Haydyn D. T. Mertens, Katharina Veith, et al. 2021. "Structure of the Endocytic Adaptor Complex Reveals the Basis for Efficient Membrane Anchoring during Clathrin-Mediated Endocytosis." *Nature Communications* 12 (1): 2889. https://doi.org/10.1038/s41467-021-23151-7.

Lizarrondo, Javier, and Florian Wilfling. 2024. "Selective Autophagy of Macromolecular Complexes: What Does It Take to Be Taken?" *Journal of Molecular Biology* 436 (15): 168574. https://doi.org/10.1016/j.jmb.2024.168574.

Lu, Rebecca, and David G. Drubin. 2017. "Selection and Stabilization of Endocytic Sites by Ede1, a Yeast Functional Homologue of Human Eps15." *Molecular Biology of the Cell* 28 (5): 567. https://doi.org/10.1091/MBC.E16-06-0391.

Mahadev, Ravi K., Santiago M. Di Pietro, John M. Olson, Hai Lan Piao, Gregory S. Payne, and Michael Overduin. 2007. "Structure of Sla1p Homology Domain 1 and Interaction with the NPFxD Endocytic Internalization Motif." *The EMBO Journal* 26 (7): 1963–71. https://doi.org/10.1038/sj.emboj.7601646.

Maldonado-Báez, Lymarie, Michael R. Dores, Edward M. Perkins, Theodore G. Drivas, Linda Hicke, and Beverly Wendland. 2008. "Interaction between Epsin/Yap180 Adaptors and the Scaffolds Ede1/Pan1 Is Required for Endocytosis." *Molecular Biology of the Cell* 19 (7): 2936–48. https://doi.org/10.1091/mbc.E07-10-1019.

Manalastas-Cantos, Karen, Petr V. Konarev, Nelly R. Hajizadeh, Alexey G. Kikhney, Maxim V. Petoukhov, Dmitry S. Molodenskiy, Alejandro Panjkovich, et al. 2021. “ATSAS 3.0: Expanded Functionality and New Tools for Small-Angle Scattering Data Analysis.” *Journal of Applied Crystallography* 54 (Pt 1): 343–55. https://doi.org/10.1107/S1600576720013412.

Mann, H. B., and D. R. Whitney. 1947. “On a Test of Whether One of Two Random Variables Is Stochastically Larger than the Other.” *The Annals of Mathematical Statistics* 18 (1): 50–60. https://doi.org/10.1214/aoms/1177730491.

Massenet, Claire, Sylvie Chenavas, Claudine Cohen-Addad, Marie-Claire Dagher, Gérard Brandolin, Eva Pebay-Peyroula, and Franck Fieschi. 2005. “Effects of P47phox C Terminus Phosphorylations on Binding Interactions with P40phox and P67phox. Structural and Functional Comparison of P40phox and P67phox SH3 Domains.” *The Journal of Biological Chemistry* 280 (14): 13752–61. https://doi.org/10.1074/jbc.M412897200.

McCann, Richard O., and Susan W. Craig. 1997. “The I/LWEQ Module: A Conserved Sequence That Signifies F-Actin Binding in Functionally Diverse Proteins from Yeast to Mammals.” *Proceedings of the National Academy of Sciences of the United States of America* 94 (11): 5679. https://doi.org/10.1073/PNAS.94.11.5679.

Mertens, Haydyn D. T. 2023. “Computational Methods for the Analysis of Solution Small-Angle X-Ray Scattering of Biomolecules: ATSAS.” *Methods in Enzymology* 678: 193–236. https://doi.org/10.1016/bs.mie.2022.09.019.

Mettlen, Marcel, Ping-Hung Chen, Saipraveen Srinivasan, Gaudenz Danuser, and Sandra L. Schmid. 2018. “Regulation of Clathrin-Mediated Endocytosis.” *Annual Review of Biochemistry* 87 (1): 871–96. https://doi.org/10.1146/annurev-biochem-062917-012644.

Miles, A. J., Robert W. Janes, and B. A. Wallace. 2021. “Tools and Methods for Circular Dichroism Spectroscopy of Proteins: A Tutorial Review.” *Chemical Society Reviews* 50 (15): 8400–8413. https://doi.org/10.1039/d0cs00558d.

Morris, Kyle L., Joseph R. Jones, Mary Halebian, Shenping Wu, Michael Baker, Jean Paul Armache, Amaurys Avila Ibarra, et al. 2019. “Cryo-EM of Multiple Cage Architectures Reveals

a Universal Mode of Clathrin Self-Assembly." *Nature Structural & Molecular Biology* 26 (10): 890–98. https://doi.org/10.1038/s41594-019-0292-0.

Mund, Markus, Johannes Albertus van der Beek, Joran Deschamps, Serge Dmitrieff, Philipp Hoess, Jooske Louise Monster, Andrea Picco, François Nédélec, Marko Kaksonen, and Jonas Ries. 2018. "Systematic Nanoscale Analysis of Endocytosis Links Efficient Vesicle Formation to Patterned Actin Nucleation." *Cell* 174 (4): 884-896.e17. https://doi.org/10.1016/j.cell.2018.06.032.

Mund, Markus, Aline Tschanz, Yu-Le Wu, Felix Frey, Johanna L. Mehl, Marko Kaksonen, Ori Avinoam, Ulrich S. Schwarz, and Jonas Ries. 2022. "Superresolution Microscopy Reveals Partial Preassembly and Subsequent Bending of the Clathrin Coat during Endocytosis." *BioRxiv*, January, 2021.10.12.463947. https://doi.org/10.1101/2021.10.12.463947.

Murshudov, Garib N., Pavol Skubák, Andrey A. Lebedev, Navraj S. Pannu, Roberto A. Steiner, Robert A. Nicholls, Martyn D. Winn, Fei Long, and Alexei A. Vagin. 2011. "REFMAC5 for the Refinement of Macromolecular Crystal Structures." *Acta Crystallographica. Section D, Biological Crystallography* 67 (Pt 4): 355–67. https://doi.org/10.1107/S0907444911001314.

Nawara, Tomasz J., Yancey D. Williams, Tejeshwar C. Rao, Yuesong Hu, Elizabeth Sztul, Khalid Salaita, and Alexa L. Mattheyses. 2022. "Imaging Vesicle Formation Dynamics Supports the Flexible Model of Clathrin-Mediated Endocytosis." *Nature Communications 2022 13:1* 13 (1): 1–14. https://doi.org/10.1038/s41467-022-29317-1.

Niebling, Stephan, Katharina Veith, Benjamin Vollmer, Javier Lizarrondo, Osvaldo Burastero, Janina Schiller, Angelica Struve García, et al. 2022. "Biophysical Screening Pipeline for Cryo-EM Grid Preparation of Membrane Proteins." *Frontiers in Molecular Biosciences* 9 (June): 882288. https://doi.org/10.3389/fmolb.2022.882288.

Niu, Qian, and Joel A. Ybe. 2008. "Crystal Structure at 2.8 A of Huntingtin-Interacting Protein 1 (HIP1) Coiled-Coil Domain Reveals a Charged Surface Suitable for HIP1 Protein Interactor (HIPPI)." *Journal of Molecular Biology* 375 (5): 1197–1205. https://doi.org/10.1016/j.jmb.2007.11.036.

Obashi, Kazuki, Kem A. Sochacki, Marie Paule Strub, and Justin W. Taraska. 2023. “A Conformational Switch in Clathrin Light Chain Regulates Lattice Structure and Endocytosis at the Plasma Membrane of Mammalian Cells.” *Nature Communications* 14 (1): 1–15. https://doi.org/10.1038/s41467-023-36304-7.

Palade, G. 1975. “Intracellular Aspects of the Process of Protein Synthesis.” *Science* 189 (4206): 867–867. https://doi.org/10.1126/science.189.4206.867-b.

Paraan, Mohammadreza, Joshua Mendez, Savanna Sharum, Danielle Kurtin, Huan He, and Scott M. Stagg. 2020. “The Structures of Natively Assembled Clathrin-Coated Vesicles.” *Science Advances* 6 (30). https://doi.org/10.1126/sciadv.aba8397.

Pearse, B. M. 1976. “Clathrin: A Unique Protein Associated with Intracellular Transfer of Membrane by Coated Vesicles.” *Proceedings of the National Academy of Sciences of the United States of America* 73 (4): 1255–59. https://doi.org/10.1073/pnas.73.4.1255.

Pearse, Barbara M. F. 1975. “Coated Vesicles from Pig Brain: Purification and Biochemical Characterization.” *Journal of Molecular Biology* 97 (1): 93–98. https://doi.org/10.1016/s0022-2836(75)80024-6.

Pedersen, Ross T. A., Julian E. Hassinger, Paul Marchando, and David G. Drubin. 2020. “Spatial Regulation of Clathrin-Mediated Endocytosis through Position-Dependent Site Maturation.” *The Journal of Cell Biology* 219 (11). https://doi.org/10.1083/JCB.202002160.

Petoukhov, M. V., and D. I. Svergun. 2012. “Small Angle X-Ray Scattering/Small Angle Neutron Scattering as Methods Complementary to NMR.” In *NMR of Biomolecules*, 562–74. Weinheim, Germany: Wiley-VCH Verlag GmbH & Co. KGaA. https://doi.org/10.1002/9783527644506.ch35.

Picco, Andrea, Markus Mund, Jonas Ries, François Nédélec, and Marko Kaksonen. 2015. “Visualizing the Functional Architecture of the Endocytic Machinery.” *ELife* 2015 (4): 1–29. https://doi.org/10.7554/eLife.04535.

Pierce, B. D., Dmitri Toptygin, and Beverly Wendland. 2013. “Pan1 Is an Intrinsically Disordered Protein with Homotypic Interactions.” *Proteins* 81 (11): 1944–63. https://doi.org/10.1002/prot.24342.

Potterton, Liz, Jon Agirre, Charles Ballard, Kevin Cowtan, Eleanor Dodson, Phil R. Evans, Huw T. Jenkins, et al. 2018. “CCP4i2: The New Graphical User Interface to the CCP4 Program Suite.” *Acta Crystallographica. Section D, Structural Biology* 74 (Pt 2): 68–84. https://doi.org/10.1107/S2059798317016035.

Punjani, Ali, John L. Rubinstein, David J. Fleet, and Marcus A. Brubaker. 2017. “CryoSPARC: Algorithms for Rapid Unsupervised Cryo-EM Structure Determination.” *Nature Methods* 14 (3): 290–96. https://doi.org/10.1038/nmeth.4169.

Redlingshöfer, Lisa, and Frances M. Brodsky. 2021. “Antagonistic Regulation Controls Clathrin-Mediated Endocytosis: AP2 Adaptor Facilitation vs Restraint from Clathrin Light Chains.” *Cells and Development*. https://doi.org/10.1016/j.cdev.2021.203714.

Reider, Amanda, Sarah L. Barker, Sanjay K. Mishra, Young Jun Im, Lymarie Maldonado-Báez, James H. Hurley, Linton M. Traub, and Beverly Wendland. 2009. “Syp1 Is a Conserved Endocytic Adaptor That Contains Domains Involved in Cargo Selection and Membrane Tubulation.” *The EMBO Journal* 28 (20): 3103–16. https://doi.org/10.1038/emboj.2009.248.

Ren, Yuan, and Julien Berro. 2022. “Isolated THATCH Domain of End4 Is Unable to Bind F-Actin Independently in the Fission Yeast Schizosaccharomyces Pombe.” *MicroPublication Biology* 2022. https://doi.org/10.17912/MICROPUB.BIOLOGY.000508.

Ren, Yuan, Jie Yang, Barbara Fujita, Huaizhou Jin, Yongli Zhang, and Julien Berro. 2023. “Force Redistribution in Clathrin-Mediated Endocytosis Revealed by Coiled-Coil Force Sensors.” *Science Advances* 9 (41): eadi1535. https://doi.org/10.1126/sciadv.adi1535.

Ren, Yuan, Jie Yang, Barbara Fujita, Yongli Zhang, and Julien Berro. 2023. “A Mechanical Circuit in End4p Coordinates Force Transmission during Clathrin-Mediated Endocytosis.” *BioRxiv*. https://doi.org/10.1101/2023.10.23.563344.

Robinson, Margaret S. 1991. “Membrane Traffic COPs.” *Nature* 349 (6312): 743–44. https://doi.org/10.1038/349743a0.

Rodal, Avital A., Amity L. Manning, Bruce L. Goode, and David G. Drubin. 2003. “Negative Regulation of Yeast WASp by Two SH3 Domain-Containing Proteins.” *Current Biology: CB* 13 (12): 1000–1008. https://doi.org/10.1016/s0960-9822(03)00383-x.

Roessle, Manfred, and Dmitri I. Svergun. 2019. “Small Angle X-Ray Scattering.” In *Encyclopedia of Biophysics*, 1–12. Berlin, Heidelberg: Springer Berlin Heidelberg. https://doi.org/10.1007/978-3-642-35943-9_284-1.

Rosenthal, J. A., H. Chen, V. I. Slepnev, L. Pellegrini, A. E. Salcini, P. P. Di Fiore, and P. De Camilli. 1999. “The Epsins Define a Family of Proteins That Interact with Components of the Clathrin Coat and Contain a New Protein Module.” *The Journal of Biological Chemistry* 274 (48): 33959–65. https://doi.org/10.1074/jbc.274.48.33959.

Rothman, James E., and Felix T. Wieland. 1996. “Protein Sorting by Transport Vesicles.” *Science* 272 (5259): 227–34. https://doi.org/10.1126/science.272.5259.227.

Sabari, Benjamin R., Anthony A. Hyman, and Denes Hnisz. 2024. “Functional Specificity in Biomolecular Condensates Revealed by Genetic Complementation.” *Nature Reviews. Genetics*, October, 1–12. https://doi.org/10.1038/s41576-024-00780-4.

Schekman, Randy, and Lelio Orci. 1996. “Coat Proteins and Vesicle Budding.” *Science* 271 (5255): 1526–33. https://doi.org/10.1126/science.271.5255.1526.

Scott, Brandon L., Kem A. Sochacki, Shalini T. Low-Nam, Elizabeth M. Bailey, Quoc Ahn Luu, Amy Hor, Andrea M. Dickey, et al. 2018. “Membrane Bending Occurs at All Stages of Clathrin-Coat Assembly and Defines Endocytic Dynamics.” *Nature Communications 2018 9:1* 9 (1): 1–9. https://doi.org/10.1038/s41467-018-02818-8.

Serwas, Daniel, Matthew Akamatsu, Amir Moayed, Karthik Vegesna, Ritvik Vasan, Jennifer M. Hill, Johannes Schöneberg, Karen M. Davies, Padmini Rangamani, and David G. Drubin. 2022. “Mechanistic Insights into Actin Force Generation during Vesicle Formation from Cryo-Electron Tomography.” *Developmental Cell* 57 (9): 1132-1145.e5. https://doi.org/10.1016/j.devcel.2022.04.012.

Shin, Juhyun, Arti Nile, and Jae-Wook Oh. 2021. “Role of Adaptin Protein Complexes in Intracellular Trafficking and Their Impact on Diseases.” *Https://Doi.Org/10.1080/21655979.2021.1982846* 12 (1): 8259–78. https://doi.org/10.1080/21655979.2021.1982846.

Skruzny, Michal, Thorsten Brach, Rodolfo Ciuffa, Sofia Rybina, Malte Wachsmuth, and Marko Kaksonen. 2012. “Molecular Basis for Coupling the Plasma Membrane to the Actin Cytoskeleton during Clathrin-Mediated Endocytosis.” *Proceedings of the National Academy of Sciences of the United States of America* 109 (38): E2533-42. https://doi.org/10.1073/pnas.1207011109.

Skruzny, Michal, Ambroise Desfosses, Simone Prinz, Svetlana O. Dodonova, Anna Gieras, Charlotte Uetrecht, Arjen J. Jakobi, et al. 2015. “An Organized Co-Assembly of Clathrin Adaptors Is Essential for Endocytosis.” *Developmental Cell* 33 (2): 150–62. https://doi.org/10.1016/j.devcel.2015.02.023.

Skruzny, Michal, Emma Pohl, Sandina Gnoth, Gabriele Malengo, and Victor Sourjik. 2020. “The Protein Architecture of the Endocytic Coat Analyzed by FRET Microscopy.” *Molecular Systems Biology* 16 (5): e9009. https://doi.org/10.15252/msb.20199009.

Smith, Steven J., and Richard O. McCann. 2007. “A C-Terminal Dimerization Motif Is Required for Focal Adhesion Targeting of Talin1 and the Interaction of the Talin1 I/LWEQ Module with F-Actin.” *Biochemistry* 46 (38): 10886–98. https://doi.org/10.1021/bi700637a.

Sochacki, Kem A., and Justin W. Taraska. 2019. “From Flat to Curved Clathrin: Controlling a Plastic Ratchet.” *Trends in Cell Biology* 29 (3): 241–56. https://doi.org/10.1016/j.tcb.2018.12.002.

Sonn-Segev, Adar, Katarina Belacic, Tatyana Bodrug, Gavin Young, Ryan T. VanderLinden, Brenda A. Schulman, Johannes Schimpf, et al. 2020. “Quantifying the Heterogeneity of Macromolecular Machines by Mass Photometry.” *Nature Communications* 11 (1): 1772. https://doi.org/10.1038/s41467-020-15642-w.

Spiess, Matthias, Johan-Owen de Craene, Alphée Michelot, Bruno Rinaldi, Aline Huber, David G. Drubin, Barbara Winsor, and Sylvie Friant. 2013. “Lsb1 Is a Negative Regulator of Las17 Dependent Actin Polymerization Involved in Endocytosis.” *PloS One* 8 (4): e61147. https://doi.org/10.1371/journal.pone.0061147.

Stimpson, Helen E. M., Christopher P. Toret, Aaron T. Cheng, Barbara S. Pauly, and David G. Drubin. 2009. “Early-Arriving Syp1p and Ede1p Function in Endocytic Site Placement and

Formation in Budding Yeast." *Molecular Biology of the Cell* 20 (22): 4640–51. https://doi.org/10.1091/mbc.e09-05-0429.

Sun, Yidi, Marko Kaksonen, David T. Madden, Randy Schekman, and David G. Drubin. 2005. "Interaction of Sla2p's ANTH Domain with PtdIns(4,5)P2 Is Important for Actin-Dependent Endocytic Internalization." *Molecular Biology of the Cell* 16 (2): 717. https://doi.org/10.1091/MBC.E04-08-0740.

Sun, Yidi, Nicole T. Leong, Tiffany Wong, and David G. Drubin. 2015. "A Pan1/End3/Sla1 Complex Links Arp2/3-Mediated Actin Assembly to Sites of Clathrin-Mediated Endocytosis." *Molecular Biology of the Cell* 26 (21): 3841–56. https://doi.org/10.1091/mbc.E15-04-0252.

Sun, Yidi, Johannes Schöneberg, Xuyan Chen, Tommy Jiang, Charlotte Kaplan, Ke Xu, Thomas D. Pollard, and David G. Drubin. 2019. "Direct Comparison of Clathrin-Mediated Endocytosis in Budding and Fission Yeast Reveals Conserved and Evolvable Features." *ELife* 8 (December). https://doi.org/10.7554/eLife.50749.

Szymanska, Monika, Anne Marthe Fosdahl, Camilla Raiborg, Markus Dietrich, Knut Liestøl, Espen Stang, and Vibeke Bertelsen. 2016. "Interaction with Epsin 1 Regulates the Constitutive Clathrin-Dependent Internalization of ErbB3." *Biochimica et Biophysica Acta* 1863 (6 Pt A): 1179–88. https://doi.org/10.1016/j.bbamcr.2016.03.011.

Taylor, Nicole O., Ming-Tzo Wei, Howard A. Stone, and Clifford P. Brangwynne. 2019. "Quantifying Dynamics in Phase-Separated Condensates Using Fluorescence Recovery after Photobleaching." *Biophysical Journal* 117 (7): 1285–1300. https://doi.org/10.1016/j.bpj.2019.08.030.

Teyra, Joan, Haiming Huang, Shobhit Jain, Xinyu Guan, Aiping Dong, Yanli Liu, Wolfram Tempel, et al. 2017. "Comprehensive Analysis of the Human SH3 Domain Family Reveals a Wide Variety of Non-Canonical Specificities." *Structure* 25 (10): 1598-1610.e3. https://doi.org/10.1016/j.str.2017.07.017.

Toshima, Jiro, Junko Y. Toshima, Mara C. Duncan, M. Jamie T. V. Cope, Yidi Sun, Adam C. Martin, Scott Anderson, John R. Yates 3rd, Kensaku Mizuno, and David G. Drubin. 2007. "Negative Regulation of Yeast Eps15-like Arp2/3 Complex Activator, Pan1p, by the Hip1R-

Related Protein, Sla2p, during Endocytosis." *Molecular Biology of the Cell* 18 (2): 658–68. https://doi.org/10.1091/mbc.e06-09-0788.

Toshima, Jiro, Junko Y. Toshima, Mara C. Duncan, M. Jamie, T. V. Cope, Yidi Sun, Adam C. Martin, et al. 2007. "Negative Regulation of Yeast Eps15-like Arp2/3 Complex Activator, Pan1p, by the Hip1R-Related Protein, Sla2p, during Endocytosis □ D □ V." *Molecular Biology of the Cell* 18: 658–68. https://doi.org/10.1091/mbc.E06.

Ungewickell, E., and D. Branton. 1981. "Assembly Units of Clathrin Coats." *Nature* 289 (5796): 420–22. https://doi.org/10.1038/289420a0.

Vagin, A., and A. Teplyakov. 1997. "MOLREP: An Automated Program for Molecular Replacement." *Journal of Applied Crystallography* 30 (6): 1022–25. https://doi.org/10.1107/S0021889897006766.

Vigers, G. P. A. 1986. *Clathrin Assemblies in Vitreous Ice: A Structural Analysis by Image Reconstruction*. University of Cambridge. https://play.google.com/store/books/details?id=mxuA0AEACAAJ.

Whitworth, Karen, Mary Katherine Bradford, Nicole Camara, and Beverly Wendland. 2014. "Targeted Disruption of an EH-Domain Protein Endocytic Complex, Pan1-End3." *Traffic* 15 (1): 43–59. https://doi.org/10.1111/tra.12125.

Wilbur, Jeremy D., Chih Ying Chen, Venus Manalo, Peter K. Hwang, Robert J. Fletterick, and Frances M. Brodsky. 2008. "Actin Binding by Hip1 (Huntingtin-Interacting Protein 1) and Hip1R (Hip1-Related Protein) Is Regulated by Clathrin Light Chain." *The Journal of Biological Chemistry* 283 (47): 32870–79. https://doi.org/10.1074/jbc.M802863200.

Wilfling, Florian, Chia-Wei Lee, Philipp Erdmann, Yumei Zheng, Stefan Jentsch, Boris Pfander, Brenda A. Schulman, and Wolfgang Baumeister. 2020. "A Selective Autophagy Pathway for Phase Separated Endocytic Protein Deposits." *BioRxiv*. bioRxiv. https://doi.org/10.1101/2020.05.26.116368.

Wu, X., B. Knudsen, S. M. Feller, J. Zheng, A. Sali, D. Cowburn, H. Hanafusa, and J. Kuriyan. 1995. "Structural Basis for the Specific Interaction of Lysine-Containing Proline-Rich

Peptides with the N-Terminal SH3 Domain of c-Crk." *Structure (London, England: 1993)* 3 (2): 215–26. https://doi.org/10.1016/s0969-2126(01)00151-4.

Xing, Yi, Till Böcking, Matthias Wolf, Nikolaus Grigorieff, Tomas Kirchhausen, and Stephen C. Harrison. 2010. "Structure of Clathrin Coat with Bound Hsc70 and Auxilin: Mechanism of Hsc70-Facilitated Disassembly." *The EMBO Journal* 29 (3): 655–65. https://doi.org/10.1038/emboj.2009.383.

Ybe, Joel A., Barrie Greene, Shu-hui Liu, Ursula Pley, Peter Parham, and Frances M. Brodsky. 1998. "Clathrin Self-assembly Is Regulated by Three Light-chain Residues Controlling the Formation of Critical Salt Bridges." *The EMBO Journal* 17 (5): 1297-1303–1303. https://doi.org/10.1093/emboj/17.5.1297.

Ybe, Joel A., Sanjay Mishra, Stephen Helms, and Jay Nix. 2007. "Crystal Structure at 2.8 Å of the DLLRKN-Containing Coiled-Coil Domain of Huntingtin-Interacting Protein 1 (HIP1) Reveals a Surface Suitable for Clathrin Light Chain Binding." https://doi.org/10.1016/j.jmb.2006.12.052.

Ybe, Joel A., Samantha Perez-Miller, Qian Niu, David A. Coates, Michael W. Drazer, and Mary E. Clegg. 2007. "Light Chain C-Terminal Region Reinforces the Stability of Clathrin Heavy Chain Trimers." *Traffic* 8 (8): 1101–10. https://doi.org/10.1111/j.1600-0854.2007.00597.x.

Young, Gavin, Nikolas Hundt, Daniel Cole, Adam Fineberg, Joanna Andrecka, Andrew Tyler, Anna Olerinyova, et al. 2018. "Quantitative Mass Imaging of Single Biological Macromolecules." *Science* 360 (6387): 423–27. https://doi.org/10.1126/science.aar5839.

Yuan, Feng, Sadhana Gollapudi, Kasey J. Day, Grant Ashby, Arjun Sangani, Brandon T. Malady, Liping Wang, Eileen M. Lafer, Jon M. Huibregtse, and Jeanne C. Stachowiak. 2024. "Ubiquitin-Driven Protein Condensation Stabilizes Clathrin-Mediated Endocytosis." *PNAS Nexus*, August, gae342. https://doi.org/10.1093/pnasnexus/pgae342.

Zeno, Wade F., Jacob B. Hochfelder, Ajay S. Thatte, Liping Wang, Avinash K. Gadok, Carl C. Hayden, Eileen M. Lafer, and Jeanne C. Stachowiak. 2021. "Clathrin Senses Membrane Curvature." *Biophysical Journal* 120 (5): 818–28. https://doi.org/10.1016/j.bpj.2020.12.035.

Zhang, Yongwei, Uwe Werling, and Winfried Edelmann. 2012. “SLiCE: A Novel Bacterial Cell Extract-Based DNA Cloning Method.” *Nucleic Acids Research* 40 (8): e55. https://doi.org/10.1093/nar/gkr1288.

Zigmond, S. H. 2000. “How WASP Regulates Actin Polymerization.” *The Journal of Cell Biology* 150 (6): F117-20. https://doi.org/10.1083/jcb.150.6.f117.

10 Appendix

Table 7: Table of expression constructs

Plasmid	Construct name	N-terminal affinity tag	Protein	Residues	C-terminal affinity tag
pnEA	Sla2ccRTH	6xHis-TEV-GST-	*Sc*Sla2	351-968	-
pETM30	Sla2cc	6xHis-TEV-GST-	*Sc*Sla2	296-767	-
pETM30	Sla2 IDR	6xHis-TEV-GST-	*Sc*Sla2	270-350	-
pETM30	Sla2 TH	6xHis-TEV-GST-	*Sc*Sla2	743-968	-
pETM11	Sla2PQ-mSc-I	6xHis-TEV-SUMO-	*Sc*Sla2	281-351	-3C-mScarlet-I
pETM11	Sla2cc-mSc-I	6xHis-TEV-SUMO-	*Sc*Sla2	351-743	-3C-mScarlet-I
pETM11	Sla2PQcc-mSc-I	6xHis-TEV-SUMO-	*Sc*Sla2	281-743	-3C-mScarlet-I
pETM30	CLC FL	6xHis-TEV-GST-	*Sc*CLC	1-233	-
pETM30	CLC 1-80	6xHis-TEV-GST-	*Sc*CLC	1-80	-
pETM30	CLC 70-140	6xHis-TEV-GST-	*Sc*CLC	70-140	-
pETM30	CLC 70-233	6xHis-TEV-GST-	*Sc*CLC	70-233	-
pnEA	-vHisNusA-CLC	6xHis-TEV-NusA-	*Sc*CLC	1-233	-
pETM11	CHC-mNG	6xHis-TEV-SUMO-	*Sc*CHC	1172-1574	-3C-mNeonGreen
pETM30	Pan1cc	6xHis-TEV-GST-	*Sc*Pan1	777-987	-
pETM11	ATG16cc-mSc-I	6xHis-TEV-SUMO-	*Sc*ATG	54-144	-3C-mScarlet-I
pETM30	Sla1 SH3_3	6xHis-TEV-GST-	*Sc*Sla1	355-414	-
pnEA	ENTH	6xHis-TEV-	*Sc*Ent1	1-280	-
pETM11	Ede1PQ-mNG	6xHis-TEV-SUMO-	*Sc*Ede1	366-591	-3C-mNeonGreen
pETM11	Ede1cc-mNG	6xHis-TEV-SUMO-	*Sc*Ede1	591-900	-3C-mNeonGreen
pETM11	Ede1PQcc-mNG	6xHis-TEV-SUMO-	*Sc*Ede1	366-900	-3C-mNeonGreen
pETM30	*Ct*Sla2 FL	6xHis-TEV-GST-	*Ct*Sla2	1-1050	-
pETM30	*Ct*Sla2 TH	6xHis-TEV-GST-	*Ct*Sla2	608-1050	-
pnEA	*Ct*ENTH	6xHis-TEV-	*Ct*Ent1	1-280	-

Table 8: Summary of primary purified protein properties

Construct	MW (Da)	Extinction coefficient ($M^{-1}cm^{-1}$)	pI	Accession ID
Sla2 ccRTH	69609	37150	4.87	P33338
Sla2 cc	53116	28420	4.70	P33338
Sla2 IDR	8533	1490	10.15	P33338
Sla2 TH	24834	9970	5.62	P33338
Sla2 PQcc mScarlet-I	79726	62925	4.97	P33338S
-vHisNusA CLC	84294	46410	4.51	P17891
CLC FL	26532	13980	4.31	P17891
CLC 1-80	9129	N.A.	3.85	P17891
CLC 70-140	7703	5500	4.20	P17891
CLC 70-233	18437	13980	4.64	P17891
CHC mNeonGreen	79401	113360	5.85	P22137
Sla1 SH3_3	6922	13980	6.36	P32790
Pan1 777-987	23485	9970	5.20	P32521
ATG16cc mScarlet-I	37886	39880	6.25	Q03818
Ede1 PQcc mNeonGreen	86518	56270	5.73	P34216
*Ct*Sla2 FL	118645	78730	5.68	G0S106
*Ct*Sla2 608-1050	48136	15930	5.42	G0S106

Table 9: Cryo-EM data collection, refinement, and validation statistics for *Sc*Sla2:560-968 as released in the EMDB entry 9HDD

This table provides the parameters and statistics for the data collection, processing, refinement, and structure validation. Refinement statistics were generated using the Servalcat package in wwPDB

	Sla2 C-terminal region
PDB code	**9HDD**
EMDB code	**EMD-52061**
Data collection and processing	
Microscope/detector	**Titan Krios G3i/K3**
Magnification	**120,000 x**
Voltage	**300kV**
Electron exposure (e/Å^2)	**45**
Defocus range (μm)	**-0.5 to -2**
Pixel size (Å)	**0.68**
Symmetry imposed	**C2**
Final particle images	**249299**
Reconstruction method	**Single Particle**
Map resolution (Å) ($FSC_{0.143}$)	**3.62**
Map Sharpening B factor (Å)	**Local Filter**
Refinement	
Initial model	**AF3 model of dimeric Sla2:560-968**
Model composition	
Non-hydrogen atoms	**6296**
Protein residues	**818**
R.m.s. Deviations (RMSZ)	
Bond lengths	**0.48**
Bond angles	**0.87**
Validation	
MolProbity score	**1.2**
Clashscore	**1**
Poor rotamers (%)	**0.1**
Ramachandran plot	
Favoured (%)	**96**
Allowed (%)	**4**
Disallowed (%)	**0**

Table 10: X-ray crystallography data collection, refinement, and validation statistics for Sla1 SH3_3 as deposited in the entry 9HDB

This table provides the parameters and statistics for the data collection, processing, refinement, and structure validation. Refinement statistics were generated using the Servalcat package in wwPDB. The values in parentheses refer to the highest resolution shell.

	Sla1 SH3_3
PDB ID	**9HDB**
Data collection	
Beamline	**PETRA III / P13**
Space Group	**P 21 21 21**
Cell Dimensions	
a , b, c (Å)	**38.53, 50.42, 51.97**
α, β, γ (°)	**90.00, 90.00, 90.00**
Resolution (Å)	**30.95-1.491 (1.544 - 1.491)**
Rpim	**0.02661 (0.136)**
<I/σI>	**3.29 (at 1.49Å)**
Mean (I/sd(I))	**15.6 (4.8)**
CC 1/2	**0.998 (0.962)**
Completeness (%)	**99.9 % (99.9 %)**
Redundancy	**10.0 (10.0)**
Refinement	
No. of reflections (work/free)	**17084/847**
Rwork/Rfree	**0.142/0.189**
Ramachandran favoured regions (%)	**99.16**
Ramachandran allowed regions (%)	**0**
Ramachandran outliers (%)	**0.84**
Rotamer outliers (%)	**0.0**
Clashscore	**0.51**
No. of non-Hydrogen atoms	
Protein	**1099**
Water	**111**
B-factors (Å^2) (Average)	**19.48**
Protein	**18.27**
Water	**30.28**
RMS deviations	
Bond lengths (Å)	**0.017**
Bond angles (°)	**2.02**

Example Size Exclusion Chromatography profiles for purified proteins

*Sc*Sla2 constructs

Sla2:351-968

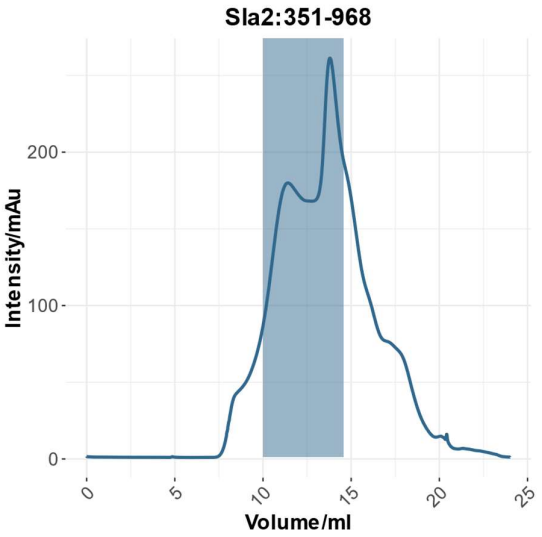

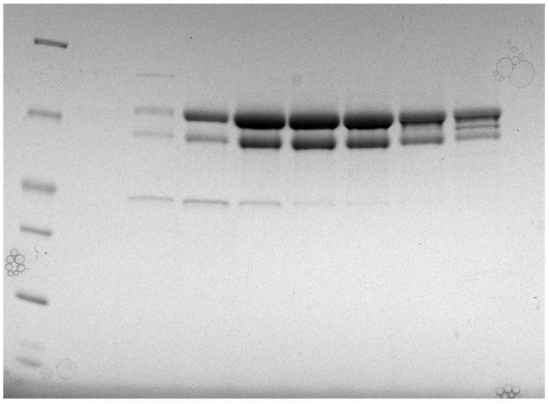

Top two dominant bands are Sla2:351-968 with minor degradation to N-terminal portion.

Sla2:296-767

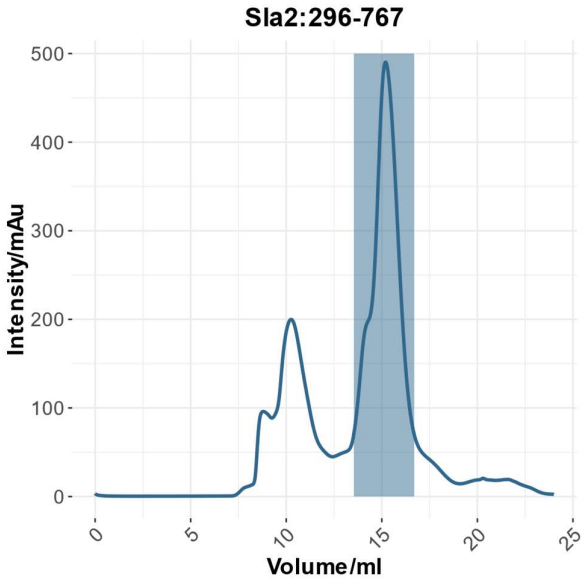

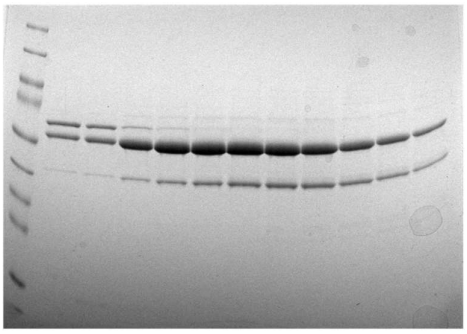

Top two dominant bands are Sla2:296-767 with minor degradation to N-terminal portion, which is an IDR.

Sla2:743-968

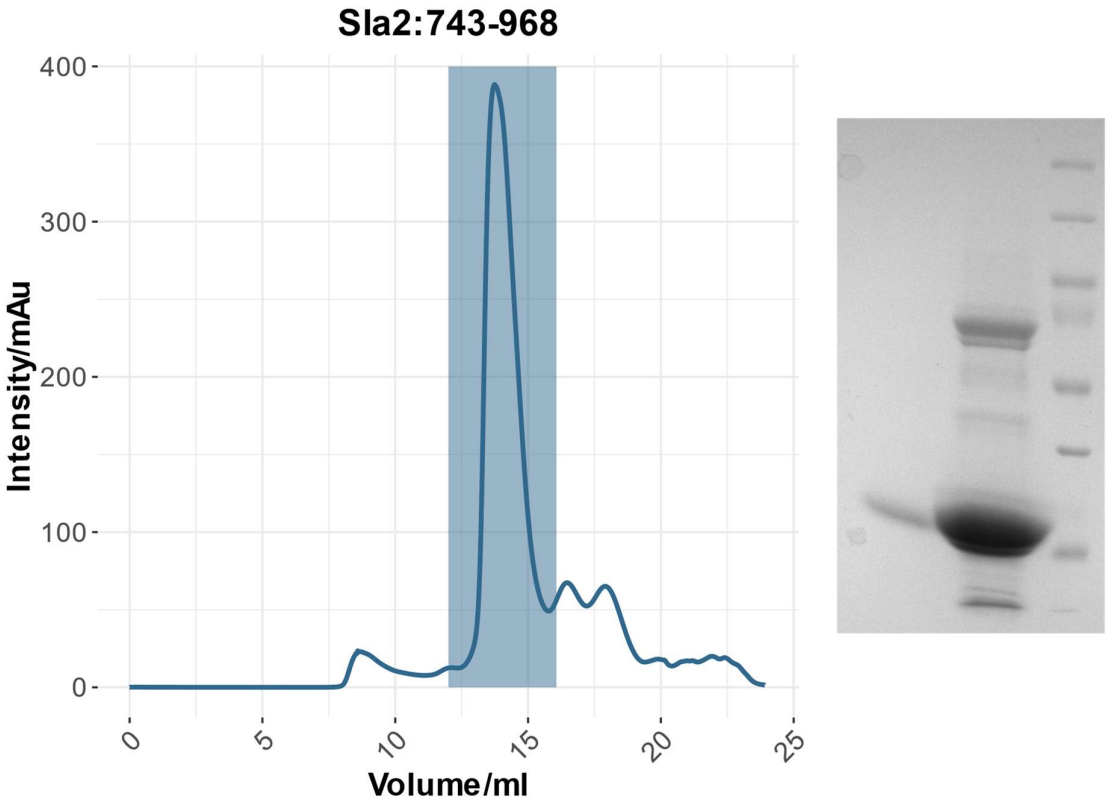

Minor band is un-cleaved GST-construct.

Sla2PQcc-mScarlet-I

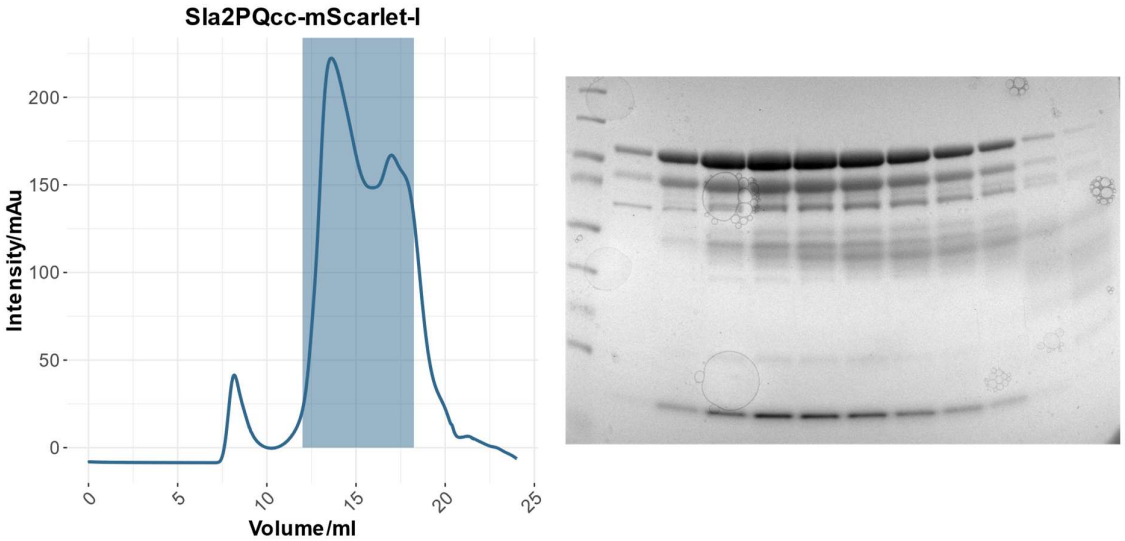

Minor bands are N-terminally degraded region of Sla2, which is an IDR and prone to such degradation.

Clathrin Light and Heavy Chain purifications

CLC FL

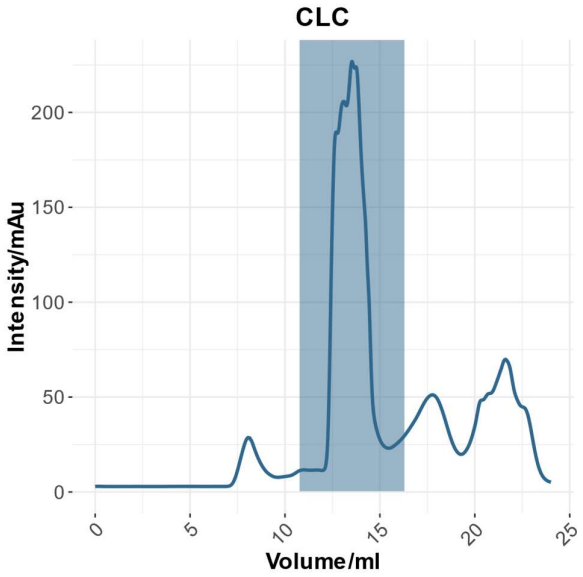

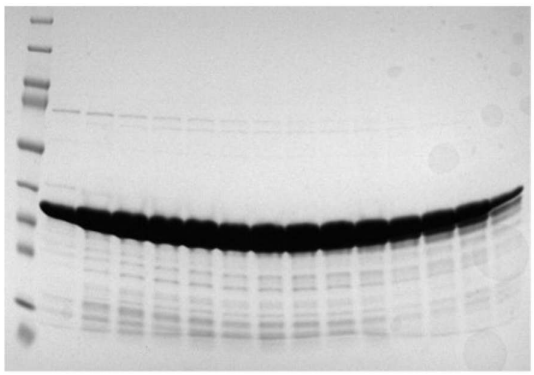

CLC 70-140

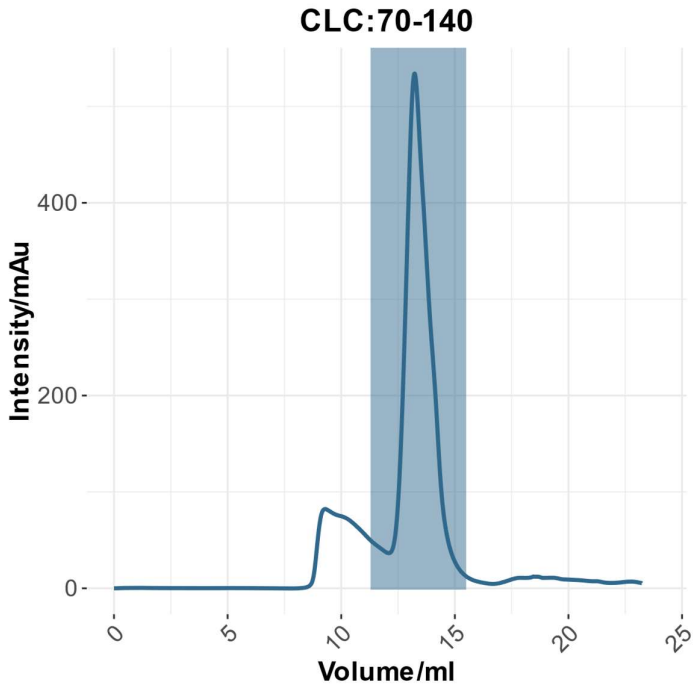

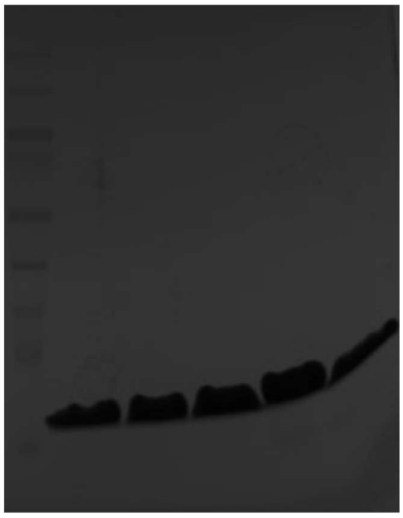

CLC 70-233

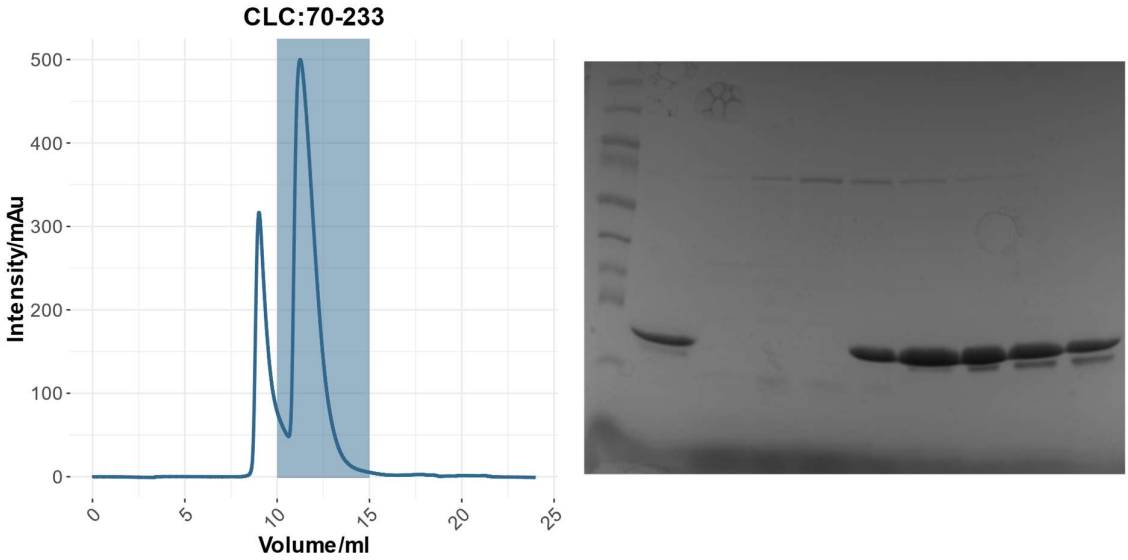

CLC 1-80

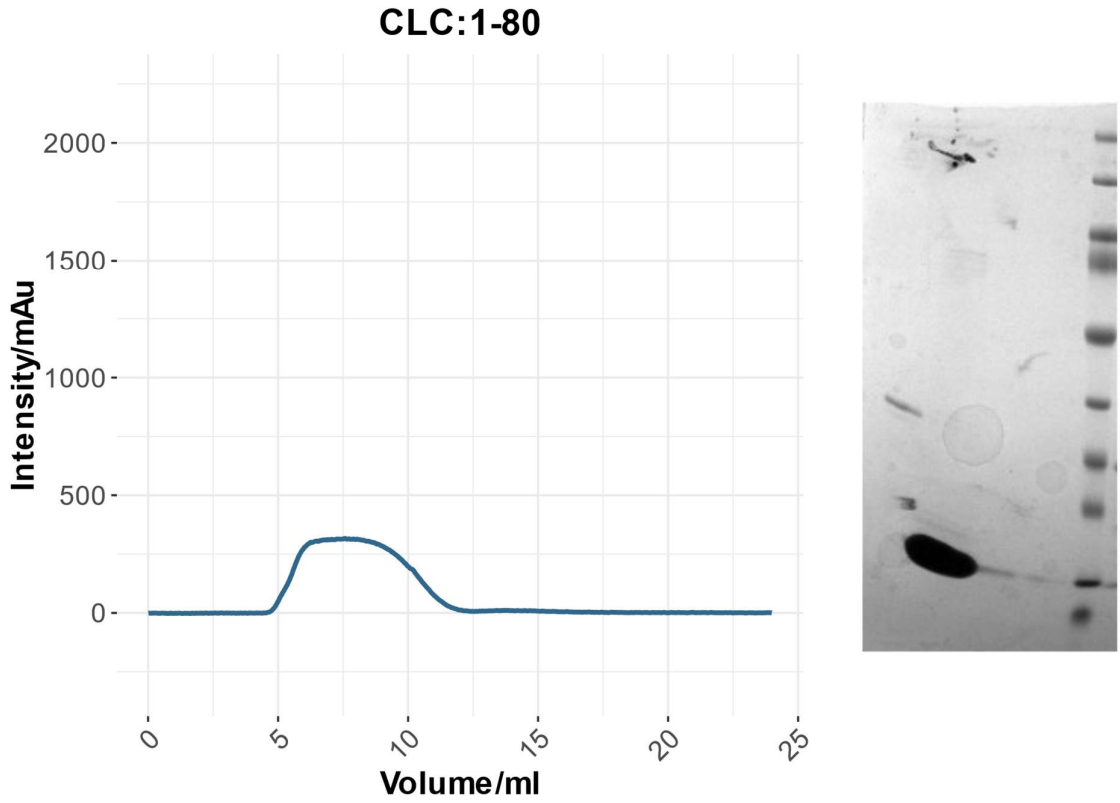

CHC:1172-1574-mNeonGreen

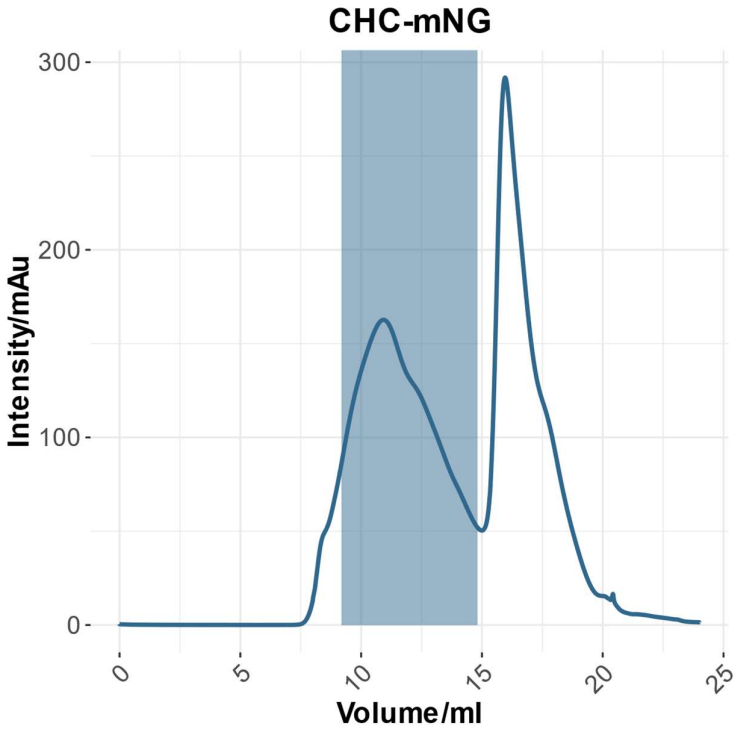

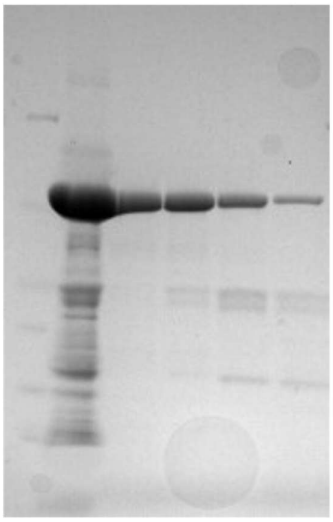

Additional protein purifications

Ede1PQcc-mNeonGreen

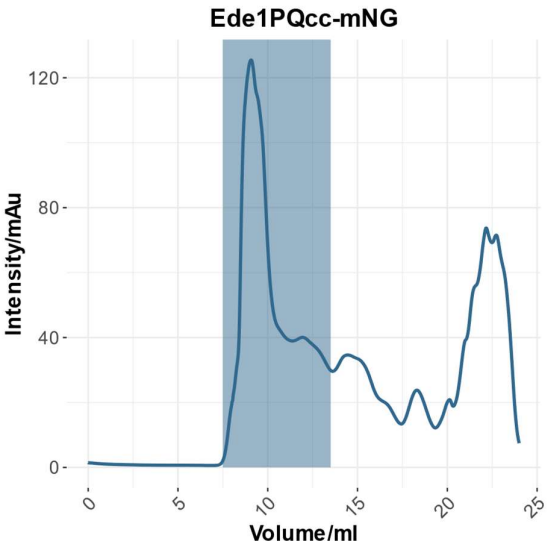

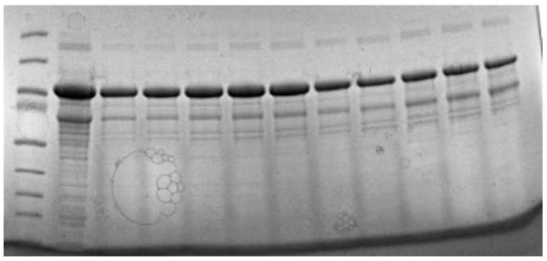

Minor band is due to N-terminal IDR degradation.

Pan1:777-987

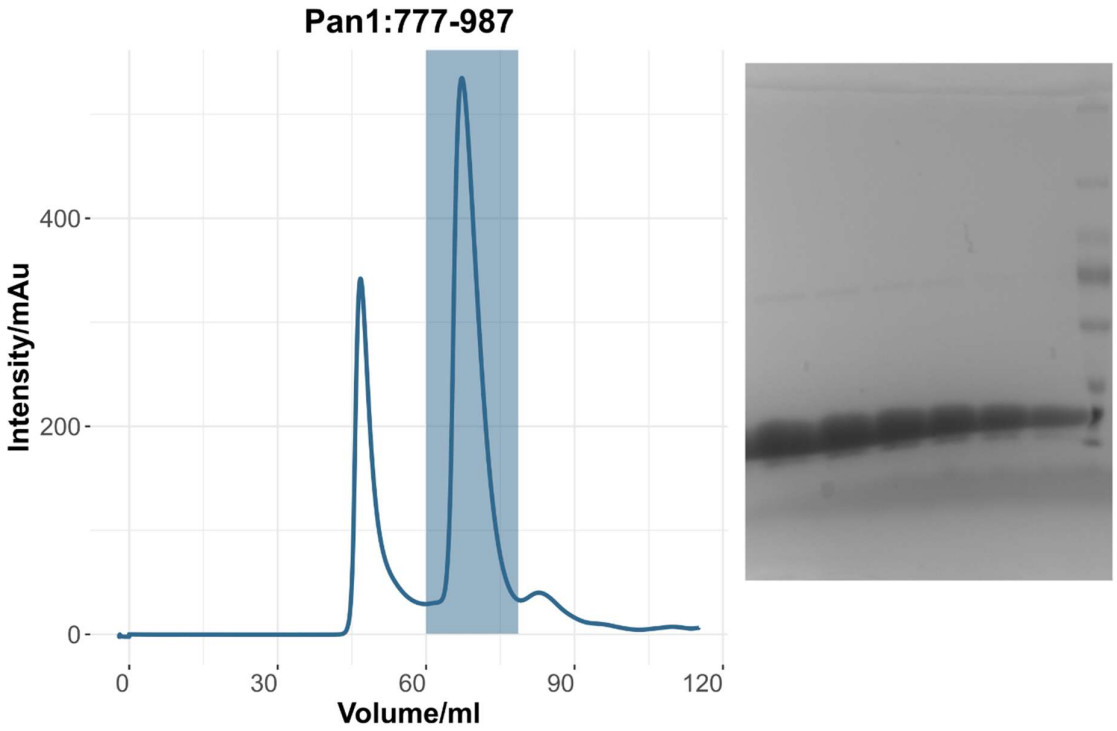

***Ct*Sla2:608-1050**

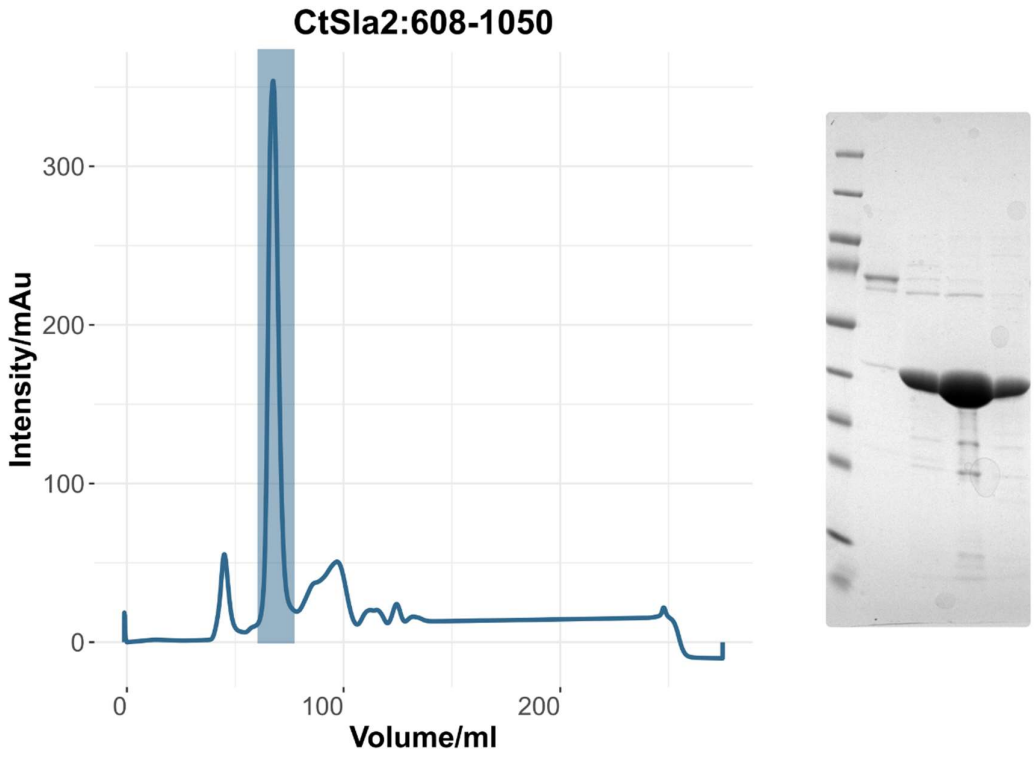

***Ct*Sla2:1-1050**

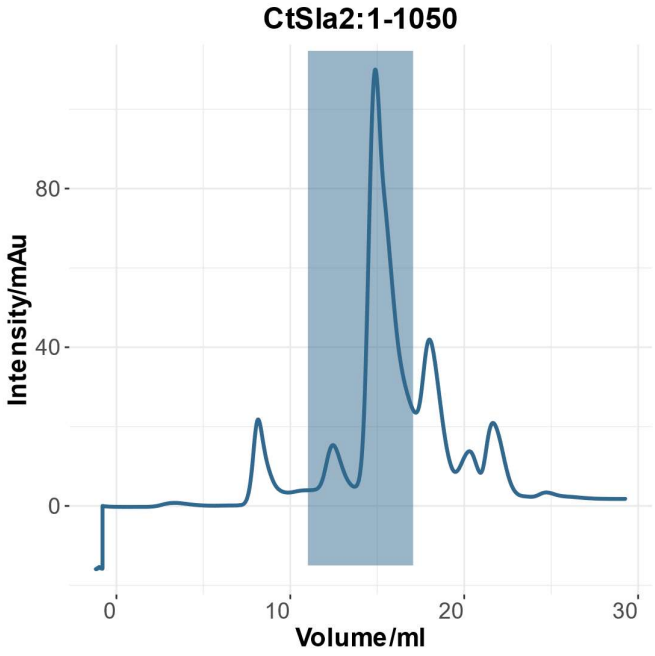

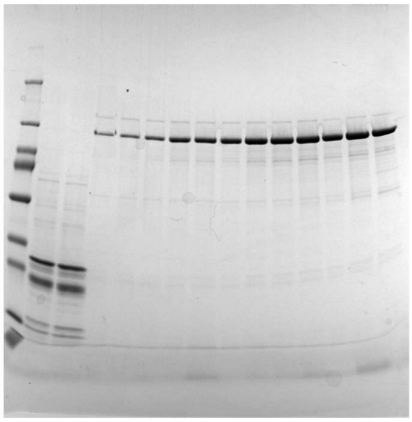

AlphaFold3 predictions of proteins purified for use in this study

AlphaFold prediction can show whether the protein construct of choice contains the region of interest, the amount of secondary structure present, and potential issues with purification.

AlphaFold confidence values:

*Sc*Sla2

Sla2: 270-350
pTM = 0.16

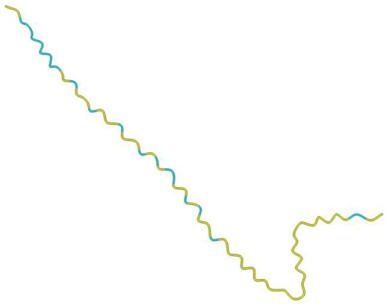

Sla2: 296-767
pTM = 0.43
ipTM = 0.4

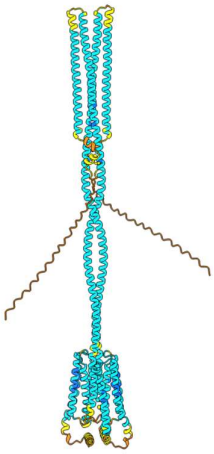

Sla2: 281-743
pTM = 0.43
ipTM = 0.4

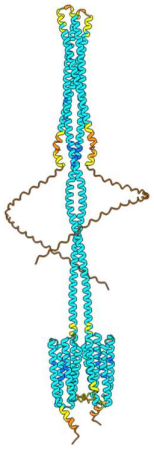

Sla2: 351-968
pTM = 0.66
ipTM = 0.64

*Ct*Sla2

Sla2: 1-1050
pTM = 0.38
ipTM = 0.4

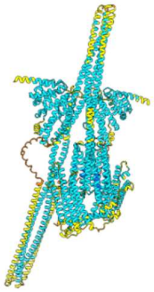

Sla2: 608-1050
pTM = 0.81
ipTM = 0.82

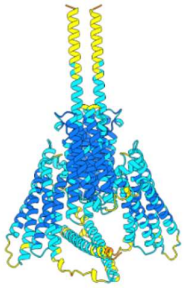

*Sc*CLC and *Sc*CHC

CHC: 1172-1574
pTM = 0.81

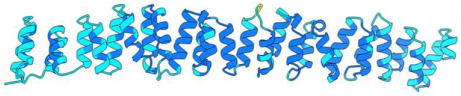

CLC: 1-233
pTM = 0.42

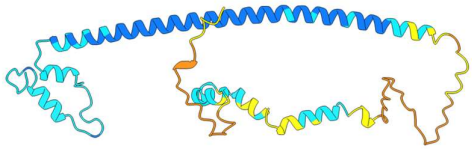

CLC: 1-80
pTM = 0.26

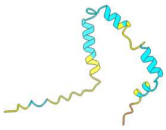

CLC: 70-140
pTM = 0.33

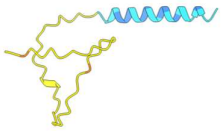

CLC:70-233
pTM: 0.47

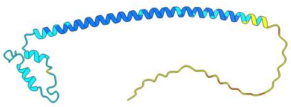

*Sc*Ede1, *Sc*Sla1, and *Sc*Pan1

Sla1: 355-414
pTM = 0.84

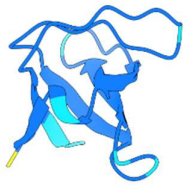

Pan1: 777-987
pTM = 0.67

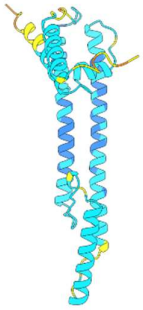

Ede1: 366-900
pTM = 0.26

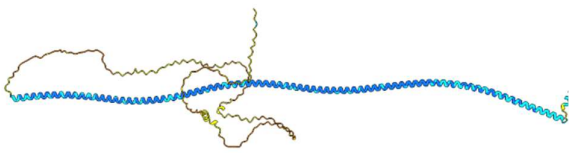

List of Hazardous Substances

Table 11: List of hazardous substances
For more information, check Globally Harmonized System of Classification and Labelling of Chemicals (GHS Rev. 10, 2023).

Name	GHS pictogram	GHS hazardous statements(H)	GHS precautionary statements(P)
1,4-dithiothreitol	GHS07	H302, H315, H319, H335	P261, P264, P264+P265, P270, P271, P280, P301+P317, P302+P352, P304+P340, P305+P351+P338, P319, P321, P330, P332+P317, P337+P317, P362+P364, P403+P233, P405, and P501
2-Propanol	GHS02, GHS07	H225, H31, H336	P210, P233, P240, P241, P242, P243, P261, P264+P265, P271, P280, P303+P361+P353, P304+P340, P305+P351+P338, P319, P337+P317, P370+P378, P403+P233, P403+P235, P405, and P501
Ampicillin disodium salt	GHS07, GHS08, GHS09	H315, H317, H319, H334, H335, H400, H411	P233, P260, P261, P264, P264+P265, P271, P272, P273, P280, P284, P302+P352, P304+P340, P305+P351+P338, P319, P321, P332+P317, P333+P317, P337+P317, P342+P316, P362+P364, P391, P403, P403+P233, P405, and P501
Calcium chloride	GHS07	H319	P264+P265, P280, P305+P351+P338, and P337+P317
Chloramphenicol	GHS05, GHS07, GHS08	H317, H318, H319, H350, H351, H361	203, P261, P264+P265, P272, P280, P302+P352, P305+P354+P338, P317, P318, P321, P333+P317, P362+P364, P405, and P501
cOmplete™ Protease Inhibitor Cocktail	GHS05	H314	P260 - P280 - P301 + P330 + P331 - P303 + P361 + P353 - P304 + P340 + P310 - P305 + P351 + P338 + P310
Dimethyl sufloxide	GHS07	H315, H319, H335	P261, P264, P264+P265, P271, P280, P302+P352, P304+P340, P305+P351+P338, P319, P321, P332+P317, P337+P317, P362+P364, P403+P233, P405, and P501
EDTA Tetrasodium salt	GHS07, GHS08	H302, H312, H315, H319, H332, H335, H373, H412	P260, P261, P264, P264+P265, P270, P271, P273, P280, P301+P317, P302+P352, P304+P340, P305+P351+P338, P317, P319, P321, P330, P332+P317, P337+P317, P362+P364, P403+P233, P405, and P501
Ethanol	GHS02, GHS07	H225, H319	P210, P233, P240, P241, P242, P243, P264+P265, P280, P303+P361+P353, P305+P351+P338, P337+P317, P370+P378, P403+P235, and P501
Ethidium Bromide	GHS06, GHS08	H302, H330, H331, H341	P203, P260, P261, P264, P270, P271, P280, P284, P301+P317, P304+P340, P316, P318, P320, P321, P330, P403+P233, P405, and P501
Glutathione	GHS08	H341	P203, P280, P318, P405, and P501

Hydrochloric acid	GHS05, GHS07	H280, H290, H314, H331, H335	P234, P260, P261, P264, P264+P265, P271, P280, P301+P330+P331, P302+P361+P354, P304+P340, P305+P354+P338, P316, P317, P319, P321, P363, P390, P403+P233, P405, P406, P410+P403, and P501
Imidazole	GHS05, GHS07, GHS08	H302, H314, H318, H360, H361	P203, P260, P264, P264+P265, P270, P280, P301+P317, P301+P330+P331, P302+P361+P354, P304+P340, P305+P354+P338, P316, P317, P318, P321, P330, P363, P405, and P501
InstantBlue™	GHS05	H315, H319	P264, P280, P302, P305, P313, P337, P338, P351, P352, P362
Kanamycin sulphate	GHS07	H360	P203, P280, P318, P405, and P501
Nickel (II) chloride hexahydrate	GHS06, GHS08, GHS09	H301, H315, H317, H331, H334, H341, H350, H350i, H360, H360d, H372, H400, H410	P203, P233, P260, P261, P264, P270, P271, P272, P273, P280, P284, P301+P316, P302+P352, P304+P340, P316, P318, P319, P321, P330, P332+P317, P333+P317, P342+P316, P362+P364, P391, P403, P403+P233, P405, and P501
Nitrogen	GHS04	H280, H281	P282, P336+P317, P403, and P410+P403
Pentane	GHS02, GHS07, GHS08, GHS09	H224, H225, H304, H336, H411	P210, P233, P240, P241, P242, P243, P261, P271, P273, P280, P301+P316, P303+P361+P353, P304+P340, P319, P331, P370+P378, P391, P403+P233, P403+P235, P405, and P501
RED-NHS 2nd generation labelling kit	GHS5, GHS07	H302, H317, H318, H335	P233, P261, P272, P280, P302, P305, P310, P313, P333, P351, P352, P338, P362, P364, P501
SDS	GHS02, GHS05, GHS07	H228, H302, H315, H318, H319, H332, H335, H412	P210, P240, P241, P261, P264, P264+P265, P270, P271, P273, P280, P301+P317, P302+P352, P304+P340, P305+P351+P338, P305+P354+P338, P317, P319, P321, P330, P332+P317, P337+P317, P362+P364, P370+P378, P403+P233, P405, and P501
Sekusept	GHS05, GHS07, GHS09	H226, H242, H301, H312, H314, H318, H330, H331, H332, H335, H400, H410	P210, P233, P234, P235, P240, P241, P242, P243, P260, P261, P264, P264+P265, P270, P271, P273, P280, P284, P301+P316, P301+P317, P301+P330+P331, P302+P352, P302+P361+P354, P303+P361+P353, P304+P340, P305+P354+P338, P316, P317, P319, P320, P321, P330, P362+P364, P363, P370+P378, P391, P403, P403+P233, P403+P235, P405, P410, P411, P420, and P501
Sodium Fluoride	GHS06	H301, H315, H319	P264, P264+P265, P270, P280, P301+P316, P302+P352, P305+P351+P338, P321, P330, P332+P317, P337+P317, P362+P364, P405, and P501
Sodium hydroxide	GHS05	H290, H314, H315, H318, H319	P234, P260, P264, P264+P265, P280, P301+P330+P331, P302+P352, P302+P361+P354, P304+P340, P305+P351+P338, P305+P354+P338, P316, P317, P321, P332+P317,

			P337+P317, P362+P364, P363, P390, P405, P406, and P501
Tris hydrochloride	GHS07	H315, H319, H335	P261, P264, P264+P265, P271, P280, P302+P352, P304+P340, P305+P351+P338, P319, P321, P332+P317, P337+P317, P362+P364, P403+P233, P405, and P501
Tris (2-carboxyethyl) phosphine	GHS05	H314, H318	P260, P264, P264+P265, P280, P301+P330+P331, P302+P361+P354, P304+P340, P305+P354+P338, P316, P317, P321, P363, P405, and P501

GHS Symbols

11 Acknowledgements

This thesis has been an accumulation of experiences and shifting paths for four and a half years. I would not have had this chance without my supervisor, Dr Maria Garcia-Alai. Maria gave me the opportunity to join her research team at the start of the pandemic. The support and confidence she placed in me to go about exploring the scientific landscape has made me a more curious and agile person. She has always found ways to help me narrow down my approach into a manageable workload, an important skill I won't forget. Thank you for everything!

I would like to thank the whole of the Garcia-Alai team, who have been there from start to finish and contributed to the success of my PhD. Through lab meetings and conversations in the corridor you all have provided feedback and a welcoming atmosphere over the years. I want to particularly thank Lucas, Fede, Stephan, Osvaldo, Agus, Katha, Angelica, and David for their help with experimental design, thoughtful discussion, suggestions for data analysis, and training.

I would also like to thank my collaborators Emil Gustavsson and Meytal Landau for their help and support with pushing my manuscript over the line. This is one of the major culminations for my PhD work and it has been amazing to have your support and feedback.

Thanks as well is needed for my Thesis Advisory Committee members, Jan Kosinski, Kay Grünewald, Simone Mattei, and Alba Diz-Muñoz. They provided much-needed feedback during the course of my PhD. This is clearly an additional responsibility on top of their crammed schedules and the yearly meetings helped set up a good routine of evaluation for myself. Looking back at my reports I can see how much has improved over the course of these four years.

This thanks also is extended to the EMBL Graduate Office, particularly Monika Lachner, that facilitated everything I have done here with the EMBL International PhD programme. The facilities available in both Hamburg and Heidelberg have greatly improved the output that I had during the course of my PhD. From Heidelberg I wish to thank the Proteomics Core Facility, Mandy Rettel and Jennifer Schwarz. In EMBL Hamburg, Cy Jeffries (Blanchet Team) and Gelb Bourenkov (Schneider Team) for

their assistance with data collection at the P12 and P13 beamlines respectively for SAXS and X-Ray crystallographic data collection. The facilities at CSSB were the primary area of my data collection and training for the techniques that shaped my project. I wish to thank the cryo-EM facility and all the staff, especially Cornelia Cazey for her patience and time training me from negative stain through to the final data collections on the Krios. Thank you as well to Roland Thünauer, whose management of the ALFM and the keenness to see users succeed was a great help.

I want to thank all my friends both in Hamburg and back home. They have provided a needed break at times from the trials and tribulations of the work. Ryan, Will, Noah, Andrew, Luther, and Henry, thank you for being there on the other end of the line when I needed to talk. Emil, Marine, Katharina, Thea, Simon, and the whole climbing crowd you have been one of the biggest and best surprises of my time here. These bonds are formed forever and wherever we are all headed there is a place on the end of the phone-line or in the pub for everyone.

Finally, to my family and Sophie, this wouldn't have been possible without you all along for the ride. All of you have been a part of picking me up when I was down, keeping my spirits up during the trying moments, and sharing in the highs. Thank you for being there, I could not have achieved what I have and enjoyed the journey as much as I did without you.

THANK YOU TO EVERYONE. IT HAS BEEN ADVENTURE.

Declaration of Oath

I hereby declare on oath that this doctoral dissertation is written independently and solely by my own based on the original work of my PhD and has not been used other than the acknowledged resources and aids. The submitted written version corresponds to the version on the electronic storage medium. I declare that the present dissertation was prepared maintaining the Rules of Good Scientific Practice of the German research Foundation and it has never been submitted in the present form or similar to any other University or board of examiners.

Signature

Date: 9th January 2025

I hereby declare and affirm that this doctoral dissertation is my own work and that I have not used any aids and sources other than those indicated. If electronic resources based on generative artificial intelligence (gAI) were used in the course of writing this dissertation, I confirm that my own work was the main and value-adding contribution and that complete documentation of all resources used is available in accordance with good scientific practice. I am responsible for any erroneous or distorted content, incorrect references, violations of data protection and copyright law or plagiarism that may have been generated by the gAI..

Signature

Datum: 9th January 2025